KU LEUVEN

ARENBERG DOCTORAL SCHOOL
Faculty of Engineering Science

Optimization of the Energy Conversion Starting from Low-Temperature Heat

Application to Geothermal Binary Cycles

Daniël Walraven

Supervisor:
Prof. dr. ir. W. D'haeseleer

Dissertation presented in partial fulfillment of the requirements for the degree of Doctor in Engineering

November 2014

Optimization of the Energy Conversion Starting from Low-Temperature Heat

Application to Geothermal Binary Cycles

Daniël WALRAVEN

Examination committee:
Prof. dr. ir. P. Van Houtte, chair
Prof. dr. ir. W. D'haeseleer, supervisor
Prof. dr. ir. M. Baelmans
Prof. dr. ir. R. Belmans
Prof. dr. ir. L. Helsen
Prof. dr. P. Valdimarsson
(Atlas Copco Energas GmbH, Germany & Reykjavik University, Iceland)
Prof. dr. P. Bombarda
(Politecnico di Milano, Italy)
Dr. B. Laenen
(VITO, Belgium)

Dissertation presented in partial fulfillment of the requirements for the degree of Doctor in Engineering

November 2014

Uitgegeven in eigen beheer, Daniël Walraven, Celestijnenlaan 300 box 2421, B-3001 Heverlee (Belgium)

ISBN 978-94-6018-907-4

D/2014/7515/131

Preface - Voorwoord

> Life is like riding a bicycle. To keep your balance, you must keep moving.
>
> Albert Einstein

For you this text is the beginning of a book, for me the end of a chapter. A text that is the result of journey in which I encountered a lot of interesting people and in which I got to know myself a bit better (perhaps does the slogan of the university make sense). But this journey was not possible without the help and support of some people to whom I want to express my gratitude.

Ten eerste wil ik mijn promotor professor William D'haeseleer bedanken voor de kans die hij mij gegeven heeft om bij hem te doctoreren. Het was een winterse dag in januari 2010 en na enkele uren wachten tijdens het examen Kernenergie (het was zo'n typisch "D'haeseleer-examen") was ik eindelijk aan de beurt. De laatste vraag was een verrassing: of ik bij hem wilde komen doctoreren. Een maand later – toen was het ook al zo moeilijk om een gaatje in zijn agenda te vinden – stelde hij een aantal onderwerpen voor. Het eerste en tweede onderwerp stonden mij niet echt aan, en dat was blijkbaar gemakkelijk van mijn gezicht af te lezen, maar er was nog een joker: diepe geothermie. Een op het eerste gezicht nogal vreemd onderwerp, maar één dat vrij snel op mijn interesse kon rekenen. Ik wil hem ook bedanken voor de vrijheid die ik gekregen heb tijdens mijn hele doctoraat.

Dit werk was ook niet mogelijk geweest zonder de financiële ondersteuning van VITO, waar dit doctoraat kadert in het plan om de eerste geothermische elektriciteitscentrale in België te bouwen en diepe geothermie in Vlaanderen op de kaart te zetten. Een straffe uitdaging waar ik met plezier aan meegewerkt heb, maar ook een project waar veel bij komt kijken. Hopelijk kunnen we er binnen enkele jaren met trots op terugblikken!

I would also like to thank the members of the examination committee for critically reviewing the manuscript, for giving valuable comments and for sharing their experience: professor Martine Baelmans, professor Ronnie Belmans, professor Lieve Helsen, professor Páll Valdimarsson, professor Paola Bombarda and Ben Laenen. Special thanks to Ben for supervising me at VITO and for professor Valdimarsson for sharing part of his immense knowledge on the topic. I would also like to thank professor Paul Van Houtte for chairing the jury.

I really enjoyed the time at TME. The discussions at lunch (if there was no Trudo/Alma day) about fundamental scientific issues or ridiculous brain teasers – often thanks/due to Tijs –, the TME-activities and the fantastic work environment were, and still are, the reasons why work and fun were/are closely related. Thank you for that. Special thanks to all my office colleagues in the previous years and especially the "fixed" ones (Juliana, Stefan, Wouter, Mats, Roel and Andreas). Ook veel dank aan Ruben voor de warmtewisselaarsdiscussies en de wederzijdse ondersteuning tijdens onze eindfase van het doctoraat, aan Joris G. voor de hulp met CasADi en aan Valérie en Frieda voor de administratieve hulp.

Although I only spent one day a week at VITO and arrived often late and frustrated (NMBS) or late and sweating (bike), I would also like to thank the colleagues at VITO.

En ten slotte degenen die het meeste met mijn (soms) nogal moeilijk karakter te maken krijgen: vrienden en familie. In het bijzonder denk ik dan aan mijn ouders die mij alle mogelijke kansen gegeven hebben, die mij een stamp onder mijn gat gegeven hebben als het nodig was en die mij terug naar de realiteit gebracht hebben (of toch geprobeerd hebben) als ik weer zo'n vreemd plan had. En bedankt aan Stefan en Andrea voor de tips, voor de steun in leuke en minder leuke momenten, de plagerijen en simpelweg voor het zijn en laten zijn, wie we zijn. Ook dank aan opa en oma/moemoe Kanne voor onder andere de fantastische zomers en de verwennerij – spijtig dat hij de verdediging van "mon petit-fils" en zoveel anders niet meer mocht meemaken –, en dank aan opa en oma Nijlen en de rest van de familie Walraven & co voor de familiefeesten en de zondagen in Nijlen. Ik heb gehoord dat Oh-Noh het leuk vond dat hij met "Oh-Noh" vermeld staat in het doctoraat van Stefan, dus hierbij dank aan Oh-Noh voor het opvrolijken van alles en nog wat en het serieus zijn wanneer we hulp nodig hebben. En de vaste vrienden uit onze studententijd Marnix en Christophe passen ook nog net op de pagina.

En voor al degenen die ik vergeten ben: sorry en dank u wel.

Daniël Walraven,
October 2014

Abstract

Low-temperature geothermal heat sources can be found in many regions in the world, but despite their huge energetic potential, only a limited amount of these sources are used. These heat sources are in most cases not free and wells have to be drilled to access the geothermal heat. One injection well and one or more production wells are usually used and depths down to several kilometers are needed to obtain a temperature high enough to be useful. These deep geothermal wells are very expensive, so, the obtained geothermal heat should be used very efficiently for electricity generation and or for heating purposes.

Due to the low temperature, the conversion efficiency of the geothermal heat into electric power is low (Carnot). The effect of this low efficiency is in fact twofold. First, relatively large amounts of heat, and thus large equipment, are needed to generate a unit of electricity. Second, most of the heat which is added to the power plant has to be dumped into the environment. This results in a relatively large and expensive cooling system and a relatively large water and or electricity consumption in this cooling system. The consequence is that the investment cost of geothermal power plants per installed capacity is high.

The goal of this work is to develop a model and algorithm which can find the optimal economic design of low-temperature geothermal power plants, with a focus on the electricity-generating system. Different types of binary power cycles, which are typically used for electricity generation from low-temperature heat, like the organic Rankine cycle (ORC) and the Kalina cycle are implemented. Detailed models for two types of heat exchangers, of an axial turbine and of both wet and dry cooling are added. A system optimization is performed by optimizing the configuration of the binary cycle and all the components together, resulting in components which are optimal to be used together and to be used in the obtained cycle.

It is shown from a *thermodynamic* point of view that well-optimized ORCs perform better than Kalina cycles and that multi-pressure, subcritical ORCs

and single-pressure, transcritical ORCs are the most promising ones. ORCs with plate heat exchangers perform usually better than ORCs with shell-and-tube heat exchangers, while not taking fouling and corrosion into account. The advantage of shell-and-tube heat exchangers is that the geometry of the hot-fluid side and the cold-fluid side are different and can vary almost independently from each other.

Cooling with water, which is cooled in a mechanical-draft wet cooling tower, results in better economics than cooling with an air-cooled condenser in the investigated case. This is especially due to the high investment cost of the air-cooled condenser, but also due to the high electricity consumption of this type of cooling. Only when water is expensive, cooling with air can be the better choice. These results are valid for the moderate climate in Belgium. For other climates these conclusions do not necessarily hold.

Beknopte samenvatting

Lage-temperatuur geothermische warmtebronnen zijn in vele regio's in de wereld te vinden, maar ondanks hun groot energetisch potentieel wordt slechts een klein deel van deze bronnen gebruikt. Meestal zijn deze bronnen niet gratis en moeten putten geboord worden om de geothermische warmte te bekomen. Eén injectiebron en één of meerdere productiebronnen worden normaal gebruikt en de diepte van de putten kan enkele kilometers bedragen opdat de temperatuur voldoende hoog is. Deze diepe putten zijn heel duur, dus de bekomen geothermische warmte moet op een efficiënte manier aangewend worden voor elektriciteitsproductie en/of voor warmtelevering.

Door de lage temperatuur is het conversierendement van de geothermische warmte naar elektriciteit laag (Carnot). Dit heeft twee gevolgen. Ten eerste is er een relatief grote hoeveelheid warmte, en dus relatief grote toestellen, nodig om een eenheid elektriciteit te genereren. Ten tweede moet het grootste deel van de warmte, die toegevoegd wordt aan de centrale, gedumpt worden in de omgeving. Het gevolg is een relatief grote en dure koelinstallatie die relatief veel water en/of elektriciteit verbruikt. Dit alles leidt tot een hoge investeringskost voor geothermische elektriciteitscentrales per geïnstalleerd vermogen.

Het doel van dit werk is om een model en algoritme te ontwikkelen dat gebruikt kan worden om het economische optimale ontwerp van lage-temperatuur geothermische centrales te vinden, met een focus op elektriciteitsproductie. Verschillende binaire cycli, die typisch gebruikt worden voor elektriciteitsproductie uit lage-temperatuur warmte, zoals de organische Rankinecyclus (ORC) en de Kalinacyclus, zijn geïmplementeerd. Gedetailleerde modellen voor twee types van warmtewisselaars, van een axiale turbine en van zowel water- als luchtkoeling zijn toegevoegd. Een systeemoptimalisatie wordt uitgevoerd door de configuratie van de binaire cyclus en de configuratie van alle componenten samen te optimaliseren. Dit leidt tot componenten die optimaal zijn om samen te werken en optimaal zijn voor gebruik in de bekomen cyclus.

In dit werk wordt aangetoond dat goed geoptimaliseerde ORC's beter presteren dan Kalinacycli vanuit *thermodynamisch* oogpunt en dat multi-druk, subkritische cycli en enkel-druk, transkritische ORC's het best presteren. ORC's met platenwarmtewisselaars presteren meestal beter dan ORC's met trommel-en-pijp-warmtewisselaars, zonder rekening the houden met fouling en corrosie. Het voordeel van trommel-en-pijp-warmtewisselaars is dat the geometrie van de warme zijde en van de koude zijde verschillend zijn en bijna onafhankelijk van elkaar kunnen veranderen.

Koeling met water in een mechanische-trek, natte koeltoren is economisch voordeliger dan het gebruik van luchtkoelers voor de onderzochte parameters. Dit komt vooral door de hoge investeringskost van luchtkoelers, maar ook door het hoge elektriciteitsverbruik van dit type koeling. Alleen wanneer water duur is, is koeling met lucht de beste optie. Deze resultaten zijn enkel geldig voor regio's met een klimaat gelijkaardig aan dat van België.

Abbreviations

ACC	Air-cooled condenser
BCV	Ball check valve
C	Condenser
CCGT	Combined cycle gas turbine
CEPCI	Chemical Engineering Plant Cost Index
CFD	Computational fluid dynamics
CHP	Combined heat and power
COP	Coefficient of performance
CP	Condensate pump
CS	Cyclone separator
CSV	Control & stop valve
CT	Cooling tower
CWP	Cooling-water pump
EGS	Enhanced/Engineered Geothermal System
EPC	Engineering, procurement & construction
EPCCI	European Power Capital Costs Index
HDR	Hot Dry Rock
IW	Injection well
LCOE	Levelized cost of electricity
MINLP	Mixed integer non-linear problem
MR	Moisture remover
NPV	Net present value

ORC	Organic Rankine cycle
PCCI	Power Capital Costs Index
PR	Particulate remover
PW	Production well
S	Silencer
SE/C	Steam ejector/condenser
SP	Steam pipe
T/G	Turbine/generator
TEMA	Tubular Exchanger Manufacturers Association
WCT	Wet cooling tower
WP	Water piping
WV	Wellhead valve

List of Symbols

Greek

α	Void fraction
β	Angle of the corrugations [rad]
Δ	Difference
δ_{bb}	Diametrical shell-to-tube bundle bypass clearance [m]
δ_{sb}	Shell-to-baffle clearance [m]
δ_{tb}	Diametrical clearance [m]
ϵ	Effectiveness
ϵ_i	Improvement of the addition of the ith pressure level
ε	Fraction of mass flow rate extracted from turbine in bleeding cycle
ε	Vapor mass fraction in Kalina cycle
η	Efficiency
Λ	Corrugation width [m]
μ	Viscosity [Pa s]
Φ	Area-enlargement factor
$\phi_{t,n}$	Correction factor for tube bundle inlet and outlet pressure drops
ρ	Density [kg/m^3]
θ	Angle in A-frame ACC [°]
ζ	Correction factor for non-ideality in pressure drop in the shell

Roman

A	Surface [m^2]
a	Corrugation amplitude [m]
a	Speed of sound [m/s]
A_{fr}	Frontal area of the packing [m^2]
$A_{fr,t}$	Area occupied by tubes in the window section [m^2]
$A_{fr,w}$	Gross window area [m^2]
$A_{o,cr}$	Cross-flow area at the shell center line [m^2]
$A_{o,sb}$	Shell-to-baffle leakage area [m^2]
$A_{o,tb}$	Total tube-to-baffle leakage area [m^2]
$A_{o,w}$	Net flow area in one window section [m^2]
a_{pa}	Area density of the packing [m$^-$1]
Bo_{eq}	Equivalent boiling number
C	Cost [€]
c	Absolute velocity [m/s]
c_p	Heat capacity at constant pressure [J/kgK]
D_{ctl}	Diameter of the circle through the center of the outermost tubes [m]
d_d	Mean diameter of a droplet [m]
$D_{h,w}$	Hydraulic diameter of the window section [m]
d_o	Tube outside diameter [m]
D_{otl}	Diameter of the outermost tubes [m]
D_s	Shell outside diameter [m]
$\dot{E}$	Exergy [W]
e	Specific flow exergy [J/kg]
f	Correction factor for non-standard material ($_M$), pressure ($_P$) or temperature ($_T$)

f	Fanning friciton factor
F_b	Correction factor for the effect of convection
F_{bp}	Flow area for bypass stream C
F_c	Fraction of tubes in the cross-flow section
F_w	Fraction of number of tubes in one window section
G	Mass velocity [kg/m^{2}s]
H	Fin height [m]
h	Heat-transfer coefficient [W/m^{2}K]
h	Specific enthalpy [J/kg]
h_d	Mass transfer coefficient [kg/m^{2}s]
Hg	Hagen number
H_i	Inlet height [m]
H_{pa}	Packing height [m]
H_{sp}	Height of the spray zone [m]
$\dot{I}$	Irreversibility [W]
I	Income [€]
i	Discount rate [%]
J	Correction factor for non-ideality in heat transfer in the shell
k	Loss coefficient
k	Thermal conductivity [W/mK]
L	Length [m]
L_b	Baffle spacing [m]
l_c	Baffle cut length [m]
Le_f	Lewis factor
L_h	Length of a plate for heat transfer [m]
L_p	Length of a plate between ports [m]

Lq	Lévêque number
L_t	Length of the tubes [m]
$\dot{m}$	Mass flow rate [ks/s]
Me_P	Merkel number
N	Number of full-load hours
n	Rotational speed [rps]
N_b	Number of baffles
N_p	Number of channels
N_r	Number of rows
$N_{r,cc}$	The number of tube rows crossed in one cross-flow section
$N_{r,cw}$	Number of effective tube rows in cross flow in the window section
N_S	Specific speed
N_t	Number of tubes
Nu	Nusselt number
p	Pressure [Pa or bar]
p_{elec}	Electricity price [€/MWh]
Pr	Prandtl number
p_t	Pitch between tubes [m]
$\dot{Q}$	Heat input [W]
$\dot{q}$	Heat flux [W/m^2]
R	Specific gas constant [J/kgK]
Re	Reynolds number
r_i	Inlet rounding [m]
S	Fin pitch [m]
s	Specific entropy [J/kg K]
T	Temperature [°C or K]

t	Time [year]
u	Blade velocity [m/s]
$\dot{V}$	Volumetric flow rate [m^3/s]
V	Volume [m^3]
v	Specific volume [m^3/kg]
v	Velocity [m/s]
$\dot{W}$	Mechanical power [W]
W	Width of a plate [m]
w	Humidity ratio [kg-water/kg-dry air]
w	Relative velocity [m/s]
W_l	Tubes' large width [m]
W_s	Tubes' small width [m]
W_t	Width of the tower [m]
X	Dimensionless corrugation parameter
x	Concentration mixture
x	Vapor quality
Y^2	Chisholm parameter

Sub- and superscripts

∞	Property at infinite distance
0	Dead state
0	Reference state
$1 \cdots 11$	Number of the state
a	Dry air
air	Air
$Amin$	Minimum flow area
av	Average

$available$	Available
B	Bottom
b	Flow between baffles
$brine$	Brine
c	Center
c	Critical
$cond$	Condenser
$cond$	Condensing
$cooling$	Cooling
cr	Cross flow
$crit$	Critical
ct	Tower inlet
cw	Cooling water
$cycle$	Cycle
de	Drift eliminator
$drilling$	Drilling
E	Equipment
el	Electrical
en	Energetic
EPC	EPC
$evap$	Evaporation
ex	Exergetic
fan	Fan
fr	Frictional
h	Homogeneous flow
$high$	High

HX	Heat exchanger
i	Inlet
id	Ideal
il	Inlet louvers
in	Inlet
int	Intermediate
is	Isentropic
l	Saturated liquid
lam	Laminar flow
lo	All fluid saturated liquid
low	Low
LT	Lifetime
M	Middle
ma	Wet air
$masw$	Saturated wet air at water temperature
min	Minimum
mix	Mixing
nb	Nucleate boiling
nc	Natural convection
net	Net
o	Outlet
$O\&M$	Operation and maintenance
ORC	ORC
out	Outlet
P	Pump
pa	Referenced to the packing section

$pack$	Packing
$plant$	plant
ps	Packing support structure
r	Reduced
$recup$	Recuperator
rz	Rain zone
s	Isentropic
s	Shell
sa	Saturated at air temperature
sat	Saturation
$single$	Single-phase flow
sp	Spray region
ss	Supersaturated air
sw	Saturated at water temperature
T	Top
T	Turbine
Td	Dry turbine
tot	Total
$turb$	Turbulent flow
Tw	Wet turbine
up	Fan upstream
v	Saturated vapor
v	Water vapor
w	Liquid water
w	Window flow
$water$	Water

T_{wb}	Wet-bulb temperature
wd	Water distribution
wf	Working fluid

Contents

Chapter 1

Introduction

Renewable electricity generation is becoming more and more important. Especially hydropower, bioenergy, wind and solar PV have grown strongly over the last decade [53]. The increase of the installed capacity of geothermal power plants was also very strong, but the worldwide electric energy generation remains marginal. The share of direct use[1] of geothermal heat is also relatively low [52], although the amount of stored thermal energy in the earth is huge. The interior of our planet is hot because of the primordial thermal energy, which was generated during the formation of the earth, and because of the decay of long-lived radioactive isotopes. The hard part of deep geothermal energy is that in most regions of the world, this geothermal heat appears at the surface at a temperature which is far too low to be used. In the first section of this chapter, geothermal heat sources are described, followed by an overview of typical geothermal power plants. Afterwards, the challenges for the development of low-temperature geothermal energy conversion are described and the goals of this work are given.

1.1 Geothermal heat sources

The core of the earth has a temperature of about 4000°C, while the average surface temperature of the earth is about 10°C [11]. This means that the temperature increases with increasing depth inside the earth. The average temperature gradient near the surface is about 30°C/km, but it can be more than 100°C/km in regions with active volcanism. To capture the heat at a

[1] Geothermal heat pumps are not seen as direct use of the heat.

temperature which is high enough for electricity generation and or for the direct use of the heat, two different systems exist: hydrothermal systems, in which a water reservoir is available subsurface, and Enhanced/Engineered Geothermal Systems (EGS), also known as Hot Dry Rock (HDR).

1.1.1 Hydrothermal systems

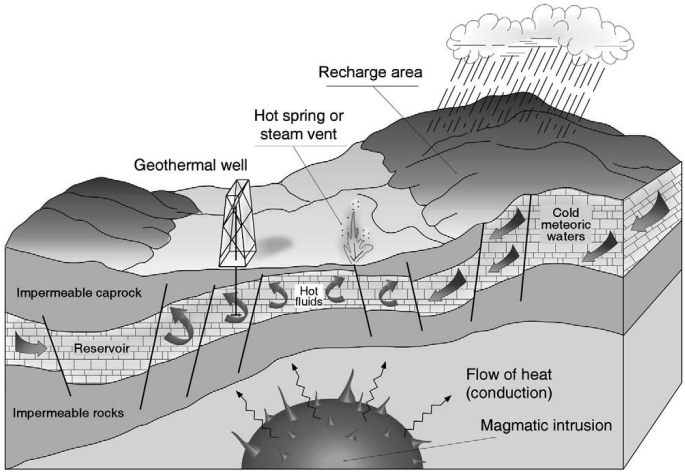

Figure 1.1: Scheme of a hydrothermal system with the necessary conditions. Figure from Barbier [11].

The classical geothermal heat source is a hydrothermal system, which is shown in figure 1.1, with all the necessary conditions for geothermal energy conversion. The first condition is that a water reservoir should exist subsurface. This means that layers of impermeable rock have to exist, so that water is trapped between the layers . A recharge area is/was needed so that water gets/could get between the layers. Second, the water should be at a relatively high temperature, which is achieved by heat conduction through the rocks below the reservoir. As a third condition, the reservoir should be accessible for drilling. In some regions of the world, the reservoir is manifested at the surface in the form of hot springs, geysers, etcetera, and the hot water and or steam can be directly captured. In most cases, drilling is needed to reach the reservoir and at least one production well is needed to bring the hot fluid to the surface. An injection well is often used to avoid a strong decrease of the pressure in the reservoir and to avoid the dumping of the, often not clean, geothermal fluid into the surroundings. A system with one production well and one injection well is called a doublet. A triplet and a quadruplet have two and three production wells, respectively [29].

Often, a distinction is made based on the temperature and phase of the fluid in the hydrothermal system. Vapor-dominated fields exist in which vapor at a high temperature and pressure is found, but most hydrothermal fields are water-dominated, in which the fluid can be wet steam or completely liquid.

1.1.2 Enhanced geothermal system

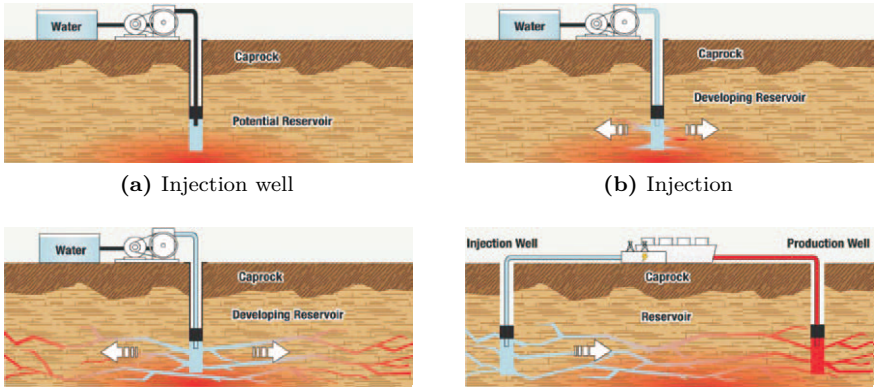

(a) Injection well **(b)** Injection

(c) Hydro-fracture **(d)** Production

Figure 1.2: The development of an EGS. Figure from IEA [52].

In many regions, the three conditions for a hydrothermal system are not met; often the underground is warm, but no water reservoir is available. In such cases, Enhanced/Engineered Geothermal Systems (EGS), also known as Hot Dry Rock (HDR), can be used. At the moment, the technology is still in the research phase, but the goal is to create an underground heat exchanger. Figure 1.2 shows how such a system would be developed. First, an injection well is drilled (figure 1.2a) in which water is pumped at a high pressure (figure 1.2b) in order to fracture part of the rocks (figure 1.2c). Chemicals can be dissolved in the water to facilitate the fracturing[2]. This last step is critical in the development of EGS systems. The rocks have to be fractured enough so that water can flow through them with a limited pressure drop, but they should not be fractured too much so that the contact area between water and rocks remains large. Afterwards, a production well is drilled (figure 1.2d) in order to bring part of the injected water, which is heated in the meantime, back to the

[2]This "fracturing" process is "similar" to the so-called "fracking" to retrieve shale gas; however, this sort of "fracturing" is supposedly less harmful than in the shale-gas case because less permeability of the rocks is needed and no hydraulic fracturing proppants are used.

surface. In the ideal case, the water flows from the bottom of the injection well to the bottom of the production well, but non-desirable short cuts of the water can occur.

Drilling more wells is of course also possible. According to Hettkamp et al. [49], a triplet is considered to be the optimum base for commercially viable EGS.

1.1.3 Drilling technology

Part of the drilling technology used in geothermal wells is the same as in the oil and gas industry. The big difference is that oil and gas are found in softer rock in the sediment layer (top layer of the earth's crust) at a lower temperature [109]. Therefore, to be applicable for EGS purposes, the oil and gas drilling technology must be adapted to work in harder and warmer rocks, which leads to a higher cost. The costs for geothermal wells are 2-5 times larger than for comparable oil and gas wells [90]. The orders of magnitude for the drilling costs for EGS in the USA are given in table 1.1, but the costs are generally higher in Europe. Drilling costs account for 60-70% of the total project costs [90, 109]. Especially in low-grade, low-gradient sources, the share of the drilling costs is very high.

The maximum reachable well depths are lower for geothermal wells than for oil or gas wells due to the much higher flow rates in geothermal wells (fluid is less valuable), resulting in a lower amount of heat that can be captured. In the oil and gas industry well depths of 7 km are routinely reached and maximum depths of 9-12 km are possible. For geothermal wells, only depths of 3-7 km are possible with drilling times of 3-6 months [90]. In the European EGS research project at Soultz-sous-Forêts, several wells of a depth around 5 km have been drilled. Drilling times of 4-5 months were realized there [49].

Shallow			Mid Range			Deep		
Depth, m (ft)	No. of Casing Strings	Cost, million $	Depth, m (ft)	No. of Casing Strings	Cost, million $	Depth, m (ft)	No. of Casing Strings	Cost, million $
1,500 (4,900)	4	**2.3**	4,000 (13,100)	4	**5.2**	6,000 (19,700)	5	**9.7**
2,500 (8,2000)	4	**3.4**	5,000 (16,400)	4	**7.0**	6,000 (19,700)	6	**12.3**
3,000 (9,800)	4	**4.0**	5,000 (16,400)	5	**8.3**	7,5000 (24,600)	6	**14.4**
						10,000 (32,800)	6	**20.0**

Table 1.1: EGS well drilling-cost estimates for a single well from the "Well cost Lite model" (in 2004 U.S. $), based on costs in the USA[3]. Table from Tester et al. [109].

1.1.4 Chemical composition of geothermal fluids

The water used in geothermal systems is in most cases not clean, therefore it is often called a brine. Minerals can be dissolved in it [102], but it can also contain more than "usual" radioactive isotopes [26]. The fluid has been in contact with the rock for a very long time, so chemical equilibrium between the rock and the fluid is reached; everything that can be dissolved is dissolved. Any use of the field (lower pressure, lower temperature and gas release) will result in a different chemical equilibrium, which can lead to precipitation in the wells and in the above-ground equipment. This fouling, which is often called scaling in the geothermal sector, has to be avoided because it leads to lower heat-transfer coefficients and higher pressure drops. Different actions can be taken to reduce the amount of scaling, like increasing the pH [29], keeping the fluid temperature high enough [38, 39] or the application of a scaling-inhibitor system [102]. The plant has to be designed in such a way that scaling does not occur at all in the wells.

1.2 Geothermal power plants

When the warm geothermal fluid is brought to the surface, it can be used to generate electricity and or for direct heating. First three different types of

[3]Note that power-plant-related costs have escalated strongly since 2004. See e.g. www.ihs.com/info/cera/ihsindexes/index.aspx, the PCCI and EPCCI. See also the Chemical Engineering Plant Cost Index (CEPCI). Whether this also applies to the drilling costs of the wells is an open question.

geothermal electric power plants are discussed, followed by possible options for combined generation of electric power and the delivery of heat.

1.2.1 Dry-steam power plants

Dry-steam power plants are the oldest geothermal plants that have been built and are used for vapor-dominated, dry-steam reservoirs which exist only in a very limited amount of regions in the world (Larderello (Italy) and The Geysers (CA, USA)[29]). Figure 1.3 gives the schematic of a dry-steam plant. The steam is pumped up from the production well (PW), cleaned in the particulate remover (PR), dried in the moisture remover (MR) and then expanded in a turbine (T). Before the expanded steam is returned subsurface, it is condensed in the condenser (C). The geothermal plants in Larderello have an additional chemical plant for the removal of H_2S and mercury, resulting in a loss of the natural superheat of the steam in these plants.

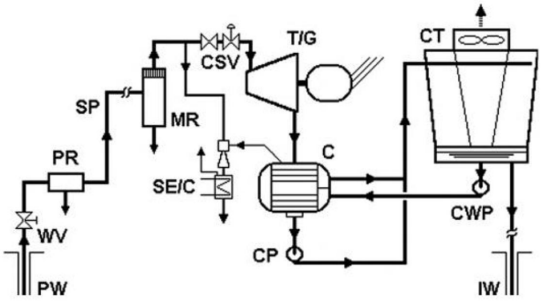

Figure 1.3: Schematic flow diagram of a dry-steam plant. The indicated components are the production well (PW), the wellhead valve (WV), the particulate remover (PR), the steam piping (SP), the moisture remover (MR), a control & stop valve (CSV), the turbine with generator (T/G), the steam ejector/condenser (SE/C), the condenser (C), the condensate pump (CP), the cooling tower (CT), the cooling-water pump (CWP) and the injection well (IW). Figure from DiPippo [29].

In 2011, 71 dry-steam power plants were in operation with a total installed capacity of 2893MW_e, which results in an average installed capacity of 40.75 MW_e per power plant. Almost all of these power plants are located in Italy and the USA and a few in Indonesia. Iceland, New Zealand and Japan all have one installed dry-steam power plant [29].

1.2.2 Flash power plants

The schematic of a flash power plant (figure 1.4) is very similar to the one of a dry-steam plant. The geothermal fluid at the inlet of the power plant is a mixture of liquid and vapor, which is obtained by flashing the pressurized geothermal fluid to a lower pressure in the reservoir, wells or with a valve. The flashing is mostly a result of the hydrostatic pressure reduction and the friction in the production well. The vapor and liquid part are separated in a cyclone separator (CS). The vapor part runs through the cycle of a dry-steam plant, while the liquid part is sent to the injection well (IW) (single-flash plant as in figure 1.4) or is flashed again (double-flash plant).

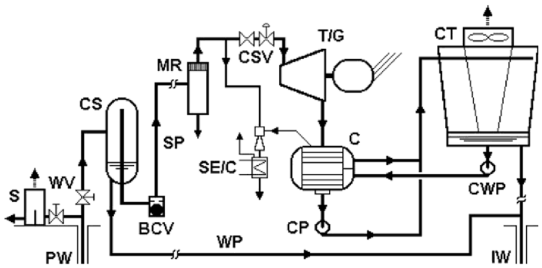

Figure 1.4: Schematic flow diagram of a single-flash plant. The difference with figure 1.3 is the component CS, which stands for cyclone separator. In this component, the vapor and liquid after the flash process are separated. The indicated components are the production well (PW), the wellhead valve (WV), the silencer (S), the cyclone separator (CS), the ball check valve (BCV), the steam piping (SP), the water piping (WP), the moisture remover (MR), a control & stop valve (CSV), the turbine with generator (T/G), the steam ejector/condenser (SE/C), the condenser (C), the condensate pump (CP), the cooling tower (CT), the cooling-water pump (CWP) and the injection well (IW). Figure from DiPippo [29].

The number of single-flash, double-flash and triple-flash power plants running in 2011 was 169, 59 and 6, respectively, and the installed electric capacity was 4581, 1856 and 226 MW_e, respectively. This results in an average installed capacity of 27.11, 31.46 and 37.63 MW_e per power plant. Flash power plants are located where dry-steam power plants are found and in the Philippines, Russia, Kenya, China, Turkey and in many countries in Middle America [29].

1.2.3 Binary power plants

For wellhead temperatures below 150°C, it becomes difficult to build efficient flash power plants and binary power plants are typically used [29]. For higher temperatures, binary plants are also used. In the dry-steam power plants and in the flash power plants, it is the geothermal fluid which performs the thermodynamic cycle. In a binary power plant, the geothermal fluid exchanges heat with a second fluid, the working fluid, which performs the thermodynamic cycle in which mechanical and electrical power are generated. Two typical binary cycles are the organic Rankine cycle (ORC) and the Kalina cycle. An ORC is in fact a Rankine cycle which uses another working fluid than water and a Kalina cycle uses a mixture of ammonia and water with a varying concentration instead of pure water. These two cycles are well suited for electricity generation from low-temperature heat sources [29]. Ample information about these binary cycles is given in chapter 2, because of our focus on low-temperature heat sources.

In total 234 binary geothermal power plants were in operation in 2011 with a total installed capacity of 708 MW_e, resulting in an average installed capacity of 3.02 MW_e per power plant. These plant can also be found in geothermally colder countries like Germany, Austria and Australia [29].

1.2.4 Combined heat and power

The geothermal heat can be used for electricity generation and or for the heating of buildings, green houses, pools, etcetera and or for cooling purposes by using absorption or adsorption chillers. These chillers are not investigated in this work, but are considered to be heat-demanding equipment. This means that only combinations of electricity generation and heating are investigated.

When a part of the heat source is used for electricity generation and a part for heating purposes, a combined heat and power (CHP) plant is used. Different configurations for such a power plant are possible. Kather, Rohloff, and Filleböck [59] propose three different configurations. The first one is a classical system (figure 1.5a) in which a single thermodynamic process generates the electricity and the heat. This can for example be done by using a Rankine cycle and using the condensation heat for the heating purpose, but this system is only useful for high-temperature heat sources. Other options are the parallel connection (figure 1.5b), in which a part of the mass flow of the brine is sent to the heating system and the remaining part to the electricity generating system. In the series connection (figure 1.5c) all the mass flow of the brine is first sent to the electricity generating system and afterwards to the heating system. The temperature of the brine after the electricity generating system has to be high

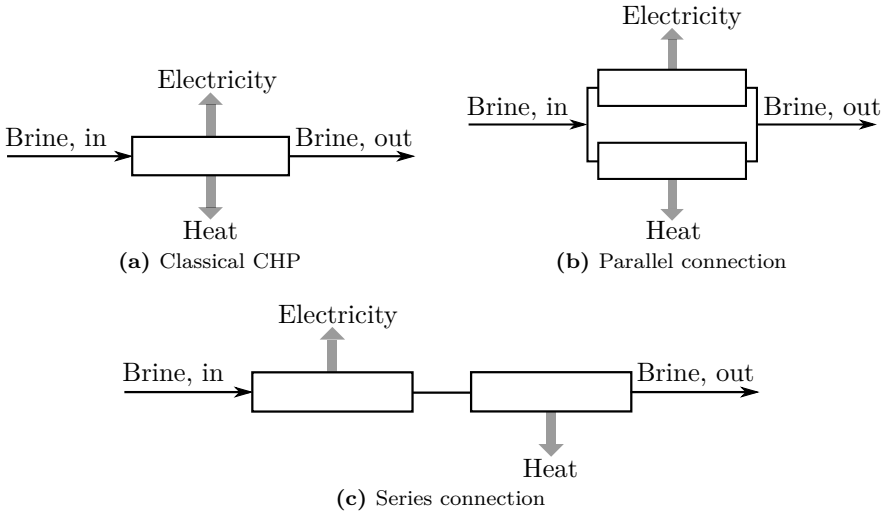

Figure 1.5: Configurations for a geothermal CHP plant. Figure based on Kather, Rohloff, and Filleböck [59].

enough so that the necessary amount of heat can be transferred to the heating network. Typically, much more of the geothermal heat is used for heating purposes than for electricity generation.

Combinations of the series and the parallel connection are also used. The heat network of the power plant in Neustadt-Glewe (shown in figure 1.6) can be put in a series connection, a parallel connection or a combination [64]. This type of connection allows a large amount of flexibility throughout the year, which is desirable for a strongly fluctuating heat demand. The configuration in Neustadt-Glewe did not result in the expected performance and only in summer electricity is generated.

1.3 Challenges for low-temperature geothermal energy conversion

Challenges exist both for subsurface and above-surface geothermal systems. Reducing the high cost of the drilling, reducing the risk of lower than expected temperatures or less than expected mass flow, reducing the risk for earthquakes, etcetera are all subsurface challenges, but these are outside the scope of this work.

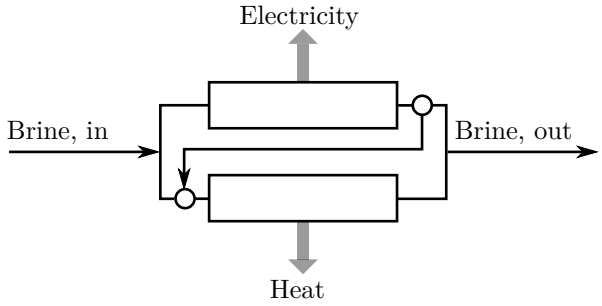

Figure 1.6: Scheme of the CHP-configuration used in Neustadt-Glewe. Figure based on Köhler [64].

The above-surface challenges are the efficient conversion of low-temperature geothermal heat to useful energy carriers, the cost of power plants, the prediction and control of fouling and corrosion of equipment, etcetera. In this work, the focus lies on the first two challenges for low-temperature geothermal heat sources and low temperatures refer to temperatures between 100 and 150°C.

The conversion efficiency for heat supply coming from a low-temperature reservoir into electricity is low for "normal" environmental temperatures (Carnot), but this is the case for all low-temperature heat sources (geothermal, waste heat, thermal solar energy, etcetera). So, geothermal heat sources with a higher temperature are favored. However most regions in the world are, geothermally spoken, cold and in most cases low-temperature heat sources are available at depths accessible for drilling [90, 109].

The effect of a low conversion efficiency of the power cycle is in fact twofold. First of all, only a small part of the heat (order of magnitude 10% for the gross efficiency [30]) which is added to the power cycle is converted into electricity. This means that about 90% of the heat which is added to the cycle has to be dumped into the surroundings, which is not for free. So, for 1 unit of electricity generated, 9 units of heat have to be cooled away. For fossil-fueled and nuclear power plants, this fraction is 1 to 2 or (much) better. This shows that an efficient cooling system is very important for low-temperature heat sources.

Due to the low inlet temperature of the heat source, the temperature difference between the highest (heat-source inlet) and the lowest (surroundings) temperature is small compared to classical thermal power plants. The consequence is that low pinch-point-temperature differences and low condensing temperatures are critical, which is shown in chapter 3. This has of course also a consequence on the cost of the equipment. The design of heat exchangers and of the cooling system is therefore crucial.

Connected to the previous challenge is the use of geothermal heat sources for a CHP plant. When heat is needed at moderate temperatures (for example heating of older buildings with radiators or convectors), the heating system needs already a significant part of the available temperature range between heat-source-inlet temperature and the ambient temperature. Another issue is the in time strongly fluctuating heat demand for the heating of buildings, greenhouses, etcetera. Only steady-state calculations are performed in this work, so this last effect is not taken into account.

The above mentioned, thermodynamic challenges are in fact valid for all low-temperature heat sources. Typical for geothermal heat sources is the high investment cost of the source (section 1.1.3). A large part of the investment cost is needed for the heat source, while the power plant/CHP plant generates the income. This means that it is possible to invest more in a more efficient power plant/CHP plant, because the extra cost for the total project is relatively limited. This is of course only valid under the assumption of a profitable project. Another challenge is reducing the relatively high cost of low-temperature power plants, which is also connected to the low conversion efficiency. Large amounts of heat have to be transferred or cooled away to generate a small amount of electricity. This means that large, thus expensive, heat exchangers and cooling installations are needed.

So, to further develop low-temperature geothermal electricity generation, it is important to increase the efficiency of the power plants (and thus the revenues from the electricity generating part) and to reduce their investment costs and auxiliary power consumption. When direct use of the geothermal heat is possible, selling the heat is an extra way of generating revenues and it is important that the electricity generating system and the heat generating system are designed to work well together.

1.4 Research objectives and approach

The goal of this work is to develop a model & algorithm which can find the *economic* optimal design of low-temperature geothermal power plants. It is important that also more advanced types of power plants are included, so that relatively high conversion efficiencies can be obtained. The model should not only incorporate the technical aspect of the plants, but should also be able to give good predictions of the investment and operational cost of the modeled plants. Although the focus lies on electricity generation, the influence of the heat demand is also important. As already mentioned in the previous section, only steady-state design is taken into account and dynamics are neglected. Only

the influence of heat-demand on the electricity generating system in a series connection and not in a parallel connection is investigated, because the latter connection can be seen as two separate geothermal plants in a steady-state calculation.

Approach

Typically, binary power plants are used for low-temperature heat sources, as mentioned in section 1.2. In order to obtain the optimal configuration of binary power plants, models for different configurations are needed. For a large number of configurations, which are proposed in the literature, simple thermodynamic models are developed. Optimizations with these models show that the configuration of the heat exchangers and the cooling system are very important.

These thermodynamic models are extended by implementing existing correlations for different types of heat exchangers and for different types of cooling systems. In order to optimize their configuration, it is necessary that these models are detailed enough; the performance of the components should be given as a function of their geometry and size.

All these models are then combined to one power-plant model, with which a system optimization is performed. In such a system optimization, *the configurations of all the components and of the cycle are optimized together*. This results in components which are optimal to be used together and optimal to be used in the obtained optimal system. Such a system optimization is a hard optimization problem. To find the optimal solution in a reasonable time, the gradients are calculated with automatic differentiation in reverse mode and a robust non-linear solver [20] is used.

Both thermodynamic and economic optimizations are performed. For the latter optimization, detailed cost functions for all the components are necessary. At the end, a model is obtained which can be used to find the economic optimal configuration of binary power plants, powered by any kind of low-temperature heat.

1.5 Outline of the work

Chapter 2 gives an overview of the most relevant literature with respect to this work. First, a large number of possible configurations of binary power plants

are given, followed by an overview of components used in these power plants and the way they are modeled.

In chapter 3, simple models with, mostly ideal components are developed for a number of binary power plants and these models are optimized with a thermodynamic objective function. From this optimization it is concluded that the modeling of heat exchangers and the cooling system is very important for low-temperature power plants.

Models for heat exchangers are implemented and added to the binary-power-plant model in chapter 4. The configuration of the heat exchangers is optimized together with the configuration of the binary cycle, while using again a thermodynamic objective function. Different types and configurations of heat exchangers are investigated and the results show that a detailed model for the cooling system is vital.

In chapter 5, models for two different types of cooling are added and a complete system optimization is performed. This time, two different economic objective functions are used. The economic parameters are based on a recent geothermal research project in Belgium [119].

The conclusions of this work and recommendations for future research are given in chapter 6.

Correlations to calculate the heat transfer and pressure drop in shell-and-tube and plate heat exchangers, depending on their geometry are given in appendix A. Correlations for single-phase flow, condensation and evaporation are given.

Appendix B gives correlations for the performance of wet cooling towers.

For the efficiency of axial turbines, it is referred to appendix C.

In appendix D more information is given about the software used to calculate the fluid properties and the numerical adaptations needed to calculate the gradient of these fluid properties.

Chapter 2

Literature survey

In this chapter, an overview is given of different aspects of the conversion of low-temperature geothermal heat. Different types and configurations of binary power cycles are discussed in the literature and much research has been performed to optimize these cycles. Other research focuses on the main components of binary power plants like heat exchangers, cooling system and turbines. Some researchers combine the cycle level and the component level, which is discussed at the end of this chapter.

2.1 Binary power cycles

Binary power cycles are typically used for the conversion of low-temperature heat to mechanical power, but other possibilities to convert the heat have also been proposed in the literature. Low-temperature heat sources can be used in combination with a classical, high-temperature power plant. Poullikkas [96] mentions the preheating of fuel of a combined cycle gas turbine (CCGT) and Yang et al. [137] mention the feed-water preheating of a classical Rankine cycle. Two main remarks should be made about these two proposals. The first one is that a classical, high-temperature power plant should be available in the close neighborhood of the low-temperature heat source. Second, in many proposed configurations is the geothermal heat used *instead* of the heat obtained by burning fossil fuels. This means that the fossil fuel is used less efficiently, unless the composition of the flue gases does not allow to cool them down to a too low temperature. Due to these two remarks, the use of low-temperature geothermal

heat in fossil-fueled power plants is not further investigated and the focus lies on binary power plants.

The main two groups of binary cycles are the organic Rankine cycle (ORC) and the Kalina cycle. The beginning of this section explains why a classical Rankine cycle is not the best option when low-temperature heat sources are used, followed by an overview of ORCs and Kalina cycles, their efficiency and some illustrations of optimizing these cycles.

2.1.1 Classical Rankine cycle

The scheme of a simple Rankine cycle is shown in figure 2.1. The water is pumped to a high pressure (1→2), heated by the low-temperature heat source[1] (2→6), expanded in the turbine (6→7) and condensed (7→1).

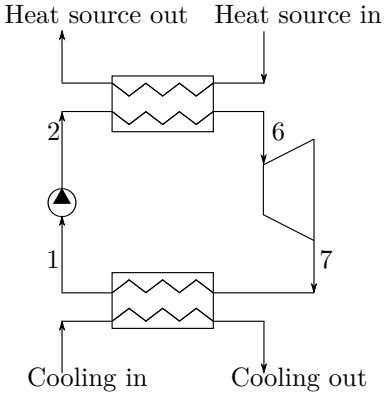

Figure 2.1: Schematic flow diagram of a simple Rankine cycle.

A steam Rankine cycle is not a good choice when low-temperature heat sources are used. A temperature-entropy diagram for a steam Rankine cycle is shown in figure 2.2. At low temperatures, the vapor saturation line of water has a small slope in a temperature-entropy diagram. To avoid a high degree of condensation[2] in the turbine, a relatively large amount of superheating is needed (point 6). Therefore, evaporation happens at a low pressure, at which a large heat of vaporization[3] exists. This is shown in figure 2.3. This last figure shows

[1] Although most of the theory in this chapter is valid for all types of low-temperature heat sources, the word brine is often used to denote the heat source.

[2] Condensation is allowed when included in the design of the turbine. Saturated steam turbines in geothermal and nuclear applications run with up to 20% liquid ratio. The liquid is usually removed between stages in these turbine. (P. Valdimarsson, personal communication)

[3] The energy needed to transform a saturated liquid to saturated vapor.

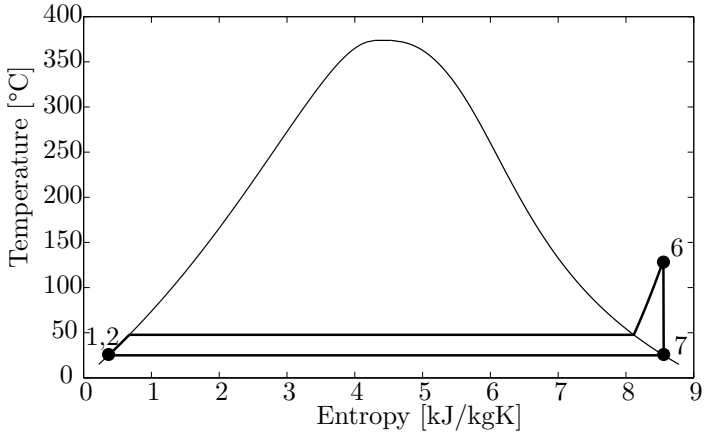

Figure 2.2: Temperature-entropy diagram of water in a binary Rankine cycle.

the temperature of the brine and the temperature of the water, as a function of the transferred heat per kilogram of brine. The water, at a constant pressure, boils at a constant temperature, while having a large evaporation value. Due to this large evaporation value, a large temperature difference between the brine and the water exists, leading to high irreversibilities and to a low efficiency.

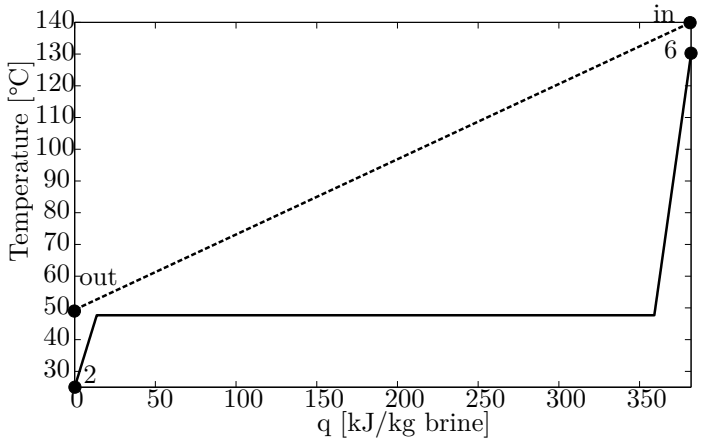

Figure 2.3: Temperature-heat diagram of water in a binary Rankine cycle, with the cooling curve of the brine (· · ·) and the heating curve of the working fluid (–).

Another disadvantage is the low pressure of the classical Rankine cycle. In this example, the condensation temperature is 25°C at a condensation pressure of 0.0317 bar and the high pressure is 0.11 bar. The cycle works completely

at a sub-atmospheric pressure, hence, a lot of air is leaking into the system. Therefore, special arrangements should be taken. Other disadvantage of the low pressure are the high specific volume of the water, leading to large and costly equipment and the problems with non-condensable gases.

2.1.2 Organic Rankine cycle

An organic Rankine cycle (ORC), is a normal Rankine cycle, but with a working fluid different from water[4]. The advantage of the typically used organic fluids is that their critical temperatures and pressures are lower than the ones of water, so they can better fit to the low-temperature geothermal fluid. An extra advantage is that most of them condense at ambient temperatures at pressures above atmospheric, so organic Rankine cycles have no problems with air getting into the cycle. Due to the higher pressure in the cycle, lower specific volumes than in a steam Rankine cycle can be obtained, leading to smaller and cheaper components.

Subcritical cycle

The most simple organic Rankine cycle uses the same principle as a simple Rankine cycle, of which the schematic is shown in figure 2.1. An example of a subcritical cycle with R152a is shown in figure 2.4.

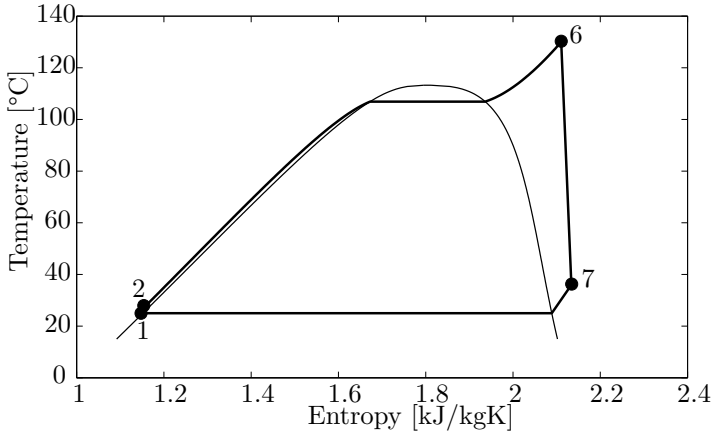

Figure 2.4: Temperature-entropy diagram of an ORC with R152a.

[4]Although the name suggests that only organic working fluids are use, this is not true and the name ORC is used for Rankine cycles with all kind of working fluids, except for water.

The heating curve of this fluid fits better to the cooling curve of the brine than water does, as illustrated in the temperature-heat diagram in figure 2.5.

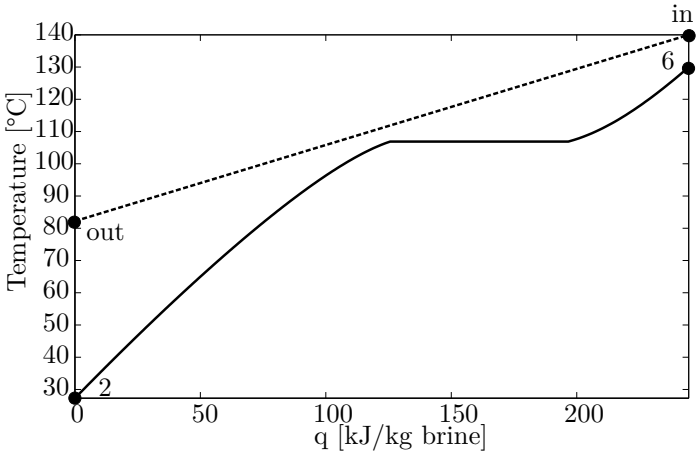

Figure 2.5: Temperature-heat diagram of an ORC with R152a, with the cooling curve of the brine (dashed line) and the heating curve of the working fluid (solid line).

In some cases, state 7 is superheated vapor and some of its heat can be used to heat up state 2. That way, a recuperated cycle is obtained as shown in figure 2.6a. Another proposed improvement in the literature is the use of turbine bleeding as shown in figure 2.6b.

As seen in figure 2.5, the temperature difference between the brine cooling curve and the working fluid heating curve is still relatively large due to the evaporation process at constant temperature. Many methods have been proposed to decrease this temperature difference and consequently lowering the creation of irreversibilities. The following methods are discussed in the next subsections:

- A different working fluid
- Mixture of fluids
- Multi-fluid cycle
- Multi-pressure cycle
- Transcritical cycle
- Absorption-desorption in the Kalina cycle

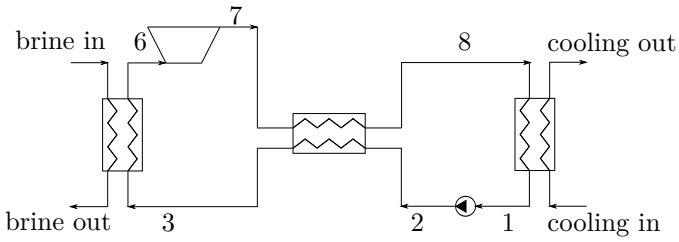

(a) Recuperation

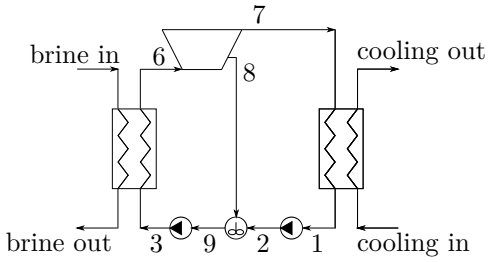

(b) Turbine bleeding

Figure 2.6: Schematic flow diagram of a recuperated ORC (a) and an ORC with turbine bleeding (b).

Working fluid

Many possible working fluids exist. These fluids can be divided in three categories:

- Wet fluid: the vapor saturation line in the temperature-entropy diagram has a negative slope, like R152a (figure 2.4).
- Dry fluid: the vapor saturation line in the temperature-entropy diagram has a positive slope, like R227ea (figure 2.7).
- Isentropic fluid: the vapor saturation line in the temperature-entropy diagram has an infinite slope.

A list of working fluids with their critical temperature, pressure and type is given in appendix D.3.

The choice of the working fluid is not only determined by the thermodynamic properties, but also by the stability temperature, flammability, corrosivity, ozone depletion factor, global warming potential, etcetera [98].

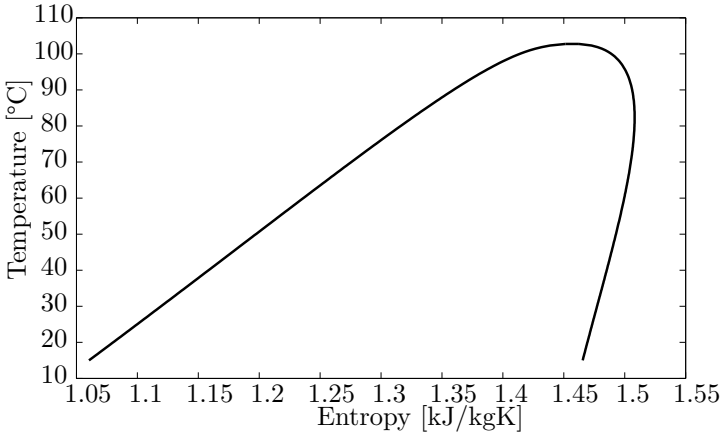

Figure 2.7: Temperature-entropy diagram of R227ea.

Mixture of fluids

Mixtures of working fluids can be used instead of pure fluids. Here, the advantage is that a mixture, at a constant pressure, does not boil at a constant temperature; hence the working fluid can better fit the cooling curve of the brine while heating as shown in the temperature-heat diagram in figure 2.8 in the middle panel. A problem that arises by using mixtures is discussed by Bliem and Mines [17]. If a normal shell-and-tube condenser is used with the cooling fluid in the tubes, the heavy fluid of the mixture condenses first, leading to a high concentration of the light fluid in the vapor phase. Bliem and Mines [17] have shown that integral condensation, in which thermal equilibrium between the phases is maintained, leads to lower condensing pressures and thus a higher efficiency of the cycle. Special arrangements must be taken to achieve this. Instead of condensing on the shell side in a horizontally oriented shell-and-tube heat exchanger, Bliem and Mines [17] propose to use tube-side condensation in a vertically oriented shell-and-tube heat exchanger.
For the evaporator, analogous comments can be made.

Multi-fluid cycle

The efficiency of the cycle can be improved by using more than one fluid. A cycle with two different fluids is shown in figure 2.9, one that receives heat from the high-temperature part of the brine (cycle a) and one that receives heat from the low-temperature part (cycle b), hereby trying to get a better fit with the brine in a temperature-heat diagram. This is for example done in the

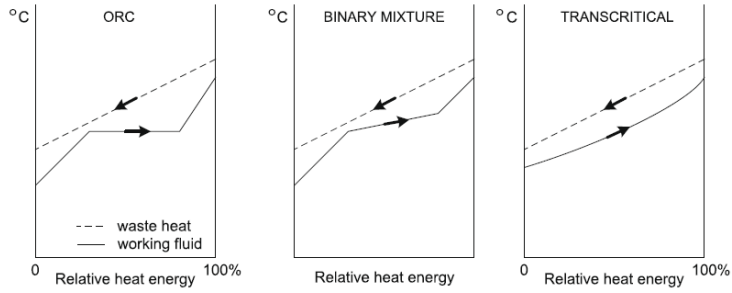

Figure 2.8: Temperature-heat diagram of a simple, subcritical ORC (left), an ORC with a binary mixture (middle) and a transcritical cycle (right). Figure from Cayer et al. [22].

East Mesa plant in California, USA [29]. The consequence of this configuration is that two binary cycles have to be developed; one for the high-temperature part of the brine and one for the low-temperature part of the brine. So, one disadvantage of this type of cycle is the higher capital cost.

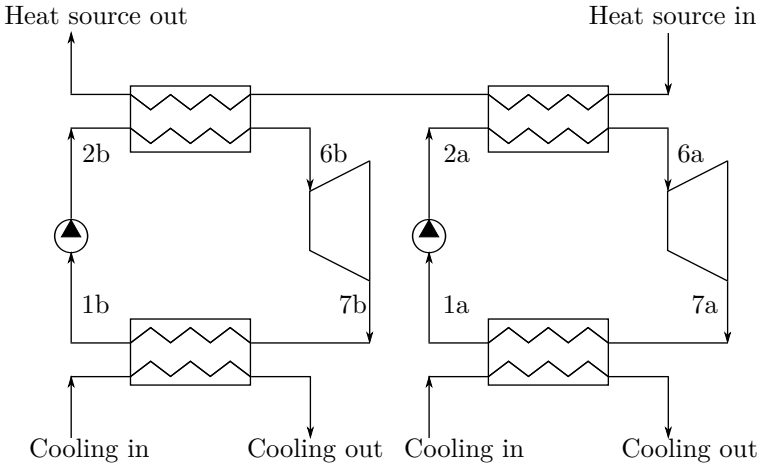

Figure 2.9: Schematic flow diagram of two Rankine cycles (a and b). They can work with a different fluid and or at a different pressure.

Multi-pressure cycle

A similar cycle (also shown in figure 2.9) is obtained when two or more pressure levels are used. The high-pressure fluid (cycle a) extracts heat from the high-

temperature part of the brine and the intermediate-pressure fluid (cycle b) from the low-temperature part of the brine. Because in this case only one fluid is used, a turbine with a high-pressure inlet and an intermediate-pressure inlet can be used and only one condenser is necessary. This way, the increase of the capital cost compared to a simple, subcritical ORC can be reduced.

A double-pressure ORC is currently the standard in industry and generates about 25% more electricity than a single-pressure ORC, with a cost increase of more than 25% (P. Valdimarsson, personal communication).

Transcritical cycle

A "transcritical" cycle is used to get a good fit with the brine as shown in the temperature-heat diagram in figure 2.8 on the right-hand side. This cycle approaches the triangular cycle [31], which describes a triangle in a temperature-entropy diagram, and the Lorenz cycle, which is the theoretical best cycle that works between to heat sources with a temperature glide. In a transcritical cycle, the fluid condenses at a subcritical pressure, but is heated at a supercritical pressure[5]. The advantage is that the fluid does not pass through the two-phase region when heated at a supercritical pressure. Therefore, the fluid at a constant pressure does not "boil" at a constant temperature and the temperature difference with the heat source can be smaller as shown in figure 2.8 (RHS).

Only working fluids with low critical temperatures and pressures can be used. The critical temperature needs to be lower than the maximum temperature of the brine and the pressure is limited by practical constraints. Thicker tubes are needed to withstand the high pressure, leading to higher costs and lower heat transfer [29]. Bliem and Mines [16] propose to keep the pressure lower than 41 bar, so 600 psi flanges can be used. Marcuccilli and Thiolet [73] recently proposed to keep the pressure lower than 60 bar. These pressures are still low compared to supercritical steam Rankine cycles (critical pressure p_{crit}=221 bar). Another disadvantage of the high pressure is the high amount of pumping power needed.

The temperature-entropy diagram of a typical transcritical cycle is shown in figure 2.10 for R134a as working fluid. The only difference with a subcritical cycle is that the pressure in the "boiler" is higher than p_{crit}, so the cycle does not pass through the two-phase region.

[5] In "common" water-based Rankine cycles such cycles are called "supercritical" cycles. In the context of ORCs the term "supercritical" is reserved for cycles which operate completely at supercritical pressures.

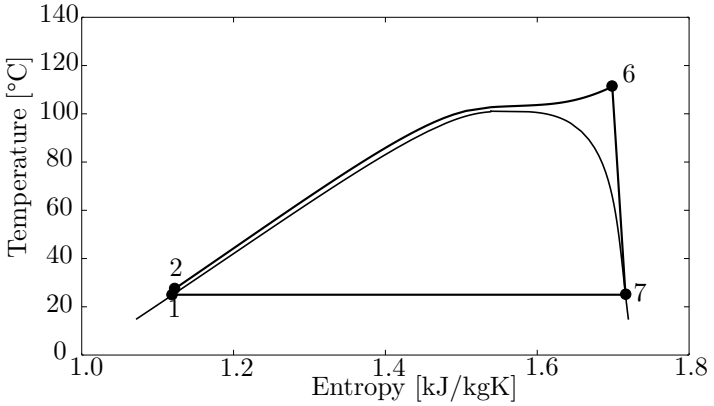

Figure 2.10: Temperature-entropy diagram of a transcritical Rankine cycle with R134a.

The advantage of the cycle is seen from the temperature-heat diagram in figure 2.11. The temperature difference between the brine and the working fluid can be smaller than in a subcritical cycle, so the irreversibilities of the heat exchange are smaller, but this results in larger heat exchangers.

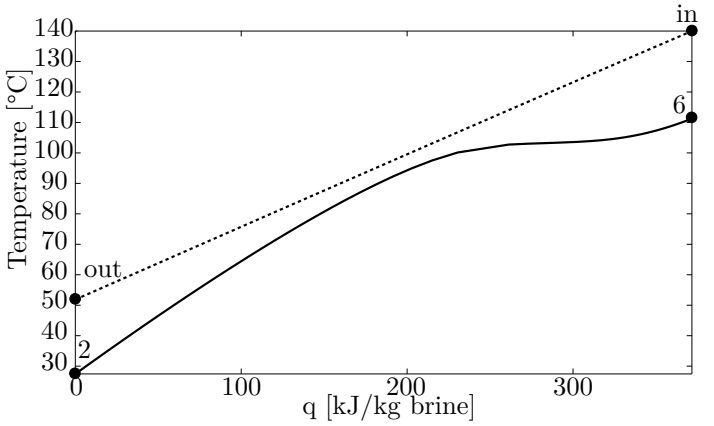

Figure 2.11: Temperature-heat diagram of a transcritical Rankine cycle with R134a with the cooling curve of the brine (dashed line) and the heating curve of the working fluid (solid line).

The temperature-entropy diagram of a transcritical cycle with a dry fluid is shown in figure 2.12. In this case, the fluid expands in the turbine, while passing through the two-phase region. Extensive experimental studies from

Bliem, C.J. and Mines, G.L. [15] and Mines, G.L. [79] show that an expansion through the two-phase region has no bad effects on the turbine, if the expansion starts with an entropy higher than that of the critical point and ends in the superheated region. Apparently the fluid stays in a metastable state, so no condensation occurs. According to these experiments, the turbine efficiency remains the same under "normal" expansion conditions and does not suffer from increased erosion. As can be seen from figure 2.13, this particular cycle

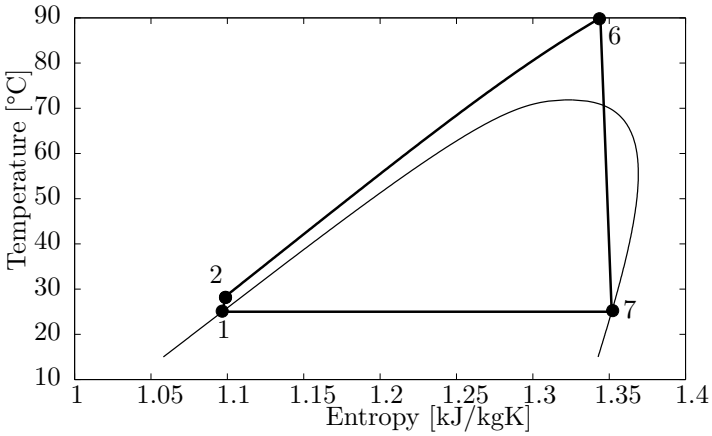

Figure 2.12: Temperature-entropy diagram of a transcritical Rankine cycle with R218, which expands in the turbine while passing through the two-phase region.

is not very efficient because the temperature difference between the brine and working fluid is very high. This does not mean that the type of cycle is bad, but that the cycle parameters are not adopted to the brine conditions.

The properties of fluids, like corrosivity and flammability, can be different above the critical point from those beneath it. Attention must be paid to this.

Cost

The cost of an ORC plant strongly depends on the technology used and the scope of supply. Bruno et al. [19] mention capital costs for commercialized ORC varying from 1150 $\$^{2004}/\mathrm{kW}_e$ to 3000 $€^{2007}/\mathrm{kW}_e$. An average value for the cost of the ORC system was set by them to 2000 $€^{2007}/\mathrm{kW}_e$. Franco and Villani [38] mention costs of 2000-4000 $€^{2000}/\mathrm{kW}_e$. It is noted that some of the numbers date from 2000 and 2004, which is before and during the massive costs

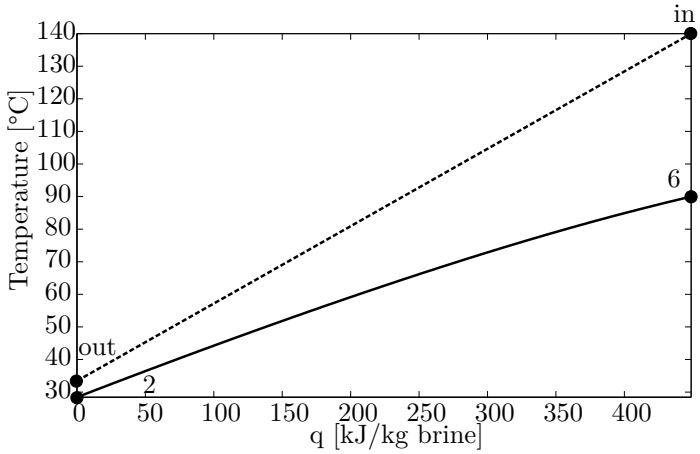

Figure 2.13: Temperature-heat diagram of a transcritical Rankine cycle with R218 with the cooling curve of the brine (dashed line) and the heating curve of the working fluid (solid line).

escalation of power-plant equipment. The numbers of 2007 are from after the escalation and hence these values are still quite representative[6].

The cost of the turbine, which is determined by its size, is a big part of the total cost of the plant. DiPippo [29] gives an estimation of the exit area A of the turbine, which is a measure for its total size. The mass flow rate of working fluid through the turbine can be written as:

$$\dot{m} = \rho_{out} A_{out} V_{out} \tag{2.1}$$

$$\dot{m} = \frac{\dot{W}_T}{h_{in} - h_{out}} \tag{2.2}$$

where ρ_{out} is the density of the working fluid at the outlet, V_{out} its velocity, $\dot{W}_T$ the mechanical power generated by the turbine and h_{in} and h_{out} are the specific enthalpy of the fluid at the inlet and outlet of the turbine, respectively. Combining these equations results in an expression for the exit area of the turbine:

$$A_{out} = \frac{\dot{W}_T}{h_{in} - h_{out}} \frac{v_{out}}{K a_{out}} \tag{2.3}$$

where v_{out} and a_{out} are the specific volume and speed of sound at the outlet of the turbine, respectively. K is a fraction. The results of equation (2.3) for

[6]See, the European Power Capital Cost Index (EPCCI) of IHS CERA at http://www.ihs.com/info/cera/ihsindexes/index.aspx.

different fluids are shown in table 2.1. A comparison is made with the results of Milora and Tester [78] who used a different approach, but the results are in good agreement. The table shows that a turbine for n-pentane is almost 15 times larger than one for ammonia for the same mechanical-power output, and thus more expensive.

Fluid	Formula	Molar mass	Relative exit area[(2)]
Ammonia	NH_3	17.03	1.0 (1.0)
Propane	C_3H_8	44.09	2.3 (1.9)
i-Butane	i-C_4H_{10}	58.12	4.1 (4.9)
n-Butane	C_4H_{10}	58.12	5.5 (6.3)
i-Pentane	i-C_5H_{12}	72.15	12.2 (n.a.)
n-Pentane	C_5H_{12}	72.15	14.6 (n.a.)

[(1)] Turbine-inlet temperature = 400 K, saturated, except superheated for NH_3 and C_3H_8; Condensing temperature = 320 K.
[(2)] Numbers in parentheses are from Milora and Tester [78].

Table 2.1: Turbine size comparisons for several working fluids. Table from DiPippo [29].

2.1.3 Kalina cycle

The Kalina cycle is a binary cycle in which a mixture of water and ammonia is used. The concentration of ammonia in the cycle changes to improve the efficiency of the cycle. Figure 2.14 shows a simple Kalina cycle (KCS 34). The ammonia-water mixture is heated by the brine in the boiler. Afterwards, the flow is separated in a strong mixture (high concentration of ammonia) and a lean mixture (low concentration of ammonia). The strong mixture is expanded in the turbine and is recombined with the lean mixture, that passed through a heat exchanger. The flow is then condensed in the regenerator and the condenser. Then it is pumped to a higher pressure and heated in the regenerator and the second heat exchanger.

The Kalina cycle has the same advantages as an ORC with a mixture, because of the variable evaporation temperature. The difference with an ORC is the absorption-desorption process, in which the boiling and dew temperatures are important. At the boiling-point temperature, the mixture is fully condensed, while the mixture is fully evaporated at the dew-point temperature. The advantage of the absorption-desorption process can be seen on the boiling (figure 2.15a) and dew (figure 2.15b) temperature diagrams. From figure 2.15 it is seen that, for a given boiling-point temperature, the pressure is lowest for mixtures

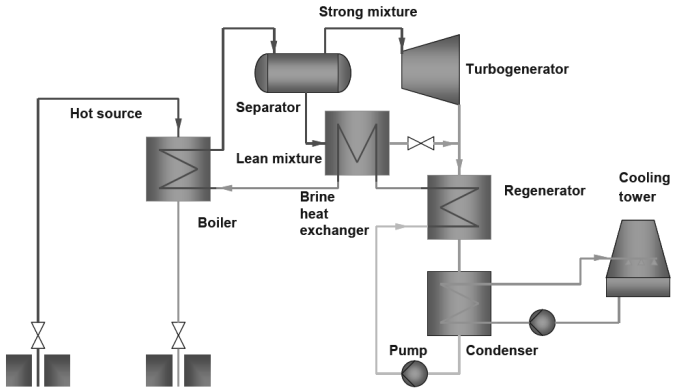

Figure 2.14: Schematic flow diagram of a Kalina cycle (KCS 34). Figure from Valdimarsson [116].

with low ammonia concentrations and for a given dew-point temperature, the pressure is highest for high ammonia concentrations. Therefore, the highest pressure drop in the turbine occurs when the mixture before the turbine is rich and after the condenser is lean. This is achieved by the cycle in figure 2.14. The higher enthalpy drop leads to a smaller mass flow rate in the turbine, and in turn to a cheaper turbine [116].

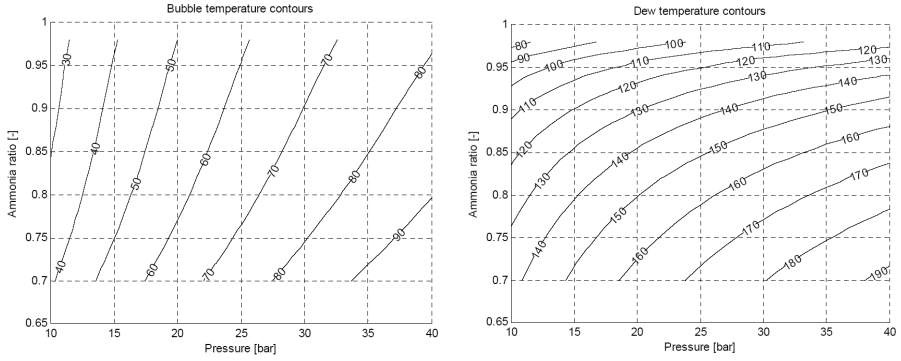

(a) Boiling temperature **(b)** Dew temperature

Figure 2.15: Boiling temperature (a) and dew temperature (b) for the ammonia-water mixture. Figures from Valdimarsson [116].

Another advantage is the flexibility of the cycle. The concentration of ammonia can be varied to adapt to a changing brine-inlet temperature over the lifetime

of the power plant or to a changing cooling-fluid temperature throughout the year. It is not practical to make these changes in concentration every day, but it is possible to change the concentration every season [117]. It is unclear if this principle is used in practice or that it is only a theoretical advantage of the Kalina cycle. Ammonia and water both have high heat-transfer coefficients, so heat exchangers can be kept small leading to a low capital cost [80, 117].

The disadvantage of the Kalina cycle is the high complexity due to the large number of parts (heat exchangers, separator)[117]. In every part irreversibilities exist, leading to a lower possible work output. Another disadvantage is the fact that Kalina cycles are still very new and need further development [117]. A mixture of ammonia and water is a wet "fluid", so condensation will always occur in the turbine if a superheater is missing like in figure 2.14. This last issue can be solved by a proper design of the turbine.

The above described cycle (KCS 34) has been improved to the so-called SG-2a cycle by M+W Zander [83]. The comparison of the efficiencies of these cycles with the efficiency of an ORC are given in figure 2.16. According to this figure (made by the producer of Kalina cycles), the SG-2a cycle has the highest efficiency. At 140°C, 11Wh/kg-brine is produced. Taking a dead-state temperature of 15°C this gives an exergetic efficiency of 44%.

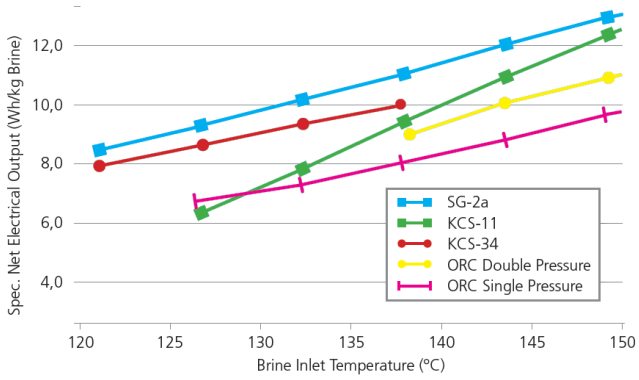

Figure 2.16: Comparison of the work output of different cycles. SG-2a, KCS-11 and KCS-34 are all Kalina cycles. Figure from M+W Zander [83].

Following Valdimarsson [117] the cost of a Kalina plant can be 1440 $\$^{2003}/\mathrm{kW}_e$, depending on the scope of supply, if cooling water is available[7] and can be used with fluid temperatures between 120 and 300°C.

[7]This cost estimation dates from 2003, which is during the massive costs escalation of power-plant equipment.

2.1.4 Efficiency of real binary plants

Energetic cycle efficiencies[8] η_{en}^{cycle} of some binary power plants are shown in table 2.2 as a function of the brine-inlet temperature T_{in}^{brine}. With the data from this table, the following correlation is proposed in Tester et al. [109]:

$$\eta_{en}^{cycle} = 0.0935\ T_{in}^{brine} - 2.3266 \tag{2.4}$$

Plant name	Location	Brine-inlet temperature [°C]	Net capacity [MW_e]	Efficiency [%]
Amedee	CA, USA	103	1.5	5.8
Wabuska	NV, USA	105	0.7	8
Brady	NV, USA	109	4.3	7
Húsavík	Iceland	122	2.0	10.6
Otake	Japan	130	1.0	12.9
Nigorikawa	Japan	140	1.0	9.8
Steamboat SB-2 & SB-3	NV, USA	152	53.0	8.2
Ormesa II	CA, USA	157	20.0	13.5
Heber SIGC	CA, USA	165	6.9	13.2
Miravalles Unit 5	Costa Rica	166	15.5	13.8

Table 2.2: Cycle energetic efficiencies for several binary power plants. Table from Tester et al. [109].

This correlation is shown in figure 2.17. In this correlation, the cooling-fluid temperature is not taken into account. This is, together with the difference in technology, the reason for the big deviation between the different power plants. For instance, the Húsavík power plant in Iceland (Kalina cycle) uses a cooling fluid available for "free" at 5°C, and has therefore a higher energetic efficiency than predicted by the correlation.

The energetic *cycle* efficiency describes how efficient the heat, which is added to the cycle, is used, but it does not describe how much of the available heat in the brine is added to the cycle. The exergetic or energetic *plant* efficiency, which is the fraction of the net electric power generated to the exergy or heat available in the brine, respectively, is a measure of the efficient use of the brine. More information about different possible efficiencies can be found in section 3.1.

DiPippo [30] has calculated both energetic cycle and exergetic plant efficiencies of existing power plants. The results are shown in table 2.3. He also compared

[8] The energetic cycle efficiency is defined in equation (3.1) and is the fraction of the net electric power generated to the heat input to the cycle.

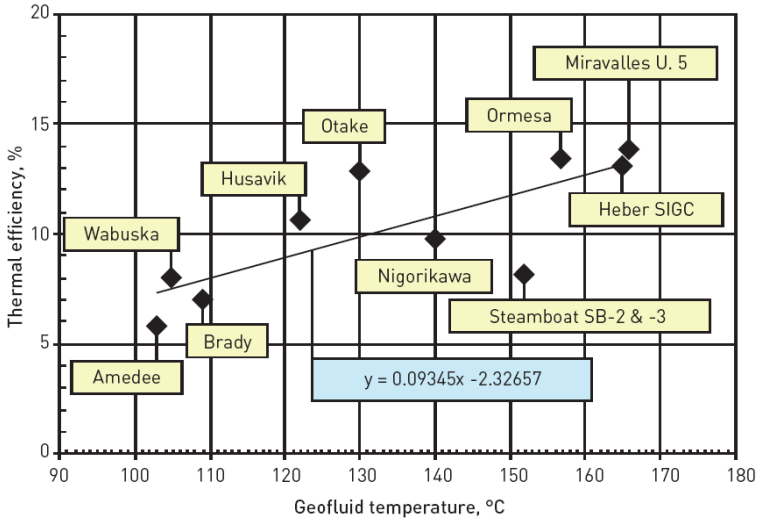

Figure 2.17: Correlation of binary plant cycle thermal efficiency as a function of the brine temperature. Figure from [109].

the Húsavík Kalina cycle (cooling water at 5°C) with the Brady binary cycle (air cooled), but now taking for the latter the same cooling conditions as for the Húsavík plant. This comparative exercise led to an exergetic efficiency of 22.5% for the Brady plant. This is only 0.6%-points or 2.6% smaller than the exergetic efficiency of the Kalina cycle. This example shows that the Kalina cycle does not generate 20-35% more electric power than an ORC, as claimed by Mlcak et al. [81]. The Kalina cycle has more internal recuperation, resulting in a high cycle efficiency, but not necessarily a high plant efficiency.

Plant name	Type plant	T_{in} [°C]	T_{out} [°C]	T_0 [°C]	η_{en}^{cycle} [%]	η_{ex}^{plant} [%]
Otake	Binary with extra steam	130	50	18	12.9	53.9
Nigorikawa	Binary	140	92	13	9.8	21.6
Heber	Dual level binary	165	68	15	13.2	43.4
Húsavík	Kalina	124	80	5	10.6	23.1
Brady	Binary	108	82	15-30	6.0-8.0	17.0-18.0

Table 2.3: Efficiencies of different power plants. Table from DiPippo [30].

The following comments are in order to put the comparison between the Húsavík Kalina cycle and the Brady binary cycle into the right perspective. The Kalina cycle receives brine at a temperature 2°C lower than designed for, the input temperature of the Brady cycle was 14°C lower than that of the Kalina cycle and the Kalina plant was a first of a kind.

Figure 2.18 shows that there seems to be no correlation between exergetic efficiency of existing plants and the temperature of the brine presented by its specific exergy. It is the plant design, which also depends on electricity prices and costs of the wells, that determines the efficiency [30].

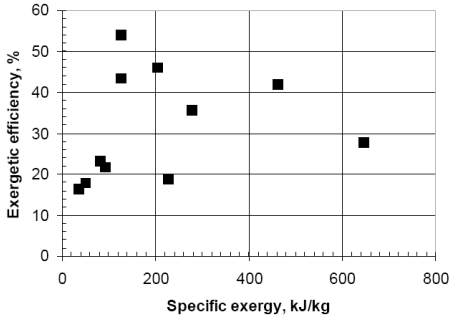

Figure 2.18: Geothermal power plant exergetic efficiency as a function of the specific exergy of the incoming geothermal fluid for various plants. Figure from DiPippo [30].

The efficiency of a power plant is strongly affected by the turbine efficiency. A conservative estimate for a dry turbine efficiency η_{Td} is 85% [29], but adaptations to this must be made when a dry turbine is used in wet conditions. For this, the Baumann rule[9] can be used [29]. This linear rule says that 1% of average moisture in the turbine, leads to 1% drop in turbine efficiency. So the wet turbine efficiency η_{Tw} can be calculated as:

$$\eta_{Tw} = \eta_{Td} \times x_{av} \tag{2.5}$$

with x_{av} the average wetness in the turbine.

2.1.5 Optimization of binary power cycles

Much research has been performed to optimize the configuration of ORCs. Cayer, Galanis, and Nesreddine [21] performed an energetic, exergetic and economic optimization of a transcritical ORC for a heat-source temperature of 100°C and a turbine-inlet temperature between 80 and 100°C. CO_2, ethane and R125 are used as possible working fluids. Only the simple ORC configuration with a pump, heat exchanger, turbine and condenser was considered. The heat

[9]The Baumann rules applies to dry steam turbines that are used under wet conditions. For turbines designed to be working under wet conditions, the wet turbine efficiency is the design one.

exchangers are modeled very simplistically. They concluded that the choice of the objective function has a strong influence on the obtained results.

Kanoglu [58] has investigated multi-pressure cycles. An exergy analysis of an existing power plant, which uses the combination of 2 subcritical cycles with isopentane, was performed. Most of the irreversibilities are created in the condenser, the turbine and the brine reinjection.

Gnutek and Bryszewska-Mazurek [44] have considered a multi-cycle ORC. The power plant consists of 4 subcritical power cycles, using the heat source in series. In this way the heat source can be cooled down more than when using a single-pressure ORC.

Heberle and Brüggemann [48] have concluded that for electric power generation from low-temperature geothermal heat sources, fluids with a low critical temperature are exergetically optimal. Only cycles which use a recuperator were investigated.

Mago et al. [71] have compared standard ORCs with ORCs which use turbine bleeding (called "regenerative" in the paper). It was concluded that the *cycle* efficiency of the so-called regenerative cycle is higher than that of the simple cycle.

Different configurations of subcritical ORCs have been compared by Yari [138]. Simple cycles, cycles with recuperation, cycles with turbine bleeding and cycles with both recuperation and turbine bleeding were simulated. All these cycles were subcritical ones with a fixed evaporation temperature of 120°C. It was shown that cycles with recuperation or turbine bleeding are the most promising ones.

Subcritical and transcritical cycles with or without recuperation have been investigated by Saleh et al. [101] for many working fluids. For low-temperature geothermal sources, it was shown that fluids with a low critical pressure in the transcritical cycles are energetically optimal.

Only limited research has been reported in the open scientific literature to optimize Kalina cycles and to make a fair comparison with ORCs. Bombarda, Invernizzi, and Pietra [18] made a comparison between Kalina cycles and ORCs for heat recovery from diesel engines. They concluded that, for low-power and medium-high temperature sources, the complexity of the Kalina cycle is not justified by the very small gain in performance in comparison with properly optimized ORCs.

This overview shows that already much research has been done optimizing binary cycles, but also that most researchers limit themselves to a small number of types of binary cycles or fluids. In order to make a fair comparison between the

different cycles and fluids, it is important to compare all of them to one another. Another issue is that most work make assumptions about the components, which can have a strong influence on the performance of the binary cycle.

2.2 Heat exchangers

Many different types of heat exchangers exist, but shell-and-tube and plate heat exchangers are the ones mostly used in binary power plants. These two types are therefore further investigated.

2.2.1 Shell-and-tube heat exchangers

Shell-and-tube heat exchangers are the most popular type of heat exchangers in the process and petrochemical industry [104]. They consist of a tube bundle which is located in a shell. A first fluid flows through the tubes and the other in the shell. The latter fluid is guided by baffles to flow around the tubes as shown in figure 2.19.

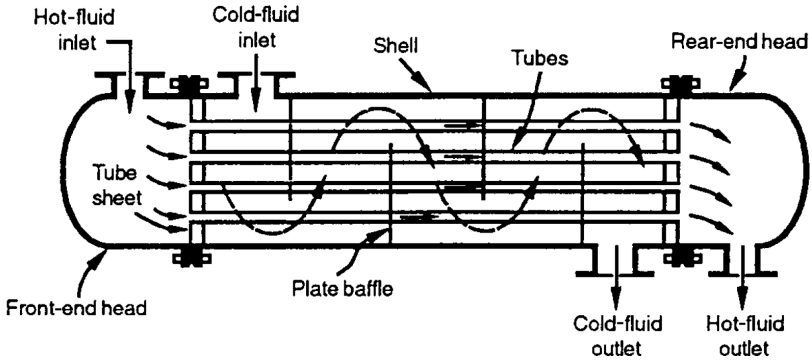

Figure 2.19: Example of a shell-and-tube heat exchanger with one shell pass and one tube pass. Figure from Shah and Sekulić [104].

Many different configurations are possible, depending on the number of tube passes, number of shell passes, inlet and outlet of the shell-and-tube fluid, tube and tube-bundle configuration, etcetera. These different configurations are classified in the TEMA standards, as shown in figure 2.20. The optimum configuration strongly depends on the application. It is common practice to let the dirty fluid (for example a geothermal brine) flow on the tube side, because it is easier to clean the inside of the tubes than the outside of the tubes, the baffles

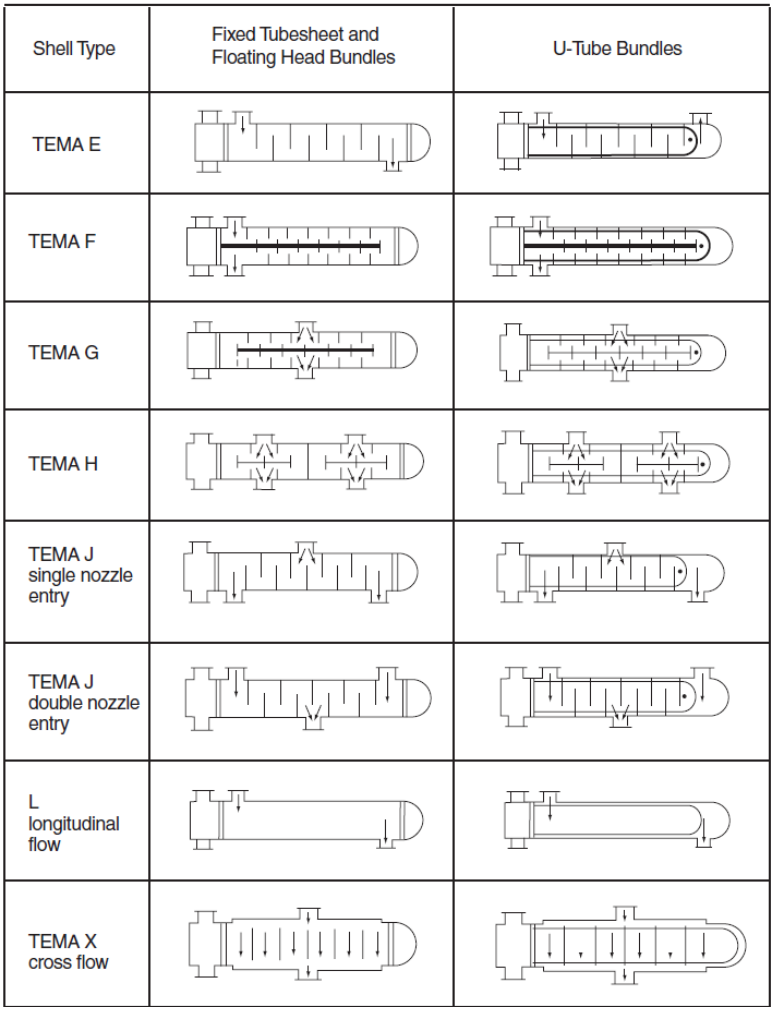

Figure 2.20: Different shell types with some tube-flow arrangements according to the TEMA standards. Figure from Shah and Sekulić [104].

and the inside of the shell. For easy cleaning of the tubes, U-tube bundles should be avoided [104]. If a counter-flow heat exchanger is desired, only the TEMA E and F shell types are possible. The latter one is not often used in this case, due to the heat transfer over the longitudinal baffle [104].

Shell-and-tube heat exchangers are commonly used and much research has been performed on them. Empirical methods for the performance analysis

and design of this type of heat exchangers were developed by Donohue [33], Kern [61], Tinker [112] and Gilmour [43] among others. Bell [13] continued the work of Tinker [112] and developed the Bell-Delaware method based on a large number of experiments on TEMA E-shell heat exchangers he performed at the university of Delaware. This method was later extended to be used for other shell geometries and it was further improved [50, 104]. Improvements [34, 45] and extensions for new geometries [132] for the Bell-Delaware method are still being proposed. The method is also used by many authors to find the optimum configuration of shell-and-tube heat exchangers [4, 10, 24, 91].

CFD-methods are also used to *analyze* shell-and-tube heat exchangers [84, 88, 97, 139, 140]. Prithiviraj and Andrews [97] compared the pressure drop calculated by the methods of Donohue [33], Kern [61], Bell [13] and their own developed CFD model with experimental data. They showed that the CFD method is the most accurate one, but also that the Bell-Delaware method is almost as accurate. The calculation time of CFD-methods is apparently too high to perform a numerical *optimization* of shell-and-tube heat exchangers.

2.2.2 Plate heat exchangers

Figure 2.21 shows a simple plate-type heat exchanger. The hot fluid (red) and the cold fluid (blue) are in this figure in counter flow. To avoid mixing between the two fluids, two major solutions exist: the gasketed and the all-welded heat exchangers [104].

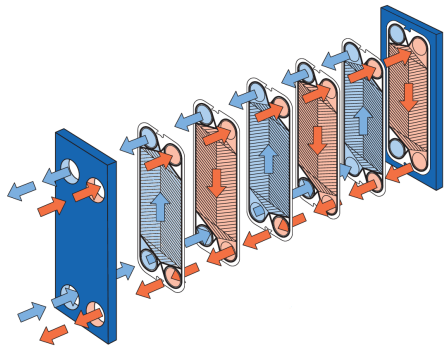

Figure 2.21: Flow distribution in a plate-type heat exchanger. Gaskets are used to avoid mixing of the fluids. Figure from Alfa Laval [3].

In a gasketed heat exchanger, gaskets are placed between the plates to avoid mixing. The gaskets are removable, so it is possible to disassemble the whole

heat exchanger for mechanical cleaning purposes, but this is an expensive process. The disadvantage is that these gaskets are the weak spots of the heat exchanger concerning temperature, pressure and corrosion. Pressures up to 30 bar and temperatures up to 150°C are possible for not too corrosive fluids [104].

In the all-welded heat exchanger, mixing is avoided by welding the plates to one another. The disadvantage is that disassembling is not possible for cleaning, but higher pressures (40 bar) and higher temperatures (350°C) are possible. By choosing the right metal for the plates, very corrosive fluids can be handled.

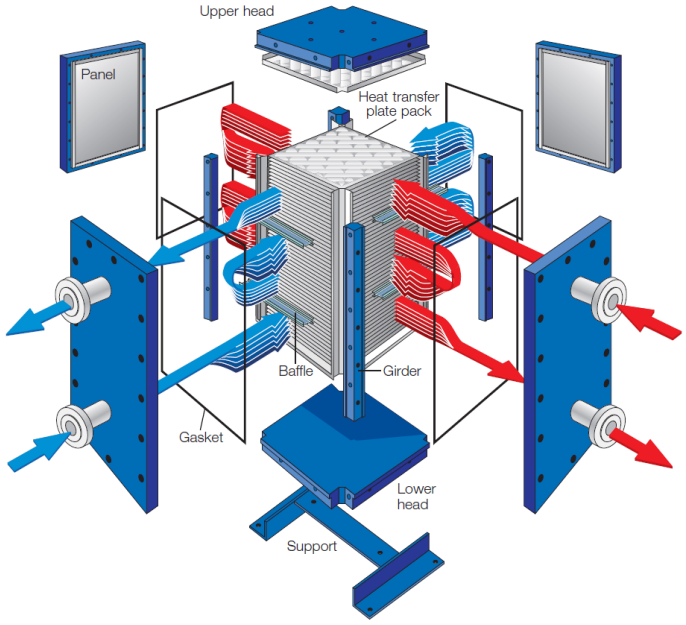

Figure 2.22: Example of an all-welded, heavy-duty plate-type heat exchanger. Figure from Alfa Laval [2].

Figure 2.22 shows an example of an all-welded heavy-duty plate-type heat exchanger. It is a counter-flow heat exchanger with cross flow in each pass. By removing the outside panels of the heat exchanger, it is nevertheless possible to mechanically clean "some part" of the heat exchanger.

Many different types of plate corrugation patterns exist, as shown in figure 2.23. The chevron, also known as herringbone, corrugations are most often used in practice and most research is focused on this type.

Many correlations have been developed for single-phase plate heat exchangers with chevron corrugations. Ayub [9] gives an overview of some of these

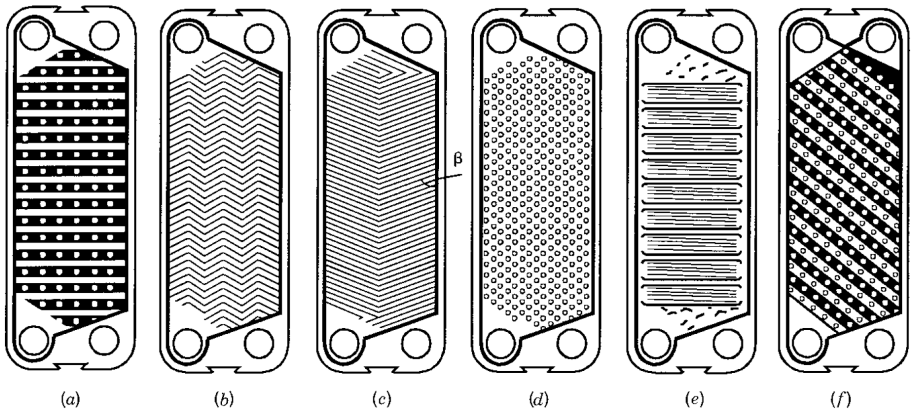

Figure 2.23: Plate patterns: (a) washboard; (b) zigzag; (c) chevron or herringbone; (d) protrusions and depressions; (e) washboard with secondary corrugations; (f) oblique washboard. Figure from Shah and Sekulić [104].

correlations. The most general one was developed by Martin [74]. The correlations originate from a combination of physical reasoning and a large number of experimental data from industrial heat exchangers. Such a general correlation, which would predict the performance of a heat exchanger as a function of its geometry, does not seem to exist for plate heat exchangers used as evaporators or condensers, although much research has been performed on the topic [9, 32, 46, 47, 56, 67, 111]. García-Cascales et al. [40] give an overview of some correlations developed for condensation and evaporation. The authors of those references propose correlations for the heat-transfer coefficient and the pressure drop based on own experiments and these correlations are therefore only valid for the investigated cases. As a matter of fact, most of these correlations are only valid for one configuration. Exceptions are the correlations developed by Han, Lee, and Kim [47] for condensation and Han, Lee, and Kim [46] for evaporation, but still much work is needed to develop generally applicable correlations for condensation and evaporation in plate heat exchangers.

2.3 Cooling system

Electric power plants can be cooled in three different ways: air cooling, water cooling with a cooling tower and direct cooling (natural cooling) with water (available in a nearly stream, lake or sea), of which the two first options are most often used. The auxiliary power consumption of air-cooled condensers (ACC) is about twice as high as the one for mechanical-draft wet cooling towers (WCT)

used for low-temperature geothermal power plants [76]. When low condensing temperatures are used in these plants, the investment cost of a binary plant with an ACC can be 50% higher than that of a plant with a WCT for the same conversion efficiency [76]. The disadvantage of using a wet cooling tower is of course that water is consumed, which is a significant drawback when water is scarce.

For ACCs, the dry-bulb temperature is relevant, while for WCTs, it is the wet-bulb temperature that is important. So, the drier and warmer the climate, the more the advantage of using a WCT instead of an ACC. A disadvantage of a WCT is that the cooling-water temperature cannot be lower than 10°C to avoid freezing of the water. In very cold climates, it is therefore better to use an ACC.

The comparison between air cooling and water cooling has already been performed in the literature. Barigozzi, Perdichizzi, and Ravelli [12] have developed a model of a CHP plant powered by burning waste, while the cooling system consists of both an ACC and a WCT. They found that when the ambient temperature is below 15°C, it is best to use the ACC. When the ambient temperature is higher, the ACC is first used to partially condense the steam and afterwards the WCT is used to further condense the steam. These results are valid for high-temperature heat sources (turbine-inlet-temperature of 450°C). Mendrinos, Karytsas, and Kontoleontos [76] compared cooling methods for geothermal binary plants. They concluded that wet cooling towers are economically the best choice, except when water is a very scarce product or when the climatic conditions are extreme.

To make a detailed comparison of the different cooling options, models that describe the performance of the cooling systems are needed. An overview of models for air-cooled heat exchangers and wet cooling towers is given hereafter.

2.3.1 Air-cooled heat exchangers

In an air-cooled heat exchanger, air flows over tubes in which a fluid cools down or condenses. Different configurations of these exchangers for power-plant applications exist as shown in figure 2.24. The vertical and horizontal configurations can be forced draft (as in figures 2.24a and 2.24b) or induced draft. In the former case, a fan blows air over the tubes and the fan is therefore located downstream. In the induced-draft case, the fan is located upstream (like in figure 2.24d). An A-frame configuration (figure 2.24c) is often used to save space.

Cooling with air has two main disadvantages. The first one is the low volumetric

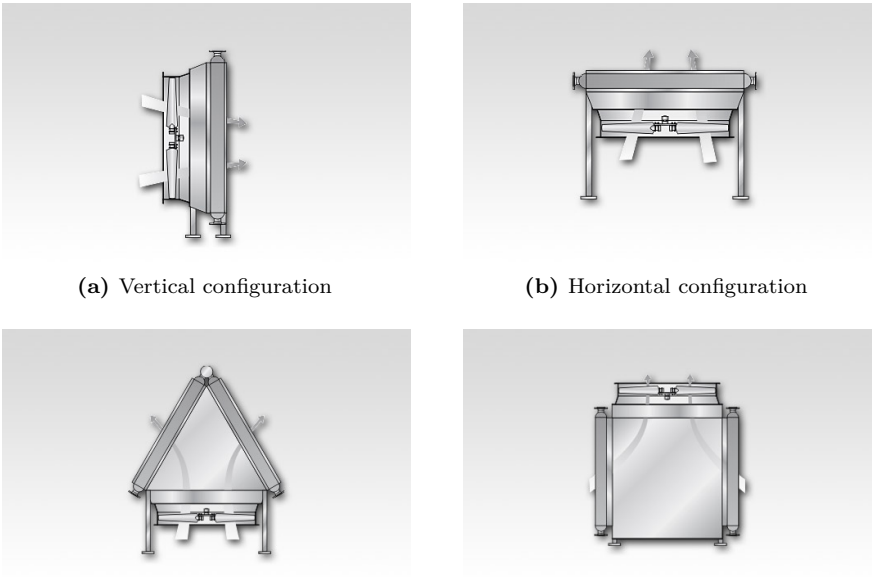

(a) Vertical configuration

(b) Horizontal configuration

(c) A-frame configuration

(d) In-line configuration

Figure 2.24: Different configurations of air-cooled heat exchangers. Figures from GEA Heat Exchangers [41].

heat capacity of air, resulting in the necessity of large volume flow rates of air for cooling. The consequence is that air-cooled heat exchangers are large. The second one is the low heat-transfer coefficient at the air side. This is improved by using finned tubes. A large number of finned-tube configurations exist.

The tubes can be round or flat (oval). Round tubes are most often used in tube banks, while only one row is used for flat tubes. The advantage of the latter type is that they result in more compact heat exchangers with a lower pressure drop [41, 110]. Also different types of fins exist: plain fins, fins with louvers, corrugated fins, wavy fins, etcetera. Some examples of finned tubes are given in figure 2.25. Thome [110] gives an overview of different finned-tube configurations and correlations developed in the literature to predict the heat-transfer coefficient and pressure drop.

Much research is performed to predict and improve the performance of finned tubes. The goal is to achieve a high heat-transfer coefficient and a low pressure drop to reduce the electric power consumption of the fans. Although the addition of louvers (figures 2.25c and 2.25d) is one of the most investigated improvements

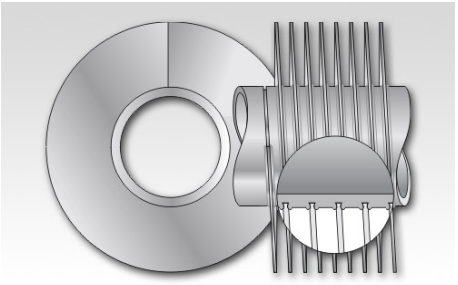

(a) Round tube with plain, round fins. Figure from GEA Heat Exchangers [41].

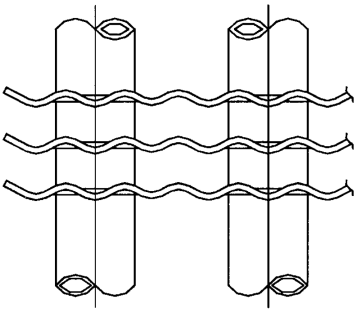

(b) Round tube with wavy fins. Figure from Wang, Hwang, and Lin [130].

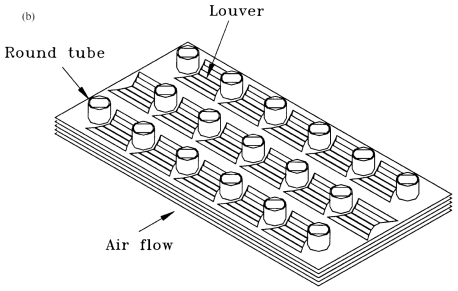

(c) Round tube with louvered fins. Figure from Wang et al. [131].

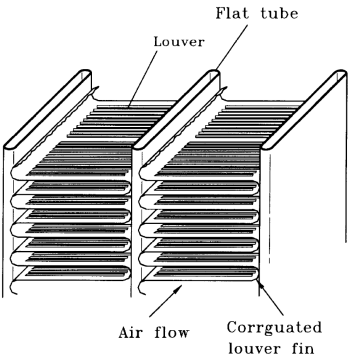

(d) Flat tube with corrugated, louvered fins. Figure from Wang et al. [131].

Figure 2.25: Different types of finned tubes used in air-cooled heat exchangers.

[1, 23, 89, 131], it seems not to be used for large installations. The most often used configuration in power plants is the one with flat tubes and corrugated fins (shown in figure 2.26a)[136]. Instead of using the configuration in figure 2.26a, Yang et al. [136] proposed to change the angle of the corrugations with respect to the tube as shown in figure 2.26b in order to reduce the amount of fouling. The drawback of this configuration is that the pressure drop increases, while almost no effect on the heat-transfer coefficient was seen. The correlation they developed for the fins under an angle can be modified for the "normal" configuration.

The optimal configuration of air-cooled heat exchangers is another field

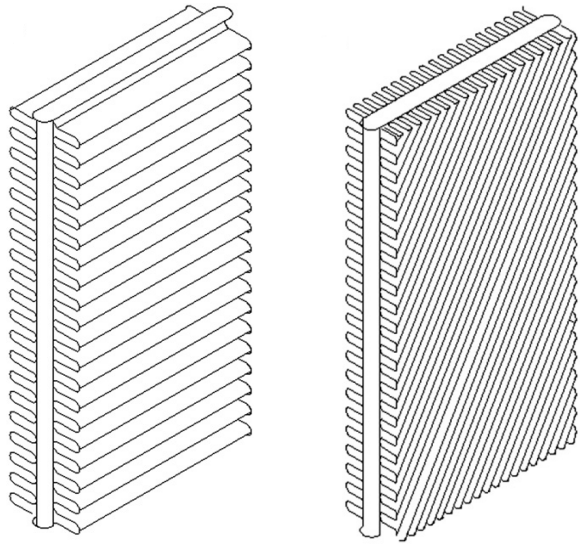

(a) Flat tube with corrugated fins

(b) Flat tube with corrugated fins put under an angle

Figure 2.26: Two different configurations of flat tubes with corrugated fins. Figures from Yang et al. [136].

of research. Doodman, Fesanghary, and Hosseini [35] minimized the cost (operational and investment cost) of a tube bank with a high number of fins. They concluded that large fin heights are not only thermodynamically, but also economically interesting. Stewart [108] performed similar research, but focused on air-cooled heat exchangers in air-conditioning systems. The coefficient of performance (COP) of air-conditioning systems can increase with about 5% if well designed louvered fins are used instead of plain fins, but the addition of non-optimized louvers can have a negative influence on the COP.

2.3.2 Wet cooling towers

Two main types of wet cooling towers exist: the natural-draft and the mechanical-draft tower. Both types are shown in figure 2.27. Only counter-flow towers are shown, but cross-flow towers also exist. In both types of towers, water is sprayed over a packing and falls down in the tower. Air flows from the bottom of the tower to the top and cools the water by evaporating part of the water. The packing is used to increase the contact area between the air and the water

droplets. A drift eliminator makes sure that no water droplets leave the tower. In a natural-draft cooling tower, it is the stack effect (buoyancy driven) which causes the air flow, while fans are used in mechanical-draft cooling towers. The natural-draft cooling tower is usually used for heat rejection capacities starting from 600 MW [42]. For lower capacities a mechanical-draft tower is used.

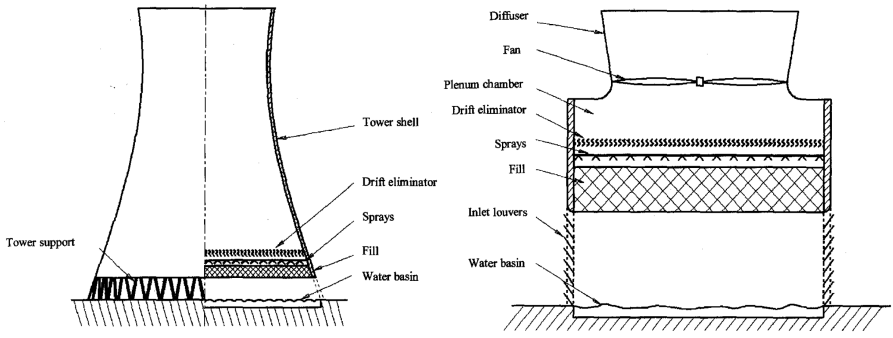

(a) Natural draft **(b)** Mechanical draft

Figure 2.27: Natural draft (a) and mechanical draft (b) cooling tower. Figures from Kloppers [62].

Two analytical methods which describe the heat and mass transfer in a cooling tower are widely used. Merkel [77] developed a simple method which is still widely used and recommended by international standards [62]. The assumptions made in the Merkel theory are that the exiting air of the cooling tower is saturated, the reduction of water flow rate by evaporation is neglected in the energy balance and the Lewis factor is equal to unity. The Lewis factor is an indication of the relative rates of heat and mass transfer in an evaporation process. The advantage of the Merkel theory is that the equations are simple and easy to apply.

Poppe and Rögener [95] did not make the assumptions made in the Merkel theory. This results in two sets of three coupled partial differential equations. The first set is valid for unsaturated air and the other one for saturated air. The three coupled partial differential equations consist of one for the absolute humidity of the air, one for the specific enthalpy of the air and one for the Merkel number. The Merkel number is a non-dimensional parameter describing the transfer characteristics in the cooling tower. It is shown by Kloppers [62] that the Poppe method is more accurate than the Merkel method.

Some researchers have used the above mentioned methods to optimize the

configuration of the cooling tower itself. Rubio-Castro et al. [100] used the work of Kloppers and Kröger [63] to simulate and optimize the performance of a mechanical-draft wet cooling tower and compared the Merkel to the Poppe method. They repeated the optimization for different packing types. They concluded that there are large differences between the optimal design and operational variables of wet cooling towers obtained by the Merkel or Poppe method due to the assumptions made in the Merkel method. They advice to use the Poppe method to obtain reliable designs of cooling towers. Serna-González, Ponce-Ortega, and Jiménez-Gutiérrez [103] performed a similar research, but defined the problem as a MINLP in which the type of packing and the type of draft were the integer optimization variables. They used the Merkel method to calculate the heat and mass transfer in the cooling tower. They found that the film packing is the best choice in all investigated cases, which was also concluded by Rubio-Castro et al. [100].

2.4 Turbines

Different types of turbines are used or proposed to be used as the expander in binary cycles. The description of these turbine types is preceded by the Euler equation for turbomachines.

2.4.1 Euler equation for turbomachines

The Euler equation for turbomachines gives the minimum specific work l needed to drive a pump or compressor or the maximum specific work a turbine can deliver. This equation is given by:

$$l = u_1 \cdot c_1 - u_2 \cdot c_2 \tag{2.6}$$

where u and c are the blade velocity and absolute velocity, respectively. The subscripts 1 and 2 denote the inlet and outlet of a stage, respectively. This equation can be transformed to:

$$l = \frac{c_1^2 - c_2^2}{2} + \frac{u_1^2 - u_2^2}{2} - \frac{w_1^2 - w_2^2}{2} \tag{2.7}$$

where w is the relative velocity.

The Euler equation gives the ideal specific work output of a turbine and gives a first idea of the maximum efficiency of a certain turbine concept.

2.4.2 Axial inflow, axial outflow

Typical steam turbines are of the axial-flow type and this type is for instance also used by Ormat [87] and Turboden [115] as the turbine in ORCs. The gathered knowledge from steam turbines can be used for axial-flow turbines with other fluids than water.

Turbine efficiency prediction

To give a very good prediction of the efficiency of a turbine, a 3D-CFD analysis is needed. Macchi [68] has shown that the much simpler mean-line models give deviations of 1 to 2% for axial flow turbines. These mean-line models give predictions of the isentropic efficiency, based on loss correlations. Different categories of losses exist in turbines: profile losses, shock losses, tip leakage losses, endwall losses and cooling losses. The loss correlations are often empirical and give predictions for the entropy increase in both the stator and the rotor, depending on the geometry of the turbine. An overview of these correlations is given by Wei [134].

Macchi and Perdichizzi [69] have used the loss correlation from Craig and Cox [25], which was developed for axial steam turbines, to find the optimum configuration and isentropic efficiency of an axial-turbine stage for different organic fluids and in- and outlet conditions. They have shown that the efficiency of an axial-flow ORC turbine depends on three main parameters:

- The specific speed: $N_S = \frac{n\sqrt{\dot{V}_{out}}}{\Delta h_{is}^{3/4}}$
- The expansion ratio: $\frac{\dot{V}_{out}}{\dot{V}_{in}}$
- A dimensional parameter: $\frac{\sqrt{\dot{V}_{out}}}{\Delta h_{is}^{1/4}}$

where n is the rotational speed [rps], $\dot{V}_{in}$ and $\dot{V}_{out}$ are the volumetric flow rate at the in- and outlet of the turbine [m^3/s] and Δh_{is} is the isentropic enthalpy drop [J/kg].

Figure 2.28a shows the efficiency prediction of axial-flow turbines at the optimum specific speed. It is clearly shown in the figure that the expansion ratio should be low to achieve a high isentropic efficiency. There exists an optimum value of the dimensional parameter $\frac{\sqrt{\dot{V}_{out}}}{\Delta h_{is}^{1/4}}$, which accounts for the size of the turbine.

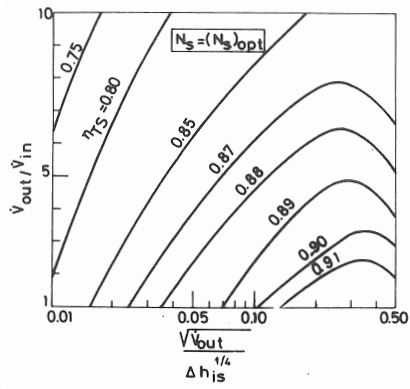

(a) Efficiency prediction for a turbine stage at optimum specific speed

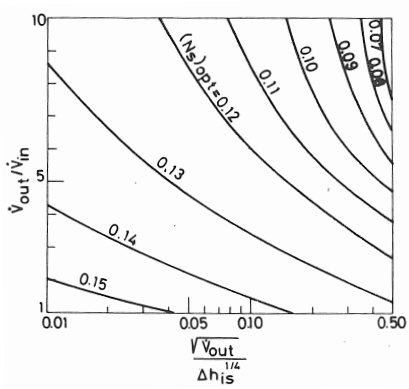

(b) Optimal values of specific speed for a turbine stage

Figure 2.28: Efficiency prediction (a) and optimal specific speed (b) according to Macchi and Perdichizzi [69].

Figure 2.28b shows the optimal values of the specific speed for a turbine stage. With this figure and the definition of the specific speed, the rotational speed of the turbine can be calculated.

2.4.3 Radial inflow, axial outflow

Radial-inflow, axial-outflow turbines, also known as centripetal turbines, are for instance used by Atlas Copco [7] and Triogen [114]. An example is shown in figure 2.29. Often, this type of turbine is an adapted centrifugal compressor, used in the reverse rotational direction.

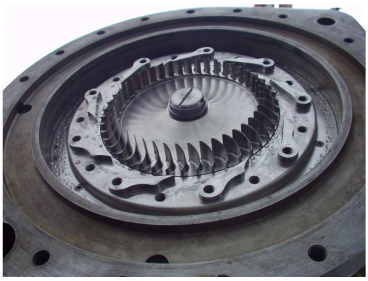

Figure 2.29: Example of a simple radial-inflow, axial-outflow turbine from Tri-o-gen. Figure from Triogen [114].

The advantage of this type of turbine is seen from equation (2.7). The inflow rotational speed u_1 is large, but the outflow rotation speed u_2 is low. The second term in equation (2.7) is large, so a high theoretical efficiency is possible. Marcuccilli and Mathiasin [72] report isentropic efficiencies ranging from 82 to 90% for this type of turbine (single-stage). They give an example of a 3.8 MW isobutane turbine with an efficiency of 88% and a wheel diameter of 40 cm, rotating at 15 300 rpm.

2.4.4 Axial inflow, radial outflow

The axial-inflow, radial-outflow turbine has been invented by Ljungstrom in the beginning of the 20^{th} century as a steam turbine. The Ljungstrom turbine can only deal with a small enthalpy drop per stage, so for the classical power plants, the axial, multi-stage turbines have been used instead. Because of the low enthalpy drop in typical binary-power-plant turbines, the centrifugal turbine has been proposed for these applications [51, 94, 107]. Figure 2.30 shows a 3-stage, 1 MW axial-inflow, radial-outflow turbine, produced by Exergy [36]. Only the 3-stage rotor is shown.

Figure 2.30: Example of a 3-stage, 1 MW axial-inflow, radial-outflow turbine, produced by Exergy. Figure from Exergy [37].

According to Spadacini et al. [107], a 3-stage, 1 MW centrifugal turbine has a theoretical isentropic efficiency of 86%. Pini et al. [94] predict an isentropic efficiency of 89.4% for a 6-stage, 1.3 MW centrifugal turbine. The diameter of the turbine is 1.4 m and it rotates at 3 000 rpm. Currently, only one axial-inflow, radial-outflow turbine has been delivered by Exergy [37].

The advantage of this type of turbine is the low rotational speed (no gearbox needed), the natural increasing flow passage and the “simplicity” of adding

extra stages [94, 107]. The disadvantage is again seen from equation (2.7): u_2 is larger than u_1.

2.5 Electrical system

The focus of the work lies on the mechanical system of binary power plants, but in this section, a brief description of the electrical system is given. Kebede [60] mentions the generator, transformer, transmission line, circuit breakers, switchgear or substation, instrumentation system, protection system and control system as the parts of the electrical system. The generator can be directly connected to the turbine or via a gearbox when the rotational speed of the turbine is too high. For low-capacity power plants located close to consumers, a transformer is not necessary, but in many cases, geothermal power plants are located in remote areas and a transformer and new transmission lines are necessary. This access to the electricity grid is a key cost consideration; according to Tester et al. [109], some geothermal projects have been dropped due to constraints on transmission access.

Geothermal power plants are currently run as base load units. If the wells have been drilled, the marginal cost of the brine is almost zero and the power plant runs at its full capacity. The fact that geothermal binary power plants are very flexible (time constants of minutes) is currently not used for electricity balancing. For balancing to happen, the owner of the power plant should be paid for not having his plant run at full capacity.

2.6 Optimization of binary power plants

Section 2.1.5 describes some of the available literature about the optimization of binary power *cycles*. In these optimizations the cycle parameters are optimized and many components of the ORC are often assumed to be ideal or modeled very simplistically; pinch-point-temperature differences are fixed, condenser temperature is fixed, etcetera. All these parameters depend in fact on the configuration of the cycle, on the configuration of the components and on the choice of the working fluid and have a strong influence on the performance and the total cost of the ORC. In sections 2.2-2.4 different components are described and in this section, existingliterature on the combination of the cycle and component level is mentioned.

The necessity of taking into account the influence of the sizing of the components has already been touched upon in the literature. Madhawa et al. [70] have

minimized the ratio of the total heat-exchanger surface and the net electric power generated by the cycle for fixed heat-exchanger configurations. Franco and Villani [38] divided the ORC in two levels: the system level and the component level. First, the authors optimized the system level. In a next step, they used this optimal system configuration to find the optimal configuration of the components. An iteration between both levels was needed to come to the final solution.

Only a limited number of studies are available in the open literature which perform a detailed economic optimization of organic Rankine cycles. Quoilin et al. [99] have minimized the specific cost of small ORCs. Recently, Astolfi et al. [6] have used the same objective function for large ORCs powered by geothermal heat.

2.7 Conclusion

Although only the most relevant studies are mentioned in this literature study, it is clear that much research has been performed to increase the applicability of low-temperature-geothermal heat sources. Most of the research focuses on the development of new cycles and on the optimization of these cycles. A large number of types of ORCs are proposed, depending on the configuration (simple, recuperated or turbine bleeding), on the number of pressure levels, on the working fluid, etcetera. Other researchers focus on the Kalina cycle, but only a limited amount of research has been performed to compare all these different types of binary cycles for different fluids.

Another field of research focuses on the modeling and the improvement of components. Much numerical and experimental research is spent on heat exchangers, cooling systems and turbines, but more experimental data are needed to improve existing correlations.

This work focuses on the combination of the system and the component level in order to optimize the cycle and the components together.

Chapter 3

Thermodynamic optimization of binary cycles

The content of this chapter was previously published as:
D. Walraven, B. Laenen, and W. D'haeseleer. "Comparison of thermodynamic cycles for power production from low-temperature geothermal heat sources". In: *Energy Conversion and Management* 66.C (2013), pp. 220–233

Simple, first-law thermodynamic models for binary cycles are developed in this chapter. The goal is to have models which can give a first impression of the performance of binary cycles in different configurations. After an overview of possible definitions of efficiencies and their meaning, the mechanical power generation of the binary cycles is maximized for a given geothermal heat source. The impact of some internal and external parameters on the performance of the power plant is investigated. Based on these results, it is concluded that pinch-point-temperature differences in heat exchangers and the condenser temperature have an enormous impact on the efficiency of the cycle.

3.1 Definition of efficiencies

In the literature, different definitions of efficiencies exist. All of these efficiencies are useful, but they often have a different meaning. Therefore, it is important

to know how the efficiencies are defined and to use the right efficiency in the appropriate circumstances and context.

Cycle efficiency

The *cycle efficiency* describes how well a thermodynamic cycle converts heat, which is added to the cycle, to mechanical power. The *energetic cycle efficiency* η_{en}^{cycle} is defined as the fraction of the net mechanical power output $\dot{W}_{net}$ to the heat input $\dot{Q}_{in}$:

$$\eta_{en}^{cycle} = \frac{\dot{W}_{net}}{\dot{Q}_{in}}. \tag{3.1}$$

When the heat source is a geothermal brine, the heat added to the cycle can be written as

$$\dot{Q}_{in} = \dot{m}_{brine}\Delta h_{brine} = \dot{m}_{brine}(h_{in}^{brine} - h_{out}^{brine}) \tag{3.2}$$

with $\dot{m}_{brine}$ the mass flow rate of brine, Δh_{brine} the specific enthalpy drop of the brine, h_{in}^{brine} and h_{out}^{brine} the specific enthalpy of the brine before and after heat is added to the cycle.

This definition of the efficiency is also used for classical cycles powered by fossil fuel, but $\dot{Q}_{in}$ is in that case the higher heating value or lower heating value of the fuel. This heating value is obtained by measuring the amount of heat that is released in the combustion of a stoichiometric mixture of fuel and oxidizer, for initial and end temperatures of 25°C. The higher heating value is calculated with water being a liquid, the lower heating value with water being a vapor.

Analogous to the energetic cycle efficiency, also an *exergetic cycle efficiency* η_{ex}^{cycle} can be defined:

$$\eta_{ex}^{cycle} = \frac{\dot{W}_{net}}{\dot{m}_{brine}(e_{in}^{brine} - e_{out}^{brine})} \tag{3.3}$$

where e_{in}^{brine} and e_{out}^{brine} are the specific flow exergy of the brine before and after heat is added to the cycle, respectively. The specific flow exergy e is defined as:

$$e = (h - h_0) - T_0(s - s_0), \tag{3.4}$$

where s is the specific entropy of the brine and the subscript 0 refers to the dead state; so T_0 is the dead-state temperature, usually being the ambient temperature. h_0 and s_0 are calculated for the same brine at the pressure p_0 and temperature T_0.

Plant efficiency

The *cycle* efficiency only describes how efficient a cycle is in converting a certain amount of heat into mechanical power, but it does not tell how efficient the heat source is used. Therefore, both energetic η_{en}^{plant} and exergetic η_{ex}^{plant} *plant efficiencies* are defined, respectively:

$$\eta_{en}^{plant} = \frac{\dot{W}_{net}}{\dot{Q}_{available}} = \frac{\dot{W}_{net}}{\dot{m}_{brine}(h_{in}^{brine} - h_0^{brine})} \tag{3.5}$$

$$\eta_{ex}^{plant} = \frac{\dot{W}_{net}}{\dot{E}_{available}} = \frac{\dot{W}_{net}}{\dot{m}_{brine} e_{in}^{brine}} \tag{3.6}$$

$\dot{Q}_{available}$ and $\dot{E}_{available}$ are the heat and exergy available in the heat source, respectively. These plant efficiencies can be rewritten as a function of the respective cycle efficiencies:

$$\eta_{en}^{plant} = \frac{\dot{W}_{net}}{\dot{m}_{brine}(h_{in}^{brine} - h_{out}^{brine})} \quad \frac{\dot{m}_{brine}(h_{in}^{brine} - h_{out}^{brine})}{\dot{m}_{brine}(h_{in}^{brine} - h_0^{brine})} \tag{3.7}$$

$$= \eta_{en}^{cycle} \frac{\dot{Q}_{in}}{\dot{Q}_{available}} \tag{3.8}$$

$$= \eta_{en}^{cycle} \epsilon_{en}^{plant} \tag{3.9}$$

$$\eta_{ex}^{plant} = \frac{\dot{W}_{net}}{\dot{m}_{brine}(e_{in}^{brine} - e_{out}^{brine})} \quad \frac{\dot{m}_{brine}(e_{in}^{brine} - e_{out}^{brine})}{\dot{m}_{brine} e_{in}^{brine}} \tag{3.10}$$

$$= \eta_{ex}^{cycle} \frac{\dot{E}_{in}}{\dot{E}_{available}} \tag{3.11}$$

$$= \eta_{ex}^{cycle} \epsilon_{ex}^{plant} \tag{3.12}$$

where ϵ_{en}^{plant} and ϵ_{ex}^{plant} are the energetic plant effectiveness and exergetic plant effectiveness, respectively. They show how efficient the geothermal brine is cooled in the energetic and exergetic sense, respectively.

When a geothermal brine is used to generate electricity, the thermodynamic goal is to maximize the net work output per unit mass of brine. So, the fraction $\dot{W}_{net}/\dot{m}_{brine}$ should be maximized. As seen from Eqs. (3.5) and (3.6) this is the same as maximizing the energetic or exergetic *plant* efficiency, because h_{in}^{brine},

h_0^{brine} and e_{in}^{brine} only depend on the geothermal source and the surroundings, which are assumed to be given.

Equations (3.9) and (3.12) show that the heat source should be cooled down as far as possible (i.e., $\eta_i^{cooling} \to 1$) *and* the heat added to the cycle should be efficiently converted to electricity, to have a high plant efficiency and thus a high power output per unit mass of brine.

3.2 Models

Simple, thermodynamic models for two types of binary cycles are described in this section. These are the organic Rankine cycle (ORC) and the Kalina cycle.

3.2.1 Organic Rankine cycle

ORCs can have a wide range of configurations; some of them are described in this section.

ORC configurations

Three ORC configurations are investigated, as shown in figure 3.1. In the simple ORC (figure 3.1a), the working fluid is pumped from the low to the high pressure (1→2), heated by the brine (2→6), expanded in the turbine (6→7) and cooled in the condenser (7→1). Often, state 7 is still at a high temperature and a recuperator can be used as shown in figure 3.1b. This configuration will improve the cycle efficiency, because less external (geothermal) heat is needed for the same power output. Another method to improve the cycle efficiency is the use of turbine bleeding as depicted in figure 3.1c. Part of the working fluid (state 8) is extracted from the turbine at an intermediate pressure and is mixed with state 2 to form state 9. Then the working fluid is pumped to the high pressure (9→3) and the rest of the cycle is analogous to the simple ORC. A disadvantage of this cycle is that part of the heated working fluid is not expanded in the turbine.

Subcritical and transcritical ORCs

A distinction has to be made between subcritical, transcritical and supercritical cycles. In a subcritical cycle, the pressure is always below the critical pressure

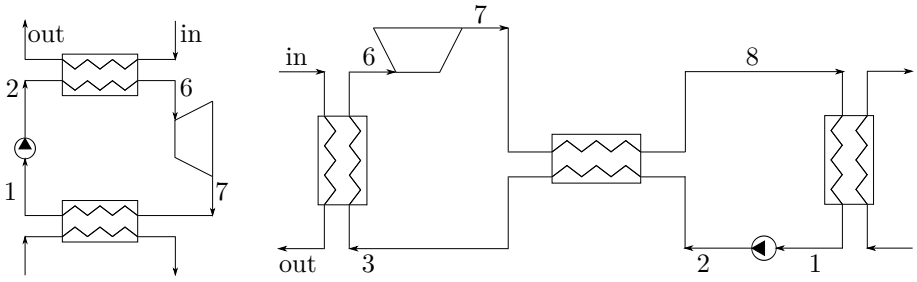

(a) Simple ORC

(b) ORC with recuperation

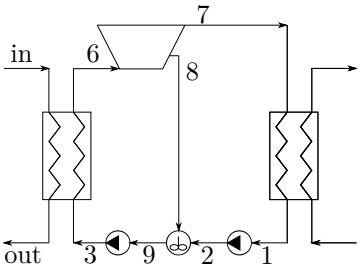

(c) ORC with turbine bleeding

Figure 3.1: Different ORC configurations: simple ORC (a), ORC with recuperator (b) and ORC with turbine bleeding (c). The brine in- and outlet are given by "in" and "out", respectively.

and in a supercritical cycle, the pressure is always above the critical pressure. In a transcritical cycle, the low pressure is below the critical pressure, and the high pressure above the critical one. In this work, only subcritical and transcritical cycles are investigated. The three configurations in figure 3.1 can all be subcritical or transcritical, depending on the maximum pressure in the cycle.

Figure 3.2 shows the temperature-heat diagram of the heating process in a subcritical and a transcritical cycle. In the subcritical cycle, the working fluid is heated in the economizer (2→4), in the evaporator (4→5) and in the superheater (5→6). Due to the evaporation at constant temperature in the subcritical cycle, large temperature differences exist between the brine-cooling curve and the working-fluid-heating curve. These temperature differences induce the creation of a high amount of irreversibility. In the transcritical cycle, the temperature differences between the brine-cooling curve and the working-fluid-heating curve are smaller. So, the irreversibilities created in the heat exchange of the transcritical case are smaller and because of the better fit between the

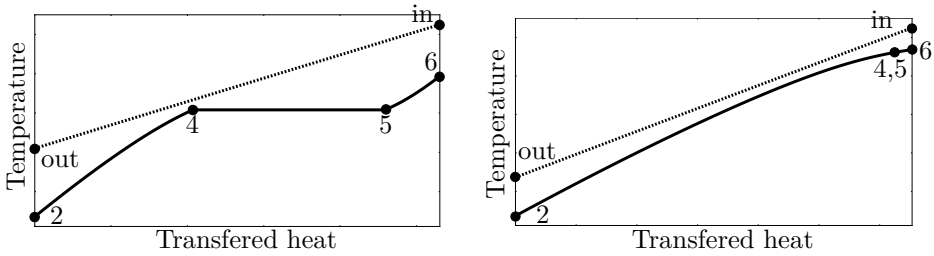

(a) Subcritical **(b)** Transcritical

Figure 3.2: Temperature-heat diagrams of the heating process in a subcritical (a) and transcritical (b) cycle. The working fluid (–) is heated by the cooling brine (· · ·).

curves, the brine can cool down more than in the subcritical case for an identical pinch-point-temperature difference.

Number of pressure levels

The cycles shown in figure 3.1 have only one high pressure level (except for the steam-bleeding case, which has an intermediate bleeding pressure). It is possible to combine two or more of these cycles. Figure 3.3a shows a simple ORC with three pressure levels, but another number of pressure levels and other configurations are also possible. The brine, which is not shown in the figure, is split into parts to heat the different cycles. This splitting is done in such a way that the hot brine first heats the working fluid at the highest temperature. Figure 3.3b shows the temperature-heat diagram of a three-pressure level, subcritical cycle without superheating. The three sub-cycles are called a, b and c and $p_a < p_b < p_c$.
It is seen that the temperature difference between the brine-cooling curve and the working-fluid-heating curve is lower than for a subcritical cycle with one pressure level. So, efficiency improvements can be obtained by applying more than one pressure level.

3.2.2 Kalina cycle

The scheme of a typical Kalina cycle, which always contains a recuperator, is shown in figure 3.4a. State 1, which has an intermediate concentration of ammonia x_{int}, is pumped to the high pressure (1→2), heated in a recuperator (2→3) and heated by the brine (3→5). State 5 is located in the two-phase region and the vapor part (state 6 with a high concentration of ammonia x_{high})

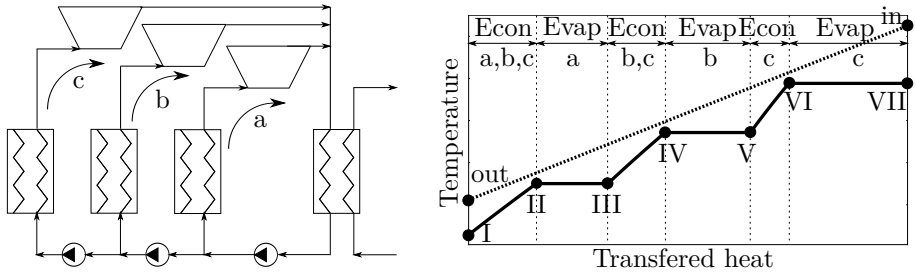

(a) Triple-pressure simple ORC **(b)** Temperature-heat diagram

Figure 3.3: Scheme and temperature-heat diagram of a triple-pressure, subcritical cycle without superheating. The working fluid (–) is heated by the cooling brine (· · ·). The three pressure levels are called *a*, *b* and *c*. The economizers and evaporators are denoted by "Econ" and "Evap", respectively.

is split from the liquid part (state 9 with a low concentration of ammonia x_{low}) in the separator. State 6 is expanded in the turbine (6→7), mixed with state 9 (7+9→11), cooled in the recuperator (11→8) and cooled in the condenser (8→1). Often a second recuperator is used to exchange heat between states 9 and 3, but in this work this heat exchanger is omitted because the mass flow rate around the turbine is small.

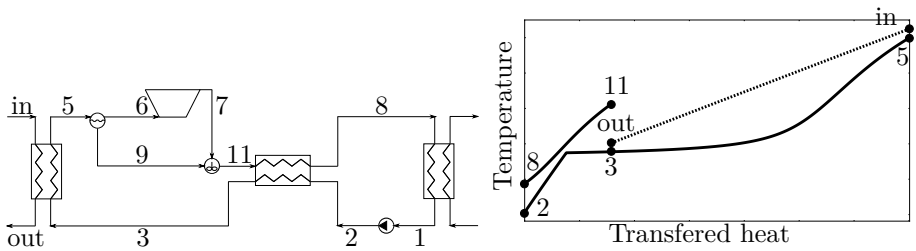

(a) Scheme of the Kalina cycle. **(b)** Temperature-heat diagram of the Kalina cycle.

Figure 3.4: Scheme and temperature-heat diagram of the Kalina cycle. The working fluid (–) is heated by the cooling brine (· · ·).

Figure 3.4b shows the corresponding temperature-heat diagram of the Kalina cycle of figure 3.4a. Because a mixture of fluids is used, the evaporation at constant pressure does not take place at a constant temperature. This "temperature glide" decreases the temperature difference in the heat exchange between brine and working fluid; so less irreversibilities are created in the Kalina cycle than in a subcritical ORC. The temperature glide at the condenser

pressure allows a strong internal heat recuperation. In figure 3.4b, boiling occurs in the preheater, but this is probably not technically feasible.

3.2.3 Component equations

For the modeling of the binary cycles, it is assumed that state 1 is saturated liquid at a given temperature T_1 and that the heat exchangers are ideal (no pressure drop and heat loss). It is allowed that the working fluid at the inlet of the turbine (state 6) is superheated for all types of fluids (even for the so-called dry ones).

For the cycle with recuperation, it is assumed that as much heat as possible is recuperated, taking into account a minimum temperature difference in the recuperator ΔT_{min}^{recup}. For the cycle with turbine bleeding, it is assumed that state 9 (figure 3.1) is saturated liquid. The mass flow rate at the inlet of the turbine is given by $\dot{m}_{wf}$. The fraction ε is extracted at the intermediate pressure and the other part (1-ε) expands to the condenser pressure.

Pump and turbine

The relationship between the states before (state 1) and after (state 2) the pump are given by:

$$h_2 = h_1 + \frac{h_{2s} - h_1}{\eta_P} \tag{3.13}$$

with state 1 at the low pressure p_{low}, state 2 at the high pressure p_{high} and state 2s at p_{high} and the same entropy as state 1. The isentropic efficiency of the pump η_P is assumed to be known. The mechanical power needed to drive the pump $\dot{W}_P$ is:

$$\dot{W}_P = \dot{m}_{wf}(h_2 - h_1) \tag{3.14}$$

with $\dot{m}_{wf}$ the mass flow rate of the working fluid. The irreversibility created in this pump, is:

$$\begin{aligned} \dot{I}_P &= (\dot{m}_{wf} e_1 + \dot{W}_P) - (\dot{m}_{wf} e_2) \\ &= \dot{m}_{wf} T_0 (s_2 - s_1) \end{aligned} \tag{3.15}$$

For the second pump in the cycle with turbine bleeding, the equations are analogous:

$$\dot{W}_P = (1 - \varepsilon)\dot{m}_{wf}(h_2 - h_1) + \dot{m}_{wf}(h_3 - h_9) \tag{3.16}$$

$$\dot{I}_P = (1 - \varepsilon)\dot{m}_{wf} T_0 (s_2 - s_1) + \dot{m}_{wf} T_0 (s_3 - s_9) \tag{3.17}$$

For the turbine, the relationship between the states at the turbine inlet (state 6) and at the turbine outlet (state 7) is given by:

$$h_7 = h_6 - (h_6 - h_{7s})\eta_T \tag{3.18}$$

with state 6 at p_{high}, state 7 at p_{low} and state 7s at p_{low} and the same entropy as state 6. The isentropic efficiency of the turbine η_T is assumed to be known. The turbine mechanical power and irreversibility generated in the turbine are:

$$\dot{W}_T = \dot{m}_{wf}(h_6 - h_7) \tag{3.19}$$

$$\dot{I}_T = \dot{m}_{wf} T_0 (s_7 - s_6) \tag{3.20}$$

For the cycle with turbine bleeding, these equations are:

$$\dot{W}_T = \dot{m}_{wf}(h_6 - h_8) + (1-\varepsilon)\dot{m}_{wf}(h_8 - h_7) \tag{3.21}$$

$$\dot{I}_T = \dot{m}_{wf} T_0 (s_8 - s_6) + (1-\varepsilon)\dot{m}_{wf} T_0 (s_7 - s_8) \tag{3.22}$$

In this chapter, the net mechanical power output is given by:

$$\dot{W}_{net} = \dot{W}_T - \dot{W}_P \tag{3.23}$$

So, the power needed for cooling and other auxiliary power is not taken into account.

Heat exchangers

The heat exchangers are assumed to be ideal; so no pressure drop is induced and no heat is lost to the surroundings.

The energy balance for the heat exchanger HX between the brine and working fluid is given by:

$$\dot{m}_{brine}(h_{in}^{brine} - h_{out}^{brine}) = \dot{m}_{wf}(h_6 - h_3) \tag{3.24}$$

A fixed pinch-point-temperature difference ΔT_{min}^{HX} is assumed in this heat exchanger.

In the recuperator, the energy balance is:

$$(h_7 - h_8) = (h_3 - h_2) \tag{3.25}$$

and the minimum temperature difference is given by ΔT_{min}^{recup}. The pinch-point-temperature differences ΔT_{min}^{HX} and ΔT_{min}^{recup} are generally not the same. In

this model it is assumed that these pinch-point-temperature differences are given (see section 3.4). The energy equation for the condenser in the simple or recuperated cycle is given by

$$\dot{m}_{wf}(h_x - h_1) = \dot{m}_{cooling}(h_{out}^{cooling} - h_{in}^{cooling}) \tag{3.26}$$

with $h_x = h_7$ in the simple cycle and $h_x = h_8$ in the cycle with recuperator. The pinch-point-temperature difference in the condenser is ΔT_{min}^{cond}, a mass flow rate $\dot{m}_{cooling}$ of cooling water is used and $h_{in}^{cooling}$ & $h_{out}^{cooling}$ are the enthalpy of the cooling water before and after the condenser, respectively.

The irreversibilities created in the heat exchanger HX and recuperator are:

$$\begin{aligned} \dot{I}_{HX} &= (\dot{m}_{brine}e_{in} + \dot{m}_{wf}e_3) - (\dot{m}_{brine}e_{out} + \dot{m}_{wf}e_6) \\ &= \dot{m}_{brine}T_0(s_{out} - s_{in}) + \dot{m}_{wf}T_0(s_6 - s_3) \end{aligned} \tag{3.27}$$

$$\begin{aligned} \dot{I}_{recup} &= \dot{m}_{wf}[(e_2 + e_7) - (e_3 + e_8)] \\ &= \dot{m}_{wf}T_0[(s_3 - s_2) + (s_8 - s_7)] \end{aligned} \tag{3.28}$$

The irreversibilities created in the cooling installation are given by

$$\dot{I}_{cooling} = \dot{m}_{wf}(e_x - e_1) \tag{3.29}$$

with $e_x = e_7$ for the simple cycle and $e_x = e_8$ for the cycle with recuperation. So, in the cooling installation, all the exergy is lost to the surroundings. For the cycle with turbine bleeding, the irreversibility creation is:

$$\dot{I}_{cooling} = (1 - \varepsilon)\dot{m}_{wf}(e_7 - e_1) \tag{3.30}$$

Mixing

In the cycle with turbine bleeding, two flows are mixed. The energy equation for the mixing process is given by:

$$\varepsilon h_8 + (1 - \varepsilon)h_2 = h_9 \tag{3.31}$$

and the irreversibility created is:

$$\begin{aligned} \dot{I}_{mix} &= \dot{m}_{wf}\left([(1 - \varepsilon)e_2 + \varepsilon e_8] - e_9\right) \\ &= \dot{m}_{wf}T_0(s_9 - [(1 - \varepsilon)s_2 + \varepsilon s_8]) \end{aligned} \tag{3.32}$$

Separator

In this component, the two-phase fluid is separated into its liquid and vapor part. The vapor part has a mass fraction ε:

$$\varepsilon = \frac{x_{int} - x_{low}}{x_{high} - x_{low}}, \tag{3.33}$$

with x_{low}, x_{int} and x_{high} the low, intermediate and high concentration of ammonia, respectively.

Mass flow rate working fluid

The mass flow rate is determined by the minimum pinch-point-temperature difference ΔT_{min}^{HX}. First the point at which this pinch-point-difference occurs is searched and at this point, the mass flow rate of the working fluid can be calculated based on energy conservation:

$$\dot{m}_{wf} = \min \left(\frac{\dot{m}_{brine} \left[h_{in}^{brine} - h^{brine}|_{T+\Delta T_{min}^{HX}} \right]}{h_6 - h} \right), \text{ for } h = h_3 \ldots h_6, \tag{3.34}$$

in which T is the temperature of the working fluid at enthalpy h and $h^{brine}|_{T+\Delta T_{min}^{HX}}$ is the enthalpy of the brine at temperature $T + \Delta T_{min}^{HX}$.

3.3 Optimization

The objective in this chapter is to maximize the net mechanical power generation of the binary cycles, while ignoring heat exchanger sizes or economics. Applying this objective directly can result in numerical issues in the optimizer subroutine due to the possible large difference in values between the objective function, the variables and the constraints. To avoid this, it is chosen to maximize the exergetic plant efficiency, which leads to the same results as maximizing the net mechanical power generation as explained in section 3.1.

3.3.1 Decision variables and constraints

ORC

Table 3.1 shows the decision variables and the constraints used in the optimization of the modeled ORCs. For simple and recuperated ORCs, the

temperature T_6^i and pressure p_6^i at the turbine inlet of every pressure level i are necessary to determine all the states in the cycle with the equations in section 3.2.3. The saturation temperature at the pressure at the turbine inlet $T_{sat}(p_6^i)$ is used instead of the pressure itself to avoid non-linear constraints (first constraint in table 3.1). This is only possible for subcritical cycles, while for transcritical cycles the temperature at p_6 and the critical entropy is used. Another linear constraint is added for multi-pressure cycles so that the pressures appear in a decreasing order. For cycles with turbine bleeding, the saturation temperature of the pressure of state 8 is added for every pressure level, together with an extra linear constraint to make sure that $p_8 < p_6$.

Variable	Lower bound	Upper bound	Configuration
T_6^i	T_1	$T_{in} - \Delta T_{min}^{HX}$	all
$T_{sat}(p_6^i)$ or $T(p_6^i, s_{crit})$	T_1	$T_{in} - \Delta T_{min}^{HX}$	all
$T_{sat}(p_8^i)$	T_1	$\min(T_{in} - \Delta T_{min}^{HX}, T_{crit})$	bleed
Constraint	**Lower bound**	**Upper bound**	**Configuration**
$T_6^i - T_{sat}(p_6^i)$	0	/	all
$T_{sat}(p_6^i) - T_{sat}(p_{6^{i+1}})$	0	/	multi-pressure
$T_{sat}(p_6^i) - T_{sat}(p_8^i)$	0	/	bleed
T_{out}	T_{out}^{min}	/	if constrained

Table 3.1: Decision variables and constraints used in the optimization of the modeled ORCs.

In the next section, the influence of a constraint on the brine-outlet temperature is investigated. In order to do this, a non-linear constraint is added (last constraint in table 3.1).

Kalina

The decision variables used for the Kalina cycle are similar to the ones used for the ORCs. The temperature T_6 and pressure p_6 at the inlet of the turbine are again used, but p_6 is replaced by the temperature of saturated liquid $T_{sat,liq}(p_6)$ at that pressure. The liquid saturation temperature is chosen, because this results in a linear constraint to avoid state 6 being subcooled liquid (see table 3.2). Another decision variable is the concentration of ammonia at the intermediate concentration x_{int}. The upper bound of this variable is chosen to avoid numerical issues when calculating fluid properties. For the same reason a non-linear constraint on the high concentration of ammonia x_{high} is added.

Variable	Lower bound	Upper bound
T_6	T_1	$T_{in} - \Delta T_{min}^{HX}$
$T_{sat,liq}(p_6)$	T_1	$T_{in} - \Delta T_{min}^{HX}$
x_{int}	0	0.97
Constraint	**Lower bound**	**Upper bound**
$T_6 - T_{sat,liq}(p_6)$	0	/
x_{high}	0	0.97
T_{out}	T_{out}^{min}	/

Table 3.2: Decision variables and constraints used in the optimization of the modeled Kalina cycle.

3.3.2 Optimization approach

The models of the binary cycles are developed in Python and the fluid properties are obtained from RefProp [66], which is a software package that contains correlations for many properties of a large number of fluids. More information about RefProp itself and about the connection of RefProp to Python by using F2PY [92] can be found in appendix D. The OpenOpt software [65] is used to calculate the necessary gradients with finite differences and for the coupling of optimizers. The SLSQP subroutine from Scipy [57], which uses a sequential least squares method, is used for the optimization of the ORCs. For the optimization of the Kalina cycle, the more robust, but slower optimizer Ralg [65] is used.

The optimization is schematically shown in figure 3.5.

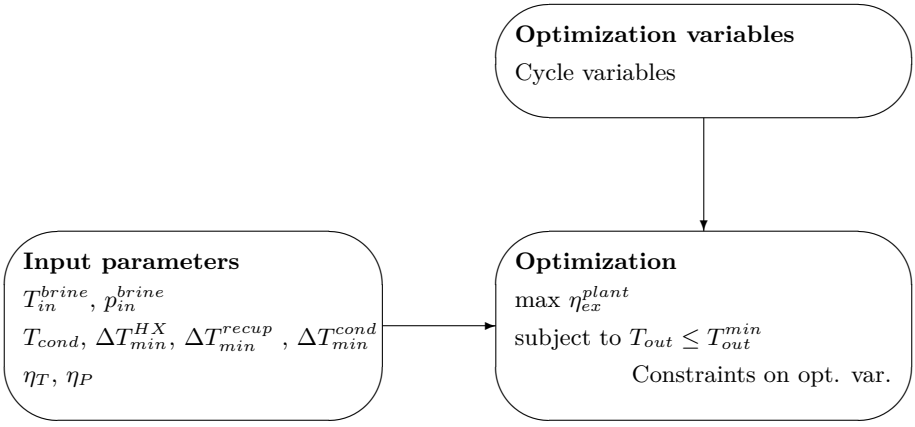

Figure 3.5: Schematic of the optimization used in this chapter.

3.4 Results and discussion

In this section, the models and optimization method are first validated, followed by the definition of a reference case. The ORC configurations of figures 3.1 & 3.3 and the Kalina cycle of figure 3.4 are compared to each other for this reference case. The influence of the reference parameters is investigated afterwards.

3.4.1 Validation of the models and optimization

The model for the subcritical, single-pressure ORC and the optimization routine are validated with the data published by Dai, Wang, and Gao [27]. The optimization is performed for the same working conditions and for various fluids. The comparison shows very good agreement, as seen from table 3.3.

Working fluid	T_6 [°C]	p_{high} [bar]	T_{out} [°C]	η_{en}^{cycle} [%]	Specific net power output [kJ/kg-wf]	Type	Source
R236ea	87.73	12.0	59.59	11.53	22.71	Subcritical,	[27]
	87.28	11.9	59.57	11.48	22.57	simple	Present
R113	120	6.81	≈ 105	14.45	-	Subcritical,	[138]
	120	6.81	105.83	14.44	25.37	recuperated	Present
R113	120	6.81	≈ 110	14.34	-	Subcritical,	[138]
	120	6.81	112.51	14.24	22.42	turbine bleeding	Present
CO_2	100	119	-	8.4	20.1	Transcritical,	[21]
	100	118.8	25.60	8.43	20.08	simple	Present

Table 3.3: Validation of the single-pressure ORC-model and the optimization routine with data published in the literature.

Subcritical cycles without superheating have been optimized by Yari [138]. Simple cycles, recuperated cycles and cycles with turbine bleeding with a fixed evaporation temperature of 120°C were treated. The results are given in table 3.3. From this table, it is concluded that the models for recuperation and turbine bleeding are validated. Cayer, Galanis, and Nesreddine [21] have maximized the specific net power output per unit of working fluid for a transcritical cycle with CO_2 as working fluid. As seen from table 3.3, it can be concluded that the present model works fine for transcritical cycles.

The model of the Kalina cycle is validated by comparison to Ogriseck [86] as shown in table 3.4.

Inputs				Results					Source
T_5 [°C]	p_5 [bar]	T_1 [°C]	x_{int} [-]	$\dot{m}_{wf}$ [kg/s]	x_{low} [-]	x_{high} [-]	T_{out} [°C]	$\dot{W}_{net}$ [kW$_e$]	
122	32.3	8	0.82	16.8	0.50	0.97	80	2195	[86]
122	32.3	8	0.82	16.3	0.50	0.97	79	2185	Present

Table 3.4: Validation of the single-pressure ORC-model and the optimization routine with data published in the literature.

3.4.2 Parameters of the reference case

Table 3.5 shows the parameters which are used in the remainder of this chapter, unless denoted otherwise. The brine-inlet temperature and pressure are given by T_{in}^{brine} and p_{in}^{brine}, respectively. The cooling-water temperature is taken to be equal to T_0. The results in this chapter are given per unit of mass flow rate of brine.

T_{in}^{brine}	125°C	η_P	80 %
p_{in}^{brine}	5 bar	η_T	85 %
T_1	25°C	ΔT_{min}^{HX}	5°C
T_0	15°C	ΔT_{min}^{recup}	5°C
p_0	1 bar	ΔT_{min}^{cond}	5°C

Table 3.5: Parameters of the reference case.

For some fluids available in RefProp, only supercritical cycles are possible and they are therefore not considered. All other fluids, the list is given in appendix D.3, are used in the calculations to obtain the thermodynamic optimal cycle configuration. Only thermodynamic properties of the fluids are taken into account. Other properties like ozone depletion potential, global warming potential, flammability, etcetera are not taken into account. More information of these properties can be found in other work (for example IPCC Working Group I [54]). For the Kalina cycle, a maximum ammonia concentration of 97% is used, because for higher concentrations RefProp is not always able to find the thermodynamic properties of the mixture.

3.4.3 Brine-cooling temperature without constraint

In this section, there is no constraint on the brine-outlet temperature and the brine can cool down to its optimal outlet temperature. In the next section, a minimum brine-outlet temperature of 75°C is used. This is done to simulate cases where scaling and fouling has to be avoided or when the brine is used for heating or cooling (absorption or adsorption cooling).

Single pressure

Figure 3.6 shows the exergetic plant efficiency and the energetic cycle efficiency for the 20 fluids with the highest mechanical power output in a single-pressure-level cycle for the simple configuration. The fluids are ordered from the best (R227ea) to the worst fluid (C5F12) of the 20 fluids shown (in terms of exergetic plant efficiency). As mentioned in section 3.1, it is the plant efficiency that should be maximized. In figure 3.6, it is chosen to plot the *exergetic* plant efficiency, because this characteristic allows an easier comparison between power plants with different brine-inlet temperatures or dead-state temperatures (as done in section 3.4.5). The energetic cycle efficiency is added to the figure, because this value shows that maximizing the plant efficiency is not equal to maximizing the cycle efficiency. It is also a characteristic that is often used in the literature and is added as a reference.

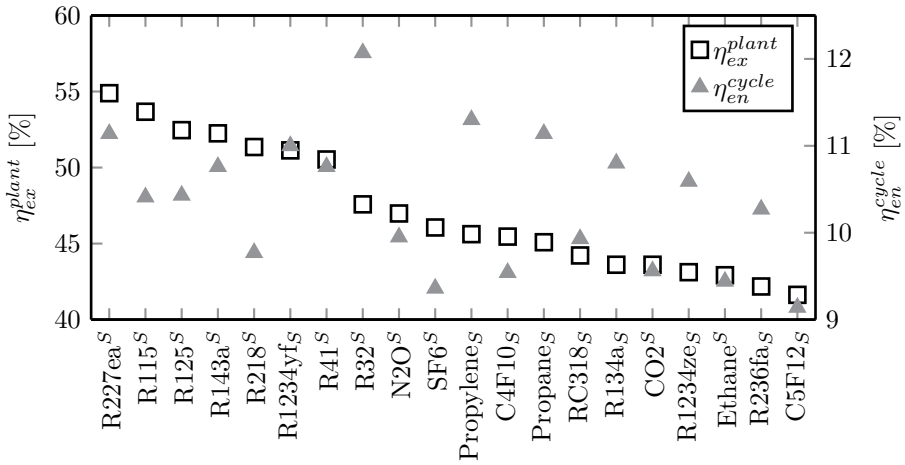

Figure 3.6: Exergetic plant efficiency (□) and energetic cycle efficiency (△) of the 20 fluids with the highest mechanical power output in a single-pressure-level cycle for the simple (S) configuration. Subcritical cycles are denoted with a *sub*script S and transcritical cycles with a *super*script S.

When the fluids are sorted by decreasing exergetic plant efficiency, the energetic cycle efficiency does not. It is seen from Eqs. (3.9) and (3.12) that the plant efficiency is the product of the cycle efficiency and the plant effectiveness. This means that the cycle with R115 can cool the brine further down than a cycle with R125, because both have about the same cycle efficiency, but a different plant efficiency. The other way around is also possible, as seen in the case of R41 and R32. In geothermal wells, the inlet flow rate is limited and it is the

plant efficiency that is important. In other cases, the heat input is limited and the cycle efficiency is the determining parameter.

In figure 3.6, only cycles with a simple configuration are shown, because the model shows that it is not useful to use a recuperator or turbine bleeding. Recuperation and turbine bleeding can increase the cycle efficiency, but not the plant efficiency in this case. When an internal heat exchanger is used, the amount of heat transferred between the brine and the working fluid is decreased and the brine cools down less. The cycle efficiency increases, but the plant effectiveness decreases. The net result is exactly zero; part of the working fluid is heated in the recuperator instead of heated by the brine, but the rest of the cycle remains the same.

The best cycles are all transcritical ones and have critical temperatures below 80°C. The only exception is R227ea, which has a critical temperature of 101.75°C. In the obtained cycle with R227ea, the expansion occurs partially through the two-phase region. This has no consequences on the performance of the turbine if the outlet state of the turbine is superheated [15, 79]. Only R236fa and C5f12 have critical temperatures equal to, or higher than, the brine-inlet temperature.

R245fa is often used as the working fluid in ORCs. An optimization with this fluid leads to a subcritical cycle with an exergetic plant efficiency of 39.7% and an energetic cycle efficiency of 10.4%. The mechanical power output of this cycle does not belong to the top-20 and is therefore not mentioned in figure 3.6.

All pure fluids condense at a constant temperature, so that the cooling-water temperature increases from 15°C to about 20°C ($T_{cond} - \Delta T_{min}^{cond}$) (not shown). In the Kalina cycle, the minimum temperature in the condenser is assumed to be 21°C instead of 25°C, so that the cooling water heats up from 15 to about 20°C. Even with this assumption, the exergetic plant efficiency of the Kalina cycle is only 41.5%. So, the Kalina cycle is even thermodynamicaly outperformed by simple subcritical ORCs. The obtained, optimal Kalina cycle, is not a "real" Kalina cycle, because the working fluid before the separator (state 5) is saturated vapor. So, a separator is not needed and a recuperated subcritical ORC with a mixture of water and ammonia with a constant concentration is obtained.

In the Kalina cycle, the temperature glide at the condenser pressure allows a high amount of recuperation. As shown in figure 3.4b, the pinch point is in the optimal configuration somewhere in the evaporator and not at the end of the economizer. This allows a higher mass flow rate of working fluid per unit brine and a higher mechanical power output.

Figure 3.7 shows the net mechanical power generation and irreversibilities as a fraction of the incoming brine exergy for 4 optimized cycles. The first one

is a transcritical cycle with R227ea, the second one is a subcritical cycle with propylene, the third one is the Kalina cycle considered and the fourth one is a subcritical cycle with R245fa, which serves as a reference. The cycle with R227ea performs the best because of the low irreversibilities created in the heat exchange between brine and working fluid and because of the high plant effectiveness. The pressure ratio in this cycle is high, so the irreversibilities created in the pump and turbine are high too. The combination of the high plant effectiveness and the average cycle efficiency causes relatively high irreversibilities in the cooling installation.

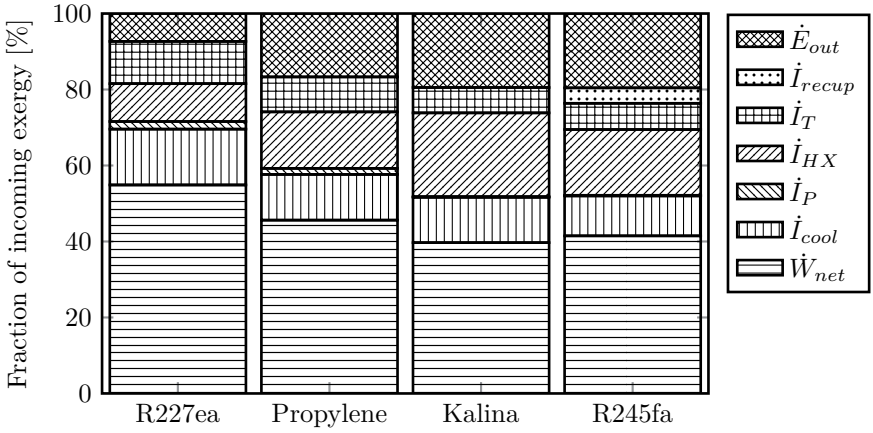

Figure 3.7: Net mechanical power generation and irreversibilities created, as fraction of the incoming brine exergy for the optimal transcritical cycle with R227ea, the optimal subcritical cycle with propylene, the optimal Kalina cycle and the optimal cycle with R245fa as a reference.

The subcritical cycle with propylene performs better than the Kalina cycle because of the higher plant effectiveness and the lower irreversibilities created in the high-pressure heat exchange ($\dot{I}_{HX}$ and $\dot{I}_{recup}$). In the Kalina cycle, the lower irreversibilities created in the condenser (temperature glide), turbine and pump cannot compensate for this. The cycle with R245fa generates less mechanical power than the other cycles because of the very high irreversibilities created in the heat exchanger. This is a consequence of the high heat of vaporization of R245fa. To cool the brine sufficiently down, the optimal evaporation temperature should be low and a high amount of irreversibility is created in the heat exchanger.

One of the advantages of the Kalina cycle would be the temperature glide. This temperature glide causes a low creation of irreversibilities in the condenser, but

not in the high-pressure heat exchanger. Some simple subcritical ORCs even outperform the Kalina cycle considered in this context. This comparison is only thermodynamical, so no economic conclusions are made.

Dual pressure

It is also possible to use more than 1 pressure level in the ORCs. The exergetic plant and energetic cycle efficiency for the 20 fluids with the highest mechanical power output in a dual-pressure level cycle are shown in figure 3.8. Again, only the simple configuration is shown because of the same reason as before.

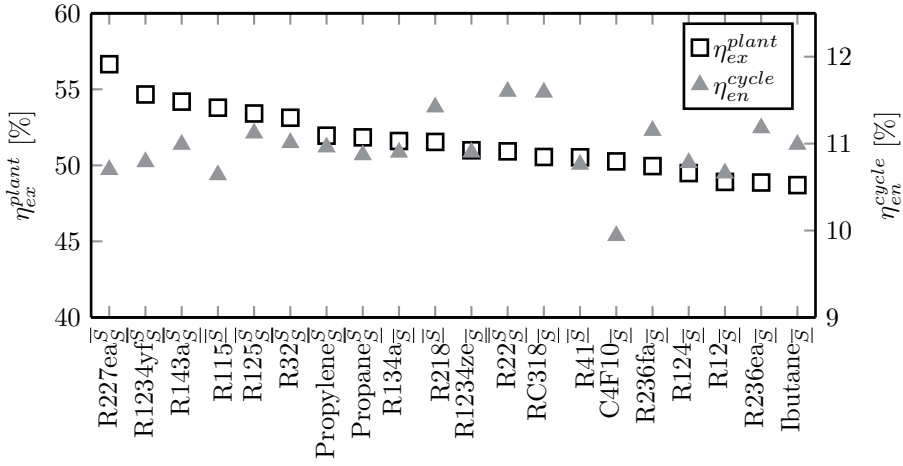

Figure 3.8: Exergetic plant efficiency (□) and energetic cycle efficiency (△) of the 20 fluids with the highest mechanical power output in a dual-pressure level cycle for the simple configuration. Subcritical cycles are denoted with a *sub*script S and transcritical cycles with a *super*script S. The low-pressure sub-cycle is underlined, the high-pressure sub-cycle has an overbar.

The cycles with the highest mechanical power output are almost all a combination of a subcritical cycle with a transcritical one, but the addition of the subcritical part does not improve the plant efficiency very much (for example for R227ea an increase of 3% is obtained by using 2 pressure levels instead of one). For subcritical cycles, the effect is much stronger. The dual-pressure level cycle with R134a generates almost 20% more mechanical power than the single-pressure-level cycle. Because of the strong improvement of the subcritical cycles and the poor improvement of the transcritical cycles, the difference between the best and the worst fluid/cycle becomes smaller. The best

15 fluids have an exergetic efficiency above 50%. So, it can be concluded that subcritical cycles with two pressure levels are almost as efficient as transcritical cycles.

For the single-pressure cycle in figure 3.6, many fluids with a low critical temperature like R41, N_2O, SF6, CO_2 and ethane perform well. Their optimal cycle is a transcritical one, with a pressure much above their critical pressure. Due to this high pressure, the irreversibilities created in the pump and the turbine are high. When two pressure levels are allowed (figure 3.8), most of these fluids are not among the 20 best performing fluids and are replaced by fluids with a higher critical temperature like R22, C4F10, R124, R12, R236ea and isobutane. Their critical temperature ranges from 110 to 140°C and the both pressure levels are subcritical.

For the single-pressure level cycles (figure 3.6), the energetic cycle efficiency fluctuates strongly. For the dual-pressure level cycles, the energetic cycle efficiency is more constant and is about 11%. So, the extra pressure level does not only reduce the difference in plant efficiency, but also in cycle efficiency.

Triple and multi-pressure

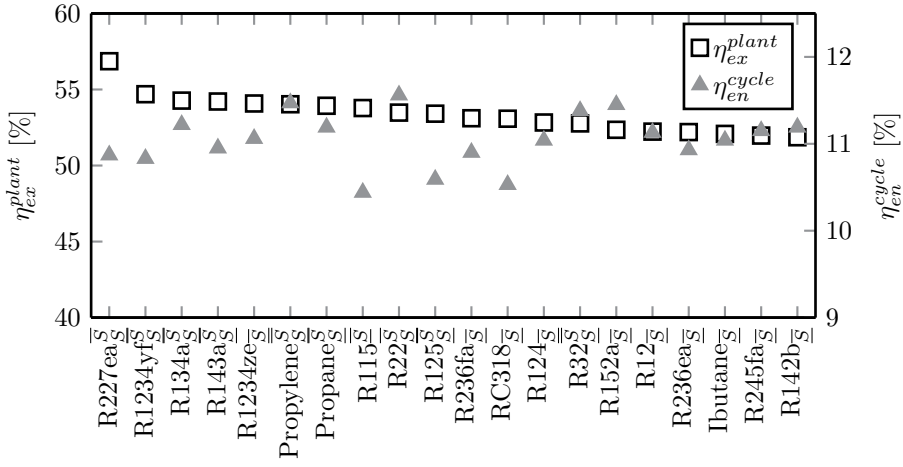

Figure 3.9: Exergetic plant efficiency (□) and energetic cycle efficiency (△) of the 20 fluids with the highest mechanical power output in a triple-pressure level cycle for the simple configuration. Subcritical cycles are denoted with a *sub*script S and transcritical cycles with a *super*script S. The low-pressure sub-cycle is underlined, the intermediate pressure sub-cycle is lined through and the high-pressure sub-cycle is overlined.

Figure 3.9 shows the efficiencies when a third pressure level is added. The exergetic plant efficiency improves a bit for the subcritical cycles, but the effect is much less than the addition of the second pressure level. The difference in performance between the fluids has become smaller and the energetic cycle efficiency is about 11%. Addition of more pressure levels will improve the power plant performance, but every extra pressure level will have less effect. By addition of this extra pressure level, fluids with higher critical temperatures (for example R152a, R245fa, etcetera) are performing relatively better, replacing fluids with lower critical pressures (for example R41, R218, etcetera).

Figure 3.10 shows the exergetic efficiency of a multi-pressure cycle with isobutane for different pressure levels. The improvement of the addition of an extra pressure level is shown on the right-hand side. This improvement is defined as:

$$\epsilon_i = \frac{\dot{W}^i_{net} - \dot{W}^{i-1}_{net}}{\dot{W}^{i-1}_{net}} \tag{3.35}$$

with ϵ_i the improvement of addition of the ith pressure level and $\dot{W}^i_{net}$ the net power output of a cycle with i pressure levels. From the figure, it is seen that the addition of an extra pressure level is thermodynamically useful, but the effect decreases with increasing number of pressure levels.

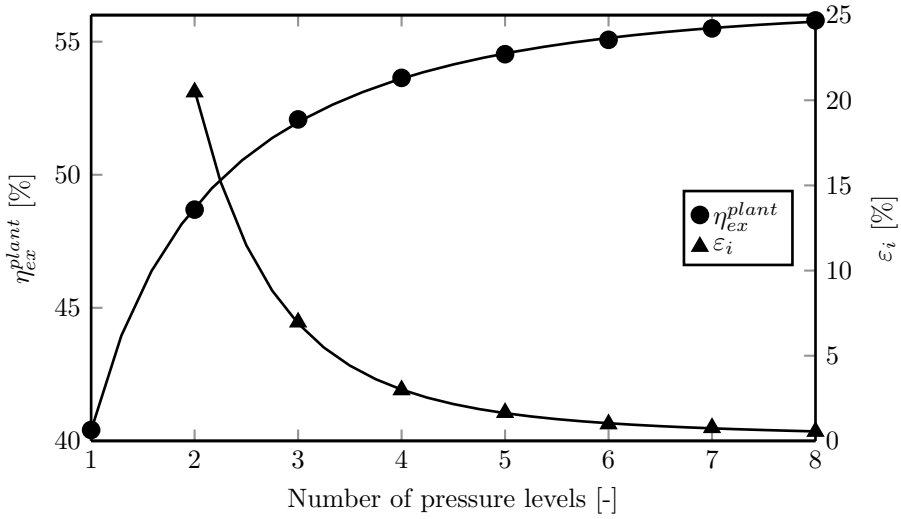

Figure 3.10: Exergetic plant efficiency (○) of a multi-pressure simple cycle with isobutane as a function of the number of pressure levels. The improvement of an extra pressure level is shown (△).

Figure 3.11 shows the net mechanical power generation and irreversibilities created in the single, dual and triple-pressure cycle with isobutane. The addition of extra pressure levels improves the plant effectiveness and decreases the irreversibility created in the high-pressure heat exchanger. Because of the higher pumping power and turbine power, also more irreversibilities are created in these components.

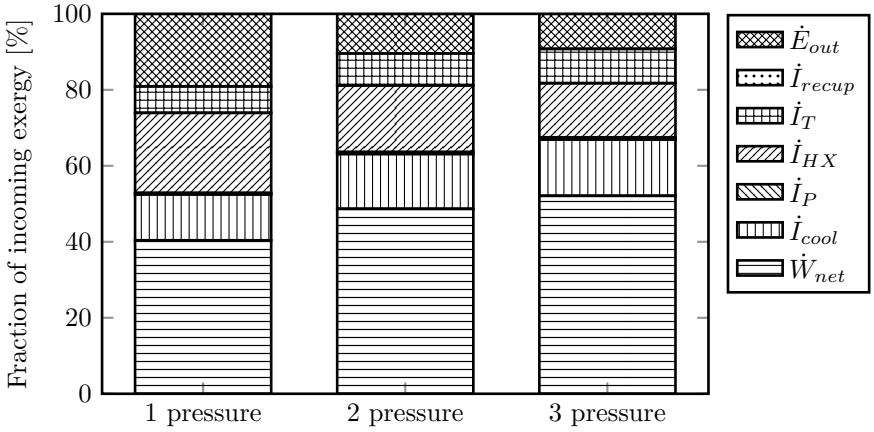

Figure 3.11: Net mechanical power generation and irreversibilities created, as fraction of the incoming brine exergy for the optimal single, dual and triple-pressure cycle with isobutane.

3.4.4 Constraint on brine-outlet temperature

Figure 3.12 shows the exergetic plant and energetic cycle efficiencies in the case when the minimum brine-outlet temperature is limited to 75°C. Again the 20 fluids with the highest mechanical power output in a single-pressure-level cycle are given. In this case, the cycles with recuperation or turbine bleeding can have higher power outputs than the simple ones. This follows from equation (3.12). The brine cooling is limited to a temperature which is higher than the brine-cooling temperature in the case without constraint. So, in every cycle the brine will be cooled to 75°C and the plant effectiveness is fixed. Recuperation and turbine bleeding can improve the cycle efficiency; so in the constrained case, they can improve the plant efficiency. This also explains the strong correlation between the cycle and plant efficiency in figure 3.12. The often used R245fa, which can be seen as a reference case, performs best in a subcritical, recuperated

cycle, with an exergetic plant efficiency of 37.4% and an energetic cycle efficiency of 12.6% (not in the figure).

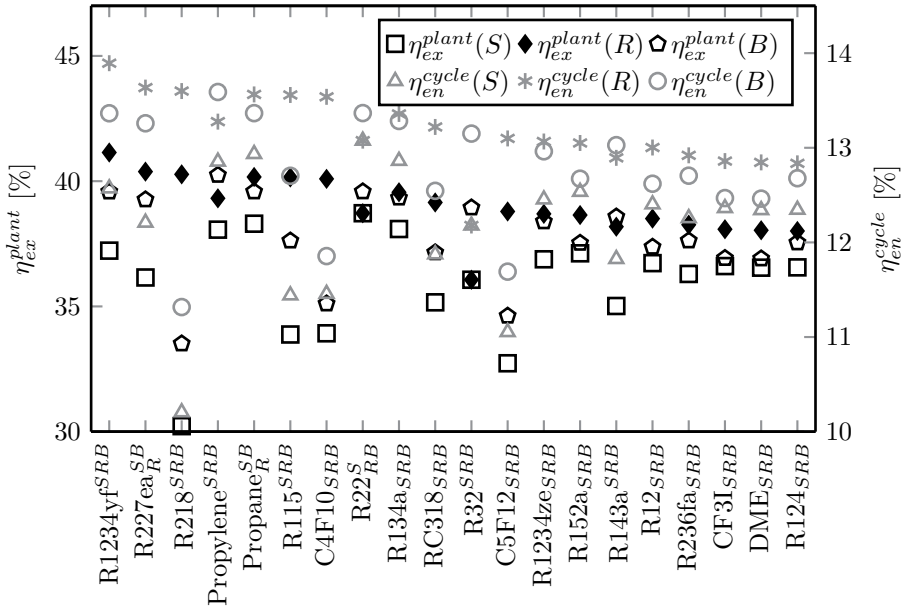

Figure 3.12: Exergetic plant efficiency and energetic cycle efficiency of the 20 fluids with the highest mechanical power output in a single-pressure-level cycle with a constrained brine-outlet temperature of 75°C. *S* stands for the simple cycle, *R* for the cycle with recuperation and *B* for the cycle with turbine bleeding. Subcritical cycles are denoted with a *sub*script, transcritical ones with a *super*script.

As seen in figure 3.12, recuperation is always useful, except for R22 and R32. These are very wet fluids, so they would need very high superheating to be able to recuperate. The gain in mechanical power output because of the recuperation is apparently lower than the loss in mechanical power output due to the extra superheating.

The transcritical cycles are not as superior as in the unconstrained case. For recuperation or turbine bleeding, superheating before the turbine is often needed. The maximum temperature of the working fluid is limited by the temperature of the brine. So, when superheating is used, the maximum pressure has to decrease. Therefore, only for fluids with a low critical pressure, transcritical cycles with recuperation or turbine bleeding are the optimum. Fluids with very low critical temperatures like R41, N_2O and CO_2, which perform well in the unconstrained case with one pressure level, are not the best choice in

the constrained case. Their critical temperature is very low (30-45°C) and the maximum pressure in the cycle is much above the critical pressure to decrease the amount of irreversibility created in the heat exchanger. Due to this high pressure, the temperature rise in the pump is high and recuperation becomes hard. Turbine bleeding is also not succesful enough. The bleeding pressure is limited from above by the critical pressure. For the fluids mentioned above, the critical pressure is low and the temperature of state 3 will be low too. This leads to higher irreversibilities in the heat exchange and a low plant efficiency. It can be concluded that the optimal fluids in the constrained case have higher critical temperatures than in the unconstrained one.

For the optimization of the Kalina cycle with a constrained brine-outlet temperature, a minimum temperature in the condenser of 21°C is used. Because of the high cycle efficiency of the Kalina cycle, it performs relatively[1] better than in the unconstrained case. An exergetic efficiency of almost 40% is obtained, which is almost the same as for the unconstrained case. The performance of the Kalina cycle is in this case similar to the best ORCs, mainly because of the temperature glide in the condenser which allows a lower minimum temperature in the condenser. When the minimum condenser temperature is limited to 25°C, an exergetic efficiency of 37% is obtained.

The effect of an extra pressure level is shown in figure 3.13. It shows that the 20 best fluids are optimal when using recuperation and the difference in performance between the fluids is very small. Turbine bleeding is almost always better than the simple cycle, except for the very dry fluid perfluorobutane (C4F10). By adding a pressure level, fluids with a high critical temperature become relatively better.

The transcritical cycles have not much benefit from the extra pressure level. Because of the small difference in performance between transcritical and subcritical cycles for one pressure level, the optimal cycles for 2 pressure levels are almost all subcritical. The addition of more pressure levels has the same effect as in the unconstrained case.

3.4.5 Influence of changing parameters

In this section, the influence of some parameters is investigated. These parameters are the brine-inlet temperature, the constraint on the brine-outlet temperature, the condenser temperature and the minimum temperature difference between the brine and the working fluid. These parameters are varied, while all other parameters have the value given in table 3.5. For every

[1] Relative to the different ORCs.

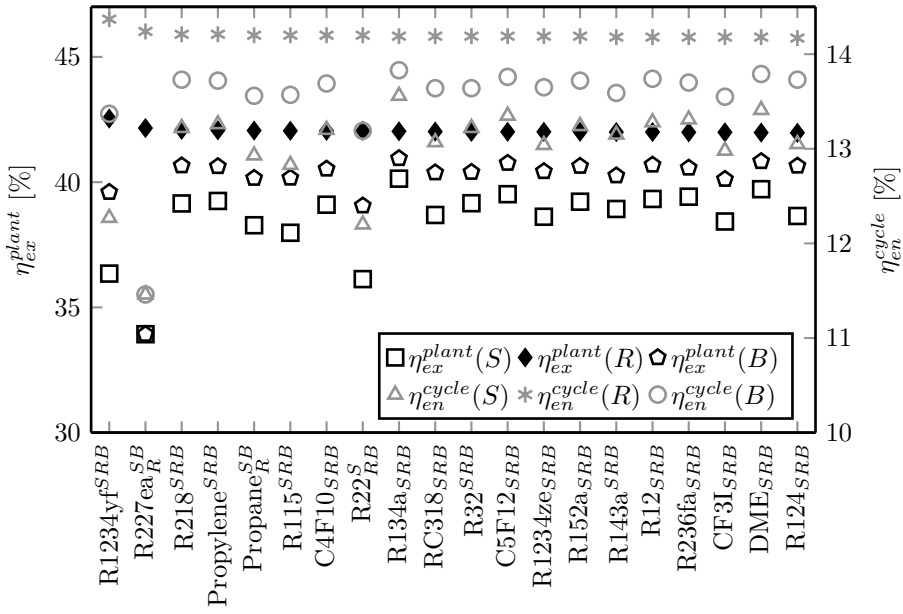

Figure 3.13: Exergetic plant efficiency and energetic cycle efficiency of the 20 fluids with the highest power output in a dual pressure level cycle with a constrained brine-outlet temperature of 75°C. *S* stands for the simple cycle, *R* for the cycle with recuperation and *B* for the cycle with turbine bleeding. Subcritical cycles are denoted with a *sub*script, transcritical ones with a *super*script. The low pressure sub-cycle is underlined, the high pressure sub-cycle is overlined.

influencing parameter, the effect on one or a few of the best performing ORCs is shown. Only single-pressure ORCs are shown, but they can be simple or recuperated. Comparison with a, for the new parameters optimized, Kalina cycle is added.

Brine-inlet temperature

The brine-inlet temperature is varied from 100 to 150°C. There is no constraint on the brine-outlet temperature and for every brine-inlet temperature, the optimal working fluid is selected. The exergetic efficiency with these fluids is given in figure 3.14. It is seen that the optimal fluid depends strongly on the brine-inlet temperature and fluids with a higher critical temperature perform relatively better when the brine-inlet temperature is increased. For the fluids R227ea and RC318, the exergetic plant efficiency increases almost linear for low

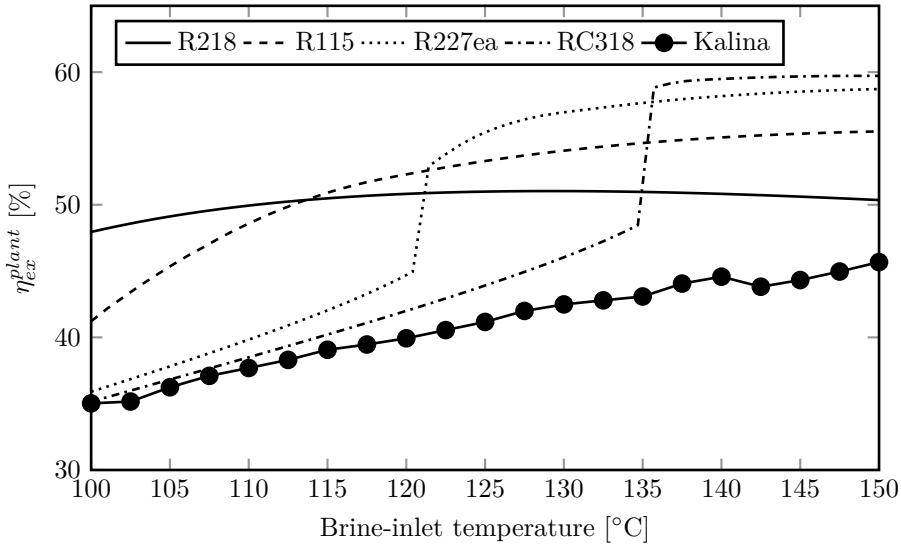

Figure 3.14: Exergetic efficiency of the temperature-dependent optimal fluids without constraint on the brine-outlet temperature. The ORCs are all single-pressure recuperated ones. The Kalina cycle is added as a comparison.

brine-inlet temperatures (subcritical cycles). The transition of a subcritical to a transcritical cycle is discontinuous, followed by a weak rise in the efficiency for higher temperatures. For even higher temperatures the exergetic plant efficiency is almost constant and starts to decrease. The specific power output on the contrary keeps increasing (not in figure). The plant efficiency decreases, but the increase of the incoming exergy of the brine is higher (see equation (3.6)). The investigated Kalina cycle is added as a comparison and is clearly outperformed by the ORCs. The figure also shows that the maximum exergetic efficiency depends on the brine-inlet temperature. This is because of the fixed temperature differences in the heat exchangers, which are relatively more important for low brine-inlet temperatures.

In a second case, the minimum brine-outlet temperature is limited to 75°C. These results are given in figure 3.15. The exergetic efficiency rises with the brine-inlet temperature, because the available brine temperature drop $T_{in} - T_{out}$ rises linearly for a fixed T_{out}. For the constrained case, there is no clear transition from a subcritical to a transcritical cycle. Again the investigated Kalina cycle is added as a comparison. For higher brine-inlet temperatures, the Kalina cycle performs almost as good as the best ORCs.

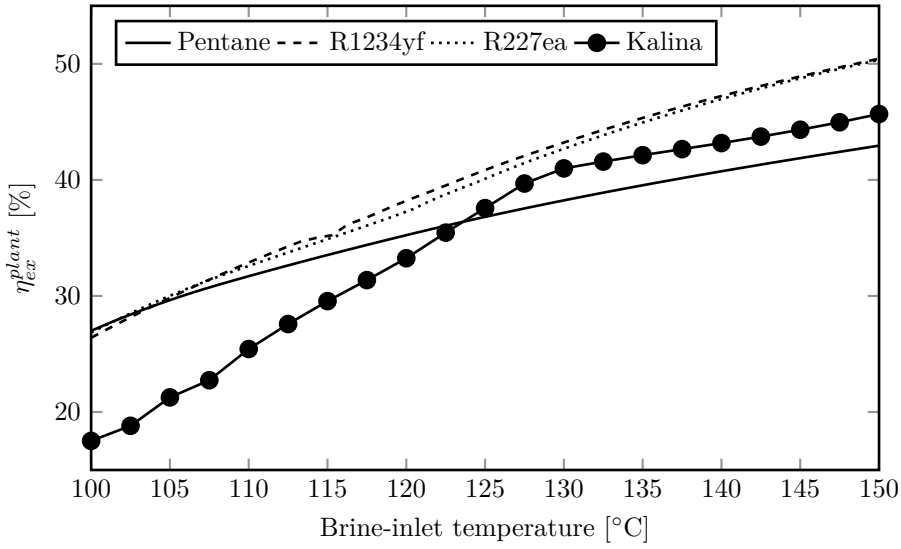

Figure 3.15: Exergetic efficiency of the brine-inlet-temperature-dependent optimal fluids (all single-pressure recuperative), for a brine-outlet temperature limit of 75°C. The Kalina cycle is added as a comparison.

Constraint on brine-outlet temperature

The constraint on the brine-outlet temperature is varied between 25 and 100°C. Both the temperature at which scaling occurs and the temperature of a possible heat demand depend strongly on the location (brine composition, old or new houses, etcetera). Therefore, a wide range in brine-outlet temperatures is chosen and the influence is investigated. Figure 3.16 shows the exergetic efficiency for 4 single-pressure recuperated ORCs and the Kalina cycle considered. In the unconstrained case, the brine-outlet temperature is about 50-70°C, depending on the fluid. So, the exergetic plant efficiency is only influenced by the constraint when the constraint temperature is above the unconstrained brine-outlet temperature.

The fluids shown are the best ones for a certain range in brine-outlet-temperature constraint and a comparison with the Kalina cycle is made. For relatively low brine-outlet-temperature constraints, the best fluids for the unconstrained case (low critical temperature) perform the best. But when the constrained brine-outlet temperatures become high, fluids which perform badly in the unconstrained case (high critical temperature) become the better ones. Up to an outlet temperature of 60°C, the efficiency is decreased by only 10%, but

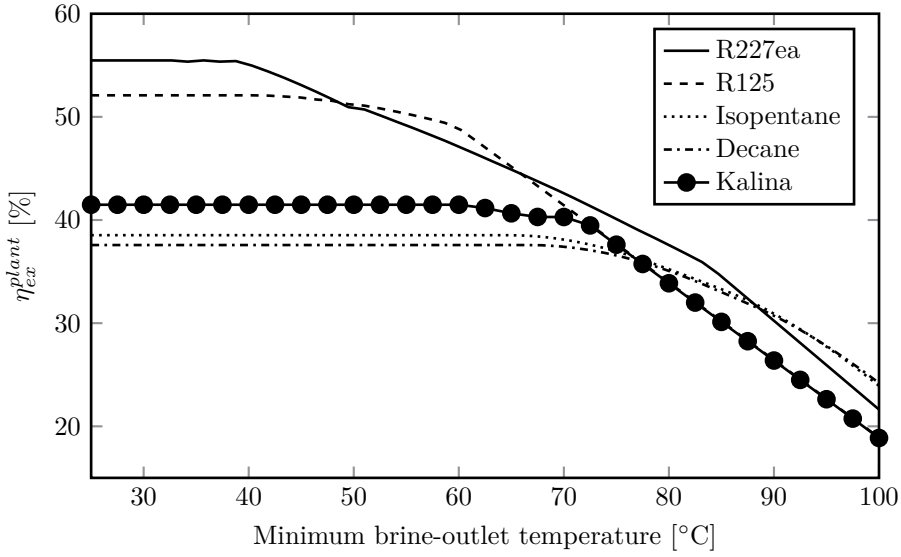

Figure 3.16: Exergetic efficiency of R227ea, R125, isopentane, decane and Kalina as a function of the limit on the brine-outlet temperature. The brine-inlet temperature is fixed at 125°C. All ORCs are single-pressure recuperated ones.

for higher temperatures the efficiency decreases strongly, because the available temperature drop becomes small. For constrained brine-outlet temperatures around 70°C, the Kalina cycle performs equally well as the best ORCs, but for lower or higher temperatures ORCs are the better choice.

Figure 3.16 shows that the exergetic plant efficiency is constant for low values of the minimum brine-outlet temperature. This implies that an optimal value for the brine-outlet temperature exist, which is seen from figure 3.17. The specific work output is shown as a function of the real brine-outlet temperature, which results in a "nose" diagram. For every fluid, a brine-outlet temperature exists that results in the maximum reachable output of the cycle. Brine-outlet temperatures below this optimal value are never useful, temperatures above the optimal value can be necessary to avoid scaling or for heating purposes.

Condenser temperature

For the ORCs, the condenser temperature is varied from 20 to 35°C. Figure 3.18 shows the exergetic plant and energetic cycle efficiency for a simple cycle with R227ea in comparison with the standard case ($T_{cond} = 25$°C). Also the outlet

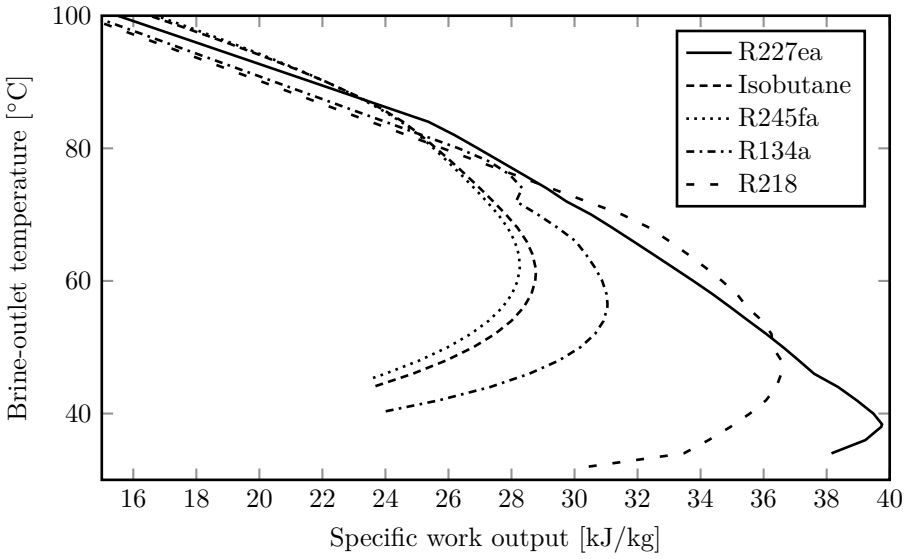

Figure 3.17: Nose diagram, showing the specific work output of the brine as a function of the real brine-outlet temperature. All ORCs are simple, single-pressure ones and the input parameters are taken from table 3.5.

temperature of the brine is shown. The energetic cycle efficiency decreases with increasing condenser temperature, because the cycle low-temperature-heat reservoir increases in temperature (T_{cond}). The brine-outlet temperature increases almost linearly with the condenser temperature; for R227ea the temperature difference between the condenser temperature and the brine-outlet temperature is about 15°C.

The exergetic plant efficiency decreases strongly with increasing condenser temperature, because the cycle efficiency decreases and the brine-outlet temperature increases. This strong, linear decrease has earlier been described [133]. The figure shows that increasing the condenser temperature with 10°C decreases the plant efficiency with about 20%.

Minimum temperature difference in HX

The minimum temperature difference in the heat exchanger between brine and working fluid HX is varied from 1 to 20°C for the unconstrained case. The exergetic plant efficiency, energetic cycle efficiency and brine-outlet temperature

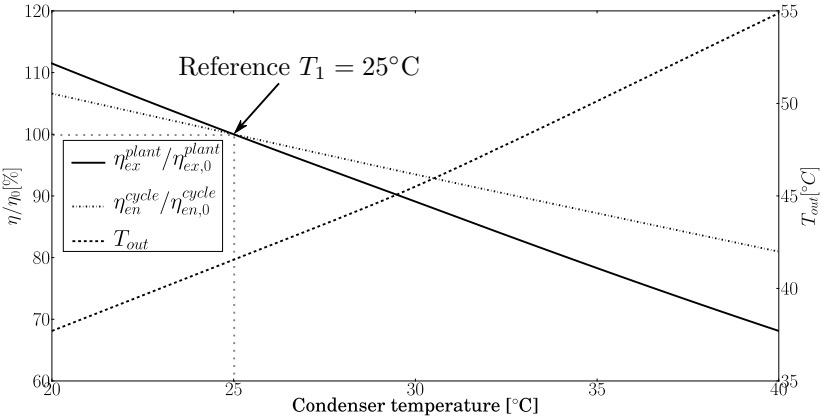

Figure 3.18: Exergetic plant efficiency η_{ex}^{plant}, energetic cycle efficiency η_{en}^{cycle} and brine-outlet temperature as a function of the condenser temperature for a simple cycle with R227ea. $\eta_{ex,0}^{plant}$ and $\eta_{en,0}^{cycle}$ are the exergetic plant and energetic cycle efficiency when the condenser temperature is 25°C, respectively.

for cycles with R227ea are shown in figure 3.19. In the reference state for the efficiencies, the temperature difference is 5°C.

For low temperature differences, the cycle is of the transcritical type. The cycle efficiency is constant, because the cycle itself (pressure, maximum temperature) does not change. So, the variation in plant efficiency is completely determined by the variation in brine-outlet temperature for this transcritical cycle.

At a temperature difference of about 8.5°C there is a sudden drop in the cycle efficiency and an increase in the outlet temperature due to the transition from a transcritical to a subcritical cycle for this fluid. For the subcritical cycle, the cycle efficiency does depend on the temperature difference, because the pinch point is at the beginning of the evaporator. When the temperature difference increases, the maximum pressure of the cycle has to decrease to allow a reasonable plant effectiveness.

3.5 Conclusions

In this chapter, many different types of binary power cycles, which have already been described in the literature, are modeled. The comparison of all these types of cycles is the main contribution of this chapter to the existing literature and the developed models are the base for the following chapters.

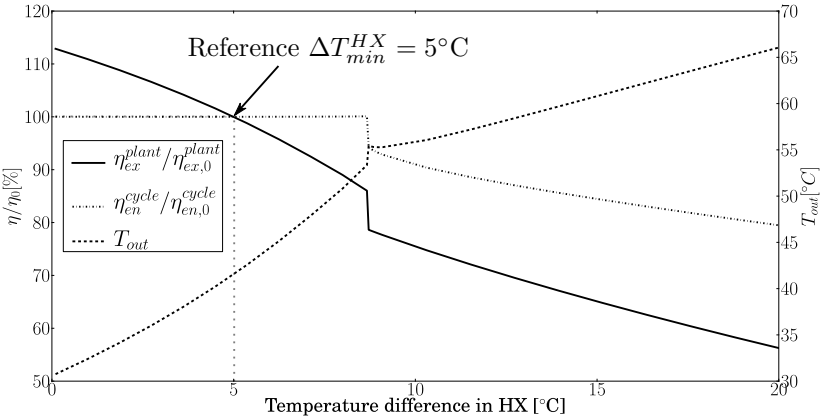

Figure 3.19: Exergetic plant efficiency, energetic cycle efficiency and brine-outlet temperature for cycles with R227ea as a function of the temperature difference in the heat exchanger HX.

For a geothermal power plant, it is important to maximize the plant efficiency, which is the product of the cycle efficiency and the plant effectiveness. So, the brine should be cooled down as much as possible and the heat added to the cycle should be converted to mechanical power as efficient as possible. The exergetic plant efficiency η_{ex}^{plant} describes how well a certain cycle approaches the ideal one.

Transcritical and multi-pressure subcritical ORCs are in most cases the best performing cycles and can achieve exergetic plant efficiencies of more than 50%. They outperform the investigated Kalina cycle for low minimum brine-outlet temperatures. For brine-outlet temperatures around 70°C, the best ORCs and the Kalina perform similarly.

When there is no constraint on the brine-outlet temperature, recuperation or turbine bleeding are not useful. Both techniques improve the cycle efficiency, but the plant effectiveness decreases and the combination of these two effects has zero influence on the plant efficiency. A constraint on the brine-outlet temperature causes a strong decrease in the power plant output, but in this case the decrease can partly be compensated by the use of recuperation or turbine bleeding. The Kalina cycle performs relatively better when the brine-outlet temperature is limited.

The choice of the optimal working fluid depends strongly on the conditions. In the single-pressure unconstrained case, fluids with a low critical temperature perform the best and a transcritical cycle is optimal. When an extra pressure

level is allowed or a constraint is added to the brine-outlet temperature, fluids with higher critical temperatures become relatively better and (multi-pressure) subcritical cycles are equally good or better than transcritical cycles.

The maximum theoretical temperature drop of the brine is low, because of the low brine-inlet temperature. A small increase in the condenser temperature or the pinch-point-temperature difference has a relatively strong influence on the available temperature drop of the brine and therefore also on the plant efficiency. So, for low-temperature-heat sources, it is very important to have a low condenser temperature and low pinch-point-temperature differences.

Due to the large impact of the pinch-point-temperature difference and the condenser temperature on the efficiency of the binary plant, it is hard to make an assumption about their optimal value, definitely when taking economics into account. To avoid making these assumptions, heat exchangers and cooling systems are modeled in the following chapters, so that the pinch-point-temperature difference and the condenser temperature become optimization variables instead of parameters.

Chapter 4

Optimal configuration of shell-and-tube & plate heat exchangers in ORCs

The content of this chapter was previously published as:
D. Walraven, B. Laenen, and W. D'haeseleer. "Optimum configuration of shell-and-tube heat exchangers for the use in low-temperature organic Rankine cycles". In: *Energy Conversion and Management* 83.C (2014), pp. 177–187
and
D. Walraven, B. Laenen, and W. D'haeseleer. "Comparison of shell-and-tube with plate heat exchangers for the use in low-temperature organic Rankine cycles". In: *Energy Conversion and Management* 87.C (2014), pp. 227–237

In the previous chapter, it is shown that the pinch-point-temperature difference in the heat exchangers has a strong influence on the performance of binary cycles powered by low-temperature heat sources. Instead of making assumptions about the value of these temperature differences and about the pressure drop in the heat exchangers, detailed models of both shell-and-tube and plate heat exchangers are used in this chapter. The goal is to optimize the configuration of the heat exchangers together with the configuration of the binary cycles. In this way, a first step towards a system optimization is taken. The performance

of ORCs with plate heat exchangers is compared to ORCs[1] with shell-and-tube heat exchangers in the last part of this chapter.

4.1 Models

The focus of this section lies on the description of the heat exchanger models, but first some changes in the models of the binary cycles, developed in the previous chapter, are mentioned.

4.1.1 Organic Rankine cycles

The Kalina cycle is omitted in the remainder of this work, because of the unavailability of transport properties of mixtures in RefProp. The number of different configurations of ORCs is reduced in comparison to the previous chapter. Only simple and recuperated ORCs with one or two pressure levels are used. More than 2 pressure levels would increase the calculation time, while it is shown in figure 3.10 that the effect of more pressure levels is limited. Cycles with turbine bleeding are omitted because they are only better than simple and recuperated ORCs for very wet fluids like R22 and R32, but RefProp does not contain correlations for the transport properties of these fluids.

Figure 4.1 shows the scheme of a single-pressure recuperated and a double-pressure simple ORC. In these figures, all the possible heat exchangers are explicitly drawn to draw attention to them. The different heat exchangers are the recuperator (2→3 and 7→8), the economizer (3→4), the evaporator (4→5), the superheater (5→6), the desuperheater (8→9) and the condenser (9→1). Not all of these heat exchangers are always necessary.

4.1.2 Shell-and-tube heat exchanger

Geometry

Shell-and-tube heat exchangers can be constructed with many different configurations. In this work, it is chosen to only investigate the TEMA E type, which is the only possible type for the ORC preheaters. This is the most basic type, with a single shell pass and with the inlet and the outlet at the

[1] The Kalina cycle is omitted from now on, because transport properties of mixtures are not available in RefProp (see section 4.2.2).

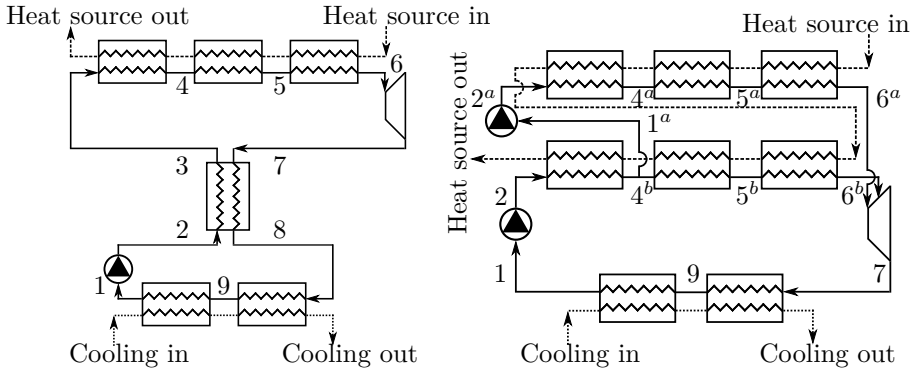

(a) Single-pressure recuperated ORC **(b)** Double-pressure simple ORC

Figure 4.1: Scheme of a single-pressure recuperated (a) and double-pressure simple (b) ORC.

opposite ends of the shell. The working fluid always flows on the shell side[2], so models for the pressure drop and heat-transfer coefficient in single-phase flow, evaporation and condensation in a TEMA E shell are needed. The tube-side fluid (the heat source and heat sink) will always be single phase.

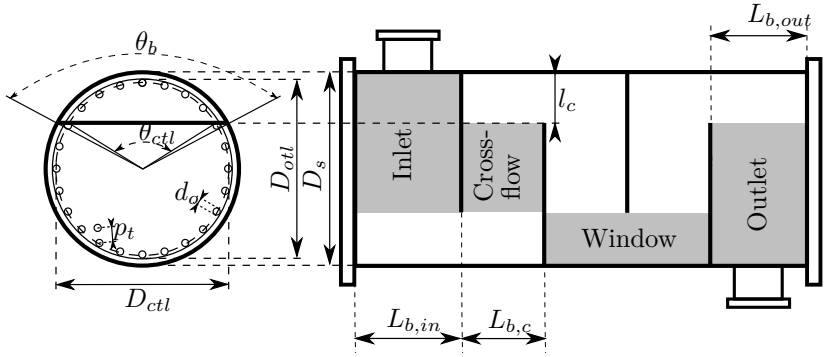

Figure 4.2: Shell-and-tube geometrical characteristics. Figure based on Shah and Sekulić [104].

Figure 4.2 shows the basic geometrical characteristics of a shell-and-tube heat exchanger. These are the shell outside diameter D_s, the outside diameter of a

[2]The dirty fluid (brine or cooling water) flows through the tubes because it is much easier to clean the inside of the tubes than the outside of the tubes, the baffles and the inside of the shell.

tube d_o, the pitch between the tubes p_t, the baffle cut length l_c and the baffle spacing at the inlet $L_{b,in}$, outlet $L_{b,out}$ and the center $L_{b,c}$. The expressions to calculate other geometrical characteristics are given in appendix A.1.1, which can also be found in the literature [50, 104]. The inlet, the outlet, a cross-flow and a window section are also indicated on figure 4.2.

Bell-Delaware

The Bell-Delaware method [50, 104], which is based on the reasoning of Tinker [112], is used to calculate the pressure drop and heat-transfer coefficient on the shell side. Tinker [112] divided the flow in the shell in a number of streams, as shown in figure 4.3:

- Stream B: ideal cross-flow stream
- Stream A: tube-to-baffle hole leakage stream
- Stream C: bundle-to-shell bypass stream
- Stream E: shell-to-baffle leakage stream
- Stream F: tube-pass bypass stream

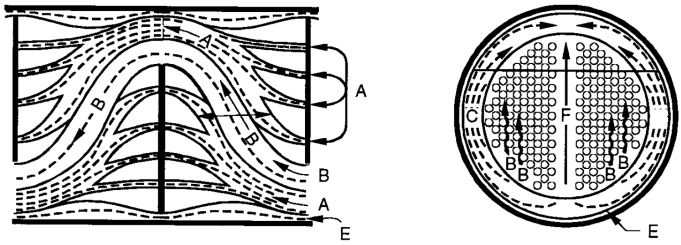

Figure 4.3: Shell-side flow distribution and different streams. Figure from Shah and Sekulić [104].

The shell-side heat-transfer coefficient is given as:

$$h_s = h_{id} J_c J_l J_b J_s J_r, \tag{4.1}$$

with h_{id} the ideal heat-transfer coefficient for cross flow over a tube bundle and J_x correction factors for non-idealities:

- J_c: correction factor for the baffle configuration, given by $J_c = 0.55 + 0.72F_c$. F_c is the fraction of tubes in the cross-flow section and is given in appendix A.

- J_l: correction factor for baffle leakage, given by $J_l = 0.44(1 - r_s) + [1 - 0.44(1 - r_s)]e^{-2.2r_{lm}}$ with $r_s = \frac{A_{o,sb}}{A_{o,sb}+A_{o,tb}}$ and $r_{lm} = \frac{A_{o,sb}+A_{o,tb}}{A_{o,cr}}$. $A_{o,sb}$, $A_{o,tb}$ and $A_{o,cr}$ the shell-to-baffle leakage area, the total tube-to-baffle leakage area and the cross-flow area at the shell center line (see appendix A).
- J_b: correction factor for bundle and pass partition bypass. In this work it is assumed that enough sealing strips are available, so that $J_b = 1$.
- J_s: correction factor for larger baffle spacing at the inlet and outlet. In this work it is assumed that $L_{b,in} = L_{b,out} = L_{b,c}$, so that $J_s = 1$.
- J_r: correction factor for an adverse temperature gradient in laminar flow. This effect is neglected in this work because it normally does not occur in optimized heat exchangers and to avoid numerical issues.

The shell-side frictional pressure drop is given as:

$$[\Delta p_s]_{fr} = [\Delta p_{cr}]_{fr} + [\Delta p_w]_{fr} + [\Delta p_{in-out}]_{fr}, \tag{4.2}$$

$$= \{(N_b - 1)[\Delta p_{b,id}]_{fr}\zeta_b + N_b[\Delta p_{w,id}]_{fr}\}\,\zeta_l + ...$$

$$...2[\Delta p_{b,id}]_{fr}\left(1 + \frac{N_{r,cw}}{N_{r,cc}}\right)\zeta_b\zeta_s, \tag{4.3}$$

where $[\Delta p_{cr}]_{fr}$, $[\Delta p_w]_{fr}$ and $[\Delta p_{in-out}]_{fr}$ are the frictional pressure drops in the cross-flow, window and inlet-outlet sections, respectively. $[\Delta p_{b,id}]_{fr}$ and $[\Delta p_{w,id}]_{fr}$ are the ideal frictional pressure drops in cross flow and window flow, respectively. N_b is the number of baffles, $N_{r,cw}$ and $N_{r,cc}$ the effective number of rows crossed in one window flow and one cross flow, respectively. ζ_x is a correction factor for non-idealities:

- ζ_l: correction factor for baffle leakage, given by $\zeta_l = \exp\left[-1.33(1 + r_s)r_{lm}^p\right]$ with $p = [-0.15(1 + r_s) + 0.8]$
- ζ_b: correction factor for bypass flow. In this work it is assumed that enough sealing strips are used, so that $\zeta_b = 1$.
- ζ_s: correction factor for larger baffle spacing at the inlet and outlet. In this work, all baffle spacings are assumed to be equal, so that $\zeta_s = 1$.

Ideal heat transfer and pressure drop

To apply the Bell-Delaware method, the ideal heat-transfer coefficient and the ideal pressure drops in the cross-flow and window-flow section are needed.

Correlations for these parameters are given in appendix A.1 for single-phase flow, condensation and evaporation in the shell, together with correlations for single-phase flow on the tube side, which can also be found in the literature [50, 104].

Implementation of the models

To account for non-uniform fluid properties, each heat exchanger is divided into five parts with an equal heat load[3] as a starting point. This number is chosen because it leads to a reasonable accuracy and calculation time. For each heat exchanger, the configuration (D_s, d_o, p_t, l_c and $L_{b,c}$), the inlet states at one side of the heat exchanger and a necessary outlet condition (for example the working fluid has to be saturated vapor at the end of the evaporator) are needed. With these data, the total heat that has to be transferred in the case of no pressure drop can be calculated. In each of the five parts one fifth of the total heat will be exchanged. With the equations above, the heat-transfer coefficient and the pressure drop in the first part can be calculated. In this way, the state after the first part, the necessary heat-transfer surface and the fictive tube length of the first part L_1 can be calculated. This procedure is repeated for the other parts, except in the last part for which the heat to be transferred is corrected for the pressure drop in the previous parts and the expected pressure drop in the last part.

The problem which occurs in this procedure is that the frictional pressure drop in the cross-flow section is different from the one in the window section, while the heat-transfer coefficient is an average of both sections. Therefore it is chosen to average the frictional pressure drop in each section:

$$[\Delta p_s^{parts\ 1,5}]_{fr} = \left\{ \frac{L_i}{L_{b,c}} [\Delta p_{b,id}]_{fr} \zeta_b + \left(\frac{L_i}{L_{b,c}} - \frac{1}{5} \right) [\Delta p_{w,id}]_{fr} \right\} \zeta_l + ...$$

$$...[\Delta p_{b,id}]_{fr} \frac{N_{r,cw}}{N_{r,cc}} \zeta_b \zeta_s, \tag{4.4}$$

$$[\Delta p_s^{parts\ 2,3,4}]_{fr} = \left\{ \frac{L_i}{L_{b,c}} [\Delta p_{b,id}]_{fr} \zeta_b + \left(\frac{L_i}{L_{b,c}} - \frac{1}{5} \right) [\Delta p_{w,id}]_{fr} \right\} \zeta_l, \tag{4.5}$$

with L_i the fictive length of the ith part. Adding these pressure drops for the different parts, leads again to equation (4.3) when taking into account that $N_b = \sum_i L_i / L_{b,c} - 1$.

[3] These parts generally do not have the same physical size.

4.1.3 Plate heat exchanger

Plate heat exchangers can have many different types of corrugations [104], but in this work only plate heat exchangers with chevron, also known as herringbone, corrugations are used. This type of corrugation is commonly used and models which describe the pressure drop and heat transfer depending on the heat exchanger geometry are available [46, 47, 74]. The number of passes on both sides of the heat exchangers are assumed to be equal in this work.

Geometry

Figure 4.4 shows the geometrical parameters of a chevron plate. The corrugations are determined by the corrugation amplitude a, the corrugation width Λ and the angle of the corrugations β. The width of a plate W, the length of a plate between ports L_p and the length of a plate for heat transfer L_h are also indicated.

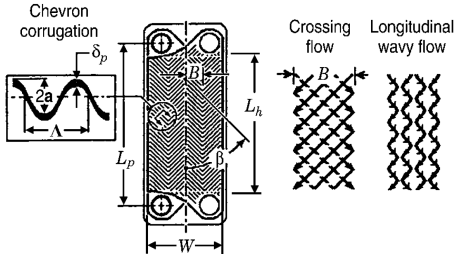

Figure 4.4: Geometrical parameters of a chevron plate. Figure from Shah and Sekulić [104].

The hydraulic diameter is defined as:

$$D_h = \frac{4a}{\Phi}, \tag{4.6}$$

where $\Phi = \frac{1}{6}\left(1 + \sqrt{1+X^2} + 4\sqrt{1+X^2/2}\right)$ is the area-enlargement factor and $X = \frac{2\pi a}{\Lambda}$ the dimensionless corrugation parameter.

Heat-transfer and pressure-drop correlations

The correlations of Martin [74] are used to predict the heat-transfer coefficient and the pressure drop in the single-phase heat exchangers. For the evaporator

and the condenser, the correlations of Han, Lee, and Kim [46] and Han, Lee, and Kim [47] are used, respectively. An overview of these correlations is given in appendix A.2.

Implementation of the models

The implementation is analogous to the implementation of the shell-and-tube-heat-exchanger models; each heat exchanger is divided into five parts with an equal heat load. For each heat exchanger, the configuration (a, Λ, β and W N_p), the inlet states at one side of the heat exchanger and a necessary outlet condition (for example the working fluid has to be saturated vapor at the end of the evaporator) are needed. The variables W and N_p (the number of channels) are combined to one variable, because only their product appears in the equations.

4.2 Optimization

The configuration of the cycle parameters and the geometry of each heat exchanger[4] are optimized together. In this way, a system optimization is performed, although the system model is still relatively simple. Instead of a system optimization, it would also be possible to perform an iteration between the optimization of the system level and the component level as performed by Franco and Villani [38]. First the system level is optimized to minimize the mass flow rate of brine needed for a specified turbine expansion power, while making a guess for the optimal value of the pressure drop, the condensation temperature and the pinch-point-temperature differences. Afterwards, the heat-exchanger surface of each exchanger is minimized separately, while respecting the load of each heat exchanger, and the size of the cooling system is minimized. This results in new values of the pressure drop and the auxiliary electricity consumption of the fans, so that an iteration between the system level and the component level is necessary. The results of this method are the power output, the heat-exchanger surface of each heat exchanger and the size of the cooling system for the given pinch-point-temperature differences. It is possible that a cycle with other values of the pinch-point-temperature differences generates more electricity for the same total heat-exchanger surface and size of the cooling system and the obtained result is therefore not necessarily a global optimum. So, it is necessary to vary the value of these pinch-point-temperature differences to obtain the optimal system, which results in large calculation times. Another

[4] Every heat exchanger in the schemes in figure 4.1 can have a different geometry

issue is that the decoupling of the system and the component level will not necessarily result in an optimum for the combination of the two levels. The minimization of the heat exchanger surface for example will result in large pressure drops, which will probably result in a decreasing mass flow rate of working fluid on the system level instead of a heat exchanger with a smaller pressure drop.

The advantage of the system optimization described in this chapter is that the optimal pinch-point-temperature differences are a result of the method, because all components are coupled directly and the optimization solver can choose how to allocate the total heat-exchanger surface.

The objective function is the same as in the previous chapter: maximizing the exergetic plant efficiency.

4.2.1 Decision variables and constraints

The decision variables which determine the cycle configuration are the same as in the previous chapter (table 3.1), but they are supplemented with the mass flow rate of working fluid $\dot{m}^i_{wf}$ for every pressure level i and with the effectiveness ε of the recuperator. The former parameter influences the pinch-point-temperature difference in the heat exchange between brine and working fluid and the latter parameter influences the pinch-point-temperature difference in the recuperator. The effectiveness is constrained from above to 90% to avoid numerical problems, however those high values of the effectiveness are rarely optimal for the recuperator. The upper bounds of turbine-inlet temperature and saturation temperatures are changed, because the pinch-point-temperature differences are not fixed. To avoid numerical problems, a minimum superheating of state 6 with 1°C is imposed[5]. The decision variables and constraints used for the cycle configuration are summarized in table 4.1.

From this table it is also seen that two extra non-linear constraint are added. The lower bound of the minimum pinch-point-temperature difference in all heat exchangers is set to 1°C. This temperature difference should of course always be positive; otherwise unphysical situations are obtained. Because the constraint is non-linear, it is not always fulfilled[6], which can cause problems in the optimizer. To avoid negative pinch-point-temperature differences in any iteration step, the lower bound of this difference is set a bit above 0°C; a value of 1°C is chosen.

[5] This can have a small, negative influence on the performance of cycles with dry fluids.

[6] Non-linear constraints can only be checked after the decision variables of an iteration step have been chosen.

Variable	Lower bound	Upper bound	Configuration
T_6^i	T_1	T_{in}	all
$T_{sat}(p_6^i)$	T_1	T_{in}	all
$\dot{m}_{wf}^i/\dot{m}_{brine}$	0	/	all
ε	0	0.9	all
Constraint	**Lower bound**	**Upper bound**	**Configuration**
$T_6^i - T_{sat}(p_6^i)$	0	/	all
$T_{sat}(p_6^i) - T_{sat}(p_{6^{i+1}})$	0	/	multi-pressure
T_{out}	T_{out}^{min}	/	if constrained
ΔT_{pp}	1°C	/	all
A^{tot}	0	A_{max}^{tot}	

Table 4.1: Decision variables and constraints used for the cycle configuration in the system optimization.

If no constraint on the heat-exchanger surface of each heat exchanger is imposed, the pinch-point-temperature differences would become very small and the total heat-exchanger surface would become huge. Therefore, a non-linear constraint[7] on the total heat-exchanger surface of all heat exchangers together A^{tot} is imposed: $A^{tot} \leq A_{max}^{tot}$. In this way, the optimizer can choose itself how to distribute the available surface optimally amongst the different heat exchangers.

Shell-and-tube heat exchanger

The decision variables and constraints imposed for each shell-and-tube heat exchanger are given in table 4.2. In fact, another non-linear constraint should be used for the maximum length of the heat exchanger when taking into account transportation issues (40' container), but this is ignored in this work.

Plate heat exchanger

The decision variables and constraints used for the plate-type heat exchangers are given in table 4.3.

[7] The total heat-exchanger surface is a result of the optimization program and the constraint is therefore non linear.

Variable	Lower bound	Upper bound
Shell diameter D_s	0.3 m	2 m
Tube outside diameter d_o	5 mm	50 mm
Relative tube pitch p_t/d_o	1.15	2.5
Relative baffle cut l_c/D_s	0.25	0.45
Baffle spacing $L_{b,c}$	0.3 m	5 m
Constraint	**Lower bound**	**Upper bound**
Ratio of tube diameter to shell diameter d_o/D_s	/	0.1

Table 4.2: Decision variables and constraints used for shell-and-tube heat exchangers and their lower and upper bounds.

Variable	Lower bound	Upper bound
Corrugation amplitude a	1 mm	200 mm
Corrugation width Λ	1 mm	200 mm
Corrugation angle β	0°	90°
Product of plate width and number of channels WN_p	10 mm	10 m
Constraint	**Lower bound**	**Upper bound**
Ratio of corrugation width to corrugation amplitude Λ/a	2.5	3.5

Table 4.3: Decision variables and constraints used for plate-type heat exchangers and their lower and upper bounds.

4.2.2 Optimization approach

A gradient-based optimization method is used to find the optimal system configuration. However, calculation of the gradient of the objective function and non-linear constraints with finite-differences gives two problems:

- Slow calculation time: the calculation time is directly proportional to the number of decision variables
- Low accuracy: an inaccurate[8] gradient results in a higher number of iterations

To avoid these issues, the gradients are calculated with automatic differentiation in reverse/adjoint mode. Following this method, the calculation time is independent of the number of optimization variables and the method is accurate up to machine precision.

The ORC and heat-exchanger models are self-written in Python and the CasADi software [5] is used for the optimization. CasADi is a symbolic framework for

[8] A comment on the inaccuracy of finite-differences is given in appendix D.2.1.

automatic differentiation and numeric optimization, which can calculate the gradient of the Python-code with automatic differentiation. Many optimizers can be connected to CasADi, but the one used in this work is WORHP [20], because this solver performs better for our problem than Ipopt [120] or the SQP-solver from CasADi [5].

CasADi accepts external functions[9] if both the function value and the gradient of the function are given externally. So, both the fluid properties, which are obtained from RefProp [66], and the gradient of the fluid properties are required by CasADi. This gradient is needed because CasADi has to be able to calculate the gradient of the objective function and the constraints. Therefore the RefProp Fortran code is adapted; the complex-step derivative method [75] is used to obtain the derivative of the fluid properties. This is in fact automatic differentiation in forward mode, which is fast enough because the gradient has only two components (pure fluid). The connection between Fortran and Python is made by F2PY [92]. More information about the calculation of the fluid-properties derivative and the connection to Python can be found in appendix D. A flow chart which shows the connection between the different software packages is shown in figure 4.5.

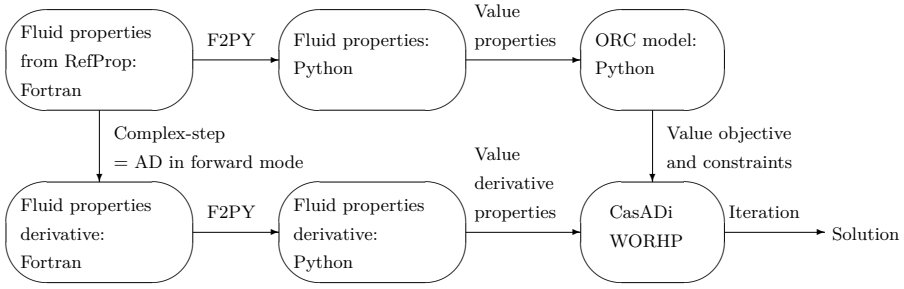

Figure 4.5: Flow chart showing the connection between the different software packages.

A remark has to be made about the use of CasADi. It is not the case that standard Python code can be used, but special CasADi-objects and -commands are needed so that the gradients can be calculated and the optimization can be performed.

The optimization is schematically shown in figure 4.6. Comparison with figure 3.5 shows that the heat-exchanger optimization variables are added, the fixed condenser temperature and pinch-point temperature differences are replaced by

[9] In this case, this are functions that are not written in Python.

the cooling-water-inlet temperature and mass flow rate, and the constraint on the maximum allowed total heat exchanger surface is added.

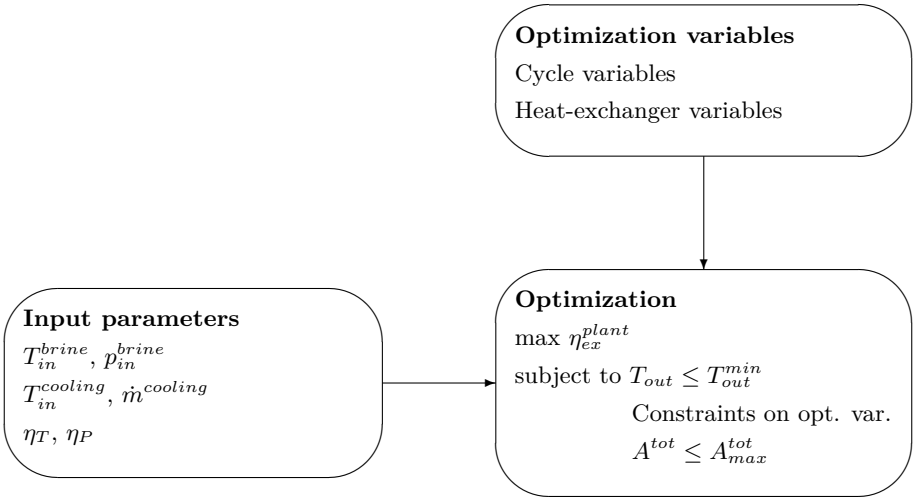

Figure 4.6: Schematic of the optimization used in this chapter.

4.3 Results and discussion

The tube layout of a shell-and-tube heat exchanger is not an optimization variable because this would result in a mixed-integer non-linear problem (MINLP), which is much harder to solve than a NLP. This is solved by performing an optimization for the different tube layouts for the reference case. The best performing layout is than used for the comparison with plate heat exchangers.

4.3.1 Parameters of the reference case

The brine has a mass flow rate of 100 kg/s and it is assumed that the brine has the same thermodynamic and transport properties as clean water. The other parameters of our defined reference case are given in table 4.4. The values of these parameters have of course a strong influence on the performance and cost of the power plant and their values are therefore varied at the end of this section.

The number of fluids used in this chapter is reduced in comparison with the number used in the previous chapter because transport properties are not

Parameter	Symbol	Value
Brine-inlet temperature	T_{in}^{brine}	125°C
Maximum allowed heat-exchanger surface	A_{max}^{tot}	4000 m^2
Cooling-fluid-inlet temperature	$T_{in}^{cooling}$	20°C
Cooling-fluid mass flow rate	$\dot{m}^{cooling}$	800 kg/s

Table 4.4: Parameters of the reference case.

available for all fluids in RefProp. Only eight different fluids are used in the remainder of this work.

4.3.2 Optimal tube-layout in shell-and-tube heat exchangers

ORCs with shell-and-tube heat exchangers with different tube layouts (30, 45, 60 or 90° - See appendix A.1.1 for the layout of the tubes) are optimized for use in the reference case, so that the optimal tube layout is found. Shell-and-tube heat exchangers with this optimal tube layout are compared with plate heat exchangers later in this chapter.

Unconstrained heat-source-outlet temperature

No constraint is imposed on the heat-source-outlet temperature. The optimizer can choose the optimal heat-source-outlet temperature to maximize the plant efficiency, while respecting the boundary conditions. Figure 4.7 shows the influence of the tube layout on the exergetic plant efficiency, the net mechanical power output and energetic cycle efficiency for single-pressure simple ORCs.

Five different cases are shown; the first four cases (30, 45, 60 or 90°) have the same tube configuration in all heat exchangers, while the last case uses the 30° configuration in the single-phase heat exchangers (economizer, superheater and desuperheater) and the 60° configuration in the two-phase heat exchangers (evaporator and condenser), which will be called the 30°&60°-tube configuration in the remainder of this chapter. The results show that the 30°&60°-tube configuration performs the best. 30°&60°-tube configuration can combine high heat-transfer coefficients with relatively low pressure drop in single-phase configurations and two-phase flow, respectively [50]. Figure 4.7a shows that the tube configuration has a very strong effect on the plant performance for transcritical cycles (for example R218, R227ea). The cycle with R218 as working fluid and the 30°&60°-tube configuration has an exergetic plant efficiency of 34.3%. When using the 60°-tube configuration in all heat exchangers, the plant

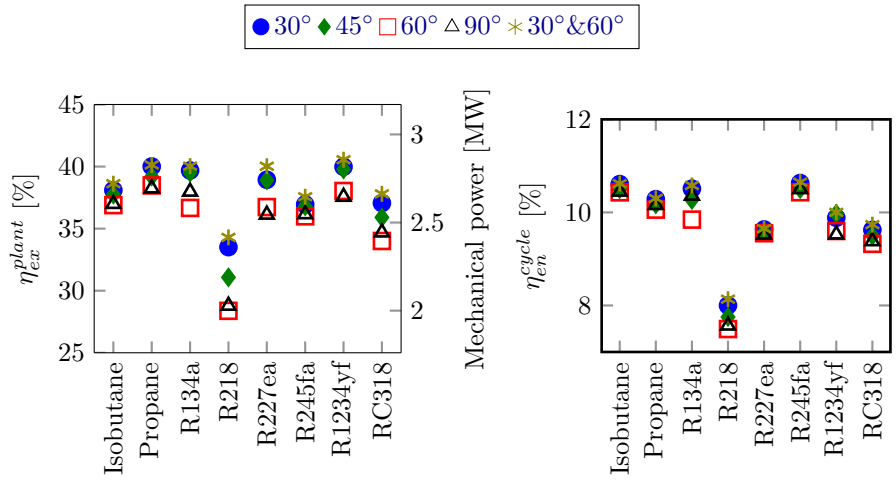

(a) Exergetic plant efficiency and net mechanical power

(b) Energetic cycle efficiency

Figure 4.7: Exergetic plant efficiency and net mechanical power output (a) and energetic cycle efficiency (b) for single-pressure simple ORCs with all shell-and-tube heat exchangers for different fluids and different tube configurations. (For the layout of the tubes, see appendix A.1.1.)

efficiency decreases to 28.4%. These results show that the configuration of heat exchangers can have a very strong influence on the performance of an ORC. The energetic cycle efficiency in figure 4.7b is also influenced by the tube configuration, but not as strong as the plant efficiency. This means that the heat-source-outlet temperature decreases too when selecting a "better" tube configuration.

Comparison of figures 3.6 and 4.7a shows that the exergetic plant efficiency is lower in the latter figure than in the former. This is explained by the difference in condenser temperature. In figure 3.6, the condenser temperature is 25°C, while in figure 4.7a, the cooling-fluid-inlet temperature is 20°C, which results in a condenser temperature of about 30°C.

Another difference between the two figures is the relative performance of the different fluids. In figure 3.6, the pinch-point-temperature difference was fixed at 5°C, while it is optimized in figure 4.7a. In the latter figure, the pinch-point-temperature difference for the transcritical cycles is higher than that of the subcritical cycles, because the average temperature difference is lower for transcritical cycles than for subcritical cycles for the same pinch-point-

temperature difference. This shows that conclusions about the best fluids and types of cycles, drawn from simple thermodynamic models like the ones in chapter 3, can be wrong when taking more details into account.

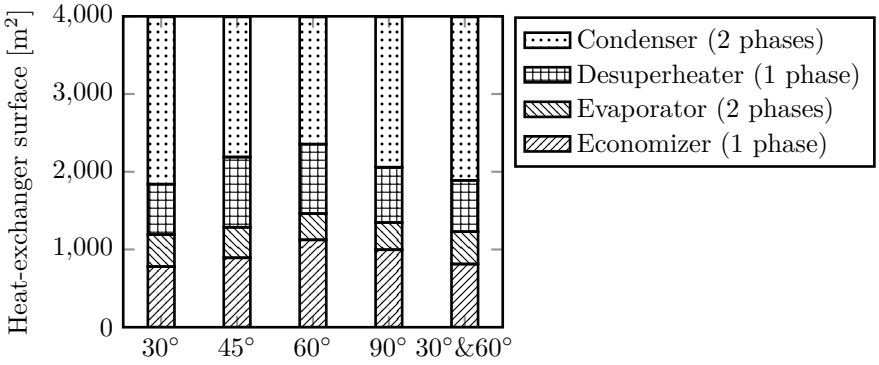

Figure 4.8: Distribution of the heat-exchanger surface for different tube configurations with isobutane as the working fluid. The surface of the superheater is very small in all cases and is not shown in the figure.

Figure 4.8 shows the distribution of the heat-exchanger surface amongst the different heat exchangers for the five investigated tube-configurations with isobutane as the working fluid. The 30°-configuration uses a relatively large part of the available surface in the two-phase heat exchangers, while the 60°-configuration on the other hand uses a relatively large part of the surface in the single-phase heat exchangers. The 30°&60°-tube configuration results in about the same distribution as in the 30°-case, but leads to smaller pinch-point-temperature differences (not shown).

The same is seen in figure 4.9. The 30°-tube configuration and the 60°-tube configuration have the highest average heat-transfer coefficient in the single-phase heat exchangers and the two-phase heat exchangers, respectively, for isobutane. Combining these two (mono-layout) tube configurations (30°&60°) for different heat exchangers results in relatively high heat-transfer coefficients in all heat exchangers.

For stand-alone shell-and-tube heat exchangers, it is common practice to select the 30°-tube configuration for the single-phase heat exchangers and to select the 60°-tube configuration for phase-change flow heat exchangers [50, 104]. The foregoing results show that the experience with the tube configuration of stand-alone exchangers is also valid for heat exchangers in an ORC.

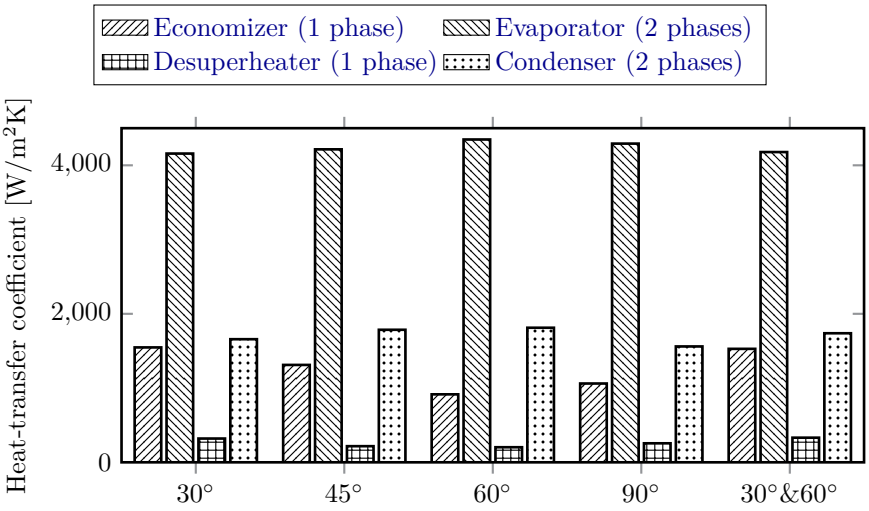

Figure 4.9: Average heat-transfer coefficient for different tube configurations with isobutane as the working fluid. The surface of the superheater is very small and the average heat-transfer coefficient is therefore not shown in the figure.

The 30°&60°-tube configuration performs the best for all fluids and will be used in the remainder of this work.

Figure 4.10 shows the exergetic plant, the net mechanical power output and energetic cycle efficiency for single- and double-pressure ORCs. Both use the 30°-tube configuration and the 60°-tube configuration for the single-phase and two-phase heat exchangers, respectively. The exergetic plant efficiency of subcritical cycles (isobutane, propane, R134a, R245fa and RC318) can increase strongly by adding a second pressure level. The extra pressure level has a limited effect for transcritical cycles. These transcritical cycles are outperformed by the dual-pressure subcritical ones, due to the higher pinch-point-temperature differences in the transcritical cycles than in the subcritical ones.

The energetic cycle efficiency (see figure 4.10b) does not increase or even slightly decreases by adding an extra pressure level. This means that the increase of the plant efficiency results from a decrease in the heat-source-outlet temperature, which is shown in figure 4.11. The outlet temperature can decrease almost 10°C for subcritical cycles, while the decrease is limited for transcritical cycles.

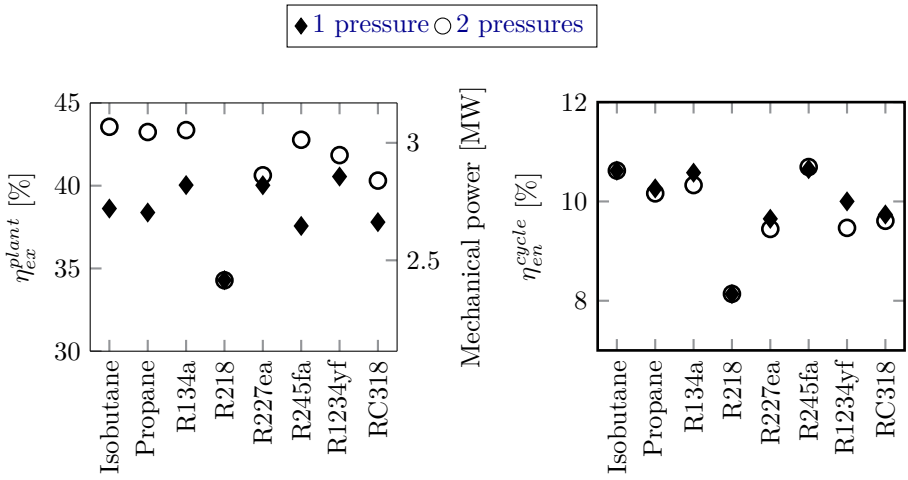

(a) Exergetic plant efficiency and net mechanical power output

(b) Energetic cycle efficiency

Figure 4.10: Exergetic plant efficiency and net mechanical power output (a) and energetic cycle efficiency (b) for single-pressure and double-pressure simple ORCs with all shell-and-tube heat exchangers for different fluids. Single-phase heat exchangers use the 30°-tube configuration and the two-phase heat exchangers use the 60°-tube configuration.

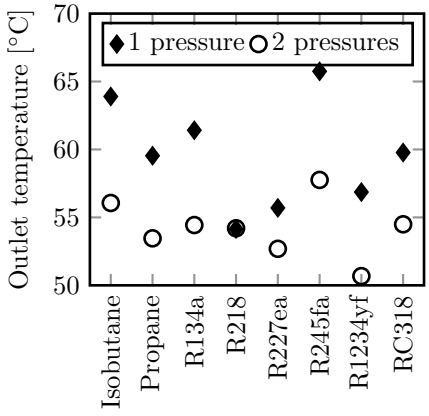

Figure 4.11: Heat-source-outlet temperature for single-pressure and double-pressure simple ORCs with all shell-and-tube heat exchangers for different fluids. The transcritical cycles are the ones with R218, R227ea and R1234yf.

Constrained heat-source-outlet temperature

It is possible to use the heat source for both electricity generation and useful heat delivery. When a series configuration is used, the temperature of the heat source after the ORC has to be high enough to deliver the heat. In this section the heat-source-outlet temperature is constrained and the influence on the performance of the power plant is investigated.

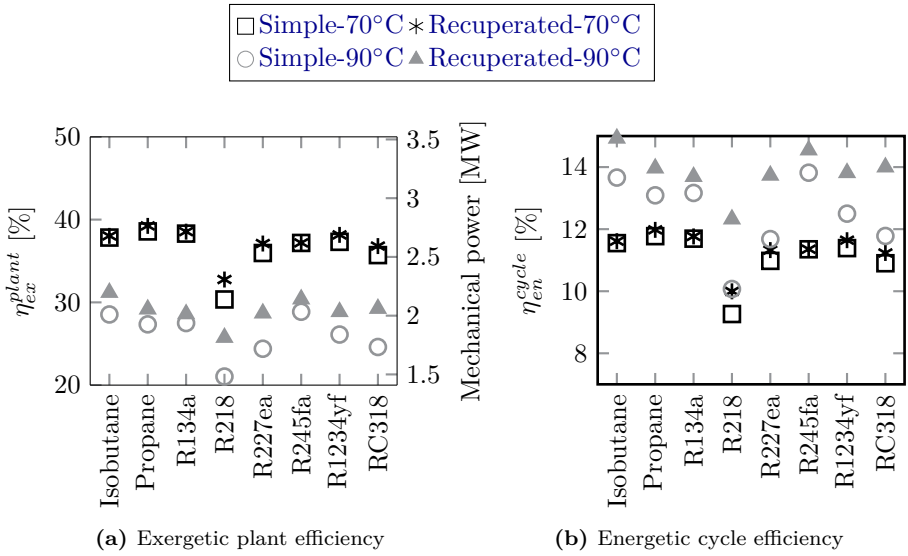

(a) Exergetic plant efficiency **(b)** Energetic cycle efficiency

Figure 4.12: Exergetic plant efficiency and net mechanical power output (a) and energetic cycle efficiency (b) for single-pressure simple and recuperated ORCs with all shell-and-tube heat exchangers for different fluids. The heat-source-outlet temperature is constained to 70 or 90°C.

Figure 4.12a shows the exergetic plant efficiency and the net mechanical power output for both simple and recuperated cycles when the minimum heat-source-outlet temperature is 70 or 90°C. The exergetic plant efficiency increases in most cases by adding a recuperator. The higher the required heat-source-outlet temperature, the higher the effect of the recuperator is. The exergetic plant efficiency is of course higher when the constraint on the heat-source-outlet temperature is lower.

Because of the internal heat recuperation in the recuperated cycle, less heat is added to the cycle and the cycle efficiency is higher than in the simple cycle. This is seen in figure 4.12b. When the heat-source-outlet temperature

is limited to 90°C, the cycle efficiency is (much) higher than in the case of a 70°C-limit for both the simple and recuperated cycle. When the heat-source-outlet temperature increases, the plant effectiveness decreases and the optimizer chooses to increase the cycle efficiency in order to limit the decrease of the plant efficiency.

4.3.3 Influence maximum allowed heat-exchanger surface

In this section the influence of the maximum allowed heat-exchanger surface on the performance of ORCs with all shell-and-tube or all plate heat exchangers is investigated. The other parameters are the ones given in table 4.4. The constraint on the maximum allowed heat-exchanger surface allows the optimizer to distribute the heat-exchanger surface where it is needed the most to obtain a high exergetic plant efficiency. The consequence is that pinch-point-temperature differences will be different for different fluids, for different heat-exchanger types (shell-and-tube or plate) and for different purposes (condenser, economizer et cetera).

Figure 4.13 shows the exergetic plant efficiency for simple ORCs with all plate heat exchangers or all shell-and-tube[10] heat exchangers for different working fluids as a function of the maximum allowed heat-exchanger surface. The efficiency increases with increasing A_{max}^{tot}, as expected.

This increase of the exergetic plant efficiency with increasing maximum allowed surface is explained by the increase of the energetic cycle efficiency (figure 4.14) and the decrease of the heat-source-outlet temperature (figure 4.15). So, more heat is added to the cycle and this heat is converted more efficiently to mechanical power when the total heat-exchanger surface increases.

For low values of A_{max}^{tot} ORCs with all plate heat exchangers generate more mechanical power than ORCs with all shell-and-tube heat exchangers. It is generally known that plate heat exchangers can achieve higher heat-transfer coefficients and therefore lower pinch-point-temperature differences for the same heat-exchanger surface as seen in figure 4.16. For high values of A_{max}^{tot}, ORCs with all shell-and-tube heat exchangers perform equally well or even better. The pinch-point-temperature differences in figure 4.16 become very small and the efficiency of the ORCs almost reaches the upper limit.

For the working fluids R245fa, isobutane and RC318 the exergetic plant efficiency of ORCs with all shell-and-tube heat exchangers is better than the one for ORCs with all plate heat exchangers for $A_{max}^{tot} > 2000, 3000$ and 6000 m^2, respectively. Comparison of figures 4.16a and 4.16b shows that the pinch-point-temperature

[10] These have the 30°&60°-configuration.

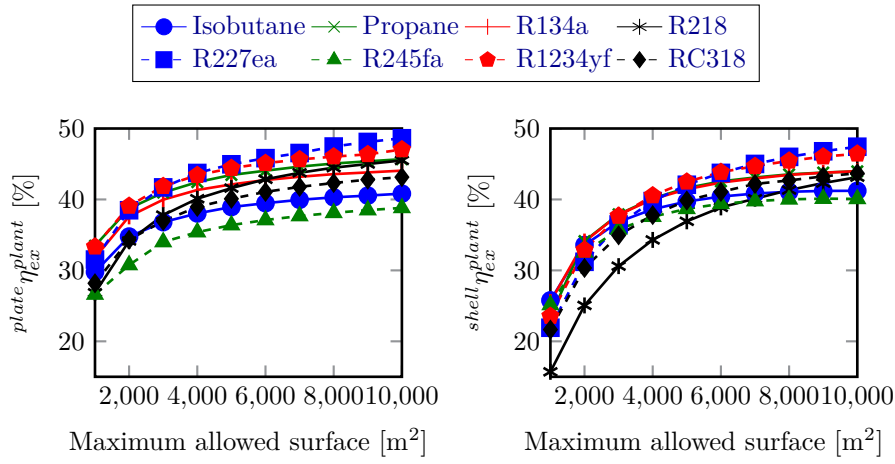

(a) Plate heat exchangers **(b)** Shell-and-tube heat exchangers

Figure 4.13: Exergetic plant efficiency for single-pressure simple ORCs with all plate heat exchangers (a) and all shell-and-tube heat exchangers (b) for different fluids.

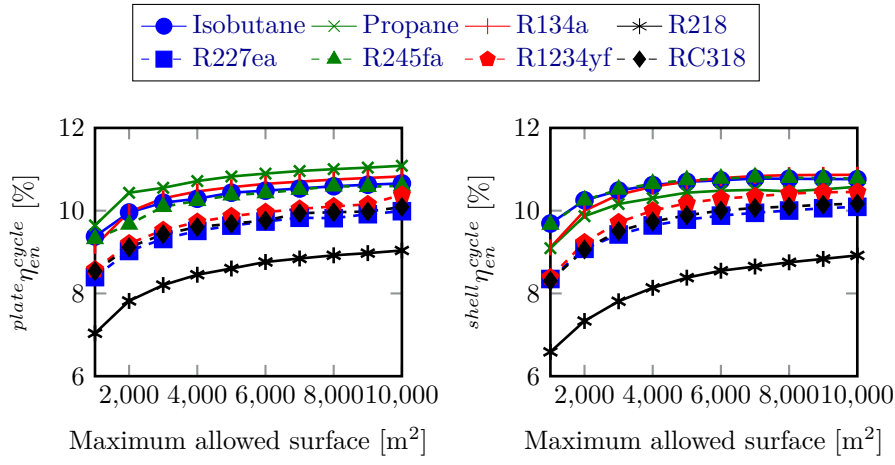

(a) Plate heat exchangers **(b)** Shell-and-tube heat exchangers

Figure 4.14: Energetic cycle efficiency for single-pressure simple ORCs with all plate heat exchangers (a) and all shell-and-tube heat exchangers (b) for different fluids.

difference between the working fluid and cooling fluid ΔT_{min}^{low} decreases much faster in the case of shell-and-tube heat exchangers with increasing A_{max}. This is due to fact that the cold and the hot side of plate heat exchangers with the

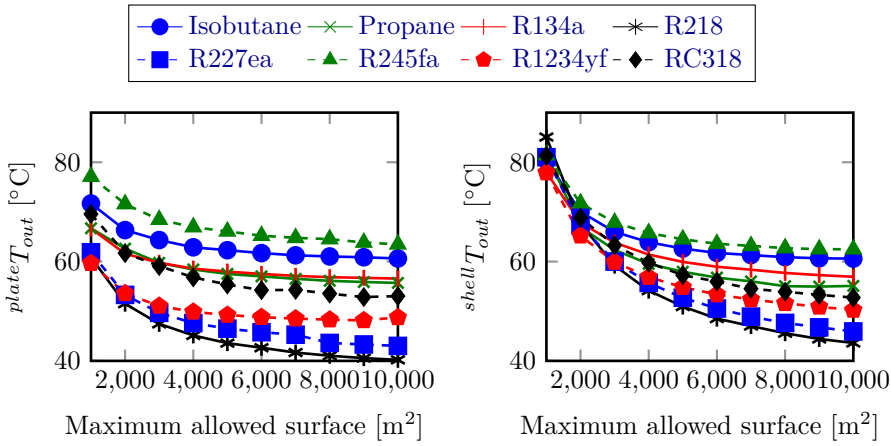

(a) Plate heat exchangers **(b)** Shell-and-tube heat exchangers

Figure 4.15: Outlet temperature of the heating fluid for single-pressure simple ORCs with all plate heat exchangers (a) and all shell-and-tube heat exchangers (b) for different fluids.

same number of passes at both sides have exactly the same geometry, which is of course not the case for shell-and-tube heat exchangers. The mass flow rate of the cooling water is much higher than the one of the working fluid, which can result in a large difference between the optimal geometry of the cold side and the one of the hot side in a plate heat exchanger, leading to relatively high pinch-point-temperature differences. This effect can be seen from figure 4.17, in which the average heat-transfer coefficient for the different heat exchangers is given, both for ORCs with all plate heat exchangers and all shell-and-tube heat exchangers. The parameters of the reference case (table 4.4) are used and isobutane is the working fluid. For the evaporator and the desuperheater, both types of heat exchangers perform about the same. For the liquid-liquid economizer, plate heat exchangers are the better choice, but for the condenser it is best to select a shell-and-tube heat exchanger. This figure also implies that it is best to use a shell-and-tube condenser (and perhaps evaporator) and plate heat exchangers for all other exchangers. The case of an ORC with a shell-and-tube condenser and plate heat exchangers for all other exchangers has been tested and results in most cases in the best performance.

The reasoning above also explains why certain fluids perform relatively, in comparison with the other fluids, better when shell-and-tube heat exchangers are used instead of plate heat exchangers, or the other way around.

It can also be noticed from figure 4.16 that ΔT_{min}^{high} is lower than ΔT_{min}^{low} for

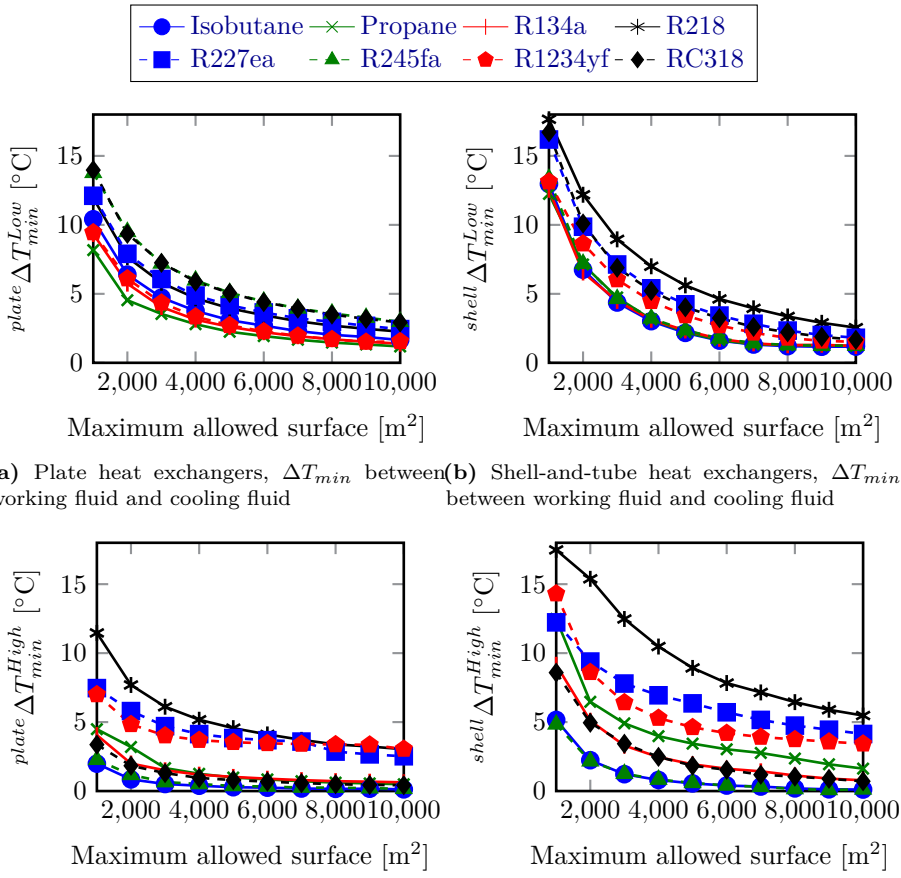

(a) Plate heat exchangers, ΔT_{min} between working fluid and cooling fluid

(b) Shell-and-tube heat exchangers, ΔT_{min} between working fluid and cooling fluid

(c) Plate heat exchangers, ΔT_{min} between heating fluid and working fluid

(d) Shell-and-tube heat exchangers, ΔT_{min} between heating fluid and working fluid

Figure 4.16: Minimum temperature difference between working fluid & cooling fluid (a,b) and minimum temperature difference between heating fluid and working fluid (c,d) for single-pressure simple ORCs with all plate heat exchangers (a, c) and all shell-and-tube heat exchangers (b, d) for different fluids.

subcritical cycles (for example Isobutane, R245fa), while they are about equal for transcritical cycles (for example R227ea, R1234yf). Because of the high cooling-fluid mass flow rate, ΔT_{min}^{low} is relatively close to the average temperature difference, which applies also to ΔT_{min}^{high} in transcritical cycles. In subcritical cycles, ΔT_{min}^{high} is much lower than the average temperature difference.

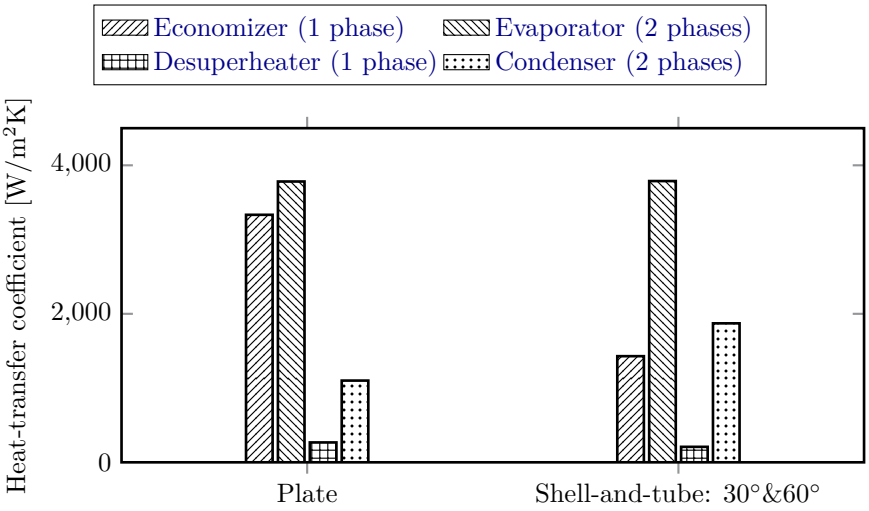

Figure 4.17: Comparison of the average heat-transfer coefficient for an ORC with all plate heat exchangers or all shell-and-tube heat exchangers for the reference case with isobutane as the working fluid. The results for the shell-and-tube heat exchanger are already given in figure 4.9. The surface of the superheater is very small and the average heat-transfer coefficient is therefore not shown in the figure.

4.3.4 Influence heat-source-inlet temperature

In this section the heat-source-inlet temperature is varied between 100 and 150°C, while keeping the other parameters constant as given in table 4.4. It is seen from figure 4.18 that every fluid performs optimally for a certain heat-source-inlet temperature[11]. ORCs with all shell-and-tube heat exchangers have their maximum plant efficiency at a lower heat-source-inlet temperature than plate heat exchangers. A heat source with a higher inlet temperature contains more energy and more energy will be transferred in the heat exchangers. However, for a fixed maximum allowed heat-exchanger surface, the pinch-point-temperature differences will increase with increasing heat-source-inlet temperature. This increase will in most cases be faster if shell-and-tube heat exchangers are used instead of plate heat exchangers. Higher pinch-point-temperature differences have of course a negative influence on the exergetic plant efficiency and this efficiency will therefore start to decrease earlier when shell-and-tube heat exchangers are used instead of plate heat exchangers.

[11] For some fluids this optimal temperature is outside the range of the figure

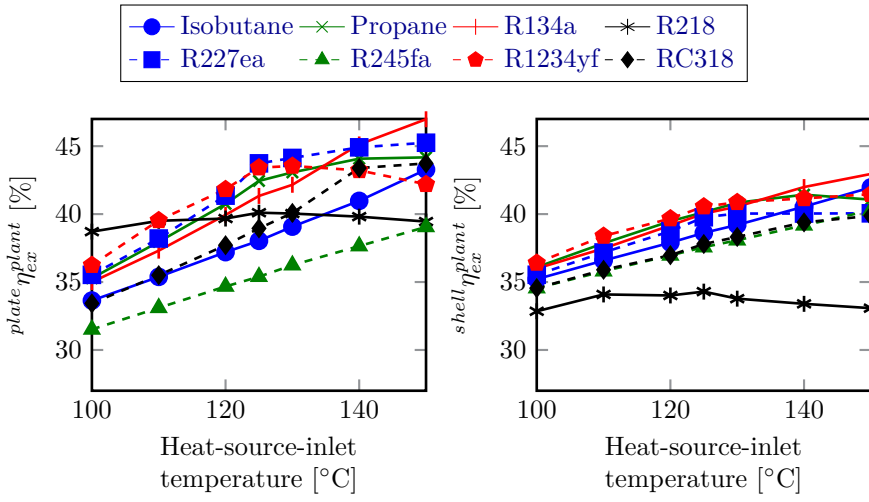

(a) Plate heat exchangers **(b)** Shell-and-tube heat exchangers

Figure 4.18: Exergetic plant efficiency for single-pressure simple ORCs with all plate heat exchangers (a) and all shell-and-tube heat exchangers (b) for different fluids. The parameters are those of table 4.4.

4.3.5 Influence constraint on heat-source-outlet temperature

Often the heat source cannot be cooled down too much; for example to avoid scaling[12] in geothermal brines or when the heat source after the ORC is used for heating. In this section, the heat-source-outlet temperature is constrained to values between 40 and 90°C. The other values are the same as in the reference case (table 4.4). Both simple and recuperated single-pressure cycles are investigated.

Figure 4.19 shows the comparison between simple and recuperated cycles. When the heat-source-outlet temperature is limited to a relatively low temperature, both type of cycles perform equally well as explained in chapter 3. When the limit is set at a higher temperature, the recuperated cycles perform better than the simple ones. The internal heat recuperation increases the cycle efficiency, which leads to a higher plant efficiency for a hig enough constraint on the heat-source-outlet temperature.

[12]The temperature at which scaling occurs depends very strongly on the composition of the brine and the pressure.

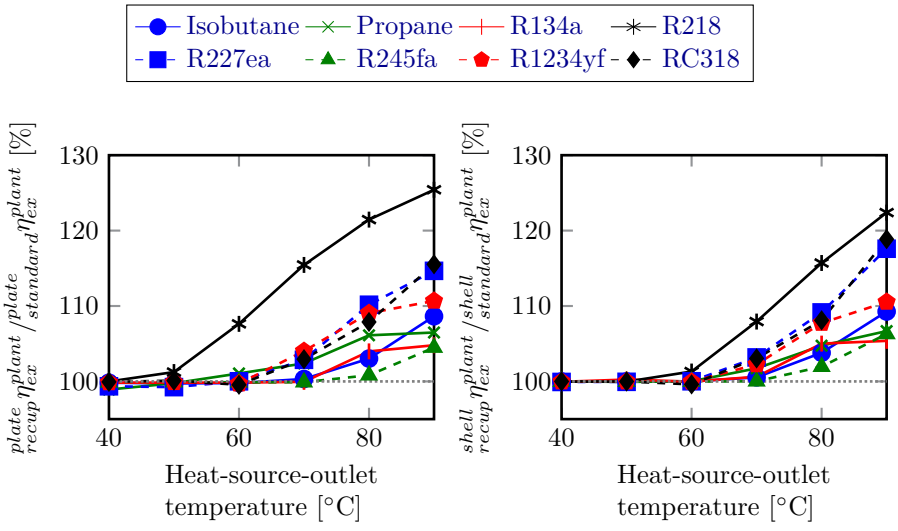

(a) Plate heat exchangers **(b)** Shell-and-tube heat exchangers

Figure 4.19: Comparison of the exergetic plant efficiency of single-pressure simple and recuperated ORCs with all plate heat exchangers (a) and all shell-and-tube heat exchangers (b) for different fluids. Other parameters are those of table 4.4.

4.3.6 Influence cooling-fluid-inlet temperature

The cooling-fluid-inlet temperature is varied between 10 and 40°C, while keeping the other parameters constant (table 4.4). Only the results for ORCs with all plate heat exchangers are given, because the results in the case of all shell-and-tube heat exchangers show the same trend. The exergetic plant efficiency decreases linearly as shown in figure 4.20a, but the decrease is less strong than in the case when ideal components – the influence of the condenser temperature in the ideal case is shown in figure 3.18 – are used. Figure 4.20b shows the pinch-point-temperature difference between the working fluid and the cooling fluid. This temperature difference decreases with increasing cooling-water-inlet temperature, in order to counteract the effect of the increasing cooling-water temperature on the condenser temperature.

4.3.7 Influence cooling-fluid mass flow rate

In this section the cooling-water mass flow rate is varied between 200 and 2000 kg/s. The other parameters are given in table 4.4 and only the results for

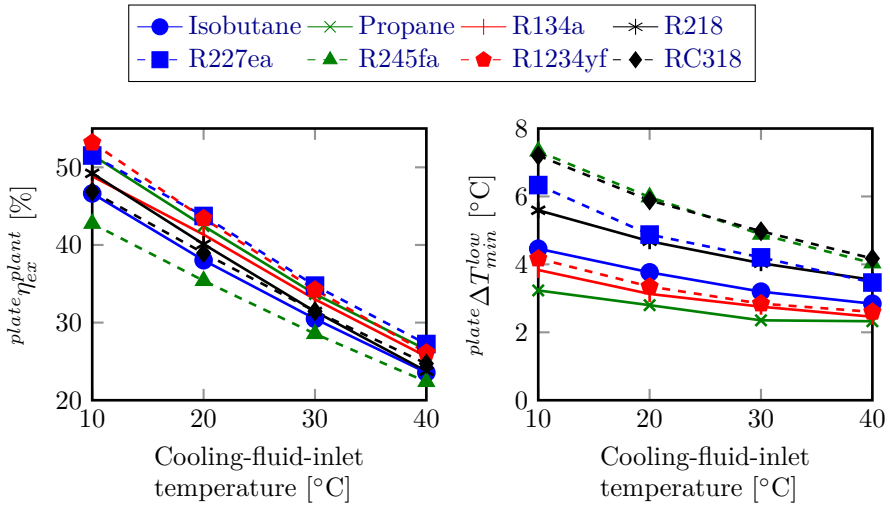

(a) Exergetic plant efficiency

(b) ΔT_{min} between working fluid and cooling fluid

Figure 4.20: Exergetic plant efficiency (a) and ΔT_{min}^{low} (b) for single-pressure simple ORCs with all plate heat exchangers for different fluids. Other parameters are those of table 4.4.

ORCs with all plate heat exchangers are shown; the results for ORCs with all shell-and-tube heat exchangers are analogous. Figure 4.21a shows the exergetic plant efficiency as a function of the cooling-water mass flow rate. At low values of the cooling-water mass flow rate, an increase of this mass flow rate will lead to an increase in the plant efficiency. This efficiency reaches a maximum for a mass flow rate of about 800 kg/s for ORCs with Propane and for a mass flow rate of about 1100 kg/s for ORCs with Isobutane, R134a, R218 and RC318. For the other investigated fluids the maximum is reached at higher mass flow rates. The same effect is also seen when shell-and-tube heat exchangers are used, but it is then less pronounced. The maximum in the exergetic plant efficiency at a certain mass-flow rate is explained by figure 4.21b, which shows the minimum temperature in the condenser. This temperature decreases with increasing cooling-water mass flow rate, which results in a better plant efficiency. The pressure drop on the cooling-water side increases on the other hand. The combination of the increasing pressure drop and increasing mass flow rate results in an increasing pumping power. This effect becomes more important than the decreasing condenser temperature for a high cooling-fluid mass flow rate, which results in a maximum plant efficiency for a certain cooling-fluid mass flow rate.

Figure 4.21c shows the pinch-point-temperature difference in the condenser. If

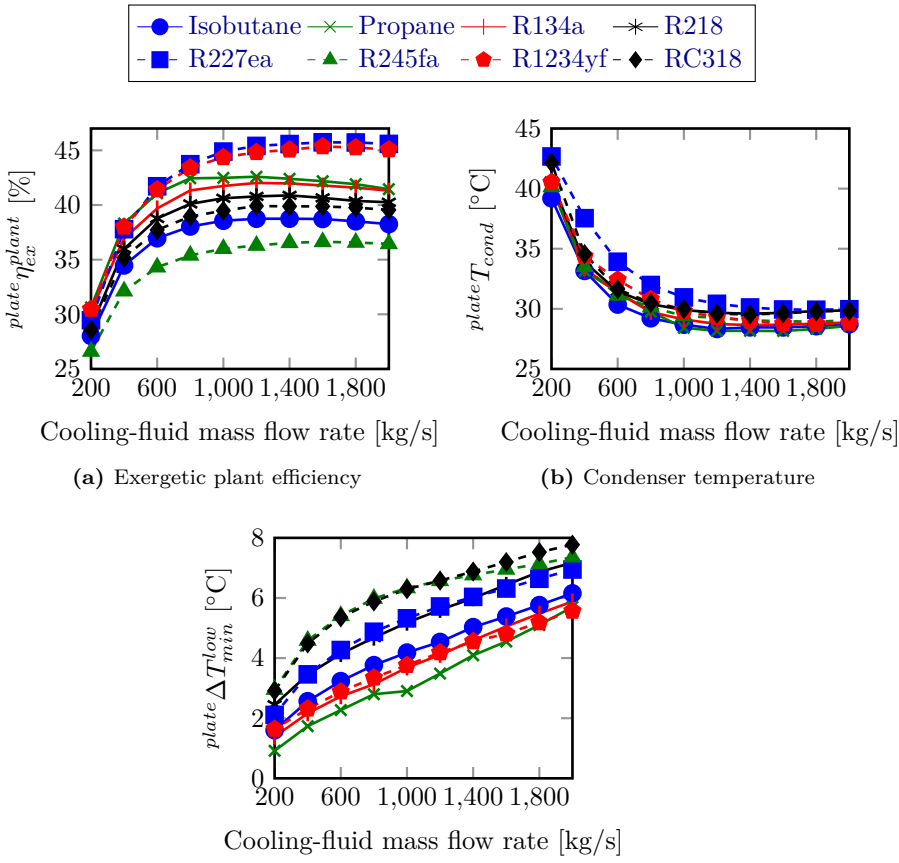

(a) Exergetic plant efficiency

(b) Condenser temperature

(c) Pinch-point-temperature difference in condenser

Figure 4.21: Exergetic plant efficiency (a), minimum temperature in the condenser (b) and ΔT_{min}^{low} (c) for single-pressure simple ORCs with all plate heat exchangers for different fluids.

the cooling-fluid mass flow rate increases, the cooling-fluid-outlet temperature will decrease and the curve of the cooling fluid will become flatter in a temperature-heat diagram. In order to keep the average temperature difference in the condenser more or less constant (the total amount of available heat-exchanger surface is limited), the pinch-point-temperature difference in the condenser has to increase.

4.3.8 Influence number of pressure levels

The effect on the plant efficiency of adding extra pressure levels is shown in figure 4.22a. The reference parameters are used (table 4.4) and the results for both plate heat exchangers and shell-and-tube heat exchangers are shown.

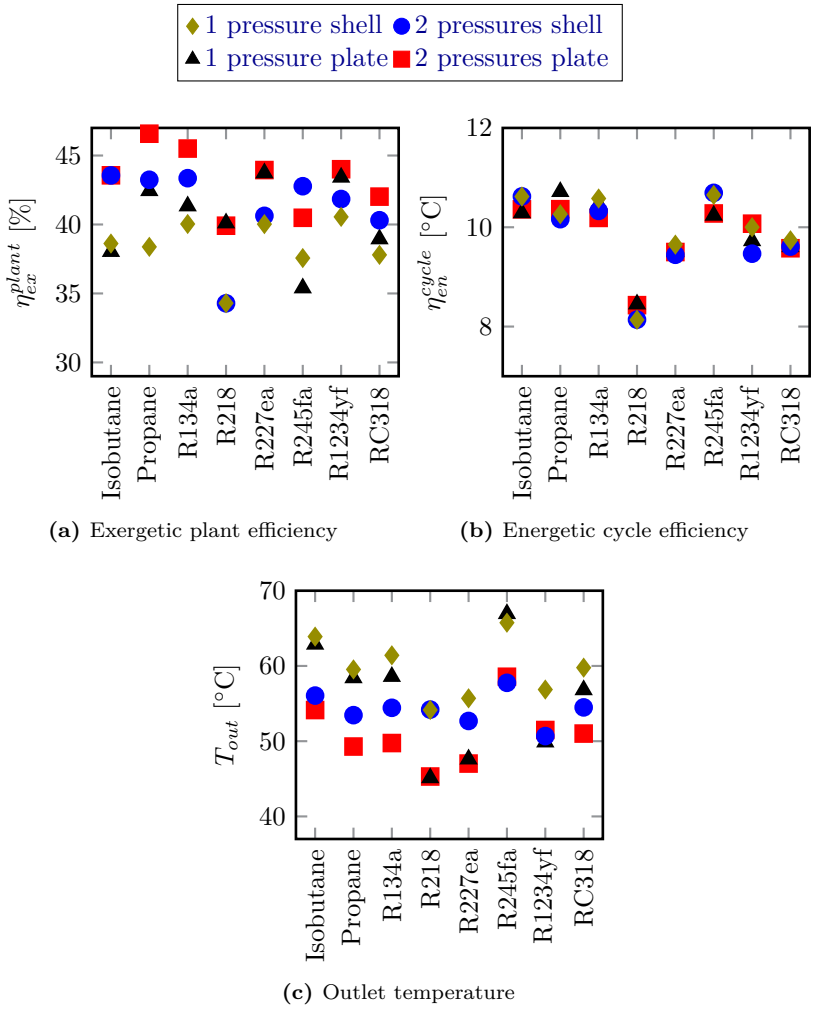

(a) Exergetic plant efficiency

(b) Energetic cycle efficiency

(c) Outlet temperature

Figure 4.22: Exergetic plant efficiency (a) and heat-source-outlet temperature (b) for simple ORCs with all plate heat exchangers or all shell-and-tube heat exchangers for different fluids.

Adding an extra pressure level to subcritical cycles (Isobutane, Propane, R134a,

R245fa) has a positive effect on the plant performance. Transcritical cycles do not use the second pressure level and their plant efficiency remains therefore constant. Double-pressure subcritical cycles can cool down the heat source more than single-pressure subcritical cycles (figure 4.22c) and obtain better plant efficiencies, while the energetic cycle efficiency remains about constant when adding a second pressure level as seen from figure 4.22b.

The performance gain by adding an extra pressure level is lower than the gain in chapter 3. In figures 3.6 and 3.8, the pinch-point-temperature differences are fixed at 5°C. Adding more pressure levels results in a better fit between the brine-cooling curve and the working-fluid-heating curve in a temperature-heat diagram and results in a lower brine-outlet temperature. This means that the average temperature difference decreases and that more heat has to be transferred, if the pinch-point-temperature differences would remain the same. For a constraint on the maximum allowed heat-exchanger surface, this results in increasing pinch-point-temperature differences, explaining the decreased effect of the extra pressure level with respect to the results in chapter 3.

4.4 Conclusions

In this chapter, it is shown that it is numerically possible to perform a, still simple, system optimization of a binary cycle, based on existing models for the components. The developed model can be extended with other components, as done in chapter 5, or used for other thermodynamic systems (for example heat pumps).

The system optimization of different configurations of ORCs with both plate heat exchangers and shell-and-tube heat exchangers is compared in this chapter. Models for heat exchangers used in single-phase flow, evaporation and condensation which are available in the literature are implemented and added to the ORC models developed in the previous chapter. The configuration of all heat exchangers and the cycle parameters are optimized together. The total heat-exchanger surface of all heat exchangers together is constrained in order to avoid an unrealistically large and expensive power plant.

First the optimal tube layout of shell-and-tube heat exchangers is investigated for the use in ORCs. Five different tube configurations are compared to each other. If all heat exchangers should have the same tube configuration, it is best to use the 30°-tube configuration. An efficiency improvement can be obtained by applying the 30°-tube configuration and the 60°-tube configurations in the single-phase and two-phase heat exchangers, respectively. This combined

configuration is used for the comparison to ORCs with all plate heat exchangers.

It is shown that ORCs with all plate heat exchangers perform mostly better than ORCs with all shell-and-tube heat exchangers. The disadvantage of plate heat exchangers with an equal number of passes at both sides of the exchanger is that the geometries of both sides of the heat exchanger are identical, which can lead to an inefficient heat exchanger when the two fluid streams require strongly different channel geometries.

The influence of the maximum allowed heat-exchanger surface, heat-source-inlet temperature, constraint on the heat-source-outlet temperature, cooling-fluid-inlet temperature and mass flow rate and the number of pressure levels on the performance of the ORC has been investigated. It is shown that the efficiency of an ORC increases with increasing heat-exchanger surface and that every fluid has a heat-source-inlet temperature for which the plant efficiency is maximal. Recuperated ORCs are only useful when the heat-source-outlet temperature is constrained and the best double-pressure subcritical ORCs perform better than the best single-pressure transcritical cycles.

In this chapter it is also shown that the results of chapter 3 are not always valid, when taking the configuration of heat exchangers into account in the optimization. This clearly shows that the assumption of a fixed pinch-point-temperature difference is not valid. The assumption of the value of the maximum allowed heat-exchanger surface is also an assumption, but it is removed from the optimization when economics are taken into account as done in chapter 5.

The cooling-fluid-inlet temperature and mass flow rate have a strong influence on the performance of the ORCs. In order to avoid making assumptions about these parameters, the cooling system is modeled and added to the system optimization in the next chapter.

Chapter 5

Economic system optimization of ORCs

The content of this chapter is based on:
D. Walraven, B. Laenen, and W. D'haeseleer. "Economic system optimization of air-cooled organic Rankine cycles powered by low-temperature geothermal heat sources". Submitted for publication in Energy. 2014
and
D. Walraven, B. Laenen, and W. D'haeseleer. "Minimizing the levelized cost of electricity production from low-temperature geothermal heat sources: water or air cooled?" Submitted for publication in Applied Energy. 2014

In the previous chapter it is shown that the cooling system is a very important component in an organic Rankine cycle (ORC). Both the cooling-fluid temperature and mass flow rate have a strong influence on the performance of ORCs. In this chapter, detailed models of air-cooled condensers and wet cooling towers are implemented and the configuration of these cooling systems is optimized in the system optimization. Also a model for an axial-inflow, axial-outflow turbine is used.

Instead of performing a thermodynamic optimization, two different economic objective functions are chosen. The first one is the maximization of the net present value (NPV) of the power plant, while the second one is the minimization of the levelized cost of electricity (LCOE). For the latter objective function, a comparison is made between air cooling and water cooling.

5.1 Models

In this section a model for an air-cooled condenser and a model for a mechanical-draft, wet cooling tower are described.

5.1.1 Air-cooled condenser

Geometry

Different types of air-cooled condensers (ACCs) exist, but in this work only the A-frame air-cooled condenser with flat tubes and corrugated fins is used. This type of tubes is often used in power plants because the pressure drop is lower than the one in ACCs with round tubes [110, 136]. Figure 5.1 shows the geometry of such an A-frame air-cooled condenser and the bundle geometry of flat tubes with corrugated fins.

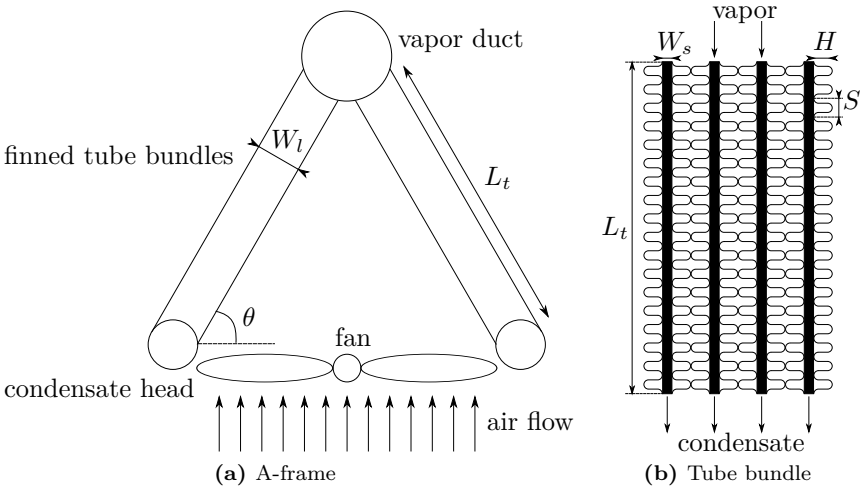

(a) A-frame **(b)** Tube bundle

Figure 5.1: Geometry of an A-frame air-cooled condenser (a) and the bundle geometry of flat tubes with corrugated fins (b).

The tube-bundle geometry is determined by the tubes' small width W_s, the fin height H, the fin pitch S, the tubes' large width W_l and the length of the tubes L_t. In an A-frame ACC the tube bundles are placed at an angle θ with the horizontal. The vapor/two-phase fluid enters the condenser at the top in the vapor duct, flows down the tubes, in which it condenses, and the condensate is

collected at the bottom in the condensate head. A fan at the bottom blows air over the tube bundles.

Model description

The correlation of Yang et al. [136] is used to model the heat-transfer coefficient and the pressure drop at the air side of the heat exchanger. The Nusselt correlation is given as[1]:

$$Nu = 0.05922\ Re^{0.9172} \left(\frac{S}{W_s}\right)^{0.9993} \left(\frac{H}{W_s}\right)^{-0.3706}, \tag{5.1}$$

with Re the Reynolds number defined as:

$$Re = \frac{\rho_{air} v_{Amin} W_s}{\mu_{air}}, \tag{5.2}$$

with ρ_{air} the density of the air, v_{Amin} the velocity at the minimum flow area and μ_{air} the dynamic viscosity of the air. The fluid properties are all calculated at the average temperature and pressure of the air. The heat-transfer coefficient obtained from equation (5.1) is based on the total heat-exchanger-surface area, including the area of the fins.

The friction factor while neglecting natural convection is:

$$f = \frac{238.8552}{2} Re^{-0.6684} \left(\frac{S}{W_s}\right)^{-1.4129} \left(\frac{H}{W_s}\right)^{-0.1496}. \tag{5.3}$$

The factor 1/2 in equation (5.3) arrives from the fact that Yang et al. [136] developed their correlation for another type of fins. This other type of fins results in a pressure drop which is about twice as high and a heat-transfer coefficient which is about the same as the configuration investigated in this work [136]. The pressure drop of the air flowing through the tube bundle is then:

$$\Delta p_{air} = f \frac{\rho_{air} v_{Amin}^2}{2}. \tag{5.4}$$

The electrical-power consumption of the fan is calculated as:

$$\dot{W}_{fan} = \frac{\Delta p_{air} \dot{m}_{air}}{\rho_{air} \eta_{fan} \eta_{el,fan}}, \tag{5.5}$$

[1] Formula (13) in the original paper of Yang et al. [136] gives a Nusselt number which is 10 times too high, which is confirmed in a personal communication by professor Yang.

with $\dot{m}_{air}$ the mass-flow rate of air, η_{fan} the fan efficiency and $\eta_{el,fan}$ the efficiency of the fan engine. The product of the last two parameters is assumed to be 60%.

Equations (5.1) and (5.3) are valid for $\theta = 60°$, $W_l = 219$ mm, $W_s = 19$ mm and for

$$0.06 \leq \frac{S}{W_s} \leq 0.16$$

$$0.75 \leq \frac{H}{W_s} \leq 1.25$$

$$700 \leq Re \leq 14500.$$

5.1.2 Wet cooling tower

Another cooling option is to use a desuperheater and a condenser, coupled to a wet cooling tower (WCT). Natural-draft cooling towers are not modeled in this work, because they are typically used for large cooling needs. For lower cooling loads, mechanical-draft cooling towers are better suited. Both induced and forced-draft towers exist. In the former type, the fan is located downstream (at the exit of the air) of the tower, while the fan is located upstream (at the inlet of the air) in forced-draft towers. The velocity of the air at the outlet is higher for induced-draft towers and the chance of recirculation of wet air is therefore lower. This is the reason why induced-draft towers are more often used and are the focus in this work. Such an induced-mechanical-draft tower is shown in figure 5.2. The warm cooling water enters the tower in the sprayers in which it is sprayed over the packing. The packing is used to increase the contact surface between droplets and air in order to enhance the heat and mass transfer. At the bottom, the cooled water is caught and it is sent back to cool the ORC condenser. The air flows in the opposite direction; it enters the tower from the sides at the bottom and flows through the inlet louvers. These louvers are used to prevent the inflow of unwanted elements, to prevent water splash and to decrease the amount of sunlight irradiation. When flowing upwards in the tower, the air heats up and the humidity increases. The drift eliminators are used to decrease the amount of water droplets taken by the airflow. The height of the inlet H_i, the height of the packing H_{fi}, the height of the spray zone H_{sp} and the width of the tower W_t are shown in figure 5.2.

In this work, only square towers with a film packing are modeled. The model of the cooling tower is based on the work of Kloppers [62]. He developed empirical correlations for the performance of different packing types and used a fourth

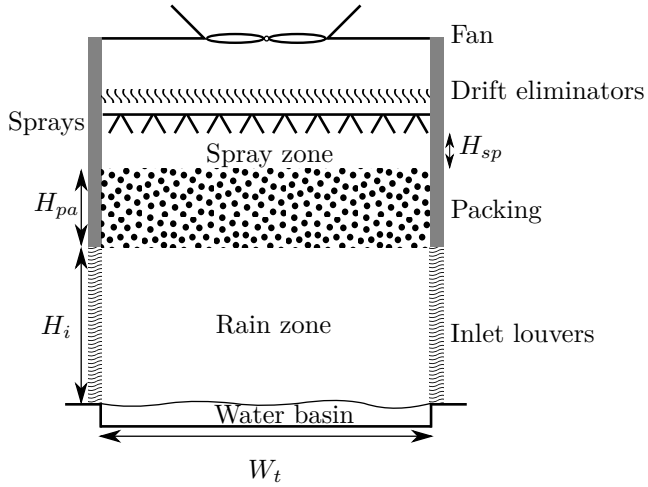

Figure 5.2: Geometry of an induced mechanical-draft wet cooling tower. Figure adapted from Kloppers [62].

order Runge-Kutta method to solve the Poppe equations. The pressure drop of the air in the tower is also based on the above mentioned work. These equations are given in appendix B.

For a given inlet temperature and required outlet temperature of the cooling water, the required Merkel number[2] Me is calculated. Based on the geometry of the tower, the properties of the air and the water, the Merkel number in the spray zone Me_{sp} and the rain zone Me_{rz} can be calculated (equations (B.12) and (B.21)). From this the required Merkel number in the packing Me_{pa} follows and the height of the packing can be calculated (equation (B.22) and (B.23)). To calculate the electrical power consumption of the fan, the pressure drop of the air in the inlet zone, the inlet louvers, rain zone, packing support structure, packing, spray zone, water distribution, drift eliminator and fan upstream are calculated [62]. It is assumed that the fan has a total efficiency (isentropic and electric) of 60%.

[2]The Merkel number is a non-dimensional parameter describing the transfer characteristics in the cooling tower, defined as $Me = \frac{h_d a_{pa} L_{pa}}{G_w}$ with h_d the mass transfer coefficient, a_{pa} the area density of the packing and G_w the mass velocity of the water.

5.1.3 Turbine

Three different types of turbines are used in ORCs: the axial-flow turbine, the centripetal turbine and the radial-inflow, radial-outflow turbine. As given in appendix C, these different types of turbines have typically isentropic efficiency between 80 and 90%. In this study, the focus lies on the first type because of the availability of correlations. Macchi and Perdichizzi [69] used the Craig and Cox-model [25] to optimize the performance of axial flow-turbines. This resulted in an efficiency prediction of a turbine stage based on the inlet state of the turbine and the isentropic outlet state. The original prediction was given as a figure, which is curve fitted in appendix C. Comparison of the obtained correlation with available experimental data is also provided.

5.1.4 Shell-and-tube heat exchangers

Only shell-and-tube heat exchangers are used in this chapter because of the lack of cost-correlations for large plate heat exchangers. Only the 30°&60° configuration is used, because it is the best performing configuration as shown in the previous chapter.

5.2 Economics

Two economic characteristics are used: the net present value and the levelized cost of electricity.

5.2.1 Net present value

The net present value (NPV) is the current value of money that will be available at the end of the lifetime of the project. It is calculated as [28]:

$$\text{NPV} = -C_{EPC} + \sum_{t=1}^{t_{LT}} \frac{I_t}{(1+i)^t}, \tag{5.6}$$

with C_{EPC} the engineering, procurement & construction overnight cost (EPC) of the installation[3], t_{LT} the lifetime of the installation, I_t the income in year t and i the discount rate. The EPC cost consists of two parts: the cost of the

[3]There is a caveat: C_{EPC} is not the total investment cost. Some reflections on the investment cost are given in section 5.2.4.

drilling $C_{drilling}$ which is considered to be given and the cost of the ORC C_{ORC} (see section 5.2.3). The income in year t can be calculated as:

$$I_t = \dot{W}_{net}\ p_{elec}\ N - C_{O\&M,t}, \tag{5.7}$$

with $\dot{W}_{net}$ the net electric power output, which takes a generator efficiency of 98% into account, expressed in MW_e, p_{elec} the price obtained per MWh of generated electricity, N the number of full-load hours per year (an availability of 95% is assumed) and $C_{O\&M,t}$ the cost of operation and maintenance of the power plant in year t, which is assumed to be 2.5% of the investment cost of the ORC per year [52].

5.2.2 Levelized cost of electricity

The levelized cost of electricity (LCOE) is the constant electricity price needed during the lifetime of the power plant to reach break even over the lifetime of the project. This means in fact that the NPV is equal to zero. The LCOE is calculated in €/MWh as [28]

$$\text{LCOE} = \frac{C_{EPC} + \sum_{t=1}^{t_{LT}} \left[\left(C_{O\&M,t} + C_{water,t} \right) (1+i)^{-t} \right]}{\sum_{t=1}^{t_{LT}} \dot{W}_{net}\ N\ (1+i)^{-t}}, \tag{5.8}$$

with $C_{water,t}$ the water cost in year t. The computed LCOE is kind of a "naked" LCOE based on the EPC overnight cost (see section 5.2.4 for the total investment cost).

5.2.3 Cost of ORC

The overnight EPC investment cost of the ORC, C_{ORC}, can be calculated as:

$$C_{ORC} = \sum_i \left(f_{M,i} f_{P,i} f_{T,i} + f_I \right) C_{E,i}, \tag{5.9}$$

with $C_{E,i}$ the equipment cost of component i and $f_{M,i}$, $f_{P,i}$ and $f_{T,i}$ correction factors (all ≥ 1) for non-standard material, pressure and temperatures, respectively. f_I is an average installation-cost factor [106]. This installation-cost factor includes the costs for erection, instrumentation and control of the power plant and is about 0.6 [105, 106]. Correlations for the equipment cost $C_{E,i}$ are given in table 5.1. These correlations should be used with care. First, they are purely based on correlations available in the literature. Second, they assume economies of scale, not taking into account size limitations. For ease of transportation, the components should fit into a container (standard 40'

Component[4]	Capacity measure	Size range	Cost correlation	Ref
Shell-and-tube heat exchanger	A [m^2]	80-4000 m^2	$3.50\ 10^4 \left(\frac{A}{80}\right)^{0.68}$ [€^{2013}]	[106]
Centrifugal pump (incl. motor)	$\dot{W}_P$ [kW]	4-700 kW	$10.51\ 10^3 \left(\frac{\dot{W}_P}{4}\right)^{0.55}$ [€^{2013}]	[106]
Air-cooled heat exchanger	Bare-tube A [m^2]	200-2000 m^2	$1.67\ 10^5 \left(\frac{A}{200}\right)^{0.89}$ [€^{2013}]	[106]
Fan (incl. motor)	$\dot{W}_{fan}$ [kW]	50-200 kW	$1.31\ 10^4 \left(\frac{\dot{W}_{fan}}{50}\right)^{0.76}$ [€^{2013}]	[106]
Turbine	$\dot{W}_T$ [kW]	0.1-20.0 MW	$-1.66\ 10^4 + 716\dot{W}_T^{0.8}$ [€^{2013}]	[113]
Film packing	V_{pack} [m^3]	/	$41.57\ V_{pack}$ [€^{2013}]	[62]
Structure tower	Outside A [m^2]	/	$332.56\ A$ [€^{2013}]	[62]

Table 5.1: Cost correlation for the different components. The data from Smith [106], Towler and Sinnott [113] and Kloppers [62] are adapted taking into account that 1€=1.35$ and with a Chemical Engineering (CE)-index of 564 in July 2013. The reference CE-index of 100 was set in the base period 1957-1959. CE-indices can be found on http://www.che.com/pci/.

container) and should easily pass under bridges (4.2 m height). These practical limitations are not taken into account in this work.

The cost correlations in table 5.1 are valid for carbon steel, for design temperatures between 0 and 100°C and for design pressures between 0.5 and 7 bar. Such "normal" designs are good enough for most components in a low-temperature ORC. Only the heat exchangers between brine and working fluid work at higher pressures and temperatures and have a higher risk for corrosion. For these heat exchangers, the values of table 5.1 are adjusted using the above mentioned correction factors; the tubes are made from stainless steel (f_M = 1.7), work at higher pressures (f_P = 1.5) and at higher temperatures (f_T = 1.6) [106]. With these factors, pressures up to 50 bar and temperatures up to 300°C are allowed. These factors are discontinuous functions of the pressure and temperature, respectively, because equipment is in practice typically designed according to standards.

No cost correlations for large plate heat exchangers are found in the literature, so only shell-and-tube heat exchangers are used in this chapter.

5.2.4 Definition investment cost

In this work only the engineering, procurement & construction cost (C_{EPC}) is taken into account, but the total investment cost consists also of other parts. Neither owner costs nor provisions for contingency nor financing costs (or interest during construction) are considered here. The most widely used delineation can be found in D'haeseleer [28]:

[4]The cost of the working fluid is not taken into account. The cost-correlations for the components should be used with care.

- Total investment cost
  - Overnight construction cost
    - Owner's cost
    - Engineering, procurement & construction cost
    - Contingency provision
  - Interest during construction

5.3 Optimization

In this chapter, two separate objective functions are used. The first one is the maximization of the net present value, while the second one is the minimization of the levelized cost of electricity. The former objective is especially interesting for an investor, while the latter one is useful for decision makers.

5.3.1 Decision variables and constraints

The same cycle decision variables and constraints as in the previous chapter (see table 4.1) are used. The only difference is that no constraint on the total heat-exchanger surface is necessary because of the economic objective function; the optimal economic total heat exchanger surface is a result of the optimization.

Shell-and-tube heat exchanger

For the decision variables and constraints used for shell-and-tube heat exchangers it is referred to table 4.2 in the previous chapter.

Air-cooled condenser

The geometry of the air-cooled condenser is determined by the tubes' small width W_s, the fin height H, the fin pitch S, the tubes' large width W_l, the length of the tubes L_t and the angle θ of the tube bundle with the horizontal axis, as explained in section 5.1.1. W_l, W_s and θ are fixed and L_t is the result of the model. So, H and S are necessary to determine the configuration of the tube bundle. Extra variables are the velocity of the wind at the minimum cross section v_{Amin} and the number of tubes N_t. A non-linear constraint is used to limit the length of the tubes. The values for the lower and upper bounds are given in table 5.2.

Optimization variable	Lower bound	Upper bound
Fin height H	14.25 mm	23.75 mm
Fin pitch S	1.14 mm	3.04 mm
Maximum air velocity v_{Amin}	1.5 m/s	10 m/s
Number of tubes N_t	1000	10000
Tube length L_t	/	20 m

Table 5.2: Decision variables and constraints used for the air-cooled condenser and their lower and upper boundaries.

The lower and upper bounds of the fin height and fin pitch are determined by the limits of the used correlation, while the bounds of the maximum air velocity and number of tubes are chosen to avoid numerical instabilities.

Wet cooling tower

Table 5.3 shows the optimization variables used for the wet cooling tower and their lower and upper bounds. T_{wb} is the wet-bulb temperature. The height of the spray zone H_{sp} is fixed at 0.5 m. The height of the packing H_{pa} is a result of the cooling-tower model and is therefore not an optimization variable.

Optimization variable	Lower bound	Upper bound
Tower width W_t	1 m	40 m
Inlet height H_i	1 m	20 m
Relative air mass flow rate $\dot{m}_{air}/\dot{m}_{brine}$	1.5	500
Relative cooling-water mass flow rate $\dot{m}_{cw}/\dot{m}_{brine}$	1.5	500
Minimum cooling-water temperature T_{cw}^{min}	T_{wb}	/

Table 5.3: Decision variables used for the wet cooling tower and their lower and upper boundaries.

The lower bounds of the air and cooling-fluid mass flow rate are chosen to avoid numerical instabilities.

5.3.2 Optimization approach

The same optimization approach is used as in chapter 4. The optimization is performed with the use of the CasADi [5] and WORHP [20] software. The models themselves are developed in Python and the fluid properties are obtained from REFPROP [66]. A *system* optimization is performed, which means that

the cycle parameters and the configuration of all the components are optimized together.

The optimization is schematically shown in figure 5.3. Comparison with figure 4.6 shows that the cooling-system optimization variables are added, the cooling-fluid properties are replaced by the conditions of the surroundings (temperatures and pressure), economic parameters are added and the constraint on the maximum allowed total heat exchanger surface is removed. In this chapter, the turbine efficiency is calculated, but an assumption is made about the fan efficiency.

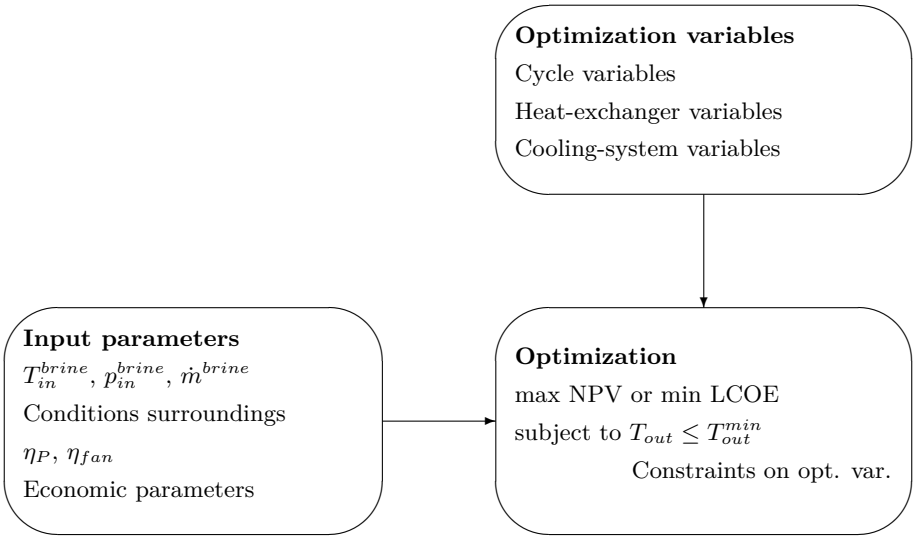

Figure 5.3: Schematic of the optimization used in this chapter.

5.4 Results and discussion

After the description of the reference case, results for the maximization of the net present value of ORCs with air-cooled condensers is performed [123]. Afterwards a comparison between air-cooled and water-cooled ORCs is performed based on the minimization of the levelized cost of electricity [125].

5.4.1 Parameters of the reference case

In this subsection the parameters of our "reference" case are defined, after which a variation of the parameters is performed. The investigated "reference" case is based on a proposed geothermal demonstration project in Belgium [119] and the "reference" parameters are given in table 5.4. In the next subsections, the influence of many of these parameters on the performance of the ORC is investigated. The well parameters are assumed to be fixed and follow from a geological analysis and optimization of the subsurface performed by VITO [118]. The cost for the wells only take the drilling costs into account and not the costs for the geological survey.

Well parameters		Conditions surroundings	
Brine-wellhead temperature	125°C	Dry-bulb temperature	10.3°C
Brine mass flow rate	194 kg/s	Wet-bulb temperature	8.6°C
Consumption well pumps	600 kW_e	Air pressure	1016 hPa
Cost wells	27.5 M€		

Economic parameters			
Electricity price	50 €/MWh_e	Electricity-price increase	5 %/year
Lifetime plant	30 years	Discount rate	4 %/year
Water price	0.5 €/m^3		

Table 5.4: Parameters of the reference case

In this chapter, only electricity generation from the geothermal heat source is investigated and heating purposes are not taken into account. Many economic parameters used in this chapter are based on the literature and the economic analysis is therefore not detailed enough to be used for a business plan.

5.4.2 Maximization of the NPV of ORCs with an ACC

Influence of the brine-inlet temperature

Figure 5.4 shows the NPV of a simple and a recuperated ORC powered by geothermal heat and cooled with an ACC, depending on the inlet temperature of the brine.

The NPV increases with increasing brine-inlet temperature, as a consequence of the decreasing specific overnight investment cost of the ORC with increasing brine-inlet temperature as shown in figure 5.5.

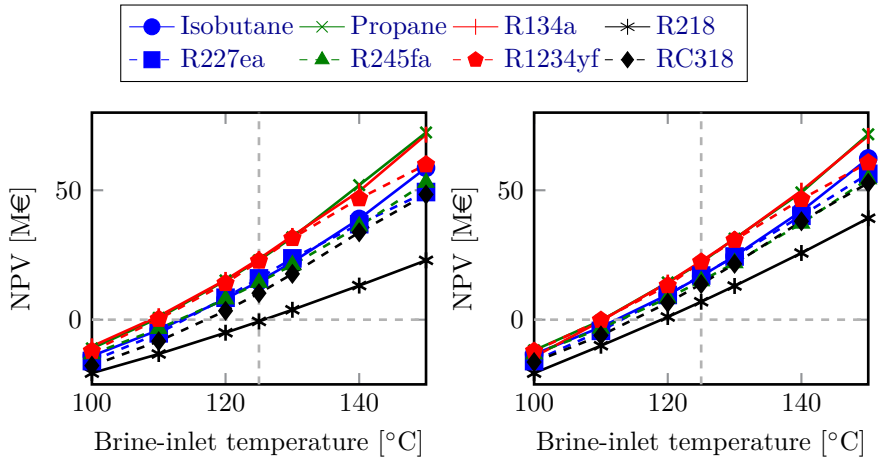

(a) Single-pressure simple cycle **(b)** Single-pressure recuperated cycle

Figure 5.4: Net present value of a single-pressure simple (a) and a single-pressure recuperated (b) ORC powered by geothermal heat and cooled with an ACC, for various thermodynamic-cycle fluids and for varying inlet temperature of the brine.

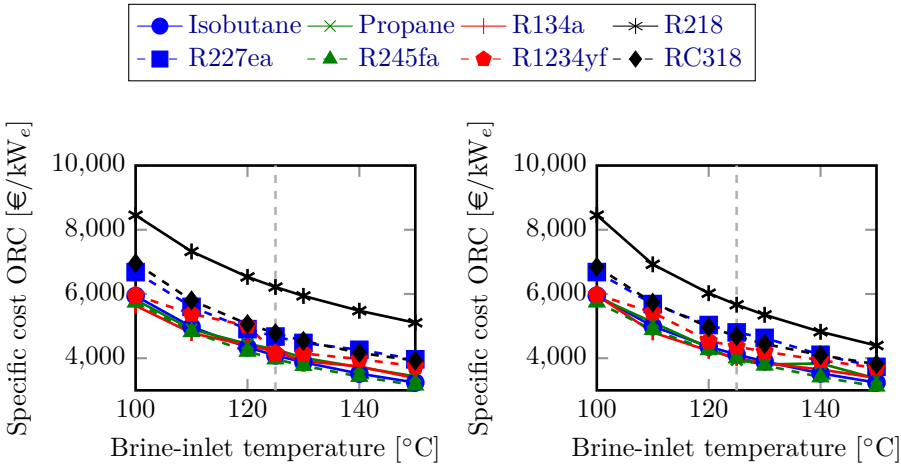

(a) Single-pressure simple cycle **(b)** Single-pressure recuperated cycle

Figure 5.5: Specific cost of a single-pressure simple (a) and a single-pressure recuperated (b) ORC powered by geothermal heat and cooled with an ACC, for various thermodynamic-cycle fluids and for varying inlet temperature of the brine. Only the cost of the ORC is shown, the costs of the wells (27.5 M€) is not included.

Two conflicting effects determine the evolution of the specific overnight ORC investment cost. The absolute cost of the ORC increases with increasing brine-inlet temperature (larger turbine, larger heat exchangers, etcetera), but the net electric power generation (see figure 5.6) also increases. This last effect is larger so that the specific overnight investment cost of the ORC decreases with increasing brine-inlet temperature.

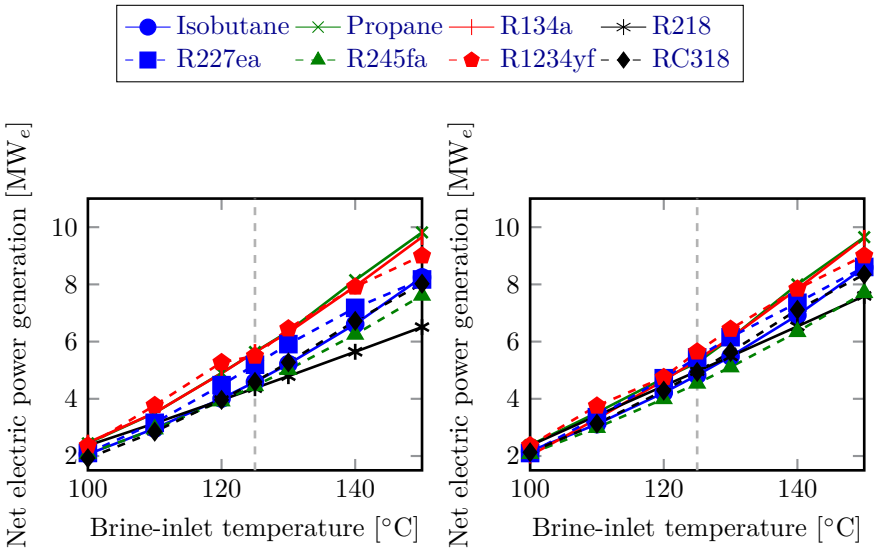

(a) Single-pressure simple cycle **(b)** Single-pressure recuperated cycle

Figure 5.6: Net electric power generation of a single-pressure simple (a) and a single-pressure recuperated (b) ORC powered by geothermal heat and cooled with an ACC, for various thermodynamic-cycle fluids and for varying inlet temperature of the brine.

The strong increase of the net electric power generation with increasing brine-inlet temperature can be explained by two effects. On the one hand, the gross electric power output of the cycle increases with increasing brine-inlet temperature (a simple consequence of the thermodynamic efficiency – Carnot). On the other hand, less electrical power (relatively speaking) is needed to drive the fans of the cooling system because the heat added to the cycle is converted more efficiently into mechanical power. So, the gross electric power output increases and the electricity consumption of the auxiliaries decreases (relatively).

Figures 5.4a and 5.4b show the NPV of simple and recuperated cycles, respectively. The addition of a recuperator results in a slightly higher NPV when dry fluids (isobutane, R218, R227ea, R245fa and RC318) are used. This

effect is only large enough to be seen in figures 5.4a and 5.4b when R218 is used. The NPV is determined by the net power output of the ORC and the cost of it. As seen from figure 5.6b, the net electric power output of the recuperated cycles is higher than the one of the simple cycles (for the dry fluids). Less cooling is needed in recuperated cycles, so that, when all other conditions are the same, less electrical power is consumed by the fans and the cooling installation can be smaller. These two effects are more important than the extra cost for the recuperator as seen in figure 5.7a. From this figure it is seen that the ACC is by far the most expensive part of the ORC; about 80% of the total overnight investment cost of the ORC is credited to the ACC. Other expensive components are the turbine, the economizer and the recuperator. The evaporator is only a small part of the total cost and the cost of the pump is negligible.

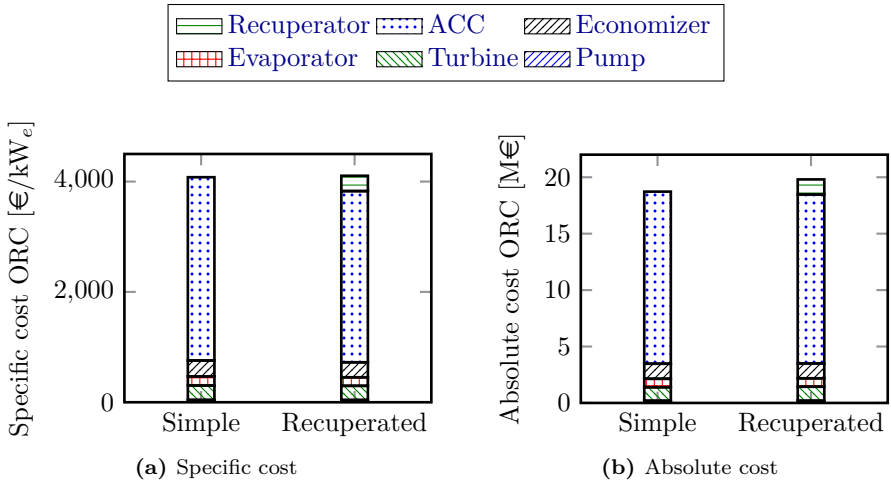

(a) Specific cost **(b)** Absolute cost

Figure 5.7: Distribution of the specific cost (a) and the absolute cost (b) for single pressure, simple and recuperated ORCs with isobutane as the working fluid for a brine-inlet temperature of 125°C. The cost of the superheater is very small in all cases and is not shown in the figure. Only the cost of the ORC is shown, the costs of the wells (27.5 M€) is not included.

For the simple configuration in figure 5.7b, the cost of the ORC accounts for about 41% of the total cost of the project, when taking into account that it is assumed that the drilling of the wells costs 27.5 M€ (table 5.4). For the recuperated configuration, the cost of the ORC is about 42% of the total cost.

In the previous chapters it was concluded that a recuperator is not useful when no constraint is set on the brine-outlet temperature, but this conclusion is no longer valid when the cooling system is modeled in detail. This shows that it is

important to model and optimize the components together with the cycle, so that as much effects as possible are taken into account.

Figures 5.7a and 5.7b give the distribution of the specific and absolute cost of simple and recuperated ORCs with isobutane as the working fluid. It is chosen to plot the results for this fluid because it is the dry fluid which results in the highest NPV. Figures 5.7a and 5.7b show that the specific cost of the optimal simple and optimal recuperated cycle are about the same, while the absolute overnight investment cost of the recuperated ORC is higher than the one of the simple ORC. This means that the net electric power generation is higher for the recuperated cycle than for the simple one. This is achieved by decreasing the condensing temperature of the recuperated ORC in comparison with the simple one.

Influence of the constraint on the brine-outlet temperature

In some cases it is necessary to have a minimum brine-outlet temperature to avoid scaling or to use the brine after the ORC for heating. In this chapter, focus lies only on electricity generation and the possible direct use for heating is not taken into account, but it can be interesting to see the influence of the minimum allowed brine-outlet temperature on the performance of the ORC.

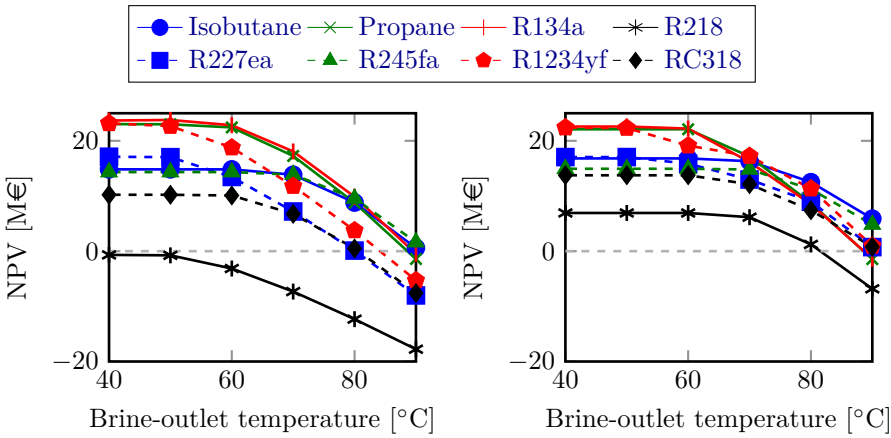

(a) Single-pressure simple cycle **(b)** Single-pressure recuperated cycle

Figure 5.8: Net present value of an ORC powered by geothermal heat and cooled with an ACC, depending on the outlet temperature of the brine. The brine-inlet temperature is 125°C.

Figure 5.8 shows the NPV as a function of the minimum brine-outlet temperature for single-pressure simple and recuperated cycles. No effect of the brine-outlet-temperature constraint is seen for temperatures up to about 50 and 60°C, which is the brine-outlet temperature in case of no constraint, for the simple and recuperated cycles, respectively. For higher minimum brine-outlet temperatures, the NPV of both the simple and the recuperated cycles starts to decrease. This decrease is stronger for the simple cycles than for the recuperated ones. It is therefore advantageous to use a recuperator for all fluids, even wet ones, when the constraint on the brine-outlet temperature is high.

In the remainder of this chapter, only the results of recuperated cycles are shown. Simple cycles are in fact recuperated cycles with an effectiveness of the recuperator, which is an optimization variable, of zero. So, recuperated cycles are the most general ones.

Impact of 2 pressure levels

Figure 5.9a shows the net present value of double-pressure recuperated ORCs, depending on the inlet temperature of the brine. Comparison of figures 5.4b and 5.9a shows that the NPV increases when another pressure level is added for all investigated fluids, except for R218. The maximum pressure in the optimal cycle for that fluid, R218, is much higher than the critical pressure. The fit between the brine-cooling curve and the working-fluid-heating curve in a temperature-heat diagram is very good, so adding another pressure level does not improve the cycle performance. The addition of an extra pressure level is especially profitable for cycles in which the evaporation temperature in the single-pressure cycle is much lower than the critical temperature (isobutane and R245fa). The effect of the second pressure level is relatively small for the other fluids.

The specific cost of double-pressure recuperated ORCs is shown in figure 5.9b. Comparison with figure 5.5b shows that the specific overnight investment cost increases by a small amount (up to 5%) if an extra pressure level is added. The net electric power output increases too as shown in figure 5.9c. Due to the high cost of the wells, the increased specific cost does result in an improved NPV.

In the remainder of this section about the maximization of the NPV, only the results of single-pressure cycles are shown, but the trends are similar for double-pressure cycles.

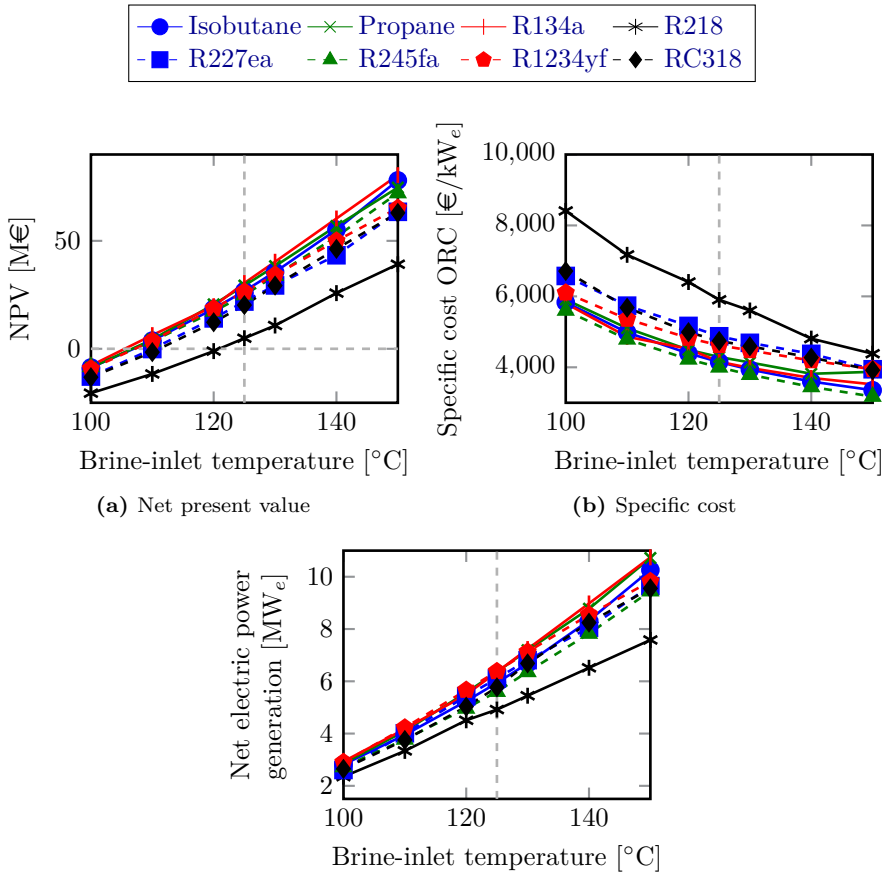

(a) Net present value

(b) Specific cost

(c) Net electric power generation

Figure 5.9: Net present value (a) and specific cost (b) of a double-pressure recuperated ORC powered by geothermal heat and cooled with an ACC, depending on the inlet temperature of the brine. Only the cost of the ORC is shown, the costs of the wells (27.5 M€) is not included.

Influence of the electricity price

Figure 5.10a shows the NPV of ORCs powered by geothermal heat and cooled with an ACC as a function of the electricity price.

The NPV increases strongly with increasing electricity price, because not only the price of the electricity increases, but the amount of electricity generated increases too. The latter effect is shown in figure 5.10b, which shows the net

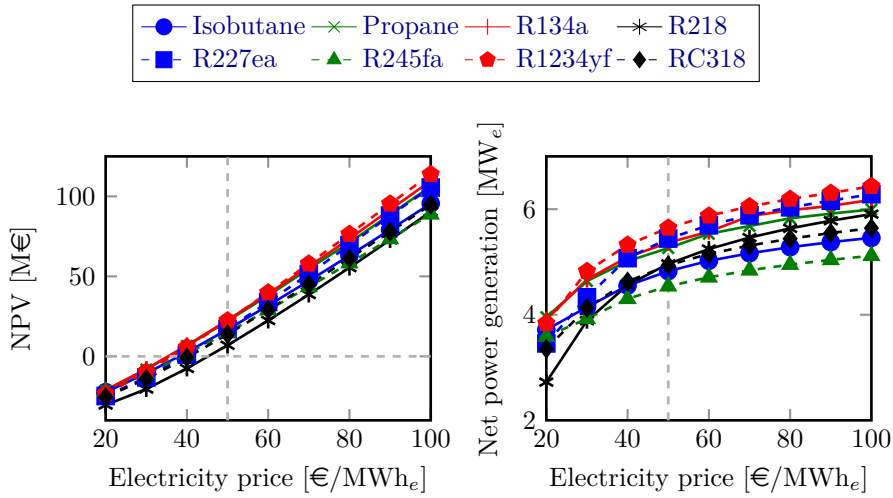

(a) NPV **(b)** Net electric power generation

Figure 5.10: Net present value (a) and net electric power generation (b) of a single-pressure recuperated ORC powered by geothermal heat and cooled with an ACC, depending on the electricity price.

electric power generated. The higher electric power generation is explained by the fact that a higher electricity price, and thus a higher income during the lifetime of the power plant, allows to invest more in a more efficient power plant. This increase in electric power generation follows from a decreasing condenser temperature, decreasing pinch-point-temperature differences and a decreasing heat-source-outlet temperature, so more heat is added to the cycle. This results also in a higher specific cost of the ORC, which is shown in figure 5.11.

Influence of the discount rate and electricity-price evolution

Figures 5.12a and 5.12b show the net present value as a function of the discount rate and the annual electricity-price evolution, respectively. The trend of a decreasing discount rate and an increasing electricity-price evolution are analogous to the effect of an increasing electricity price (figure 5.10a). The effect of the discount rate is very strong, due to the high investment and low operational costs.

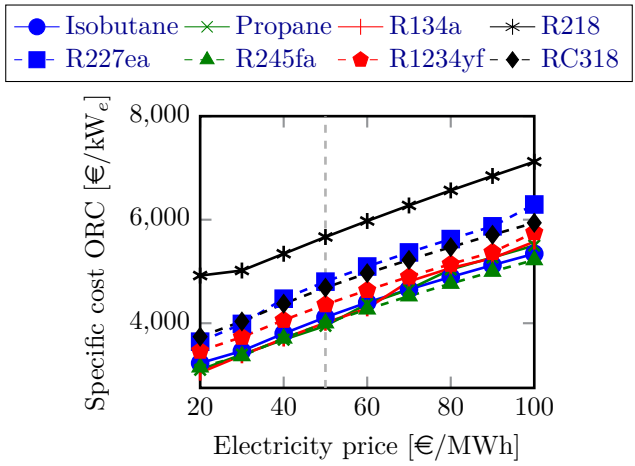

Figure 5.11: Specific cost of a single-pressure recuperated ORC powered by geothermal heat and cooled with an ACC, depending on the electricity price. Only the cost of the ORC is shown, the costs of the wells (27.5 M€) is not included.

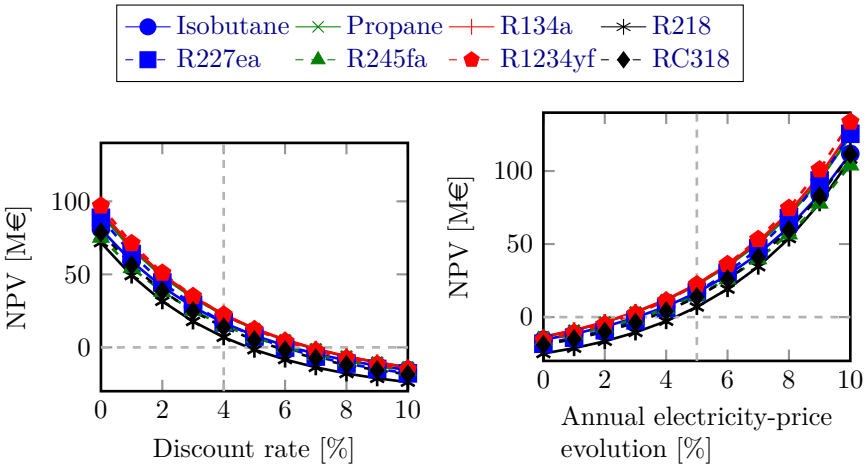

(a) Discount rate **(b)** Annual electricity price evolution

Figure 5.12: Net present value of a single-pressure recuperated ORC powered by geothermal heat and cooled with an ACC, depending on the discount rate (a) or the electricity price evolution (b).

5.4.3 Minimization of the LCOE of ORCs

In this section, the results of the minimization of the levelized cost of electricity of ORCs powered with geothermal heat and cooled with an ACC or a WCT are given.

Influence of the brine-inlet temperature

The influence of the brine-inlet temperature on the levelized cost of electricity generation for ORCs with air cooling and water cooling are shown in figures 5.13a and 5.13b, respectively.

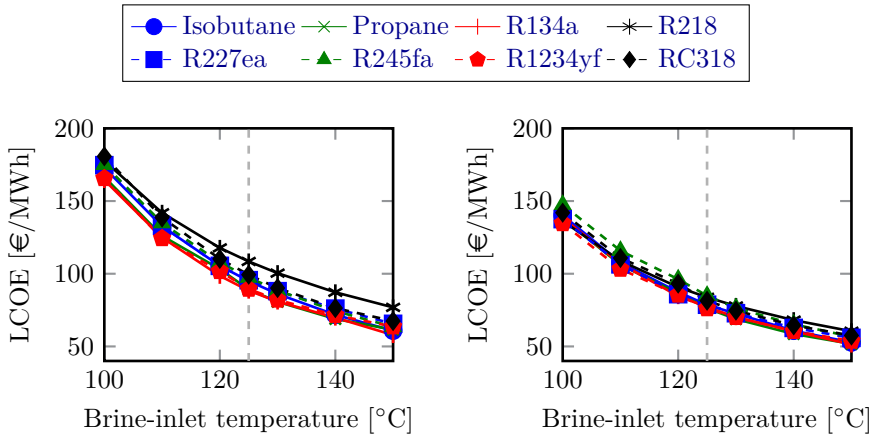

(a) Single-pressure recuperated cycle with ACC

(b) Single-pressure recuperated cycle with WCT

Figure 5.13: LCOE of a single-pressure recuperated ORC with an ACC (a) and a WCT (b) powered by geothermal heat, for various thermodynamic-cycle fluids and for varying inlet temperatures of the brine.

The LCOE decreases with increasing brine-inlet temperature as expected, influenced by the net electric power generated by the installation (figure 5.14) and thus the investment cost of the installation (specific cost of the ORCs are shown in figure 5.15). Clearly, the net electric power generation increases strongly with the brine-inlet temperature because of the increased plant efficiency, which results in a higher gross turbine power and lower cooling needs.

The comparison of figures 5.13a and 5.13b shows clearly that the LCOE for ORCs with a WCT is lower than the one for ORCs with an ACC, and especially

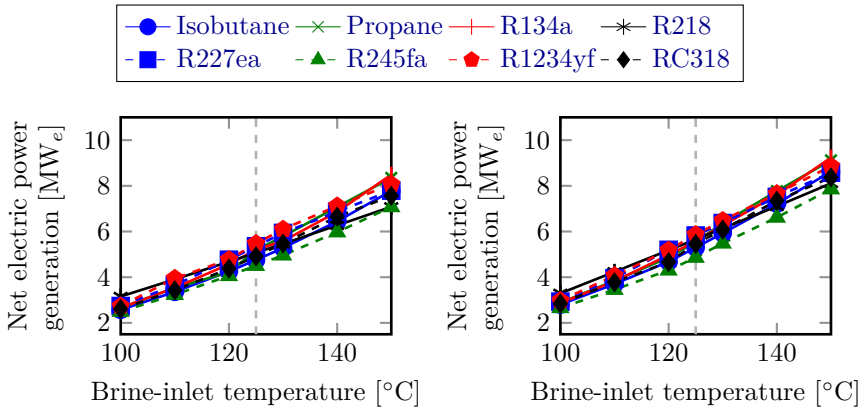

(a) Single-pressure recuperated cycle with ACC

(b) Single-pressure recuperated cycle with WCT

Figure 5.14: Net electric power generation of a single-pressure recuperated ORC with an ACC (a) and a WCT (b) powered by geothermal heat, for various thermodynamic-cycle fluids and for varying inlet temperature of the brine.

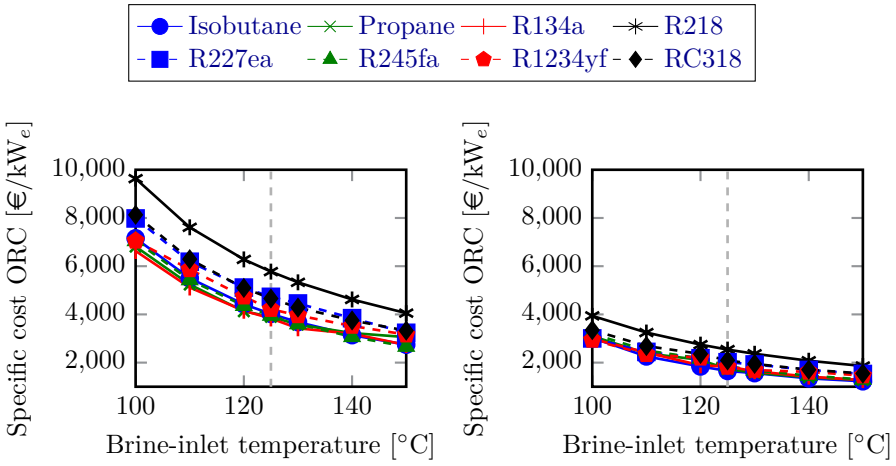

(a) Single-pressure recuperated cycle with ACC

(b) Single-pressure recuperated cycle with WCT

Figure 5.15: Specific cost of a single-pressure recuperated ORC with an ACC (a) and a WCT (b) powered by geothermal heat, for various thermodynamic-cycle fluids and for varying inlet temperature of the brine. Only the cost of the ORC is shown, the costs of the wells (27.5 M€) is not included.

for lower brine-inlet temperatures. The net electric power generation of ORCs with a WCT (figure 5.14b) is (slightly) higher than the one with an ACC (figure 5.14a) because of the lower condenser temperature and the lower auxiliary power consumption, but it is especially the lower (specific) investment cost which results in a better LCOE for the ORCs with a WCT. Indeed, the comparison of figures 5.15a and 5.15b shows that the specific cost of ORCs with a WCT is often less than 50% of the specific cost of ORCs with an ACC. This is caused by the high investment cost of an ACC.

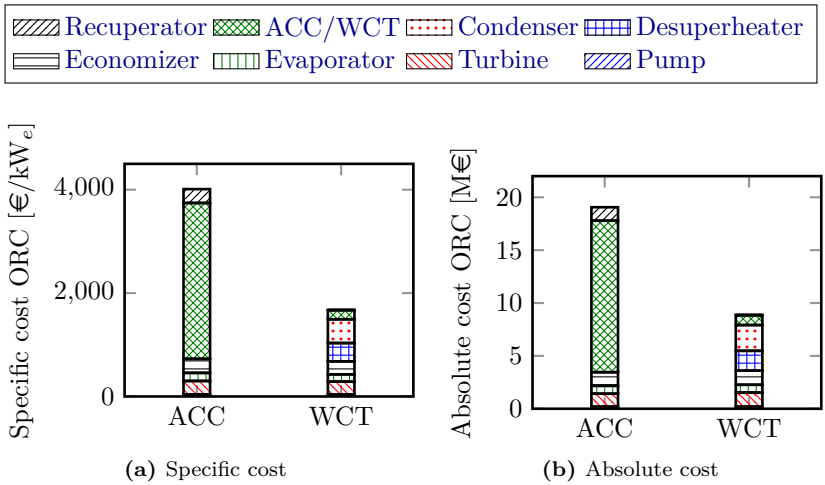

(a) Specific cost **(b)** Absolute cost

Figure 5.16: Distribution of the specific cost (a) and the absolute cost (b) for single-pressure simple and recuperated ORCs with isobutane as the working fluid for a brine-inlet temperature of 125°C. The cost of the superheater is very small in all cases and is not shown in the figure. Only the cost of the ORC is shown, the costs of the wells (27.5 M€) is not included.

Figures 5.16a and 5.16b show the distribution of the specific and absolute cost of an ORC with isobutane and a brine-inlet temperature of 125°C. Two big differences catch the eye. The first one is the very high cost of the ACC in comparison with the WCT. The cost of the ACC accounts for about 80% of the total cost of the ORC, while the cost of the WCT is about one third of the total cost if that option is chosen. The cost of the ORC accounts for 41% and 24% of the total project cost (including the costs of the wells) for air cooling and water cooling, respectively. The second notable result is the absence of a recuperator in the ORC with a WCT. The installation of a recuperator can decrease the cooling needs, which results in a lower investment and operational cost of the cooling installation. The extra cost of the recuperator is compensated by the

lower cost of the cooling system when an ACC is used, but not when a WCT is used.

Influence of the brine-outlet temperature

In this section the effect of a constraint on the brine-outlet temperature is investigated, although only electricity generation from the geothermal source is taken into account and direct use of the geothermal source for heating purposes is not considered.

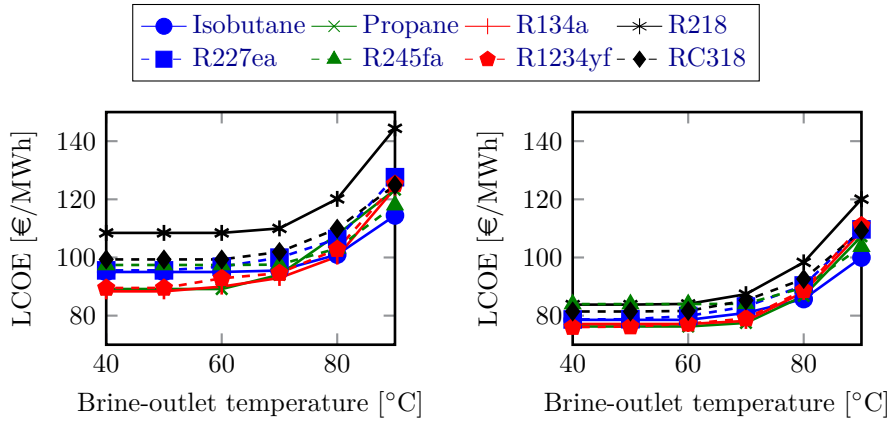

(a) Single-pressure recuperated cycle with ACC

(b) Single-pressure recuperated cycle with WCT

Figure 5.17: LCOE of a single-pressure recuperated ORC with an ACC (a) and a WTC (b) powered by geothermal heat, for various thermodynamic-cycle fluids and for varying outlet temperatures of the brine.

Figures 5.17a and 5.17b show the influence of the brine-outlet-temperature constraint on the LCOE for ORCs with an ACC and a WCT, respectively. The LCOE remains constant for both cooling methods up to a brine-outlet temperature of about 60-70°C, which is the optimal brine-outlet temperature when no constraint is used. For higher values of the constraint, the LCOE starts to increase and it becomes interesting to use a recuperator in all cases. Such a recuperator can increase the cycle efficiency and when the heat input to the cycle is limited (constraint on brine-outlet temperature), the net power output can also increase [122]. This last effect is more important than the increase in cost due to the extra heat exchanger.

Impact of 2 pressure levels

One way to improve the efficiency of a single-pressure ORC is by using more than one pressure level. In this section double-pressure ORCs are compared to single-pressure ones and the influence of the brine-inlet temperature is investigated.

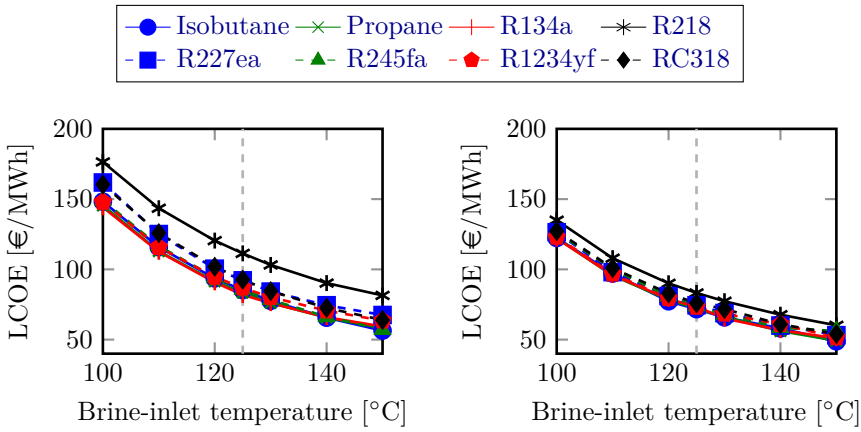

(a) Double-pressure recuperated cycle with ACC

(b) Double-pressure recuperated cycle with WCT

Figure 5.18: LCOE of a double-pressure recuperated ORC with an ACC (a) and a WCT (b) powered by geothermal heat, for various thermodynamic-cycle fluids and for varying inlet temperatures of the brine.

Figures 5.18a and 5.18b show the influence of brine-inlet temperature on the LCOE of double-pressure ORCs with an ACC and a WCT, respectively. Comparison with figure 5.13 shows that the LCOE of double-pressure cycles is considerably lower than the one of single-pressure cycles, because the net electric power output of the ORC can increase by adding another pressure level. This effect is more important than the additional cost of the extra pressure level.

Influence of the discount rate

A geothermal power plant requires a high investment in the beginning of the project and the revenues are obtained in the (far) future. The discount rate is therefore an important economic factor. In this section the discount rate is

varied between 0 and 10%, while using for all other parameters the reference value (table 5.4).

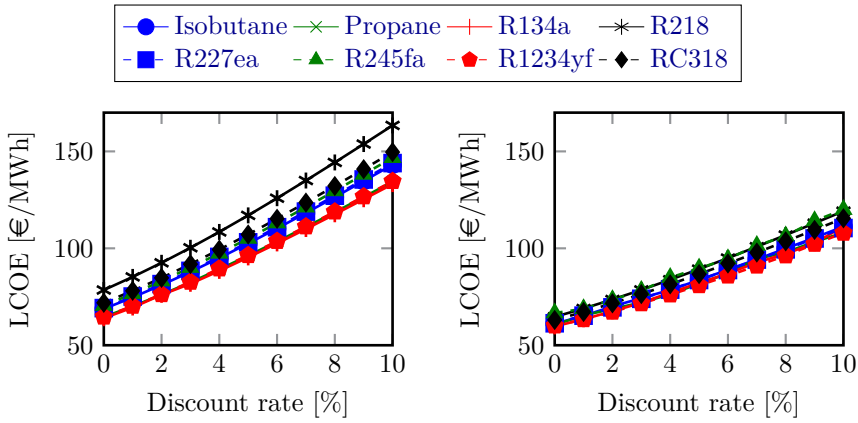

(a) Single-pressure recuperated cycle with ACC

(b) Single-pressure recuperated cycle with WCT

Figure 5.19: LCOE of a single-pressure recuperated ORC with an ACC (a) and a WTC (b) powered by geothermal heat, for various thermodynamic-cycle fluids and for varying discount rates.

As seen from figure 5.19, the value of the discount rate has a very strong influence on the LCOE, especially for ORCs cooled by an ACC. ORCs with an ACC require a higher investment cost than ORCs with a WCT (figure 5.15) and the effect of the discount rate is therefore more important if an ACC is used. For low values of the discount rate, the LCOE of an ORC with an ACC is only slightly higher than the one of an ORC with a WCT, while the difference is much larger for high values of the discount rate.

The results show that the optimal configuration of the power plant – and therefore also the net electric power output, investment cost, etcetera – is almost independent of the discount rate. This is again due to the high investment cost and the low operational cost. As seen from equation (5.8), minimizing the LCOE is almost equal to minimizing the fraction of the investment cost to the net electric power generation when the operational cost is low. Consequently, the discount rate influences only the value of the LCOE, but has almost no influence on the optimal configuration of the power plant.

Influence of the water price and yearly water-price evolution

A WCT consumes water and the water price and the yearly water-price evolution have therefore an influence on the economics of the power plant. These parameters have no effect on the performance of an ACC and only the results of ORCs with a WCT are therefore given in this section.

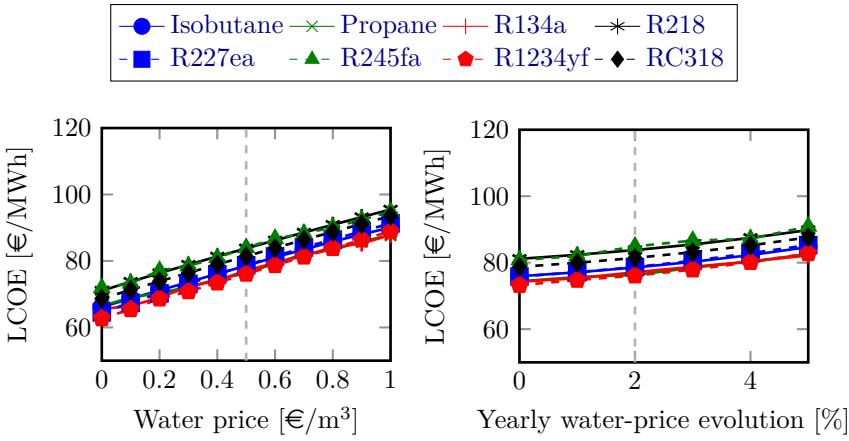

(a) Influence water price **(b)** Influence yearly water-price evolution

Figure 5.20: LCOE of a single-pressure recuperated ORC with a WTC powered by geothermal heat, for various thermodynamic-cycle fluids and for varying water price (a) and yearly water price evolution (b). The dashed vertical line represents the reference value of the water price.

Figures 5.20a and 5.20b show the influence of the water price and the yearly water-price evolution on the LCOE of the power plant. The LCOE increases as expected if water becomes more expensive (now and or in the future). Comparing figure 5.20a to figure 5.13a shows that ORCs with an ACC can become more interesting than ORCs with a WCT when water is expensive; in this reference case, if water were to cost more than 1€/m^3.

If water becomes more expensive, cooling in general costs more. To counteract this, the optimizer tries to reduce the water consumption by reducing the cooling needs and by consuming less water in the cooling tower. The first effect is obtained by increasing the cycle efficiency and by increasing the brine-outlet temperature. The drawbacks are that the plant efficiency, and therefore also the net power output, decreases slightly and that the investment cost increases. To reduce the water consumption in the cooling tower, the mass flow rate of cooling water is reduced. To compensate for the negative effect this has on

the performance of the ORC [121], the minimum cooling-water temperature is reduced. In order to obtain this, the height of the packing is increased, resulting in a higher investment cost and a higher pressure drop (auxiliary power consumption).

5.5 Conclusions

A system optimization of both air-cooled and water-cooled ORCs powered by geothermal heat is performed in this chapter. The cycle parameters of the ORC, the geometry of the heat exchangers and the geometry of the air-cooled heat exchanger or wet cooling tower are optimized together in order to obtain the maximum net present value or the minimum levelized cost of electricity of the installation. The isentropic efficiency of the turbine is calculated based on the fluid properties, the state before the turbine and the state exiting the turbine in case of an isentropic expansion.

5.5.1 Maximization of the NPV

It is shown that the brine-inlet temperature, the brine-outlet temperature, the electricity price, discount rate and electricity-price evolution have a strong influence on the net present value of the geothermal power plant. For cycles with dry fluids it is always useful to include a recuperator because this heat exchanger decreases the cooling load and adding a recuperator is cheaper than adding extra cooling over the lifetime of the power plant. A recuperator is advantageous for cycles with wet fluids only when the brine-outlet temperature is constrained.

The performance (thermodynamic and economic) of single-pressure subcritical cycles can improve by adding an extra pressure level. The lower the evaporation temperature in the single-pressure cycle, the higher the effect of this extra pressure level. The disadvantage is that both the absolute and relative cost of an ORC increase when adding an extra pressure level.

The air-cooled condenser is a very important component. It has a strong influence on the efficiency of the power plant through the condensing temperature and the power consumption of the fans and it accounts for a large part of the investment cost of the ORC (about 80% in the case study).

5.5.2 Minimization of the LCOE

Comparison of water cooling to air cooling in ORCs shows that the former type results in better economics, because of the increased net electric power output and especially because of the much lower investment cost. This higher investment cost for ACCs also results in a much higher impact of an increasing discount rate on the LCOE.

The difference between the two types of cooling decreases with increasing brine-inlet temperature. This is because the efficiency of the ORC increases and the cooling needs decrease (relatively speaking). Air cooling can become interesting if water is very expensive (more than 1€/m^3 in our reference case).

It is also shown that the addition of an extra pressure level can improve the economics and that a constraint on the brine-outlet temperature can have a negative influence on the economics of the electric power plant. For air-cooled ORCs with dry fluids, a recuperator is always useful. For the other types of cycles, a recuperator only becomes interesting when the constraint on the brine-outlet temperature is high enough.

The results in this chapter also show that a binary geothermal power plant is not economically interesting for the assumptions made and for the current electricity price. Selling heat is necessary to improve the economics of the investigated geothermal project, but it is also necessary that the heat is demanded at a relatively low temperature, so that the electricity generating system is influenced not too strongly by the heat delivering system.

Chapter 6

Summarizing conclusions and recommendations

The main conclusions of this work are summarized in this chapter. The developed model, with which an economic system optimization of organic Rankine cycles can be performed, is the main achievement of this research. This model can be the basis of a numerical tool to improve the economics of a low-temperature geothermal project. Some recommendations for further research are given in the second part of this chapter.

6.1 Summary and conclusions

Low-temperature geothermal heat sources are widely available, but the efficiency of binary power plants is often low and the costs of the plants are high. To increase the electricity generation from these low-temperature heat sources, it is important to develop power plants with the optimum ratio between efficiency and cost.

6.1.1 Thermodynamic optimization

First, different thermodynamic cycles are modeled and optimized to find the cycles with the highest thermodynamic efficiency. In a first instance, components are assumed to be ideal or modeled very simplistically.

Many different efficiencies can be defined and used to describe the performance of binary power plants. For geothermal power plants, it is important to look at the *plant* efficiency. This efficiency takes both the plant effectiveness and the *cycle* efficiency into account. To achieve a high plant efficiency, the brine should be cooled down as far as possible (high plant effectiveness) and the heat added to the cycle should be converted to electrical power as efficiently as possible (high cycle efficiency).

Two types of binary power plants are investigated for brine-inlet temperatures between 100 and 150°C: different configurations of the organic Rankine cycle (ORC) and the Kalina cycle. More complex ORCs, like transcritical and multi-pressure subcritical ones, are in most cases more efficient than the Kalina cycle. Only for high brine-outlet temperatures, the plant efficiency of the Kalina cycle is comparable to the one of the best ORCs.

The addition of a recuperator or turbine bleeding can increase the *cycle* efficiency, but only improves the *plant* efficiency when high brine-outlet temperatures are necessary.

The efficiency of ORCs is strongly dependent on the used working fluid. Fluids with a low critical temperature perform the best in transcritical cycles, but in multi-pressure subcritical cycles fluids with high critical temperatures are the better choice.

The pinch-point-temperature differences in the heat exchangers and the condenser temperature have a very strong influence on the performance of binary cycles. The temperature difference between the brine-inlet temperature and the ambient temperature is low, so every small (in absolute terms) change on the available temperature range is relatively speaking already an important change. This shows that making rough estimations about the values of the pinch-point-temperature differences and the condenser temperature can result in a strongly sub-optimal configuration. It is therefore important to include these parameters in the optimization.

6.1.2 Comparison of heat-exchanger types

Because of the importance of the pinch-point-temperature differences in the heat exchangers, in a next step models for both plate heat exchangers and shell-and-tube heat exchangers are implemented. A system optimization is performed, which means that the configuration of the binary cycles is optimized together with the configuration of the heat exchangers. In this way, the heat exchangers are optimal to work together and to work in the obtained cycle. Pinch-point-temperature differences are a result of the optimization, so no

assumptions have to be made about their values. Only ORCs are investigated due to the lack of transport properties for mixtures.

For the shell-and-tube heat exchangers, it is concluded that it is best to use the 30°-tube configuration for the single-phase heat exchangers and the 60°-tube configuration for the two-phase heat exchangers. This combined configuration is optimal for all investigated cases and is used for the comparison with plate heat exchangers.

ORCs with all plate heat exchangers perform in most cases better than ORCs with all shell-and-tube heat exchangers. Sometimes, "problems" can occur in plate heat exchangers. The geometry of both sides of a plate heat exchanger with an equal number of passes is exactly the same, which can lead to inefficient heat exchangers when the fluids on both sides have very "different" properties. This is especially the case for the condenser.

Also in this first step towards a system optimization, it is shown that the cooling system is very important and should be modeled in detail.

6.1.3 Economic optimization

In a further step, the cooling system is looked at and models for an air-cooled condenser (ACC) and a wet cooling tower (WCT) are added and an economic system optimization is performed. Two objective functions are used: the maximization of the net present value (NPV) of the power plant and the minimization of the levelized cost of electricity (LCOE).

The comparison of both types of cooling shows that water cooling results in better economics, especially because of the much lower investment cost of the installation. Due to the higher investment cost of ACCs, the influence of the discount rate is much stronger for air-cooled than for water-cooled power plants.

The lower the brine-inlet temperature, the larger the difference between cooling with air and cooling with water. Cycle efficiencies are low at low inlet temperatures, which results in high cooling needs, thus in a large cooling system and in much electric auxiliary power consumption. Only for high water prices (more than 1€/m^3), air cooling can become more interesting than water cooling for the investigated case.

In contrast to the thermodynamic results, a recuperator is always useful for air-cooled ORCs with dry fluids. This is because a recuperator can reduce the size, and thus the cost, of the ACC. This reduction is bigger than the extra cost of the recuperator, which is not the case for water-cooled ORCs.

A geothermal power plant, generating only electricity, is economically not interesting for the assumptions made and the current electricity price. Selling heat can improve the economics of a project, but it is important that the heat is demanded at a low temperature, so that the influence of the heat delivering system on the electricity generating system is limited.

6.2 Recommendations for future research

A steady-state, economic design optimization of organic Rankine cycles can be performed with the developed model. Three groups of improvements of the current model can be distinguished: better component models, optimization of a dynamic system and the extension of working fluids. The combination of the current above-surface model with existing sub-surface models is also promising.

6.2.1 Component models

In this work, most of the components are modeled with mature correlations. Especially the Bell-Delaware method [50], the Poppe theory [95] and the correlation of Martin [74] are widely applicable, used and accepted, but these correlations, can of course, still be improved. More work has to be done to develop universally applicable models for two-phase flows in heat exchangers in general and plate heat exchangers in particular.

For some components, only a small number of experimental data seems to exist, so more experiments are definitely needed. It is also important that the set-up of the experiments and the definition of non-dimensional numbers are clearly described and that the obtained measurements are also available to other researchers. If these conditions are met, it is possible to combine the experimental data of different authors to develop new correlations. This last step is not an easy one, because the correlations should be based on a physical model and the experimental data should be used to find the value of some correlating parameters.

More and more simulations and optimizations of components are done by using CFD. Often these models are too slow to be used in a system, but the models themselves can be very accurate. A CFD model, which is validated by a limited number of experiments, can be used to simulate a large number of cases. The results of these cases could in turn be used to develop simple and less accurate, but more applicable correlations. It would then be possible to use these developed correlations in the first steps of the design of a component or a

system and the CFD model in the final step of the design. In this way, the low calculation time of the empirical correlations can be combined with the high accuracy of CFD models.

A different way to improve the component models is a cooperation with industry. Companies, which construct or use these components, have experience with them and probably have more accurate models than available in the open scientific literature and have a large amount of experimental data. Cooperation with industry can improve the used component models.

The pumps and fans used in binary plants are modeled very simplistically in this work. A fixed isentropic efficiency is assumed, but this assumption can have a strong impact on the performance of the power plant, definitely for the fans in air-cooled condensers; these fans consume 10-15% of the electric power output of the turbine with the assumption of an efficiency of 60% for the fans. It would be better to implement models which predict the efficiency of these components based on their geometry. Such detailed models do not seem to exist in the open literature. The same applies to models of other types of turbines.

The cost correlations used in this work are relatively simple and are useful for first-order estimations. More detailed cost functions are necessary for industrial applications. Economic optimizations with plate heat exchangers have not been performed due to the lack of cost correlations for large plate heat exchangers. The thermodynamic optimizations have shown that plate heat exchangers perform mostly better, so it would also be interesting to perform an economic comparison between plate and shell-and-tube heat exchangers for the use in ORCs.

6.2.2 Dynamic CHP-plant

A steady-state system optimization is performed in this work. In case of a combined heat and power plant (CHP), the heat demand is generally not constant and adaptations have to be made so that dynamic simulations and optimizations are possible. The time constant of an ORC is low (minutes) and much lower than the one of a district heating network, so it can be assumed that the ORC always works at steady state. These steady-state points will often not be the design point and part-load models are needed. So, two main issues have to be tackled to model and optimize a dynamic CHP-plant: the part-load behavior of the components and the adaptations to the optimization.

In our work, the turbine has been modeled by using the work of Macchi and Perdichizzi [69], which gives the optimal efficiency of a turbine stage in its optimal working point. This model does not give the part-load behavior of

the turbine and can therefore not be used for a dynamic calculation. The full model of Craig and Cox [25] should be implemented, because this model allows for part-load calculations. The disadvantage is that this detailed model is much harder to implement, requires a longer calculation time and results in a high number of optimization variables (blade geometry, rotational speed, rotor diameter, etcetera). Also for the other components, part-load models should be implemented.

The optimization problem should be redefined too. A reference year (weather data from databases like IWEC [55] can be used) has to be defined and it has to be divided in a representative number of time intervals, so that the system can be assumed to be in steady state in such a time interval. The goal of the optimization is to find the optimal design and optimal control parameters of the system in order to maximize the income of the power plant. The number of optimization variables will increase strongly, not only due to the increased complexity of the component models, but also due to the addition of extra control variables. The mass flow rate of the working fluid, the mass flow rate of the cooling fluid, the rotational speed of the fans, etcetera, can all be different in every time interval.

The higher number of optimization variables in itself will not result in higher calculation times because of the use of automatic differentiation in reverse mode, but the more complex models and increased number of time intervals do. Instead of calculating the output of the power plant once, it should be done for every time interval. This means that the calculation time increases at least with a factor equal to the number of intervals.

Another issue is that the size of the heat exchangers, of the wet cooling tower and of the air-cooled condenser are results of the developed code. This means that, if the structure of the code would remain the same, a large number of non-linear equality constraints are needed: the size of all the components has to be equal in all time intervals. These equality constraints will probably have a very strong impact on the stability and the calculation time of the optimization routine and it should be better to avoid them.

6.2.3 Fluids and mixtures

As already mentioned in chapter 1, the use of mixtures is one of the proposed ways to improve the efficiency of binary power plants. Mixtures with a high temperature glide while evaporating and condensing are the most promising ones, but this not the case for most refrigerant or hydrocarbon mixtures. Unfortunately, RefProp, which is *the* reference program concerning fluid properties, can only handle a limited number of mixtures and often the

correlations are not numerically stable. In the new version of RefProp, more mixtures have been added and attention is paid to the stability of the correlations.

An important issue in geothermal power plants is the fouling and corrosion of equipment due to the high salinity of the brine. The developed model predicts the pressure and temperature evolution of the brine in the heat exchangers, so this information could be used to predict the amount of fouling and corrosion occurring in the heat exchangers.

6.2.4 Connection between sub-surface and above-surface design

The sub-surface part of the geothermal power plants is currently assumed to be given, but there is, of course, an interaction between the sub-surface part and the above-surface equipment. The brine mass flow rate will probably have an influence on the brine-inlet temperature of the power plant and on the economic lifetime of the system, but it is important that the design is performed according to the sustainability criterion. This sustainability criterion implies that the production rate has to be maintained for a very long time [8]. The sustainable production rate does probably depend on the brine-reinjection temperature, if the sustainable production potential is limited by energy-content rather than pressure decline.

So, if the sustainable mass flow rate is influenced by the brine-reinjection temperature, it could be better to optimize the sub-surface and above-surface parts together. Also the diameters of the wells, which have a strong influence on the cost of the drilling, can be taken into account in this optimization. The diameters also have an influence on the temperature loss of the brine in the wells and on the pressure drop in the wells. Such a full system optimization would probably result in high computational times. Because of the relatively limited amount of connecting parameters between the sub-surface and above-surface parts, it is perhaps better to set up a table with the brine-production temperature, the sustainable mass flow rate and the pumping power of the well pumps as a function of the brine-reinjection temperature and the well diameters.

This overview shows that still a lot of work can be done to improve the economics of low-temperature geothermal power plants. The research challenges are situated in very different domains, ranging from component engineering over power-plant engineering to chemical thermodynamics. And the geological challenges have not even been mentioned.

Appendix A

Heat-exchanger correlations

This appendix contains the correlations used to calculate the pressure drop and heat-transfer coefficient in shell-and-tube and plate heat exchangers. Correlations for single-phase flow, condensation and evaporation are given.

A.1 Shell-and-tube

The undermentioned equations are valid for TEMA E shell-and-tube heat exchangers with one tube pass.

A.1.1 Geometry

The equations to calculate the important geometrical parameters of a shell-and-tube heat exchanger are stated in this section. More information can be found in the literature [50, 104], on which this section is based.
The diameter of the outermost tubes D_{otl} and the diameter of the circle through the center of the outermost tubes D_{ctl} are given by:

$$D_{otl} = D_s - \delta_{bb}, \tag{A.1}$$

$$D_{ctl} = D_{otl} - d_o, \tag{A.2}$$

with δ_{bb} the diametrical shell-to-tube bundle bypass clearance, which can be estimated as $\delta_{bb} = 0.017 D_s + 0.0265$ [m] [50]. The remaining two parameters in

figure 4.2 are calculated as:

$$\theta_b = 2\cos^{-1}\left(1 - \frac{2l_c}{D_s}\right), \tag{A.3}$$

$$\theta_{ctl} = 2\cos^{-1}\left(\frac{D_s - 2l_c}{D_{ctl}}\right). \tag{A.4}$$

The number of tubes N_t in a shell without impingement plates and a single tube pass is:

$$N_t = \frac{\pi/4 D_{ctl}^2}{C_t p_t^2}, \tag{A.5}$$

with C_t a constant which depends on the tube bundle configuration. Parameters for the four most used tube bundle configurations as suggested in figure A.1 are given in table A.1.

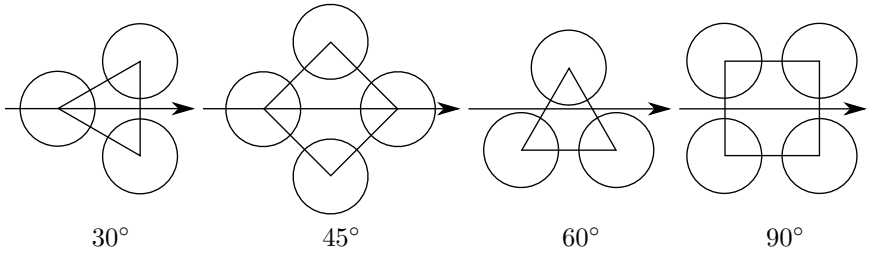

Figure A.1: Tube layout patterns. Figure based on Mukherjee [82].

	Staggered array			Inline array
	30°	45°	60°	90°
Transverse tube pitch X_t	p_t	$\sqrt{2}p_t$	$\sqrt{3}p_t$	p_t
Longitudinal tube pitch X_l	$\frac{\sqrt{3}}{2}p_t$	$\frac{p_t}{\sqrt{2}}$	$\frac{p_t}{2}$	p_t
Tube count constant C_t	$\frac{\sqrt{3}}{2}$	1	$\frac{\sqrt{3}}{2}$	1

Table A.1: Geometrical properties of some tube banks. Table adapted from Shah and Sekulić [104].

The gross window area $A_{fr,w}$, the fraction of the number of tubes in one window section F_w, the area occupied by tubes in the window section $A_{fr,t}$, the net flow area in one window section $A_{o,w}$, the hydraulic diameter of the window section $D_{h,w}$ and the number of effective tube rows in cross flow in the window

section $N_{r,cw}$ are given by:

$$A_{fr,w} = \frac{D_s^2}{4}\left[\frac{\theta_b}{2} - \left(1 - \frac{2l_c}{D_s}\right)\sin\frac{\theta_b}{2}\right], \tag{A.6}$$

$$F_w = \frac{\theta_{ctl}}{2} - \frac{\sin\theta_{ctl}}{2\pi}, \tag{A.7}$$

$$A_{fr,t} = \frac{\pi}{4} d_o^2 F_w N_t, \tag{A.8}$$

$$A_{o,w} = A_{fr,w} - A_{fr,t}, \tag{A.9}$$

$$D_{h,w} = \frac{4A_{o,w}}{\pi d_o F_w N_t + D_s\theta_b/2}, \tag{A.10}$$

$$N_{r,cw} = \frac{0.8}{X_l}\left[l_c - 0.5(D_s - D_{ctl})\right]. \tag{A.11}$$

The fraction of the number of tubes in the cross-flow section F_c, the number of tube rows crossed in one cross-flow section $N_{r,cc}$ and the cross-flow area at the shell center line $A_{o,cr}$ can be calculated as:

$$F_c = 1 - 2F_w, \tag{A.12}$$

$$N_{r,cc} = \frac{D_s - 2l_c}{X_l}, \tag{A.13}$$

$$A_{o,cr} = \left[D_s - D_{otl} + \frac{D_{ctl}}{X_t}(X_t - d_o)\right] L_{b,c}, \tag{A.14}$$

$$A_{o,cr} = \left[D_s - D_{otl} + 2\frac{D_{ctl}}{X_t}(p_t - d_o)\right] L_{b,c}. \tag{A.15}$$

The first expression for $A_{o,cr}$ is valid for 30°- and 90°-tube configurations and for 45°- and 60°-tube configurations with a high pitch. The second expression is valid for 45°- and 60°-tube configurations with a low pitch.

The flow area for bypass stream C (section 4.1.2) F_{bp}, the total tube-to-baffle leakage area for one baffle $A_{o,tb}$ and the shell-to-baffle leakage area $A_{o,sb}$ are

given by:

$$F_{bp} = \frac{(D_s - D_{otl})L_{b,c}}{A_{o,cr}}, \tag{A.16}$$

$$A_{o,tb} = \frac{\pi}{4}\left[(d_o + \delta_{tb})^2 - d_o^2\right] N_t(1 - F_w), \tag{A.17}$$

$$A_{o,sb} = \pi D_s \frac{\delta_{sb}}{2}\left(1 - \frac{\theta_b}{2\pi}\right), \tag{A.18}$$

with $\delta_{tb} = 0.4\ 10^{-3}$ [m] the diametrical clearance and $\delta_{sb} = 3.1\ 10^{-3} + 0.004 D_s$ [m] the shell-to-baffle clearance as given by TEMA standards [50].

A.1.2 Single-phase heat transfer and pressure drop

Shell side

The ideal heat-transfer coefficient on the shell-side in inline tube bundles (90° configurations) is given by [104]:

$$h_{single}^{id,shell} = \frac{k}{D_h} 0.404 Lq^{1/3} \left(\frac{Re_s + 1}{Re_s + 1000}\right)^{0.1}, \tag{A.19}$$

$$Lq = 1.18 Hg\ Pr \left(\frac{(4X_t^*/\pi) - 1}{X_l^*}\right), \tag{A.20}$$

$$Hg = Hg_{lam} + Hg_{turb,i}\left[1 - \exp\left(1 - \frac{Re_s + 1000}{2000}\right)\right], \tag{A.21}$$

$$Hg_{lam} = 140 Re_s \frac{(X_l^{*0.5} - 0.6)^2 + 0.75}{X_t^{*1.6}(4X_t^* X_l^*/\pi - 1)}, \tag{A.22}$$

$$Hg_{turb,i} = \left[\begin{array}{l} \left(0.11 + \frac{0.6(1-0.94/X_l^*)^{0.6}}{(X_t^* - 0.85)^{1.3}}\right) 10^{0.47(X_l^*/X_t^* - 1.5)} + \\ 0.015(X_t^* - 1)(X_l^* - 1) \end{array}\right] \times ...$$

$$...Re_s^{2-0.1(X_l^*/X_t^*)} + \phi_{t,n} Re_s^2, \tag{A.23}$$

$$v_m = v_\infty \frac{X_t^*}{X_t^* - 1}, \tag{A.24}$$

with k the thermal conductivity of the fluid, Lq the Lévêque number, Hg the Hagen number, Pr the Prandtl number, v_∞ the free stream velocity, $\phi_{t,n}$ a correction factor for tube bundle inlet and outlet pressure drops and Re_s the Reynolds number in the shell. These last two parameters are calculated as:

$$\phi_{t,n} = \begin{cases} \frac{1}{2X_t^{*2}}\left(\frac{1}{N_r} - \frac{1}{10}\right) & \text{for } 5 \leq N_r \leq 10 \text{ and } X_l^* \geq 0.5(2X_t^* + 1)^{1/2} \\ 2\left[\frac{X_d^* - 1}{X_t^*(X_t^* - 1)}\right]^2 \left(\frac{1}{N_r} - \frac{1}{10}\right) & \text{for } 5 \leq N_r \leq 10 \text{ and } X_l^* < 0.5(2X_t^* + 1)^{1/2} \\ 0 & \text{for } N_r > 10 \end{cases}, \tag{A.25}$$

$$Re_s = \frac{\rho v_m d_o}{\mu}. \tag{A.26}$$

X_l^*, X_t^* and X_d^* are dimensionless parameters, obtained by dividing X_l, X_t and $X_d = \sqrt{X_l^2 + X_t^2}$ by d_o, respectively. ρ is the density and μ the dynamic viscosity.

For staggered tube bundles (30, 45 and 60° configurations), the correlations are [104]:

$$h_{single}^{id,shell} = \frac{k}{D_h} 0.404 Lq^{1/3}, \tag{A.27}$$

$$Lq = \begin{cases} 0.92 Hg\ Pr \left(\frac{(4X_t^*/\pi)-1}{X_d^*} \right) & \text{for } X_l^* \geq 1 \\ 0.92 Hg\ Pr \left(\frac{(4X_t^* X_l^*/\pi)-1}{X_l^* X_d^*} \right) & \text{for } X_l^* < 1 \end{cases}, \tag{A.28}$$

$$Hg = Hg_{lam} + Hg_{turb,s} \left[1 - \exp\left(1 - \frac{Re_s + 200}{1000} \right) \right], \tag{A.29}$$

$$Hg_{lam} = \begin{cases} 140 Re_d \frac{(X_l^{*0.5} - 0.6)^2 + 0.75}{X_t^{*1.6}(4X_t^* X_l^*/\pi - 1)} & \text{for } X_l^* \geq 0.5(2X_t^2 + 1)^{1/2} \\ 140 Re_d \frac{(X_l^{*0.5} - 0.6)^2 + 0.75}{X_d^{*1.6}(4X_t^* X_l^*/\pi - 1)} & \text{for } X_l^* < 0.5(2X_t^2 + 1)^{1/2} \end{cases}, \tag{A.30}$$

$$Hg_{turb,shell} = \left[\begin{array}{l} \left(1.25 + \frac{0.6}{(X_t^* - 0.85)^{1.08}} \right) + \\ 0.2 \left(\frac{X_l^*}{X_t^*} - 1 \right)^3 - 0.005 \left(\frac{X_t^*}{X_l^*} - 1 \right)^3 \end{array} \right] \times$$

$$Re_s^{1.75} + \phi_{t,n} Re_s^2, \tag{A.31}$$

$$Hg_{turb,shell,corr} = Hg_{turb,shell} \left(1 + \frac{Re_s - 250\ 000}{325\ 000} \right), \tag{A.32}$$

$$v_m = \begin{cases} v_\infty \frac{X_t^*}{X_t^* - 1} & \text{for } X_l^* \geq 0.5(2X_t^* + 1)^{1/2} \\ v_\infty \frac{X_t^*}{2(X_d^* - 1)} & \text{for } X_l^* < 0.5(2X_t^* + 1)^{1/2} \end{cases}. \tag{A.33}$$

The pressure drop in an ideal cross-flow section $\Delta p_{b,id}$ between two baffles and in an ideal window-flow section $\Delta p_{w,id}$ are given by:

$$\Delta p_{b,id} = \frac{\mu^2}{\rho} \frac{N_{r,cc}}{d_o^2} Hg, \tag{A.34}$$

$$\Delta p_{w,id} = \begin{cases} (2 + 0.6 N_{r,cw}) \frac{G_w^2}{2\rho} & \text{for } Re_s > 100 \\ \frac{26 G_w \mu}{\rho} \left(\frac{N_{r,cw}}{p_t - d_o} + \frac{L_b}{D_{h,w}^2} \right) + \frac{G_w^2}{\rho} & \text{for } Re_s \leq 100 \end{cases}, \tag{A.35}$$

with G_w the mass velocity in the window section:

$$G_w = \frac{\dot{m}}{\sqrt{A_{o,cr} A_{o,w}}}, \tag{A.36}$$

and $\dot{m}$ the mass flow of the fluid. The hydrostatic pressure drop is neglected because the shell-side fluid flows alternately up and down and the hydrostatic pressure drop is therefore alternately positive and negative. Both are about equal and can therefore be neglected.

Tube side

The correlation of Petukhov and Popov [93] is used to calculate the single phase heat-transfer coefficient in the tubes. The friction coefficient is calculated by the correlation of Bhatti and Shah [14].

A.1.3 Heat transfer and pressure drop while evaporating

The boiling heat-transfer coefficient for evaporation on the shell-side is given by [50]:

$$h_{evap}^{id,shell} = h_{nb}F_b + h_{nc}, \tag{A.37}$$

with h_{nb} the nucleate boiling coefficient, F_b a correction factor for the effect of convection and h_{nc} the natural convection heat-transfer coefficient, which is about 250 W/m^{2}K for hydrocarbons. The other parameters are given as [50]:

$$h_{nb} = 0.00417 p_c^{0.69} \dot{q}^{0.7} F_p, \tag{A.38}$$

$$F_p = 0.7 + 2p_r \left(4 + \frac{1}{1-p_r}\right), \tag{A.39}$$

$$F_b = 1 + 0.1 \left[\frac{0.785 D_{otl}}{C_t (p_t/d_o)^2 d_o} - 1\right]^{0.75}, \tag{A.40}$$

where p_c is the critical pressure of the fluid, $\dot{q}$ the heat flux and $p_r = p/p_c$ the reduced pressure.

The frictional, ideal pressure drop is given as [50]:

$${}^{fr}\Delta p_{evap}^{id,shell} = \left(1 + (Y^2 - 1)\left[B x^{(2-n)/2}(1-x)^{(2-n)/2} + x^{2-n}\right]\right)_{lo}^{fr} \Delta p_{single}^{id,shell} \tag{A.41}$$

where ${}_{lo}^{fr}\Delta p_{single}^{shell}$ is the frictional, ideal pressure drop in the shell if all the fluid was saturated liquid, $Y^2 = {}_{lo}^{fr}\Delta p_{id,single}^{shell} / {}_{vo}^{fr}\Delta p_{single}^{id,shell}$ the Chisholm parameter and x the quality of the fluid. For the cross flow $B = 1$ and $n = 0.37$, while for the window flow $B = (\rho_h/\rho_l)^{1/4}$ and $n = 0$. ρ_h is the homogeneous flow density,

given as:

$$\rho_h = \frac{1}{\frac{1-x}{\rho_l} + \frac{x}{\rho_v}} \tag{A.42}$$

The subscripts l and v refer to saturated liquid and vapor, respectively. The acceleration pressure drop is [50]:

$${}^{ac}\Delta p_{evap}^{id,shell} = G^2 \left(\frac{(1-x)^2}{\rho_l(1-\alpha)} + \frac{x^2}{\rho_v \alpha} \right)_{out} - \left(\frac{(1-x)^2}{\rho_l(1-\alpha)} + \frac{x^2}{\rho_v \alpha} \right)_{in}, \tag{A.43}$$

with $\alpha = 1/(1 + \frac{1-x}{x}\frac{\rho_v}{\rho_l})$ the void fraction as calculated for a homogeneous flow [50].

A.1.4 Heat transfer and pressure drop while condensing

The heat-transfer coefficient for condensation on the shell-side is given by [50]:

$$h_{cond}^{id,shell} = \frac{k}{d_o} K \left(\chi^4 Re_{lv}^2 + Nu_f^4 \right)^{1/4}, \tag{A.44}$$

with

$$Nu_f^4 = 0.276 \left[\frac{d_o^3 \rho_l (\rho_l - \rho_v) g (h_v - h_l)}{\mu_l k_l (T_{sat} - T_w)} \right], \tag{A.45}$$

$$\chi = 0.9 \left(1 + \frac{1}{RH} \right)^{1/3}, \tag{A.46}$$

$$R = \left(\frac{\rho_l \mu_l}{\rho_g \mu_g} \right)^{1/2}, \tag{A.47}$$

$$H = \frac{c_{p,l}(T_{sat} - T_w)}{Pr_l (h_v - h_l)}, \tag{A.48}$$

$$Re_{lv} = \frac{d_o \frac{\dot{m} x}{L_{bc} D_s} \rho_l}{\mu_l \rho_v}, \tag{A.49}$$

where h is the specific enthalpy and c_p the heat capacity at constant pressure. The two-phase pressure drop is calculated by the same correlations as given for the evaporator.

A.2 Plate heat exchanger

The undermentioned equations are valid for plate heat exchangers with chevron/herringbone corrugations with an equal number of passes on each side of the heat exchanger.

A.2.1 Single-phase heat transfer and pressure drop

The model of Martin [74] is used to calculate the pressure drop and heat-transfer coefficient in chevron-type plate heat exchangers for single-phase flows. The frictional-pressure drop for single-phase flow in one plate is given by:

$$\left[\Delta p_{single}^{plate}\right]_{fr} = 4\frac{f_{single}^{plate} L_p}{D_h}\frac{G^2}{2\rho}, \tag{A.50}$$

with f_{single}^{plate} the Fanning friction factor, $G = \frac{\dot{m}}{2aWN_p}$ the mass velocity and N_p the number of channels. The Fanning friction factor is given by:

$$\frac{1}{\sqrt{f_{single}^{plate}}} = \frac{\cos\beta}{\left(0.045\tan\beta + 0.09\sin\beta + \frac{f_0}{\cos\beta}\right)^{0.5}} + \frac{1-\cos\beta}{\sqrt{3.8 f_1}}, \tag{A.51}$$

with f_0 the Fanning friction coefficient if $\beta = 0°$ and f_1 the Fanning friction coefficient if $\beta = 90°$. These coefficients are given by:

$$f_0 = \begin{cases} \frac{16}{Re} & \text{for } Re < 2000 \\ (1.56\ln Re - 3.0)^{-2} & \text{for } Re \geq 2000 \end{cases}, \tag{A.52}$$

$$f_1 = \begin{cases} \frac{149.25}{Re} + 0.9625 & \text{for } Re < 2000 \\ \\ \frac{9.75}{Re^{0.289}} & \text{for } Re \geq 2000 \end{cases}, \tag{A.53}$$

where $Re = \frac{GD_h}{\mu}$ is the Reynolds number.

The hydrostatic-pressure drop is neglected because the fluids flow alternately up and down and the hydrostatic pressure drop is therefore alternately positive and negative. Both are about equal and can therefore be assumed to neutralize each other.

The heat-transfer coefficient is calculated as:

$$h = \frac{k}{D_h} 0.205 Pr^{1/3} \left(\frac{\mu_m}{\mu_w}\right)^{1/6} (f_{single}^{plate} Re^2 \sin 2\beta)^{0.374}, \tag{A.54}$$

with μ_m the viscosity of the bulk fluid and μ_w the viscosity of the fluid at the wall. The difference between these viscosities is neglected. Pr is the Prandtl number.

A.2.2 Heat transfer and pressure drop while evaporating

Han, Lee, and Kim [46] developed correlations for the pressure drop and heat transfer in chevron-type plate heat exchangers during *evaporation*. The frictional pressure drop in one plate during evaporation is:

$$\left[\Delta p_{evap}^{plate}\right]_{fr} = 4\frac{f_{evap}^{plate} L_p}{D_h}\frac{G_{eq}^2}{2\rho_l}, \tag{A.55}$$

with G_{eq} the equivalent mass velocity, defined as:

$$G_{eq} = G\left[1 - x + x\left(\rho_l/\rho_v\right)^{1/2}\right], \tag{A.56}$$

where ρ_l and ρ_v are the densities of saturated liquid and saturated vapor, respectively.
The correlation for the Fanning friction factor is given by:

$$f_{evap}^{plate} = c_1 Re_{eq}^{c_2}, \tag{A.57}$$

with

$$c_1 = 64\ 710\left(\frac{\Lambda}{D_h}\right)^{-5.27}\beta^{-3.03}, \tag{A.58}$$

$$c_2 = -1.314\left(\frac{\Lambda}{D_h}\right)^{-0.62}\beta^{-0.47}, \tag{A.59}$$

$$Re_{eq} = \frac{G_{eq} D_h}{\mu_l}. \tag{A.60}$$

The acceleration pressure drop is given by:

$${}^{ac}\Delta p_{evap}^{plate} = \left(\frac{G_{eq}^2 x}{\rho_l - \rho_v}\right)_{out} - \left(\frac{G_{eq}^2 x}{\rho_l - \rho_v}\right)_{in}. \tag{A.61}$$

The heat-transfer coefficient is correlated as:

$$h = \frac{k}{D_h} c_3 Re_{eq}^{c_4} Bo_{eq}^{0.3} Pr_l^{0.4}, \tag{A.62}$$

with:

$$c_3 = 2.81 \left(\frac{\Lambda}{D_h}\right)^{-0.041} \beta^{-2.83}, \tag{A.63}$$

$$c_4 = 0.746 \left(\frac{\Lambda}{D_h}\right)^{-0.082} \beta^{0.61}, \tag{A.64}$$

$$Bo_{eq} = \frac{\dot{q}}{G_{eq}(h_v - h_l)}. \tag{A.65}$$

Bo_{eq} is the equivalent boiling number.

The experiments performed by Han, Lee, and Kim [46] were done for $\beta =$ 45, 55 and 70°, $G = 13$ - 34 kg/m^{2}s and a heat flux of 2.5 - 8.5 kW/m^2, while using R22 and R410a as working fluids.

A.2.3 Heat transfer and pressure drop while condensing

The correlations for the pressure drop and the heat-transfer coefficient while *condensing* are given by Han, Lee, and Kim [47] and are analogous to the ones for the evaporation, albeit with differently defined coefficients c_i and h:

$$\left[\Delta p_{cond}^{plate}\right]_{fr} = 4 \frac{f_{cond}^{plate} L_p}{D_h} \frac{G_{eq}^2}{2\rho_l}, \tag{A.66}$$

$$f_{cond}^{plate} = c_5 Re_{eq}^{c_6}, \tag{A.67}$$

$$c_5 = 3521.1 \left(\frac{\Lambda}{D_h}\right)^{4.17} \beta^{-7.75}, \tag{A.68}$$

$$c_6 = -1.024 \left(\frac{\Lambda}{D_h}\right)^{0.0925} \beta^{-1.3}, \tag{A.69}$$

$$h = \frac{k}{D_h} c_7 Re_{eq}^{c_8} Pr_l^{1/3}, \tag{A.70}$$

$$c_7 = 11.22 \left(\frac{\Lambda}{D_h}\right)^{-2.83} \beta^{-4.5}, \tag{A.71}$$

$$c_8 = 0.35 \left(\frac{\Lambda}{D_h}\right)^{0.23} \beta^{1.48}. \tag{A.72}$$

The experiments performed by Han, Lee, and Kim [47] were done for $\beta = 45$, 55 and 70° and $G = 13$ - 34 kg/m^{2}s, while using R22 and R410a as working fluids.

Appendix B

Wet cooling tower

In this appendix the equations used to calculate the heat and mass transfer in a wet cooling tower are listed. These equations all come from Kloppers [62].

B.1 Poppe method

The Poppe method is used to calculate the heat and mass transfer in the cooling tower. The mass flow of water $\dot{m}_w$ falling down at a point in the cooling tower is given as:

$$\dot{m}_w = \dot{m}_{wi} - \dot{m}_a(w_o - w), \tag{B.1}$$

with $\dot{m}_{wi}$ the amount of water at the sprays, m_a the mass flow of dry air, w_o the humidity ratio at the outlet of the air and w the humidity ratio at the same point as $\dot{m}_w$.

The evolution of the Merkel number, the humidity ratio and the enthalpy of the wet air are given by the Poppe equations. Different equations exist for unsaturated air and saturated air.

B.1.1 Unsaturated Poppe equations

The Lewis factor for unsaturated air is given as:

$$Le_f = 0.865^{0.667} \frac{\left(\frac{w_{sw}+0.622}{w+0.622} - 1\right)}{\ln\left(\frac{w_{sw}+0.622}{w+0.622}\right)}, \tag{B.2}$$

with w_{sw} the saturated humidity ratio at water temperature. This Lewis factor is used in the Poppe equations:

$$\frac{dMe_P}{dT_w} = \frac{c_{p,w}}{h_{masw} - h_{ma} - (w_{sw} - w)c_{p,w}T_w} \cdots$$
$$\cdots \frac{}{+(Le_f - 1)\left[h_{masw} - h_{ma} - (w_{sw} - w)h_v\right]} \tag{B.3}$$

$$\frac{dw}{dT_w} = \frac{dMe_P}{dT_w}\frac{\dot{m}_w}{\dot{m}_a}(w_{sw} - w) \tag{B.4}$$

$$\frac{dh_{ma}}{dT_w} = c_{p,w}\frac{\dot{m}_w}{\dot{m}_a}\left(1 + T_w(w_{sw} - w)\frac{dMe_P}{dT_w}\right) \tag{B.5}$$

Me_P is the Merkel number, T_w the temperature of the water, $c_{p,w}$ is the specific heat capacity of water, h_{masw} the enthalpy of saturated wet air at water temperature, h_{ma} the enthalpy of wet air and h_v the enthalpy of the water vapor.

B.1.2 Saturated Poppe equations

For saturated air, similar equations exist:

$$Le_f = 0.865^{0.667}\frac{\left(\frac{w_{sw}+0.622}{w_{sa}+0.622} - 1\right)}{\ln\left(\frac{w_{sw}+0.622}{w_{sa}+0.622}\right)}, \tag{B.6}$$

with w_{sa} the saturated humidity ratio at air temperature. The saturated Poppe equations are given as:

$$\frac{dMe_P}{dT_w} = \frac{c_{p,w}}{h_{masw} - h_{ss} + (w - w_{sw})c_{p,w}T_w} \cdots$$
$$\cdots \frac{}{+(Le_f - 1)\left[h_{masw} - h_{ss} - (w_{sw} - w_{sa})h_v + (w - w_{sa})c_{p,w}T_w\right]} \tag{B.7}$$

$$\frac{dw}{dT_w} = \frac{dMe_P}{dT_w}\frac{m_w}{m_a}(w_{sw} - w_{sa}) \tag{B.8}$$

$$\frac{dh_{ma}}{dT_w} = c_{p,w}\frac{m_w}{m_a}\left(1 + T_w(w_{sw} - w_{sa})\frac{dMe_P}{dT_w}\right) \tag{B.9}$$

h_{ss} is the enthalpy of supersaturated air.

When the inlet temperature and required outlet temperature of the cooling water are given, these sets of coupled differential equations can be solved. One of the results is the required Merkel number for the cooling tower. For each section of the cooling tower, empirical calculations exist to calculate the Merkel number.

B.2 Loss coefficients and transfer characteristics

In this section, correlations for the Merkel number Me_x and loss coefficient K_x for every section x of the cooling tower are given. The loss coefficient is used to calculate the pressure drop in the cooling tower. The air has a different velocity in every section, so the loss coefficients K_x are adapted to an expression K_{xpa} which uses the velocity in the packing as a reference.

B.2.1 Spray region

$$K_{sp} = L_{sp}\left[0.4\left(\frac{G_w}{G_a}\right)+1\right] \tag{B.10}$$

$$K_{sppa} = K_{sp}\frac{\rho_{maM}}{\rho_{maT}}\left(\frac{m_{maT}}{m_{maM}}\right)^2 \tag{B.11}$$

$$Me_{sp} = 0.2L_{sp}\frac{G_a}{G_{wT}}^{0.5} \tag{B.12}$$

G_w and G_a are the mass velocity of the water and the dry air, respectively. The subscripts maT and maM refer to states of wet air at the top and the middle of the tower. L_{sp} is the length of the spray zone and G_{wT} the mass velocity of water at the top of the tower.

B.2.2 Drift eliminator

$$K_{de} = 27.4892 Ry_{de}^{-0.14247} \tag{B.13}$$

$$Ry = \frac{m_{maT}}{\mu_{maT} A_{fr}} \tag{B.14}$$

$$K_{depa} = K_{de} \frac{\rho_{maM}}{\rho_{maT}} \left(\frac{m_{maT}}{m_{maM}} \right)^2 \tag{B.15}$$

A_{fr} is the frontal area of the packing.

B.2.3 Water distribution

$$K_{wd} = 0.5 \tag{B.16}$$

$$K_{wdpa} = K_{wd} \frac{\rho_{maM}}{\rho_{maT}} \left(\frac{m_{maT}}{m_{maM}} \right)^2 \tag{B.17}$$

B.2.4 Rain zone

$$K_{rz} = 1.5 a_v v_w \left(\frac{H_i}{d_d}\right) \times$$

$$\left[\begin{array}{l} 0.219164 - 0.30487 a_\rho \rho_a + 8278.7 a_\mu \mu_a \\ +0.954153 \left\{0.328467 \exp(135.7638 a_L d_d) + 0.47\right\} \\ \times \left\{26.28482 \left(a_L H_i\right)^{-2.95729} + 0.56\right\} \\ \times \exp\left\{\begin{array}{l} \ln(0.204814 \exp(0.066518 a_L W_i) + 0.21) \\ \times (3.9186 \exp(-0.3 a_L H_i)) \\ \times (0.31095 \ln(a_L d_d) + 2.63745) \end{array}\right\} \\ \times \left\{2.177546 (a_v v_{azo})^{-1.46541} + 0.21\right\} \end{array}\right] \tag{B.18}$$

$$K_{rzpa} = K_{rz} \frac{\rho_{maM}}{\rho_{maB}} \left(\frac{m_{maB}}{m_{maM}}\right)^2 \tag{B.19}$$

$$Me_{rz} = 3.6 \frac{D}{v_{maB} d_d} \frac{H_i}{d_d} \frac{p_a}{\rho_w R_v T_a} Sc^{0.33} \left[\ln\left(\frac{w_s + 0.622}{w + 0.622}\right) / (w_s - w)\right] \tag{B.20}$$

$$\times \left[\begin{array}{l} 4.68851 a_\rho \rho_a - 187128.8 a_\mu \mu_a - 2.29322 + \\ 22.4121 \left\{0.350396 (a_v v_{maB})^{1.38046} + 0.09\right\} \times \\ \left\{1.60934 (a_L H_i)^{-1.12083} + 0.66\right\} \times \\ \left\{34.6765 (a_L d_d)^{0.732448} + 0.45\right\} \times \\ \exp\{7.7389 \exp(-0.399827 a_L H_i) ... \\ \ln[0.087498 \exp(0.026619 a_L W_i) + 0.85]\} \end{array}\right] \tag{B.21}$$

v_w is the velocity of the water, v_{maB} is the velocity of wet air at the bottom of the tower, d_d is the mean diameter of a droplet and R_v is the gas constant of the vapor. Expressions for a_μ, a_ρ, a_v and a_L can be found in appendix D of Kloppers [62].

B.2.5 Packing

$$Me_{pa} = Me - Me_{sp} - Me_{rz} \tag{B.22}$$

$$L_{pa} = \left(\frac{Me_{pa}}{1.019766 G_{wM}^{-0.432896} G_a^{0.782744}} \right)^{1/(1-0.292870)} \tag{B.23}$$

$$K_{fdm} = (5.154914 G_{wM}^{0.877646} G_a^{-1.462034} + 10.806728 G_{wM}^{0.226578} G_a^{0.293222}) \times L_{pa}^{-0.236292} \tag{B.24}$$

$$K_{pa} = K_{fdm} + \frac{G_{maT}^2/\rho_{maT} - G_{maB}^2 \rho_{maB}}{G_{maM^2}/\rho_{maM}} \tag{B.25}$$

B.2.6 Packing support structure

$$K_{ps} = 0.5 \tag{B.26}$$

$$K_{pspa} = K_{ps} \frac{\rho_{maM}}{\rho_{maB}} \left(\frac{m_{maB}}{m_{maM}} \right)^2 \tag{B.27}$$

B.2.7 Tower inlet

$$K_{pae} = K_{fspa} + K_{pa} + K_{sppa} + K_{wdpa} + K_{depa} \tag{B.28}$$

$$K_{ct} = 0.2339 + \left(3.919\ 10^{-3} K_{pae}^2 - 6.840\ 10^{-2} K_{pae} + 2.5267\right) \tag{B.29}$$

$$\times \exp\left\{ \frac{W_i}{H_i} (0.5143 - 0.1803 \exp\{0.0163 K_{pae}\}) \right\} \tag{B.30}$$

$$- \sinh^{-1} \left[\begin{array}{l} 2.77 \exp\left\{0.958 \frac{W_i}{H_3}\right\} \times \\ \exp\left\{K_{pae} \left(2.457 - 1.015 \frac{W_i}{H_i}\right) 10^{-2}\right\} \times \\ \left(\frac{r_i}{W_i} - 0.013028\right) \end{array} \right] \tag{B.31}$$

$$K_{ctpa} = K_{ct} \frac{\rho_{maM}}{\rho_{maB}} \left(\frac{m_{maB}}{m_{maM}} \right)^2 \tag{B.32}$$

r_i is the inlet rounding.

B.2.8 Inlet louvers

$$K_{il} = 2.5 \tag{B.33}$$

$$K_{ilpa} = K_{il}\frac{\rho_{maM}}{\rho_{maB}}\left(\frac{W_i B_i}{2H_i W_i}\right)^2\left(\frac{m_{maB}}{m_{maM}}\right)^2 \tag{B.34}$$

B_i is the depth of the cooling tower, but is taken equal to W_i.

B.2.9 Fan upstream

$$K_{up} = 0.5 \tag{B.35}$$

$$K_{uppa} = K_{up}\frac{\rho_{maM}}{\rho_{maT}}\left(\frac{m_{maT}}{m_{maM}}\right)^2\left(\frac{A_{fr}}{A_c}\right)^2 \tag{B.36}$$

B.2.10 Pressure drop

The total pressure drop and electric power consumption of the fans are given by:

$$K = K_{ilpa} + K_{rzpa} + K_{fspa} + K_{pa} + K_{sppa} + K_{wdpa} + K_{depa} + K_{ctpa} + K_{uppa} \tag{B.37}$$

$$\Delta p = K\frac{(m_{maM}/A_{fr})^2}{2\rho_{maM}} \tag{B.38}$$

$$\dot{W}_{fan} = \Delta p\frac{m_{maT}/\rho_{maT}}{\eta_{Fan}} \tag{B.39}$$

Appendix C

Axial turbine

This appendix gives a curve fit of the axial-turbine-stage-efficiency prediction based on the work of Macchi and Perdichizzi [69]. This correlation is afterwards checked with available experimental data in the literature.

C.1 Efficiency prediction

The turbine-stage-efficiency prediction is given by Macchi and Perdichizzi [69] as a function of the dimensional parameter $X = \ln\left[\sqrt{\dot{Q}_{out}|_{is}}/\Delta h|_{is}^{1/4}\right]$ and the specific volume variation across the turbine stage in an isentropic process $Y = \dot{Q}_{out}|_{is}/\dot{Q}_{in}$. $\dot{Q}_{in}$ and $\dot{Q}_{out}|_{is}$ are the volume flow rate at the inlet of the turbine stage and outlet of the turbine stage in case of an isentropic turbine expansion, respectively. $\Delta h|_{is}$ is the enthalpy drop across the turbine stage in case of an isentropic turbine expansion.

Macchi and Perdichizzi [69] give a figure of the efficiency prediction (figure 2.28a), but no correlation is given. Therefore, a curve fit is performed in order to obtain an expression for the efficiency prediction, which is given in equation

(C.1).

$$\begin{aligned}\eta_{turbine} =& 0.892 - 9.08\ 10^{-2}X - 1.03\ 10^{-2}Y \\ & - 7.73\ 10^{-2}X^2 + 9.79\ 10^{-5}Y^2 - 9.61\ 10^{-4}XY \\ & - 2.34\ 10^{-2}X^3 + 3.02\ 10^{-3}X^2Y + 9.68\ 10^{-5}Y^2X \\ & - 2.55\ 10^{-3}X^4 + 1.49\ 10^{-3}X^3Y + 1.77\ 10^{-4}X^4Y \end{aligned} \tag{C.1}$$

Figure C.1 gives the comparison of the turbine-stage efficiency prediction by Macchi and Perdichizzi [69] and expression (C.1). A similar curve fit is performed for the specific speed, as given in equation (C.2).

$$\begin{aligned} N_S =& 0.148 + 1.67\ 10^{-3}X - 1.60\ 10^{-2}Y \\ & + 9.98\ 10^{-4}X^2 + 2.09\ 10^{-4}Y^2 - 8.21\ 10^{-3}XY \\ & - 2.17\ 10^{-3}X^3 - 1.91\ 10^{-4}X^2Y \end{aligned} \tag{C.2}$$

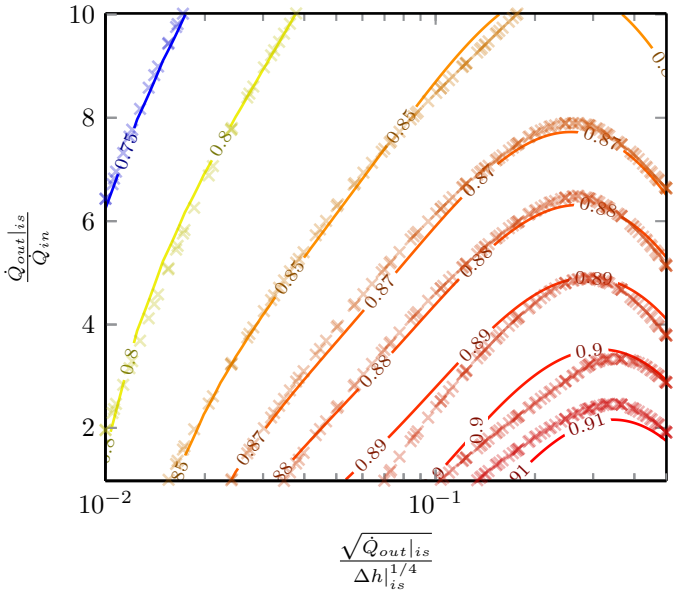

Figure C.1: Curve fit (—) of the efficiency prediction for a turbine stage according to equation (C.1). Data points (x) from Macchi and Perdichizzi [69].

C.2 Comparison of the correlation to experimental data

The result of Macchi and Perdichizzi [69], and therefore also the correlation in equation (C.1), is only valid for axial turbines. We have no experimental data available, so the correlation cannot be validated. The correlation is based on the work of Craig and Cox [25], which is a mature method for axial turbines, so it is reasonable that the correlation gives a correct efficiency prediction.

In this section, the developed correlation is compared to experimental data of other types of turbines available in the literature. In this way, it can be checked if the developed correlation gives reasonable results.

C.2.1 Comparison to a radial-inflow, axial-outflow Kalina turbine

Marcuccilli and Mathiasin [72] have plotted the isentropic efficiency of a radial-inflow, axial-outflow Kalina turbine as a function of the pressure drop. They kept the ammonia fraction, mass flow and outlet pressure constant at 84.31%, 5.47 kg/s and 7.4 bar, respectively. They give both a high and a low limit on the efficiency, as seen in figure C.2.

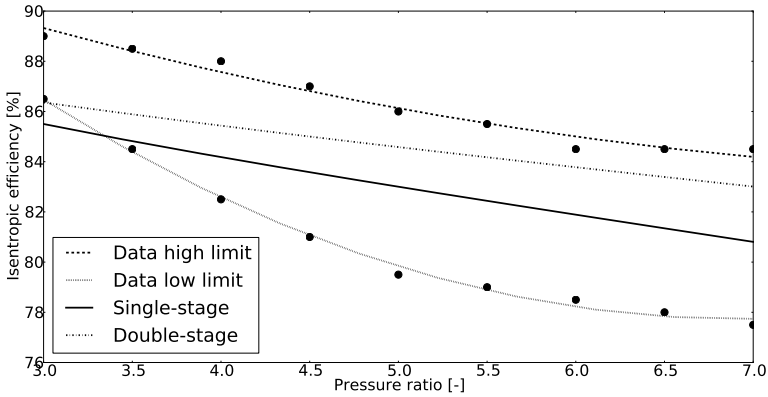

Figure C.2: Isentropic efficiency of a Kalina turbine as a function of the pressure ratio. Data from Marcuccilli and Mathiasin [72].

The correlation in equation (C.1) has been developed for an axial-inflow, axial-outflow turbine. But when this correlation is applied to the above given

conditions for a single and a double-stage turbine, it is seen that there is a good agreement with the experimental data. For low pressure ratios, the correlation underestimates the lower limit of the data, but for intermediate to high pressure ratios, the correlation is well between the upper and lower limit. From these results, it can be concluded that the correlation for axial-inflow, axial-outflow turbines gives reasonable results, also for radial-inflow, axial-outflow turbines.

C.2.2 Comparison to a radial-inflow, axial-outflow isobutane turbine

Marcuccilli and Mathiasin [72] give the isentropic efficiency of a radial-inflow, axial-outflow ORC turbine with isobutane as the working fluid. Isobutane enters the turbine at 152°C and 35 bar and leaves the turbine at 73.8°C and 3.62 bar. The mass flow through the turbine is 158 000 kg/h, the isentropic efficiency of the turbine is 88% and it rotates at 15300 rpm. For these input parameters, the isentropic efficiency is calculated with equation (C.1) for some number of stages. The result is shown in figure C.3.

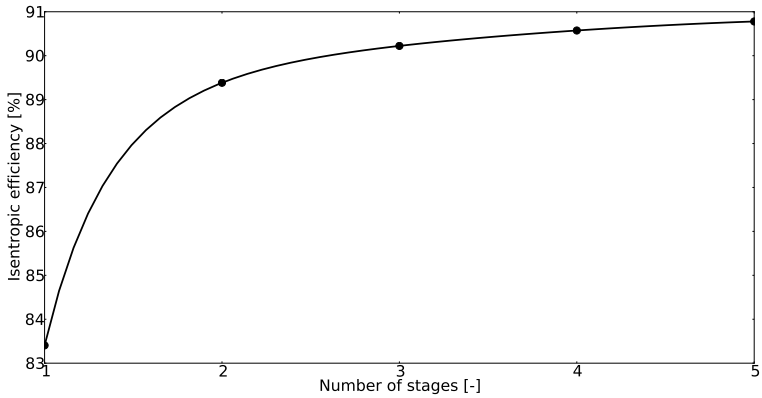

Figure C.3: Isentropic efficiency for an axial-inflow, axial-outflow turbine with isobutane as a function of the number of stages.

The single-stage axial-inflow, axial-outflow turbine has an isentropic efficiency of about 83%, while a double-stage turbine has an efficiency of 89%. This double-stage turbine rotates at 15178 rpm, which is unexpectedly in good agreement with the experimental data. So it seems that the efficiency of both the Kalina and the isobutane radial-inflow, axial-outflow turbines can be predicted with a reasonable accuracy with equation (C.1). The Kalina turbine has a power output of about 1 MW_e (depends on pressure ratio) and the isobutane turbine

has a power output of 3.6 MW. For much lower or higher power outputs, no conclusions can be drawn.

C.2.3 Comparison to an axial-inflow, radial-outflow Kalina turbine

Welch and Boyle [135] give the the experimental data of an axial-inflow, radial-outflow turbine, used in a Kalina cycle. 4.83 kg/s of mixture (92.7 mass % ammonia) enters the turbine at 115.3°C and 20 bar. The outlet pressure is 7.81 bar. The turbine rotates at 28000 rpm and has an isentropic efficiency of 82.4%.

A simulation with the above correlations gives an isentropic efficiency of 83.8% and a rotational speed of 66153 rpm for a single-stage axial-inflow, axial-outflow turbine. The efficiency is in good agreement with the experiments, but the rotational speed is strongly over predicted. So, the efficiency of an axial-inflow, radial-outflow turbine can be estimated by using the prediction for a single-stage axial-inflow, axial-outflow turbine, but conclusions about the rotational speed cannot be drawn.

C.3 Conclusion

A curve fit for the turbine-stage efficiency prediction of Macchi and Perdichizzi [69] is given. Although the developed correlation is only valid for axial-inflow, axial-outflow turbines, it seems to give also good estimations of the efficiency prediction of radial-inflow, axial-outflow and axial-inflow, radial-outflow turbines.

Appendix D

Connection to RefProp

RefProp [66] is a software package which contains correlations to calculate the thermodynamic and transport properties of a large number of fluids and some mixtures. The software itself is written in Fortran, but connections to other software (Matlab, Labview) and programming languages (C, .Net, Python, Perl) are also provided (often by volunteers). Most of these provided connections use a compiled DLL-file to get the fluid properties from RefProp.

A few years ago a connection to Matlab was provided on the RefProp website [85] by Johannes Lux. This connection used compiled Fortran in a mex-file and was about a factor of 10 faster than the connection using the DLL. Based on the connection provided by Lux, a connection between RefProp and Python is made, using compiled Fortran.

RefProp is a software program and not a database. This means that all properties are calculated by correlations and this also means that the derivative of the properties can be found by finding the derivative of the correlating equations.

D.1 Fluid properties

A connection file is written in Fortran, based on the work of Johannes Lux. Only the functions which are needed in the self-written Python code can be called from the connection file. This connection file is compiled with F2PY [92], while adding the compiled RefProp-files to the compilation. In this way, a Python-module is created, which can be easily called from Python.

D.2 Derivative of the fluid properties

In this section, it is explained how the derivative of the fluid properties are calculated from RefProp.

D.2.1 Principle of the complex-step derivative method

The complex-step derivative method [75], also known as the i-trick, is based on Taylor's theorem and is in fact very similar to finite differences. Taylor's theorem is given as:

$$f(x+\delta x) = f(x) + \frac{\delta x}{1!}\left.\frac{df}{dx}\right|_x + \frac{\delta x^2}{2!}\left.\frac{d^2f}{dx^2}\right|_x + \frac{\delta x^3}{3!}\left.\frac{d^3f}{dx^3}\right|_x + ... \tag{D.1}$$

Rewriting this equation and taking the limit for δx going to zero gives the well known formula for finite differences:

$$\left.\frac{df}{dx}\right|_x = \frac{f(x+\delta x) - f(x)}{\delta x} - \frac{\delta x}{2!}\left.\frac{d^2f}{dx^2}\right|_x - \frac{\delta x^2}{3!}\left.\frac{d^3f}{dx^3}\right|_x - ... \tag{D.2}$$

$$\left.\frac{df}{dx}\right|_x \approx \frac{f(x+\delta x) - f(x)}{\delta x} \tag{D.3}$$

The problem is that δx should be as small as possible to make sure that all terms in equation (D.2) except the first one are very small. On the other hand, when δx becomes very small, the difference between $f(x+\delta x)$ and $f(x)$ becomes very small too and due to the limited precision of floating point formats, the numerical error increases. The consequence is that finite differences are in general not accurate.

The same can be repeated for a complex step around x:

$$f(x+i\delta x) = f(x) + i\frac{\delta x}{1!}\left.\frac{df}{dx}\right|_x - \frac{\delta x^2}{2!}\left.\frac{d^2f}{dx^2}\right|_x - i\frac{\delta x^3}{3!}\left.\frac{d^3f}{dx^3}\right|_x + ... \tag{D.4}$$

$$i\left.\frac{df}{dx}\right|_x = \frac{f(x+i\delta x) - f(x)}{\delta x} + \frac{\delta x}{2!}\left.\frac{d^2f}{dx^2}\right|_x + i\frac{\delta x^2}{3!}\left.\frac{d^3f}{dx^3}\right|_x - ... \tag{D.5}$$

$$\left.\frac{df}{dx}\right|_x = \Im\left[\frac{f(x+i\delta x) - f(x)}{\delta x}\right] + \frac{\delta x^2}{3!}\left.\frac{d^3f}{dx^3}\right|_x - ... \tag{D.6}$$

$$\left.\frac{df}{dx}\right|_x \approx \Im\left[\frac{f(x+i\delta x) - f(x)}{\delta x}\right] \tag{D.7}$$

$$\left.\frac{df}{dx}\right|_x \approx \Im\left[\frac{f(x+i\delta x)}{\delta x}\right] \tag{D.8}$$

In this case, δx can be taken very small, because no subtraction of almost identical number occurs. This method is in fact automatic differentiation in forward mode and is accurate up to machine precision if δx is taken very small.

D.2.2 Implementation

In many high-level programming languages, the i-trick can be applied directly. In Fortran this is not possible, because the format of every parameter has to be declared. This means that a number of the parameters, which are declared as real numbers in RefProp, have to be declared as complex numbers. Also a certain number of mathematical functions have to be redefined. Martins, Sturdza, and Alonso [75] provide some tools to perform these adaptations automatically. Unfortunately, the adaptations are not perfect and the whole code has to be checked manually for errors. A number of errors are possible:

- Parameters are declared as complex numbers, while they are set equal to a real number
- Real functions do not work with complex numbers
- Lines that become too long
- Adapted format of the code which is not accepted by the Fortran-compiler

The connection between the adapted RefProp code and Python to calculate the derivative of the fluid properties is analogous to the connection between RefProp

and Python, explained in section D.1. The connection file is also adapted so that it can handle complex numbers.

D.2.3 Verification

The developed code for the calculation of the derivatives is checked in two separate ways. RefProp itself contains correlations to calculate a very limited amount of partial derivatives. The available derivatives in RefProp are compared with the ones calculated with the i-trick for a large number of fluids and state points. The comparison showed that both ways of calculating the derivative are equal up to machine precision.

Finite differences are used to verify the other needed derivatives. Again a large number of fluids and state points is used. The step size δx for the finite differences was taken to be about the square root of the machine precision. A good agreement[1] is obtained and it is concluded that the method works correctly.

D.3 Working fluids

Table D.1 gives the critical temperature T_c, critical pressure p_c and type of the fluids used as possible working fluid in an ORC in chapter 3.

[1] Not perfectly, because finite differences are not correct up to machine precision.

Fluid	T_c [$°C$]	p_c [bar]	Type	Fluid	T_c [$°C$]	p_c [bar]	Type
Acetone	234.95	47.00	Wet	R11	197.96	44.076	Isentropic
Ammonia	132.25	113.33	Wet	R113	214.06	33.922	Dry
Benzene	288.9	48.94	Dry	R114	145.68	32.57	Dry
Butane	151.98	37.96	Dry	R115	79.95	31.29	Dry
Butene	146.14	40.051	Dry	R12	111.97	41.361	Wet
Carbon dioxide (CO2)	30.978	73.773	Wet	R1234yf	94.7	33.822	Dry
Carbonyl sulfide (COS)	105.62	63.7	Wet	R1234ze	109.37	36.363	Dry
Cis-butene	162.6	42.255	Dry	R123	183.68	36.618	Dry
Cyclohexane	280.49	40.75	Dry	R124	122.28	36.243	Dry
Cyclopropane	125.15	55.797	Wet	R125	66.023	36.177	Wet
Decafluorobutane	113.176	23.234	Dry	R13	28.85	38.79	Wet
Decane	344.55	21.03	Dry	R134a	101.06	40.593	Wet
Dimethylether (DME)	127.15	53.405	Wet	R141b	204.35	42.12	Dry
Docecane (C12)	384.95	18.17	Dry	R142b	137.11	40.55	Wet
Ethane	32.172	48.722	Wet	R143a	72.707	37.61	Wet
Ethanol	240.75	61.48	Wet	R152a	113.26	45.168	Wet
Heptane	266.98	27.36	Dry	R21	178.33	51.812	Wet
Hexane	234.67	30.34	Dry	R218	71.87	26.400	Dry
Hydrogen sulfide (H2S)	99.95	90	Wet	R22	96.145	49.9	Wet
Isobutane	134.66	36.29	Dry	R227ea	101.75	29.25	Dry
Isobutene	144.94	40.098	Dry	R236ea	139.29	35.02	Dry
Isohexane	224.55	30.4	Dry	R236fa	124.92	32	Dry
Isopentane	187.2	33.78	Dry	R245ca	174.42	39.25	Dry
Methanol	239.45	81.035	Wet	R245fa	154.01	36.51	Dry
Neopentane	160.59	31.96	Dry	R32	78.105	57.82	Wet
Nitrous oxide (N2O)	36.37	72.45	Wet	R365mfc	186.85	32.66	Dry
Nonane	321.4	22.81	Dry	R41	44.13	58.97	Wet
Octane	296.17	24.97	Dry	RC318	115.23	27.775	Dry
Pentane	196.55	33.7	Dry	Sulfur dioxide (SO2)	157.49	78.84	Wet
Perfluorobutane (C4F10)	113.18	23.234	Dry	Sulfur hexa-fluoride (SF6)	45.573	37.55	Wet
Perfluoropentane (C5F12)	147.41	20.45	Dry	Toluene	318.6	41.263	Dry
Propane	96.74	42.512	Wet	Trans-butene	155.46	40.273	Dry
Propylene	91.061	45.55	Wet	Trifluoroiodo-methane (CF3I)	123.29	39.53	Wet
Propyne	129.23	56.26	Wet	Water	373.95	220.64	Wet

Table D.1: Possible organic fluids. Data from Lemmon, Huber, and Mclinden [66].

Bibliography

[1] A. Achaichia and T.A. Cowell. "Heat transfer and pressure drop characteristics of flat tube and louvered plate fin surfaces". In: *Experimental Thermal and Fluid Science* 1.2 (1988), pp. 147–157.

[2] Alfa Laval. *Compabloc*. date accessed: August 22, 2014. URL: http://www.alfalaval.com/solution-finder/products/compabloc/Documents/PPM00033EN.pdf.

[3] Alfa Laval. *Plate Heat Exchanger*. date accessed: August 22, 2014. URL: http://www.alfalaval.com/solution-finder/products/gasketed-industrial-range-phe/Documents/TS6_plate_heat_exchanger.pdf.

[4] B. Allen and L. Gosselin. "Optimal geometry and flow arrangement for minimizing the cost of shell-and-tube condensers". In: *International Journal of Energy Research* 32.10 (2008), pp. 958–969.

[5] J. Andersson, J. Åkesson, and M. Diehl. "CasADi – A symbolic package for automatic differentiation and optimal control". In: *Recent Advances in Algorithmic Differentiation*. Ed. by S. Forth et al. Vol. 87. Lecture Notes in Computational Science and Engineering. Springer Berlin Heidelberg, 2012, pp. 297–307.

[6] M. Astolfi et al. "Binary ORC (Organic Rankine Cycles) power plants for the exploitation of medium–low temperature geothermal sources–Part B: Techno-economic optimization". In: *Energy* 66 (2014), pp. 435–446.

[7] Atlas Copco. URL: http://www.atlascopco-gap.com.

[8] Gudni Axelsson et al. "Sustainable management of geothermal resources and utilization for 100–300 years". In: *Proceedings World Geothermal Congress*. Vol. 8. 2005.

[9] Z.H. Ayub. "Plate heat exchanger literature survey and new heat transfer and pressure drop correlations for refrigerant evaporators". In: *Heat Transfer Engineering* 24.5 (2003), pp. 3–16.

[10] B.V. Babu and S.A. Munawar. “Differential evolution strategies for optimal design of shell-and-tube heat exchangers”. In: *Chemical Engineering Science* 62.14 (2007), pp. 3720–3739.

[11] E. Barbier. “Geothermal energy technology and current status: an overview”. In: *Renewable and Sustainable Energy Reviews* 6.1 (2002), pp. 3–65.

[12] G. Barigozzi, A. Perdichizzi, and S. Ravelli. “Wet and dry cooling systems optimization applied to a modern waste-to-energy cogeneration heat and power plant”. In: *Applied Energy* 88.4 (2011), pp. 1366–1376.

[13] K.J. Bell. *Final report of the cooperative research program on shell and tube heat exchangers*. University of Delaware, Engineering Experimental Station, 1963.

[14] M.S. Bhatti and R.K. Shah. “Turbulent and transition convective heat transfer in ducts”. In: *Handbook of Single-Phase Convective Heat Transfer*. Ed. by S. Kakaç, R.K. Shah, and W. Aung. New York: Wiley, 1987. Chap. 4.

[15] Bliem, C.J. and Mines, G.L. “Supersaturated Turbine Expansions for Binary Geothermal Power Plants”. In: *Geothermal Energy and the Utility Market - The Opportunities and Challenges for Expanding Geothermal Energy in a Competitive Supply Market*. 1992, 105–109.

[16] C.J. Bliem and G.L. Mines. “Advanced Binary Geothermal Power Plants Limits Of Performance”. In: *Proceedings of the 25th Intersociety Energy Conversion Engineering Conference* (1991), pp. 85–90.

[17] C.J. Bliem and G.L. Mines. “Relative performance of supercritical binary geothermal power cycles with in-tube condensers in different orientations”. In: *Proceedings of the 24th Intersociety Energy Conversion Engineering Conference* (1989), pp. 2167–2172.

[18] P. Bombarda, C.M. Invernizzi, and C. Pietra. “Heat recovery from Diesel engines: A thermodynamic comparison between Kalina and ORC cycles”. In: *Applied Thermal Engineering* 30.2 (2010), pp. 212–219.

[19] J. Bruno et al. “Modelling and optimisation of solar organic rankine cycle engines for reverse osmosis desalination”. In: *Applied Thermal Engineering* 28.17-18 (2008), pp. 2212–2226.

[20] C. Büskens and D. Wassel. “The ESA NLP Solver WORHP”. In: *Modeling and Optimization in Space Engineering*. Springer, 2013, pp. 85–110.

[21] E. Cayer, N. Galanis, and H. Nesreddine. “Parametric study and optimization of a transcritical power cycle using a low temperature source”. In: *Applied Energy* 87.4 (2010), pp. 1349–1357.

[22] E. Cayer et al. “Analysis of a carbon dioxide transcritical power cycle using a low temperature source”. In: *Applied Energy* 86.7-8 (July 2009), pp. 1055–1063.

[23] Y.-J. Chang and C.-C. Wang. “A generalized heat transfer correlation for Iouver fin geometry”. In: *International Journal of heat and mass transfer* 40.3 (1997), pp. 533–544.

[24] A. LH Costa and E.M. Queiroz. “Design optimization of shell-and-tube heat exchangers”. In: *Applied Thermal Engineering* 28.14 (2008), pp. 1798–1805.

[25] H.R.M. Craig and H.J.A. Cox. “Performance estimation of axial flow turbines”. In: *Proceedings of the Institution of Mechanical Engineers* 185.1 (1970), pp. 407–424.

[26] N. Cuenot et al. “Evolution of the natural radioactivity within the Soultz geothermal installation”. In: *Proceedings of the European Geothermal Congress 2013*. PS3-05. Pisa, June 2013.

[27] Y. Dai, J. Wang, and L. Gao. “Parametric optimization and comparative study of organic Rankine cycle (ORC) for low grade waste heat recovery”. In: *Energy Conversion and Management* 50.3 (2009), pp. 576–582.

[28] W. D’haeseleer. *Synthesis on the Economics of Nuclear Energy*. Study for the European Commission, DG Energy. available at: http://ec.europa.eu/energy/nuclear/forum/doc/final_report_dhaeseleer/synthesis_economics_nuclear_20131127-0.pdf. Nov. 2013.

[29] R. DiPippo. *Geothermal power plants: Principles, applications, case studies and environmental impact*. Elsevier, 2008.

[30] R. DiPippo. “Second Law assessment of binary plants generating power from low-temperature geothermal fluids”. In: *Geothermics* 33.5 (2004), pp. 565–586.

[31] Ronald DiPippo. “Ideal thermal efficiency for geothermal binary plants”. In: *Geothermics* 36.3 (2007), pp. 276–285.

[32] E. Djordjevic and S. Kabelac. “Flow boiling of R134a and ammonia in a plate heat exchanger”. In: *International Journal of Heat and Mass Transfer* 51.25 (2008), pp. 6235–6242.

[33] D.A. Donohue. “Heat transfer and pressure drop in heat exchangers”. In: *Industrial & Engineering Chemistry* 41.11 (1949), pp. 2499–2511.

[34] G.H. Doo, W.M. Dempster, and J.M. McNaught. “Improved prediction of shell side heat transfer in horizontal evaporative shell and tube heat exchangers”. In: *Heat Transfer Engineering* 29.12 (2008), pp. 999–1007.

[35] A.R. Doodman, M. Fesanghary, and R. Hosseini. “A robust stochastic approach for design optimization of air cooled heat exchangers”. In: *Applied Energy* 86.7 (2009), pp. 1240–1245.

[36] Exergy. URL: http://exergy-orc.com.

[37] Exergy. *Exergy supplies to ENEL Green Power world’s first radial outflow turbine in a geothermal binary plant*. date accessed: August 22, 2014. URL: http://www.exergy-orc.com/newspressred/2012/exergy-supplies-to-enel-green-power-worlds-first-radial-outflow-turbine-in-a-geothermal-binary-plant.

[38] A. Franco and M. Villani. “Optimal design of binary cycle power plants for water-dominated, medium-temperature geothermal fields”. In: *Geothermics* 38.4 (2009), pp. 379–391.

[39] D. Gallup. “Aluminum silicate scale formation and inhibition: Scale characterization and laboratory experiments”. In: *Geothermics* 26.4 (Aug. 1997), pp. 483–499.

[40] J.R. García-Cascales et al. “Assessment of boiling and condensation heat transfer correlations in the modelling of plate heat exchangers”. In: *International Journal of Refrigeration* 30.6 (2007), pp. 1029–1041.

[41] GEA Heat Exchangers. *Air Fin Coolers: Configurations*. http://www.gea-heatexchangers.com/products/finned-tube-heat-exchangers/air-fin-coolers-for-oil-and-gas/. date accessed: August 22, 2014.

[42] GEA Heat Exchangers. *GEA Cooling Towers with HX-Factor*. http://www.gea-heatexchangers.com/products/wet-cooling-towers/natural-draft-cooling-towers/file/778e695ddac1db3da1d7eaca2c4fd0d6/?eID=downloadManager. date accessed: August 22, 2014.

[43] C.H. Gilmour. “Shortcut to heat exchanger design-VII”. In: *Chemical engineering* (1954), p. 199.

[44] Z. Gnutek and A. Bryszewska-Mazurek. “The thermodynamic analysis of multicycle ORC engine”. In: *Energy* 26.12 (2001), pp. 1075–1082.

[45] D. Gulley. “More Accurate Exchanger Shell-Side Pressure Drop Calculations”. In: *Hydrocarbon Processing* (June 2004).

[46] D.-H. Han, K.-J. Lee, and Y.-H. Kim. “Experiments on the characteristics of evaporation of R410A in brazed plate heat exchangers with different geometric configurations”. In: *Applied Thermal Engineering* 23.10 (2003), pp. 1209–1225.

[47] D.-H. Han, K.-J. Lee, and Y.-H. Kim. “The characteristics of condensation in brazed plate heat exchangers with different chevron angles”. In: *Journal of the Korean Physical Society* 43 (2003), pp. 66–73.

[48] F. Heberle and D. Brüggemann. "Exergy based fluid selection for a geothermal Organic Rankine Cycle for combined heat and power generation". In: *Applied Thermal Engineering* 30.11-12 (2010), pp. 1326–1332.

[49] T. Hettkamp et al. "Electricity Production from Hot Rocks". In: *Proceedings of the Twenty-Ninth Workshop on Geothermal reservoir Engineering*. Stanford University, Stanford, CA, USA. 2004, pp. 184–193.

[50] G.F. Hewitt. *Hemisphere handbook of heat exchanger design*. Hemisphere Publishing Corporation New York, 1990.

[51] P.A. House. *Analysis of a Radial-Outflow Reaction Turbine Concept for Geothermal Application*. Tech. rep. Lawrence Livermore Laboratory, 1978.

[52] IEA. *Technology Roadmap: Geothermal Heat and Power*. Tech. rep. International Energy Agency, 2011.

[53] IEA. *World Energy Outlook*. Tech. rep. International Energy Agency, 2013.

[54] IPCC Working Group I. *Climate change 2007, The physical science base, Contribution of working group I to the fourth assessment report of the Intergovernmental Panel on Climate Change*. Tech. rep. 2007.

[55] IWEC. *International Weather for Energy Calculations (IWEC Weather Files) Users Manual and CD-ROM*. ASHRAE. Atlanta. 2001.

[56] A. Jokar, M.H. Hosni, and S.J. Eckels. "Dimensional analysis on the evaporation and condensation of refrigerant R-134a in minichannel plate heat exchangers". In: *Applied thermal engineering* 26.17 (2006), pp. 2287–2300.

[57] Jones, E. and Oliphant, T. and Peterson, P. and others. *SciPy: Open source scientific tools for Python*. 2001–. URL: http://www.scipy.org/.

[58] M. Kanoglu. "Exergy analysis of a dual-level binary geothermal power plant". In: *Geothermics* 31.6 (2002), pp. 709–724.

[59] A. Kather, K. Rohloff, and A. Filleböck. "Energy Efficiency of Geothermal Power Generation, Fundamentals for a Consistent Evaluation of Geothermal Projects with Binary Cycles". In: *VGB PowerTech* (May 2008), pp. 98–105.

[60] Haile Kebede. *Study of geothermal power plant electricial and control system with emphasis on reliability aspects*. Tech. rep. 7. The United Nations University, 2002.

[61] D.Q. Kern. *Process heat transfer*. Tata McGraw-Hill Education, 1950.

[62] J.C. Kloppers. "A critical evaluation and refinement of the performance prediction of wet-cooling towers". PhD thesis. Department of Mechanical Engineering, University of Stellenbosch, 2003.

[63] J.C. Kloppers and D.G. Kröger. "A critical investigation into the heat and mass transfer analysis of counterflow wet-cooling towers". In: *International Journal of Heat and Mass Transfer* 48.3 (2005), pp. 765–777.

[64] S. Köhler. "Geothermisch angetriebene Dampfkraftprozesse, Analyse und Prozessvergleich binärer Kraftwerke". PhD thesis. TU Berlin, 2005.

[65] D. Kroshko. *OpenOpt: Free scientific-engineering software for mathematical modeling and optimization*. 2007–. URL: http://www.openopt.org/.

[66] E.W. Lemmon, M.L. Huber, and M.O. Mclinden. *NIST Reference Fluid Thermodynamic and Transport Properties REFPROP*. Version 8.0. The National Institute of Standards and Technology (NIST). 2007.

[67] G.A. Longo. "R410A condensation inside a commercial brazed plate heat exchanger". In: *Experimental Thermal and Fluid Science* 33.2 (2009), pp. 284–291.

[68] E. Macchi. "Design limits, basic parameter selection and optimization methods in turbomachinery design". In: *Thermodynamics and fluid Mechanics of turbomachinery* 97.B (1985).

[69] E. Macchi and A. Perdichizzi. "Efficiency prediction for axial-flow turbines operating with nonconventional fluids". In: *Journal for Engineering for Power* 103.4 (1981), pp. 718–724.

[70] H.D.M. Madhawa et al. "Optimum design criteria for an organic Rankine cycle using low-temperature geothermal heat sources". In: *Energy* 32.9 (2007), pp. 1698–1706.

[71] P.J. Mago et al. "An examination of regenerative organic Rankine cycles using dry fluids". In: *Applied thermal engineering* 28.8-9 (2008), pp. 998–1007.

[72] F. Marcuccilli and H. Mathiasin. "Kalina & Organic Rankine Cycles: How to Choose the Best Expansion Turbine?" In: *Electricity Generation from Enhanced Geothermal Systems*. September 2006.

[73] F. Marcuccilli and D. Thiolet. "Optimizing Binary Cycles Thanks to Radial Inflow Turbines". In: *Proceedings World Geothermal Congress 2010*. Cryostar SAS, ZI, BP 48, FR-68220 Hésingue, France. Bali, Indonesia, 2010, p. 9.

[74] H. Martin. "A theoretical approach to predict the performance of chevron-type plate heat exchangers". In: *Chemical Engineering and Processing* 35.4 (1996), pp. 301–310.

[75] J.R.R.A. Martins, P. Sturdza, and J.J. Alonso. "The complex-step derivative approximation". In: *ACM Transactions on Mathematical Software (TOMS)* 29.3 (2003), pp. 245–262.

[76] D. Mendrinos, C. Karytsas, and E. Kontoleontos. “Geothermal binary plants: water or air cooled?” In: *Proceedings of the ENGINE 2nd Workpackage Meeting*. Strasbourg, 2006.

[77] F. Merkel. “Verdunstungskühlung”. In: *VDI-Zeitschrift* 70 (1925), pp. 123–128.

[78] S.L. Milora and J.W. Tester. “Geothermal energy as a source of electric power: Thermodynamic and economic design criteria”. In: *NASA STI/Recon Technical Report A* 77 (1976), p. 16623.

[79] Mines, G.L. “One year of operation of Mammoth Pacific‘s MP1-100 turbine with metastable, supersaturated expansions”. In: *Proceedings Geothermal Program Review XV*. Vol. 3. Idaho National Engineering and Environmental Laboratory (INEEL). 1997, 51–57.

[80] H.A. Mlcak. “An Introduction to the Kalina Cycle”. In: *Proceedings of the International Joint Power Generation Conference* 30 (1996), pp. 1–11.

[81] H. Mlcak et al. “Notes from the North: a Report on the Debut Year of the 2 MW Kalina Cycle® Geothermal Power Plant in Húsavík, Iceland”. In: *Transactions-Geothermal Tesources Council* (2002), pp. 715–718.

[82] R. Mukherjee. “Effectively design shell-and-tube heat exchangers”. In: *Chemical Engineering Progress* 94.2 (1998), pp. 21–37.

[83] M+W Zander. *New Kalina Cycle*. No longer available. 2006.

[84] F. Nemati Taher et al. “Baffle space impact on the performance of helical baffle shell and tube heat exchangers”. In: *Applied Thermal Engineering* 44 (2012), pp. 143–149.

[85] NIST. *NIST Reference Fluid Thermodynamic and Transport Properties Database*. date accessed: August 22, 2014. URL: http://www.nist.gov/srd/nist23.cfm.

[86] S. Ogriseck. “Integration of Kalina cycle in a combined heat and power plant, a case study”. In: *Applied Thermal Engineering* 29.14-15 (2009), pp. 2843–2848.

[87] Ormat. URL: http://www.ormat.com.

[88] E. Ozden and I. Tari. “Shell side CFD analysis of a small shell-and-tube heat exchanger”. In: *Energy Conversion and Management* 51.5 (2010), pp. 1004–1014.

[89] Y.-G. Park and A.M. Jacobi. “Air-side heat transfer and friction correlations for flat-tube louver-fin heat exchangers”. In: *Journal of Heat Transfer* 131.2 (2009), p. 021801.

[90] H. Paschen, D. Oertel, and R. Grünwald. “Möglichkeiten geothermischer Stromerzeugung in Deutschland”. In: *TAB Arbeitsbericht Nr. 84* (2003).

[91] V.K. Patel and R.V. Rao. “Design optimization of shell-and-tube heat exchanger using particle swarm optimization technique”. In: *Applied Thermal Engineering* 30.11 (2010), pp. 1417–1425.

[92] P. Peterson. “F2PY: a tool for connecting Fortran and Python programs”. In: *International Journal of Computational Science and Engineering* 4.4 (2009), pp. 296–305.

[93] B.S. Petukhov and V.N. Popov. “Theoretical calculation of heat exchange and frictional resistance in turbulent flow in tubes of an incompressible fluid with variable physical properties(Heat exchange and frictional resistance in turbulent flow of liquids with variable physical properties through tubes)”. In: *High Temperature* 1 (1963), pp. 69–83.

[94] M. Pini et al. “Preliminary design of a centrifugal turbine for ORC applications”. In: *ORC2011*. 2011.

[95] M. Poppe and H. Rögener. “Berechnung von Rückkühlwerken”. In: *VDI Wärmeatlas* Mi (1991), pp. 1–15.

[96] A. Poullikkas. “An overview of current and future sustainable gas turbine technologies”. In: *Renewable and Sustainable Energy Reviews* 9.5 (2005), pp. 409–443.

[97] M. Prithiviraj and M.J. Andrews. “Comparison of a three-dimensional numerical model with existing methods for prediction of flow in shell-and-tube heat exchangers”. In: *Heat transfer engineering* 20.2 (1999), pp. 15–19.

[98] S. Quoilin and V. Lemort. “Technological and Economical Survey of Organic Rankine Cycle Systems”. In: *5th European Conference Economics and Management of Energy in Industry*. 2009, p. 12.

[99] S. Quoilin et al. “Thermo-economic optimization of waste heat recovery Organic Rankine Cycles”. In: *Applied Thermal Engineering* 31.14 (2011), pp. 2885–2893.

[100] E. Rubio-Castro et al. “Optimization of mechanical draft counter flow wet-cooling towers using a rigorous model”. In: *Applied Thermal Engineering* 31.16 (2011), pp. 3615–3628.

[101] B. Saleh et al. “Working fluids for low-temperature organic Rankine cycles”. In: *Energy* 32.7 (2007), pp. 1210–1221.

[102] J. Scheiber et al. “Application of a Scaling Inhibitor System at the Geothermal Power Plant in Soultz-sous-Forêts, Laboratory and On-site Studies”. In: *Proceedings of the European Geothermal Congress 2013*. PS3-04. Pisa, June 2013.

[103] M. Serna-González, J.M. Ponce-Ortega, and A. Jiménez-Gutiérrez. "MINLP optimization of mechanical draft counter flow wet-cooling towers". In: *Chemical Engineering Research and Design* 88.5 (2010), pp. 614–625.

[104] R.K. Shah and D.P. Sekulić. *Fundamentals of heat exchanger design*. John Wiley and Sons, Inc., 2003.

[105] R.K. Sinnott. *Chemical Engineering Design*. Butterworth-Heinemann, 1999.

[106] R. Smith. *Chemical process design and integration*. Wiley New York, 2005.

[107] C. Spadacini et al. "A New Configuration for Organic Rankine Cycle Power Systems". In: *ORC2011*. 2011.

[108] S.W. Stewart. "Enhanced finned-tube condenser design and optimization". PhD thesis. Georgia Institute of Technology, 2003.

[109] J.W. Tester et al. *The Future of Geothermal Energy: Impact of Enhanced Geothermal Systems (EGS) on the United States in the 21st Century*. Tech. rep. Massachusetts, USA: Massachusetts Institute of Technology, 2006, p. 372.

[110] J.R. Thome. *Engineering Databook III*. Wolverine Tube, Inc., 2010.

[111] B. Thonon and A. Bontemps. "Condensation of pure and mixture of hydrocarbons in a compact heat exchanger: experiments and modelling". In: *Heat transfer engineering* 23.6 (2002), pp. 3–17.

[112] T. Tinker. "Shell side characteristics of shell and tube heat exchangers". In: *General Discussion on Heat Transfer* (1951), pp. 89–116.

[113] G. Towler and R. Sinnott. *Chemical engineering design: principles, practice and economics of plant and process design*. Butterworth-Heinemann, 2008.

[114] Triogen. URL: http://www.triogen.nl.

[115] Turboden. URL: http://www.turboden.eu.

[116] P. Valdimarsson. "Factors influencing the economics of the Kalina power cycle and situations of superior performance". In: *International Geothermal Conference*. Reykjavik, Sept. 2003, pp. 32–40.

[117] P. Valdimarsson. *ORC and Kalina Analysis and experience*. Sabbatical Lecture III. 2003.

[118] VITO. URL: http://www.vito.be.

[119] VITO. *Geothermie*. date accessed: August 22, 2014. URL: www.vito.be/NL/HomepageAdmin/Home/Subsites/Balmatt/Ontwikkeling/Geothermie/Pages/Geothermie.aspx.

[120] A. Wächter and L.T. Biegler. “On the implementation of an interior-point filter line-search algorithm for large-scale nonlinear programming”. In: *Mathematical programming* 106.1 (2006), pp. 25–57.

[121] D. Walraven, B. Laenen, and W. D’haeseleer. “Comparison of shell-and-tube with plate heat exchangers for the use in low-temperature organic Rankine cycles”. In: *Energy Conversion and Management* 87.C (2014), pp. 227–237.

[122] D. Walraven, B. Laenen, and W. D’haeseleer. “Comparison of thermodynamic cycles for power production from low-temperature geothermal heat sources”. In: *Energy Conversion and Management* 66.C (2013), pp. 220–233.

[123] D. Walraven, B. Laenen, and W. D’haeseleer. “Economic system optimization of air-cooled organic Rankine cycles powered by low-temperature geothermal heat sources”. Submitted for publication in Energy. 2014.

[124] D. Walraven, B. Laenen, and W. D’haeseleer. “Influence of the configuration of heat exchangers on the performance of ORCs, a first step to a system optimization.” In: *ASME ORC 2013 Abstracts*. 149. Rotterdam, Oct. 2013.

[125] D. Walraven, B. Laenen, and W. D’haeseleer. “Minimizing the levelized cost of electricity production from low-temperature geothermal heat sources: water or air cooled?” Submitted for publication in Applied Energy. 2014.

[126] D. Walraven, B. Laenen, and W. D’haeseleer. “Optimization of subcritical and transcritical ORC’s for low-temperature heat sources.” In: *Book of Abstracts of the 1st International Seminar on ORC Power Systems*. Delft, Sept. 2011.

[127] D. Walraven, B. Laenen, and W. D’haeseleer. “Optimization of the Energy Conversion Starting from Low-T Geothermal Heat, General Considerations & State of the Art”. Working paper. 2011.

[128] D. Walraven, B. Laenen, and W. D’haeseleer. “Optimum configuration of plate-type heat exchangers for the use in ORCs for low-temperature geothermal heat sources.” In: *Proceedings of the European Geothermal Congress 2013*. HS3-15. Pisa, June 2013.

[129] D. Walraven, B. Laenen, and W. D’haeseleer. “Optimum configuration of shell-and-tube heat exchangers for the use in low-temperature organic Rankine cycles”. In: *Energy Conversion and Management* 83.C (2014), pp. 177–187.

[130] C.-C. Wang, Y.-M. Hwang, and Y.-T. Lin. “Empirical correlations for heat transfer and flow friction characteristics of herringbone wavy fin-and-tube heat exchangers”. In: *International Journal of Refrigeration* 25.5 (2002), pp. 673–680.

[131] C.-C. Wang et al. “Heat transfer and friction correlation for compact louvered fin-and-tube heat exchangers”. In: *International journal of heat and mass transfer* 42.11 (1998), pp. 1945–1956.

[132] S. Wang, J. Wen, and Y. Li. “An experimental investigation of heat transfer enhancement for a shell-and-tube heat exchanger”. In: *Applied Thermal Engineering* 29.11 (2009), pp. 2433–2438.

[133] Wei, D. and Lu, X. and Lu, Z. and Gu, J. “Performance analysis and optimization of organic Rankine cycle (ORC) for waste heat recovery”. In: *Energy conversion and Management* 48.4 (2007), 1113–1119.

[134] N. Wei. “Significance of Loss Models in Aerothermodynamic Simulation for Axial Turbines”. PhD thesis. KTH Royal Institute of Technology, 2000.

[135] P. Welch and P. Boyle. “New turbines to Enable Efficient Geothermal Power Plants”. In: *GRC Transactions*. Vol. 33. 2009, pp. 765–772.

[136] L. Yang et al. “Thermal-flow characteristics of the new wave-finned flat tube bundles in air-cooled condensers”. In: *International Journal of Thermal Sciences* 53 (2012), pp. 166–174.

[137] Y. Yang et al. “An efficient way to use medium-or-low temperature solar heat for power generation – integration into conventional power plant”. In: *Applied Thermal Engineering* 31.2 (2011), pp. 157–162.

[138] M. Yari. “Exergetic analysis of various types of geothermal power plants”. In: *Renewable Energy* 35.1 (2010), pp. 112–121.

[139] Y. You et al. “Numerical modeling and experimental validation of heat transfer and flow resistance on the shell side of a shell-and-tube heat exchanger with flower baffles”. In: *International Journal of Heat and Mass Transfer* 55.25 (2012), pp. 7561–7569.

[140] H. Zeng, J. Meng, and Z. Li. “Numerical study of a power plant condenser tube arrangement”. In: *Applied Thermal Engineering* 40 (2012), pp. 294–303.

List of publications

Articles in international journals

a. Published

- D. Walraven, B. Laenen, and W. D'haeseleer. "Comparison of shell-and-tube with plate heat exchangers for the use in low-temperature organic Rankine cycles". In: *Energy Conversion and Management* 87.C (2014), pp. 227–237
- D. Walraven, B. Laenen, and W. D'haeseleer. "Optimum configuration of shell-and-tube heat exchangers for the use in low-temperature organic Rankine cycles". In: *Energy Conversion and Management* 83.C (2014), pp. 177–187
- D. Walraven, B. Laenen, and W. D'haeseleer. "Comparison of thermodynamic cycles for power production from low-temperature geothermal heat sources". In: *Energy Conversion and Management* 66.C (2013), pp. 220–233

b. Submitted & under review

- D. Walraven, B. Laenen, and W. D'haeseleer. "Minimizing the levelized cost of electricity production from low-temperature geothermal heat sources: water or air cooled?" Submitted for publication in Applied Energy. 2014
- D. Walraven, B. Laenen, and W. D'haeseleer. "Economic system optimization of air-cooled organic Rankine cycles powered by low-temperature geothermal heat sources". Submitted for publication in Energy. 2014

Papers in international conference proceedings

- D. Walraven, B. Laenen, and W. D'haeseleer. "Optimum configuration of plate-type heat exchangers for the use in ORCs for low-temperature geothermal heat sources." In: *Proceedings of the European Geothermal Congress 2013*. HS3-15. Pisa, June 2013

Conference presentations - abstract only

- D. Walraven, B. Laenen, and W. D'haeseleer. "Influence of the configuration of heat exchangers on the performance of ORCs, a first step to a system optimization." In: *ASME ORC 2013 Abstracts*. 149. Rotterdam, Oct. 2013
- D. Walraven, B. Laenen, and W. D'haeseleer. "Optimization of subcritical and transcritical ORC's for low-temperature heat sources." In: *Book of Abstracts of the 1st International Seminar on ORC Power Systems*. Delft, Sept. 2011

Working papers

- D. Walraven, B. Laenen, and W. D'haeseleer. "Optimization of the Energy Conversion Starting from Low-T Geothermal Heat, General Considerations & State of the Art". Working paper. 2011

FACULTY OF ENGINEERING SCIENCE
DEPARTMENT OF MECHANICAL ENGINEERING
APPLIED MECHANICS AND ENERGY CONVERSION
Celestijnenlaan 300 box 2421
B-3001 Heverlee
daniel.walraven@kuleuven.be
http://www.mech.kuleuven.be